MECHANICS OF BIOPOLYMER NETWORKS, STIMULI RESPONSIVE PARTICLE SUSPENSIONS, AND THEIR COMBINATIONS

BY

GAURAV CHAUDHARY

DISSERTATION

Submitted in partial fulfillment of the requirements
for the degree of Doctor of Philosophy in Mechanical Engineering
in the Graduate College of the
University of Illinois at Urbana-Champaign, 2019

Urbana, Illinois

Doctoral Committee:

Associate Professor Randy H. Ewoldt, Chair and Director of Research
Professor Kenneth S. Schweizer
Professor Sascha Hilgenfeldt
Professor Paul V. Braun

ABSTRACT

The key aim of this thesis is to demonstrate new paradigms in designing stiffness changing soft materials. The systems developed and studied in this work have salient and unprecedented features such as (1) the ability to controllably stiffen up to 100 times (10,000 %) when exposed to an external stimulus of temperature or magnetic field, (2) the ability to uncontrollably assemble into a ultra-soft hydrogel by undergoing 10,000 fold volume expansion within 0.4 s, and (3) transformation from a repulsive colloidal glassy state to a particulate gel thus undergoing change in the dynamics and mechanical properties. With a combination of rigorous experiments and mathematical models, this thesis offers novel ways to achieve functionality in soft materials and may have numerous applications in the fields of soft robotics, defense, and direct-write additive manufacturing.

In part one of this thesis, a naturally produced biomaterial, hagfish slime is studied to understand its design principles. Hagfish slime is a unique predator defense material containing a network of long fibrous threads each $10 - 15$ cm in length. Hagfish releases the threads in a condensed coiled state known as skeins ($\sim 100\ \mu$m), which must unravel within a fraction of a second and form a soft hydrogel to thwart a predator attack. The mechanisms of how the hagfish controls the unraveling rates, and the properties of the resulting gel are not well understood. The combined experimental and theoretical approach adopted in this thesis address these questions. First, the hypothesis that the viscous hydrodynamics may be responsible for the rapid unravelling rates is considered, and the scenario of a single skein unspooling as the fiber peels away due to viscous drag is discussed. As a result, its is shown that under reasonable physiological conditions viscous-drag-induced unravelling can occur within a few hundred milliseconds, comparable with the physiological time scales. Subsequently, through the rheological study on slime networks it is shown that key rheological and structural features of hagfish slime are insensitive to its concentration, in spite of the uncontrolled gelation process, and this peculiar characteristic may be vital for its physiological use.

In part two, the linear and nonlinear rheology of a model system of soft microgel suspensions is investigated. The interaction pair-potential between the microgel is temperature-

dependent. By increasing concentration of the suspension, a transition from a viscous liquid to an entropic glass to a soft jammed state at low temperatures where the microgels interact via a repulsive potential. Increasing the temperature of the suspension beyond the Lower Critical Solution Temperature [LCST], introduces additional attractive interactions, and results in the formation of particulate gels. The competition between repulsive and attractive interactions gives a rich temperature-dependent rheological response that is also concentration-dependent. An integrated experimental and quantitative theoretical approach is presented to understand the key linear and nonlinear of the suspensions in various regimes.

In part three, two novel soft composite systems capable of unprecedented change in their mechanical properties in response to magnetic and thermal excitation are developed. The composites were formed by integrating stimuli-responsive particles (thermoresponsive microgels and magnetic particles) into the strain stiffening network of biopolymer fibrin. The interactions between the stimuli-responsive particles and biopolymer mesh is hypothesized to induces local stresses in the mesh, which inherently stiffens under the stress owing to its semiflexible nature. This helps achieve a higher sensitivity to the external field in the fabricated composites compared to the traditional flexible-polymer matrix of composite systems. Phenomenological models are developed that quantify this hypothesis, and the derived predictions are qualitatively consistent with the experimental data. This approach of using composites based on semiflexible polymers with strong inherent nonlinearity offers a promising method for developing functional materials with actively tunable mechanical properties.

To my parents.

ACKNOWLEDGMENTS

I am indebted to many individuals in supporting me in achieving some of the goals I had set for graduate school, but more importantly for influencing my opinions, and helping me take a few steps towards becoming the person I aspire to be.

Firstly, I am grateful to my advisor, Randy Ewoldt, for providing me with numerous exciting opportunities and supporting me during the last few years. He has had an immense influence on my thinking. His push towards assigning simple physical intuition to complex phenomenon has refined my approach towards science and engineering. I have certainly not chosen the most efficient paths in many of my research projects to begin with, but his patient attitude towards me has helped me figure out, and discover things for myself. This has given me confidence and belief in myself to take on new challenges in the future.

I have learned so much from Ken Schweizer. His energy, dedication, and professionalism has been very inspiring to me. I was fortunate to have worked closely with him on multiple projects. His honest criticism and care for me, and my work has made a huge difference in my approach towards research and my career choices.

I am very grateful to Paul Braun for supporting and advising several aspects of my research. I have always been impressed with the depth of knowledge and insight Sascha Hilgenfeldt posseses. His course on Soft Solids, and his keen interest in my research has been very beneficial to me. I also thank Jean-Luc Thiffeault from the University of Wisconsin for his key contributions in our hagfish research. I thank Douglas Fudge and his research group from the University of Guelph for hosting my visits to Guelph, and helping me make the most of my time while I was there. I had very productive time in Guelph, and that would not have been possible without the support from Braulio Macias-Rodriguez and Alejandro Marangoni. I have had the luxury of walking into so many world-class facilities at Illinois, and learning from very kind and supportive staff. I am especially thankful to Leilei Yin and Cate Wallace at Beckman Institute for their help with imaging.

I am thankful to my collaborators Ashesh Ghosh, Jin Gu Kang, Chen Wang and Sean Lehman for their contributions in our collaborative projects. Ashesh has patiently taught me some aspects of statistical physics. I have enjoyed my interactions with him both as a

colleague and a friend. Thanks are due to my colleagues Erfan Mohagheghian and Shuqi Lai for their dedication and hard work in our collaborations. Both of them have exposed me to new topics in their respective areas of research. Our collaborations have been very fruitful and helped me widen my perspective.

I feel indebted to Rebecca Corman and Luca Martinetti for their invaluable friendship. I was lucky to have them around. I have sought their opinions and feedback on numerous occasions, both personal and work-related, that made decision making much easier for me on several occasions. I am very thankful to the past and present members of the Ewoldt research group, namely, Ashwin Bharadwaj, Arif Nelson, Jeremy Koch, Piyush Singh and Samya Sen. Each one of them have helped me not only with my research but have been very dependable friends. I have many fond and relaxing memories of interactions with my desk neighbor Carolyn Darling and numerous coffee/dosa breaks with Sharanya.

Finally, I express my deepest gratitude to my parents and sisters. They have always prioritized my needs above anything else. I could not imagine being the person I am today without their unwavering support in my life.

TABLE OF CONTENTS

LIST OF TABLES

LIST OF FIGURES

CHAPTER 1

INTRODUCTION

Responsive soft materials have emerged as an exciting area of research over the last two decades due to the rising demand in their engineering applications such a soft robotics, drug delivery, tissue engineering etc. Such materials are capable of achieving a wide range of switchable material properties when exposed to various external conditions, and thus provide a new dimension to the design of materials. The key idea in several such materials is the conformational and chemical changes that occur within the material as its environment is changed. Such changes often occur on multiple scales, ranging from nanoscale (e.g. in block copolymer brushes, ferrogels), to microscale (e.g. in magnetoyield stress fluids), to macroscale (e.g. geometric instabilities in venus-fly trap). Hierarchical relations often exist between different scales.

1.1 Reconfigurable and Functional Composites

One of the key approaches towards rationally designing responsive soft materials is to design composites with multiple components. The components can be triggered by an internal or external stimulus, to drive new assemblies by changing geometric features, interaction potentials etc. Useful functional behavior can be realized from such assemblies which can offer new solutions in several fields such as energy harvesting and soft robotics.

1.1.1 Responsive Materials in Biology

Many naturally occurring materials exhibit switchable material properties in response to changing physiochemical conditions. Such adaptation behavior is vital for functions such as defense, sensing, motility etc. In general, such responsiveness/adaptation arises from a cascade of events occurring on many hierarchical levels. Fig. 1.1 a-b shows the stiffness change in a sea cucumber near the contacted area. The modulus changes by a factor of 10 (from ~ 5 to ~ 50 MPa). The change is attributed to neurally controlled secretion

of glycoproteins that transiently connect the high-aspect ratio collagen fibers in the inner dermis [1, 2]. Fig. 1.1 c shows the example of a spruce cone which responds to changes in the relative humidity [3, 4]. This mechanism is attributed to the bilayered structure of the cones. The active outer layer of tissue has closely packed long parallel thick-walled cells that expand longitudinally when exposed to humidity and shrink when dried. The inner layer does not respond as strongly as the outer layer [3, 5]. Fig. 1.1 d-e shows the dynamics of a Venus flytrap. The mechanism of snapping is initiated by the mechanical stimulation of trigger hair, which causes the plant to change its principal natural curvatures by the movement of water in its hydrated leaves. This change provides mechanisms for elastic energy storage and release. The leaf then stretches until it reaches a point of instability, and undergoes span-buckling instability [6]. The hydrated nature of lead induces the rapid damping of the vibrations.

1.1.2 Bioinspired Responsive Materials and Beyond

The fascinating adaptive response of biological structures has motivated the design of numerous material systems that can either mimic the biological design or provide new solutions in other domains. An understanding of the underlying phenomenon on various structural scales paves the way for the development of synthetic materials that have numerous applications in growing fields of biomedical devices and soft robotics. Inspired by the stiffness variation in the sea cucumber, Capadona et al.[1] developed a polymer nanocomposite based on a host rubbery polymer and rigid cellulose nanofibers that can reversibly soften by a factor of 40 upon exposure to a chemical regulator. Zhao et al.[7] designed a hydrogel assembly inspired by the snap-buckling instability in a Venus flytrap [6] that exhibits such an instability based on bistable states. A building block of three hydrogels (non-responsive, thermo-responsive, and pH-responsive) achieved reversible switching as shown in Fig. 1.2 a-b. Inspired by the passive movement of pine cones based on its bilayered structure and anisotropic response to hydration, biomimetic structures have been proposed based. Such structures are made from bilayered films from different materials [5] or varying the extent of crosslinking in the layers [8]. Fig. 1.2 c shows the demonstration of a bilayered structure analogous to the pine cone made from a paper and plastic layer which can bloom and close based on the surrounding moisture.

Other strategies in designing stimuli-responsive materials have been established and evolved over the last few decades. Field-responsive materials can undergo reversible or irreversible transition in response to applied stimulus. Various physical stimuli have been of much interest since they can be applied remotely. Common examples of such stimuli

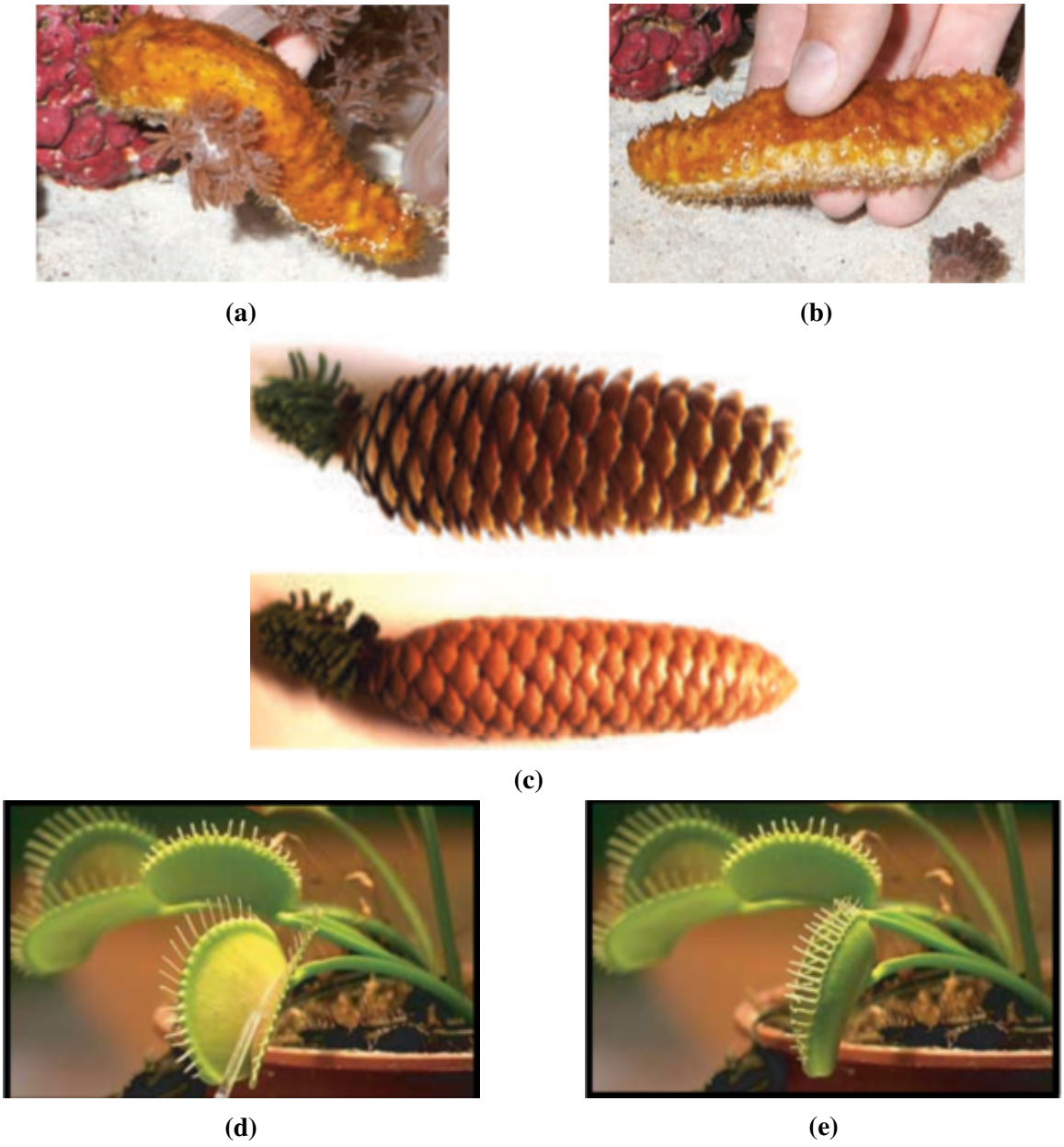

Figure 1.1: Biological responsive systems. (a-b) Sea Cucumber in its relaxed state and stiff state when touched (image adapted from [1]). (c) A spruce cone responds to ambient humidity, it changes shape and opens up when dry (top) and close when wet (bottom) (adapted from [4]). (d-e) A Venus flytrap undergoing a snap-buckling instability in going from an open to close state (adapted from [6]).

are photo [9, 10], electro [11, 12], magneto [13, 14], ultra-sound [15, 16] and temperature [17]. Fig. 1.3 a shows the temperature-controlled sol-gel transition in an organogel based on Azobenzene-containing poly(aryl ether) dendron. The gel undergoes morphological transformation from a nanofiberous network to a microsphere suspension [18]. Fig. 1.3 b

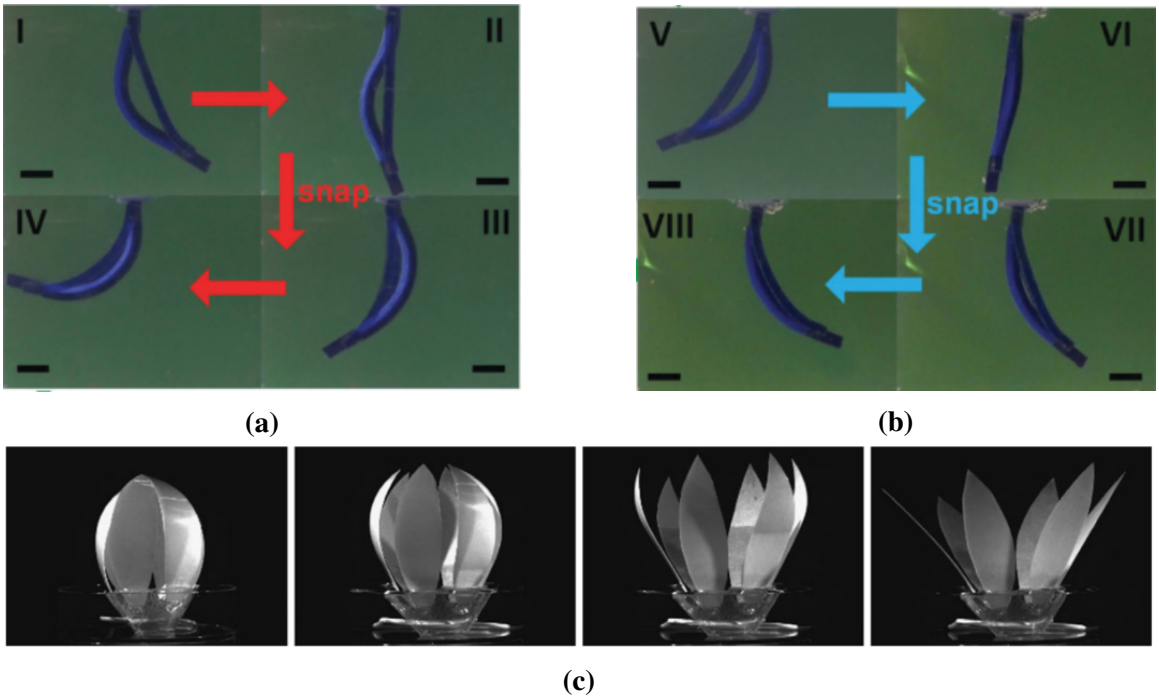

Figure 1.2: (a-b) Reversible snapping of hydrogel assembly (scale bar=5 mm). At neutral pH in (a), increasing temperature from 20 to 40°C leads to snapping. At 20°C in (b), changing pH from 7.0 to 2.0 leads to snap-back of assembly (adapted from [7]). (c) A pine-cone inspired flower-like structure (petal length $\approx$ 4 cm) of paper-plastic exhibits controllable blooming and wilting. The structure blooms in water and closes when water supply is exhausted (adapted from [5]).

shows a magnetoresponsive lattice structure built from magnetically active particle-filled tubes. Upon exposure to various strengths of magnetic field, the elements of the structure vary in their mechanical strength, and hence can bend/buckle to varying degrees [19].

1.1.3 Stimuli-Responsive Polymer-Colloid Composites

Polymer-colloid composites offer attractive opportunities to design new materials by tailoring the properties of individual components or tuning the interaction between the different components. However, synthesizing such composites is often a challenging task because of competing interactions between different building blocks. A common strategy in successfully designing stimuli-responsive materials is to organize the stimuli-responsive (active) component into a passive matrix. Under an external or internal stimulus, the collective interactions between the components are altered, hence new equilibrium/non-equilibrium rules are established. This process can potentially alter the physical properties of the composite.

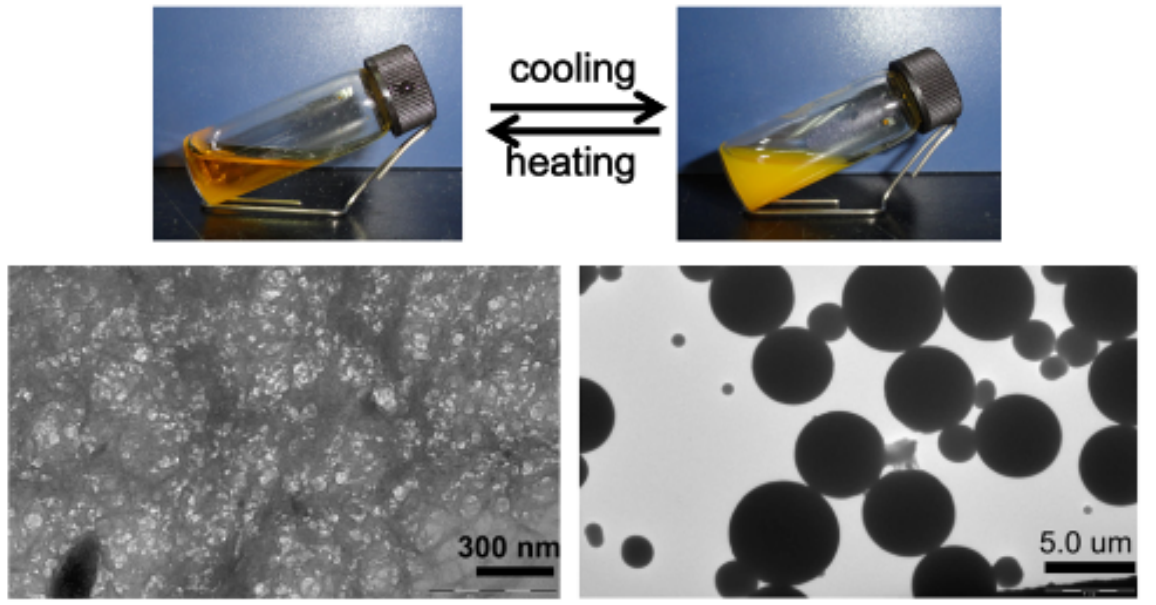

(a)

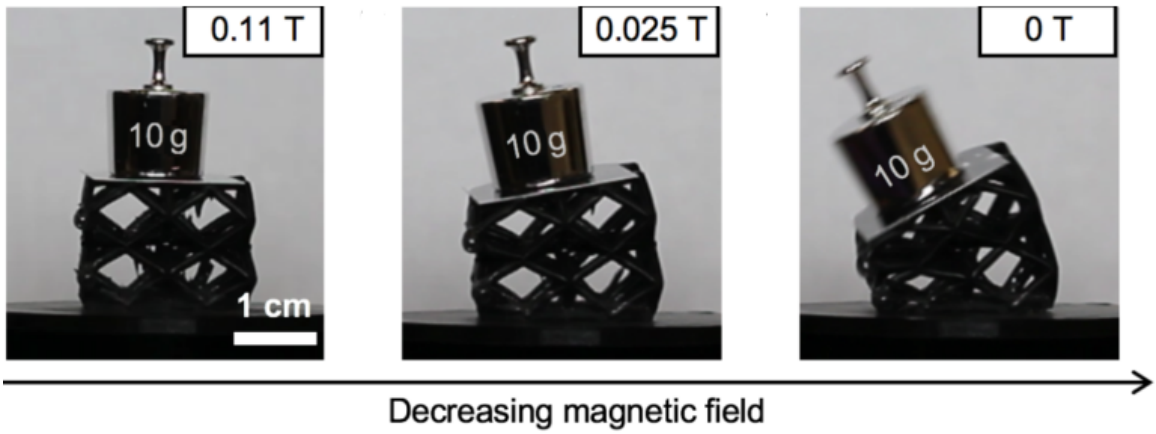

(b)

Figure 1.3: (a) Thermoresponsive sol-gel transition in an organogel. On cooling the organogel undergoes morphological change from nanofibers to microspheres and turns into suspension (liquid) (adapted from [18]. (b) Magentomechanical behavior of a lattice structure made from polymer tubes filled with magnetic particles. (adapted from [19]).

Typical polymer-colloid composites are composed of a colloidal component dispersed in a polymeric matrix. Generally, the colloid size is either larger or comparable to the mesh size. Traditionally, addition of hard colloidal particles in elastomers has been employed as a means to enhance the mechanical properties of the composite (filler effect). Interesting phenomenon arises when a colloidal component is composited with either polymer melts or transiently crosslinked networks. For example, in the case of nanocomposite polymer melts

the glass transition temperature and the viscosity of composite melt changes. Additionally, the interactions between the polymer-colloid can lead to various possible microstates. For example, attractive interactions between the colloidal component can drive the aggregation of suspended colloids if the polymer-colloid attraction strength is not strong enough. Progress has been made on the theoretical front by Schweizer and coworkers to quantitatively predict the microstructure of such composites.

Different paradigms can be realized when the colloidal size is smaller than the polymeric matrix mesh size. The colloids in such composites can diffuse/move faster and provide exciting opportunities to design re-organizable microstructures, thus enabling more dramatic stimuli-responsive property changes. The recent developments in the reversible actuation of colloidal assemblies combined with the large mesh size polymer networks can help achieve unprecedented material systems.

1.2 Systems of Interest

The responsive soft materials studied in this thesis have an underlying fibrous structure. The properties (material and geometric) of individual fibers and their connectivity in a network form determines the bulk materials properties. The specific systems studied include hagfish slime, volume-changing microgels synthesized from flexible chain polymers, and composites from semiflexible polymer fibrin. Significant work has been done with respect to certain aspects of these systems in the literature. This thesis addresses some of the lingering questions and introduces some new ideas for the development of novel materials. One of the pioneers in the field of rheology and viscoelasticity, John Ferry, also pioneered the work on hagfish slime and fibrin (see Fig. 1.4).

1.2.1 Hagfish Slime: A Volume Expanding Hydrogel

Hagfish slime is a defense mechanism of deep sea dwelling hagfish against predator attacks. Slime is formed outside the body of a hagfish from a very small quantity of biomaterial (exudate) which is secreted from hagfish slime glands which then expands in sea water achieving expansion ratios up to 10,000 [21] as shown in Fig. 1.5. This process occurs within a fraction of a second ($\approx 100 - 400$ ms) [22, 23]. Several key aspect of this biophysical process lack a rigorous understanding. The specific questions that are addressed as a part of this thesis are:

- How to account for fast timescales of slime formation?

Figure 1.4: John Douglas Ferry, who made significant contributions to polymer science and viscoelasticity, published one of the earliest work on the hagfish slime [20]. Ferry's early fibrinogen work (1942-1957) led to 41 publications. His later work (1971-1988) produced an additional 36 papers. (source: National Academy of Sciences Biographical Memoirs)

- How robust is the slime formation?
- How sensitive are the properties to the concentration?
- What roles do the various constituents of slime play?

Chapter 2 describes a theoretical framework based on experimental observations of a single thread cell unraveling, and makes a conclusive case for the hypothesis that hydrodynamic stress is a leading cause for such fast unraveling. Chapters 3 and 4 focus on the mechanics of hagfish slime networks.

1.2.2 Soft pNIPAM Microgel Suspensions

Self-crosslinked poly(N-isopropylacrylamide) (pNIPAM) microgel suspensions are used as a model system to probe the linear-nonlinear rheology of such systems. Such a system brings additional complexity in its dynamics compared to hard-sphere colloids since the particles are deformable with a fluctuating internal polymeric microstructure, which can lead to their size and even shape becoming a function of thermodynamic state (volume fraction, temperature, ionic strength) and deformation. Most microgels are charged and can be created with diverse chemistry, which introduces concentration-dependent complexities

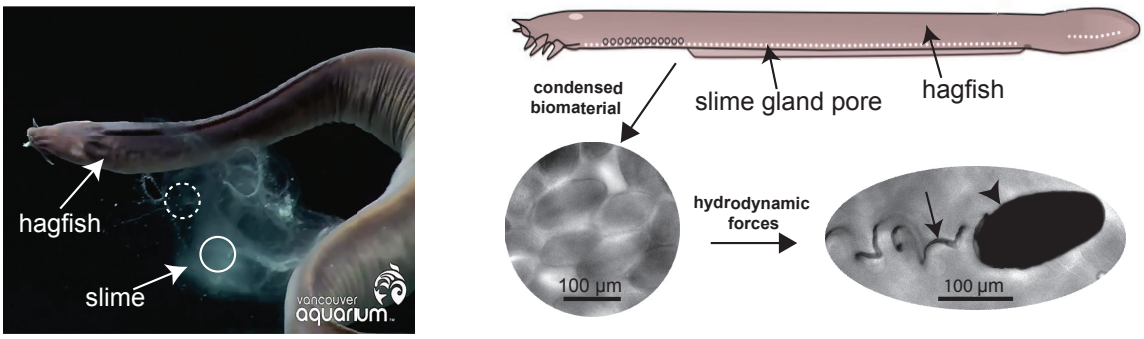

(a) (b)

Figure 1.5: (a) Hagfish produces large volumes of slime when threatened (image courtesy: Vancouver Aquarium You Tube channel). (b) Slime is produced by release of small volume of exudate which expands rapidly in sea water.

associated with osmotic decompression, the poorly known internal density profile (often core-shell), and variable single particle mechanical stiffness. Hence, the effective interaction potential between microgel particles is a complex issue, consistent with a lack of universal signatures in their rheology. Through a combined experimental and theoretical study we address the following questions:

- Quantitatively understand structure, quiescent relaxation, shear elasticity, and nonlinear yielding of dense repulsive microgel suspensions
- Quantitatively understand the transition from a glassy state to a gel-like response when the temperature is varied across the LCST

Chapter 5 describes the mechanics of such concentration-varying suspensions at low temperatures and Chapter 6 focuses on the temperature-dependent effects in such suspensions.

1.2.3 Stimuli-Responsive Semiflexible Polymer-Colloid Composite

New paradigms in designing stiffness changing soft materials are described and demonstrated. Our approach involves combining stimuli-responsive particles (thermoresponsive microgels and magnetically active particles) with a semiflexible biopolymer network of fibrin. When exposed to an external stimulus of thermal excitation or magnetic field, the interactions between the embedded particles and fibrin network lead to an unprecedented increase in stiffness by up to 100 times. We hypothesize that the stimuli responsive particles induce local stress in the biopolymer matrix which intrinsically stiffens under stress.

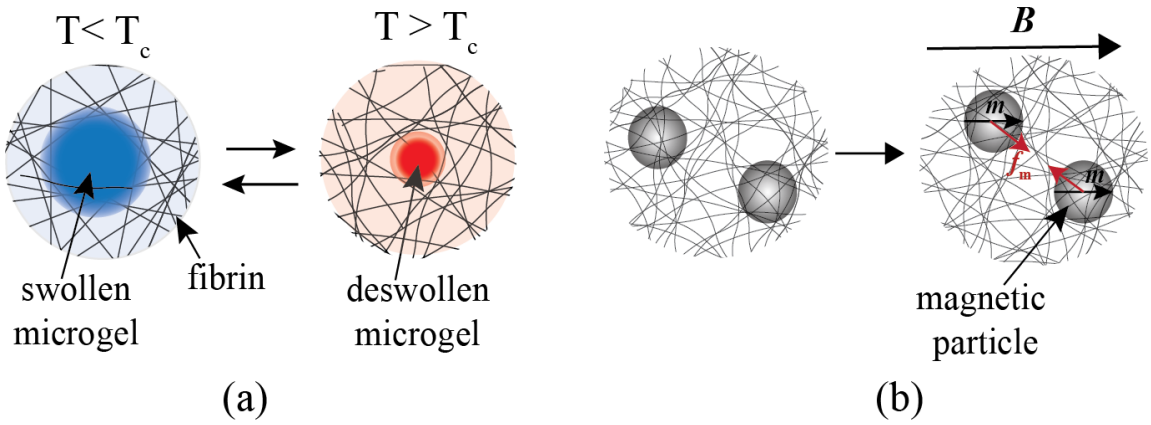

Figure 1.6: Stimuli-responsive polymer-colloid composites. (a) The microgel deswelling across a critical temperature induced changes in the polymer matrix. (b) The magnetic interactions between dipoles stresses the polymer matrix.

In the case of thermoresponsive composites the drastic deswelling of the microgels deform fibrin filaments, thus leading to stiffening. The interactions between magnetic dipoles plays an analogous role in the case of magnetoresponsive composites. Phenomenological models are developed that quantify these hypothesis, and the derived predictions are qualitatively consistent with the experimental data.

Chapter 7 describes the fabrication, characterization, and modeling of thermoresponsive composites, and Chapter 8 focuses on the magnetoresponsive composites.

CHAPTER 2

UNRAVELING HAGFISH SLIME

2.1 Introduction

Marine organisms present numerous interesting examples of fluid-structure interactions that are necessary for their physiological functions such as feeding [24, 25], motion [26], mechanosensing [27], and defense [28]. A rather remarkable and unusual example of fluid-structure interaction is the production of hagfish slime, also known as hagfish defense gel. The hagfish is an eel-shaped deep-sea creature that produces the slime when it is provoked [29]. Slime is formed from a small amount of biomaterial ejected from the hagfish's slime glands into the surrounding water [21]. The biomaterial expands by a factor of 10,000 (by volume) into a mucus-like cohesive mass, which is hypothesized to choke predators and thus provide defense against attacks (Fig. 2.1A) [23]. Such defense mechanisms have been observed in several species of hagfish [30, 23].

The secreted biomaterial has two main constituents — gland mucus cells and gland thread cells — responsible for the mucus and fibrous component of slime, respectively [29, 31]. The plasma membranes of both kinds of cells shear off when secreted from the slime glands [31, 32]. In the present study we focus on the secreted thread cells, referred to as skein from here on. Skeins possess a remarkable structure wherein a long filament (10–$16\,\mathrm{cm}$ in length) is efficiently packed in canonical loops into a prolate spheroid (120–$150\,\mu\mathrm{m}$ by 50–$60\,\mu\mathrm{m}$) [31, 21] (Fig. 2.1B). When mixed with the surrounding water, the fiber (1–$3\,\mu\mathrm{m}$ thread diameter) unravels from the skein (Fig. 2.1C) and forms a fibrous network with other threads and mucous vesicles. This process occurs on timescales of a predator attack (100–$400\,\mathrm{ms}$), as apparent from the video evidence [23, 22].

While several studies have revealed the mechanical and biochemical aspects [33, 34, 35,

This chapter appeared in the following peer-reviewed publication: Chaudhary, G., R. H. Ewoldt, and J.-L. Thiffeault, "Unraveling hagfish slime," Journal of the Royal Society Interface, 16(150), 20180710 (2019), doi: https://doi.org/10.1098/rsif.2018.0710

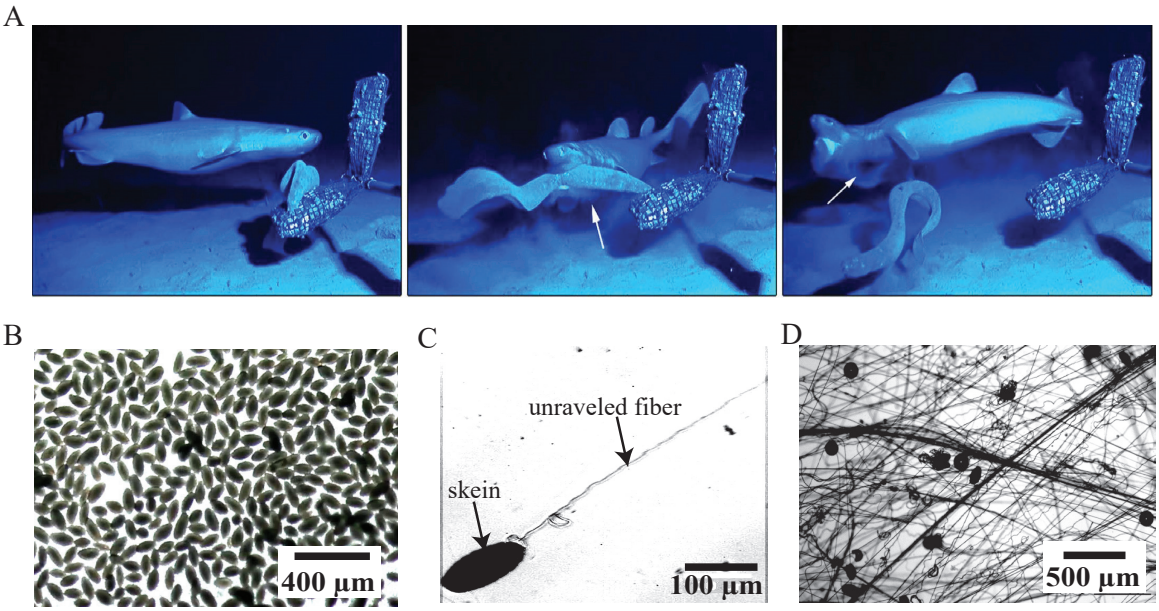

Figure 2.1: Slime defends hagfish against predator attacks. (A) Sequence of events during a predator attack (adapted from Zintzen et al. [23], by permission from SpringerNature). On being attacked, the hagfish produces a large quantity of slime that chokes the predator. The process of secretion and slime creation took less than $0.4\,\mathrm{s}$. (B) Slime is formed from the secreted biomaterial, in part containing prolate-shaped skein. (C) A skein unravels under the hydrodynamic forces from the surrounding flow field and produces a micron-width fiber of length 10–$15\,\mathrm{cm}$. (D) The unraveled fibers and mucous vesicles entrain a large volume of water to form a cohesive network. Details on materials and microscopy are provided in the Appendix A.1.

36, 37] of slime, little is known about mechanisms involved in its rapid deployment. More recently, efforts have been made to understand the mechano-chemical aspects of the mucus components, and their swelling and rupture [38, 39], but such an approach has yet to be extended to the mechano-chemical processes in the unraveling of skeins. Newby [40] postulated that the fiber is coiled under a considerable pressure and the rupture of the cell membrane allows the fiber to uncoil. However, later studies [41, 22, 42] have shown that convective mixing is essential for the production of fibers and slime. More recently, Bernards et al. [32] experimentally demonstrated that Pacific hagfish skeins can unravel even in the absence of flow, potentially due to chemical release of the adhesives holding the fiber together, but the timescales observed in their work are orders of magnitude larger than physiological timescales during the attack. Therefore, the key question about the fast timescales involved in this process remains to be answered. Deeper insights into the remarkable process of slime formation will aid the development of bioinspired material systems with novel functionality, such as materials with fast autonomous expansion and

deployment. Motivated by the aforementioned experimental studies, our objective in this paper is to investigate the role of viscous hydrodynamics in skein unraveling via a simple physical model, and thus supply a qualitative understanding of the unraveling process.

The key question we answer here is whether the viscous hydrodynamic unraveling alone can account for the fast unraveling timescales that are observed in physiological scenarios. We hypothesize that suction feeding in marine predators creates sufficient hydrodynamic stresses to aid in the unraveling of skeins and set up the slime network. We develop fundamental insight by considering only the simplest flow fields — uniform flow and extensional flow. Our modeling framework, however, generalizes to complex flow fields that occur in physiological conditions.

In Sec. 2.2, we present a simple qualitative experiment demonstrating the force-induced unraveling of a hagfish skein. This motivates the model paradigm that follows. Section 2.3 outlines the problem statement, and we derive the general governing equations. In Sec. 2.4, the equations are solved for skein unraveling in one-dimensional flows under different physically-relevant scenarios. In Sec. 2.5 we discuss the results in more detail, including the influence of constitutive model parameters for the peel strength, and comment on the qualitative comparisons between the experimental studies and theoretical work.

2.2 Unraveling Experiment

To motivate the mathematical modeling, we perform a simple experiment demonstrating the force-induced unraveling of thread from a skein (Fig. 2.2). A skein, obtained from Atlantic hagfish, is held in place by weak interactions with the substrate, and a force is applied to the dangling end using a syringe tip that naturally sticks to the filament. Figure 2.2 shows the unraveling skein at different time frames. Frame 1 shows the unforced and stable configuration, with no unraveling. Unraveling occurs only when a force is applied from frame 2 onward. There are events when the thread peels away in clumps, but the orderly unraveling recovers quickly. A minimum peeling force seems required to unravel the thread from the skein. A simple estimate of the minimum peeling force based on weak adhesion (van der Waals interaction) between unraveling fiber and skein gives an estimate of $0.1\ \mu\mathrm{N}$ (see Appendix A.2).

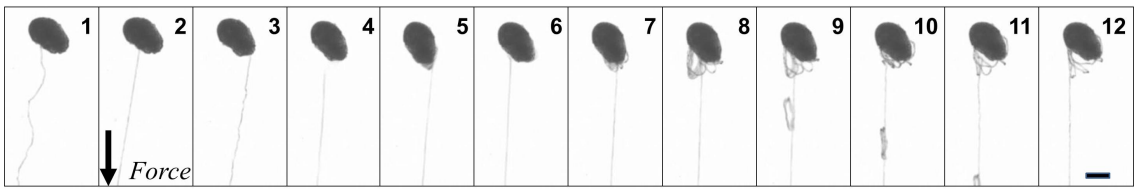

Figure 2.2: Unraveling a thread skein by pulling, as viewed with brightfield microscopy. Bottom right scale bar $50\,\mu\mathrm{m}$.

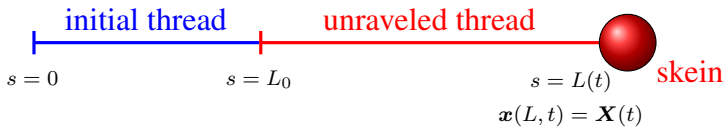

Figure 2.3: Simplified model of thread being drawn from a skein. The thread has length $L(t)$ with initial length $L(0) = L_0$. Here s is the arclength material (Lagrangian) coordinate along the unraveled thread, with $0 \leq s \leq L(t)$. The fixed lab (Eulerian) coordinate of the thread is $\boldsymbol{x}(s,t)$, with the thread peeling from the skein at $\boldsymbol{x}(L(t),t) = \boldsymbol{X}(t)$.

2.3 Problem Formulation

To determine if viscous hydrodynamic forces can account for fast skein unraveling, we consider a model of an inextensible slender thread unraveling from a spherical skein. The thread unravels and separates from the skein in response to a local force due to a viscous fluid flow surrounding the connected thread and skein. A schematic representation is shown in Fig. 2.3. Here $\boldsymbol{x}(s,t)$ is the Eulerian (lab) coordinate of the centerline of the filament as a function of the Lagrangian (material) thread arclength s, $0 \leq s \leq L(t)$, with $L(t)$ the time-dependent unraveled thread length. The thread is peeling from the skein at the Eulerian point $\boldsymbol{x}(L(t),t) = \boldsymbol{X}(t)$, which may depend on time if the skein is allowed to move.

2.3.1 Hydrodynamic Force Balance

We assume inertial effects, filament self-interactions, and external Brownian and gravitational forces to be negligible. The fluid dynamics in this situation are described by the Stokes equations. For the most general case of a thread in viscous flow, a local balance of filament forces and viscous forces (using local drag theory for a slender filament) is given by [43]

$$8\pi\mu\,\delta\left(\boldsymbol{x}_t - \boldsymbol{u}(\boldsymbol{x},t)\right) = -\left(\left(1+2\delta\right)\mathbb{I} + \left(1-2\delta\right)\hat{\boldsymbol{s}}\hat{\boldsymbol{s}}\right)\cdot\boldsymbol{f}. \tag{2.1}$$

Here the tangent to the thread is $\hat{\boldsymbol{s}}$, the dynamic viscosity is μ, and

$$\delta = -1/\log(\varepsilon^2 \mathrm{e}) > 0, \quad \text{with} \quad \varepsilon = r/L, \tag{2.2}$$

are the slenderness parameter and thread aspect ratio, respectively, with r the thread radius.

The internal net force per unit length, $\boldsymbol{f}$, of an inextensible filament is expressed by the Euler–Bernoulli bending theory for an elastic beam, and has both tensile and bending components:

$$\boldsymbol{f}(s) = -(T\,\boldsymbol{x}_s)_s + E\,\boldsymbol{x}_{ssss}\,, \qquad |\boldsymbol{x}_s| = 1. \tag{2.3}$$

Here E is the bending modulus of the thread, $T(s,t)$ is the tension in the filament, and each subscript s denotes one derivative, e.g. $\boldsymbol{x}_s = \partial \boldsymbol{x}/\partial s$. The inextensibility condition is $|\boldsymbol{x}_s| = 1$, so s and distance along the thread must always coincide.

In the spirit of rheology, we consider the response to simple flows to isolate key features of the complex behavior, obtain analytical results, and gain an understanding of the unraveling process. We only consider cases with zero curvature, $\boldsymbol{x}_{ss} = 0$, immersed in one-dimensional flow fields, with the thread aligned with the flow streamlines. Equation 2.1 then reduces to a one-dimensional statement that the component of internal net filament force per unit length $f(s)$ along the streamline (taken as the x direction) is equal to the local viscous drag per unit length:

$$4\pi\mu\,\delta\,(x_t - u(x,t)) = -f. \tag{2.4}$$

Then the one-dimensional form of Eq. (2.3) with $x_{ssss} = 0$ and the inextensibility condition $x_s = 1$ gives $f = -T_s$, so that

$$T_s = 4\pi\mu\,\delta\,(x_t - u(x,t))\,. \tag{2.5}$$

With $x_s = 1$ and $x(L,t) = X(t)$ we have $x = X - L + s$, where X is the skein position, and thus $x_t = \dot{X} - \dot{L}$. We integrate (2.5) from $s = 0$ to L to find

$$T|_{s=L} - T|_{s=0} = 4\pi\mu L\,\delta\left(\dot{X} - \dot{L} - \frac{1}{L}\int_0^L u(X - L + s, t)\,\mathrm{d}s\right). \tag{2.6}$$

We then change the integration variable to $x = X - L + s$, and finally obtain

$$T_L - T_0 = -4\pi\mu L\,\delta\left(\dot{L} - \dot{X} + \bar{u}(L, X, t)\right) \tag{2.7}$$

where $T_L = T|_{s=L}$, $T_0 = T|_{s=0}$, and $\bar{u}(L, X, t)$ is the average velocity on the filament:

$$\bar{u}(L, X, t) \coloneqq \frac{1}{L} \int_{X-L}^{X} u(x, t)\, \mathrm{d}x\,. \tag{2.8}$$

Equation (2.7) expresses the balance between the tension forces at the end of the thread and the drag force on the thread. We shall use this equation to derive a peeling formula for different thread-skein configurations in Sec. 2.4. But first we need to examine how the thread will peel from the skein to unravel.

2.3.2 Unraveling from the Skein

The relationship between R and L, respectively the radius of the spherical skein and the length of the unraveled thread, is described by volume conservation

$$\frac{d}{dt}\left(\tfrac{4}{3}\pi\eta R^3 + \pi r^2 L\right) = 0 \quad \Longrightarrow \quad \dot{L} = -4\eta R^2 \dot{R}/r^2. \tag{2.9}$$

Here r is the thread radius and $0 < \eta \leq 1$ is the packing fraction of thread into the spherical skein, assumed independent of R. (In this section we keep the packing fraction as a variable, but in all later numerical simulations we take $\eta = 1$, since the skein is fairly tightly packed.) Explicitly, we have

$$R^3 = R_0^3 - \tfrac{3}{4}(L - L_0) r^2/\eta \tag{2.10}$$

with R_0 the initial skein radius and L_0 the initial unraveled length. A convenient way of relating R and L is

$$R = R_0 \left(\frac{L_{\text{max}} - L}{L_{\text{max}} - L_0}\right)^{1/3}, \qquad L_{\text{max}} \coloneqq L_0 + \tfrac{4}{3}\eta R_0^3/r^2 \tag{2.11}$$

where L_{max} is the total length of thread that can be extracted and L_0 is the initial unraveled length.

Next, we use a modified form of the work-energy theorem [44] to describe the unraveling dynamics,

$$\dot{E}_{\text{total}} = (T_L - F_{\text{P}}(V))\, V, \qquad V = \dot{L}\,, \tag{2.12}$$

where $\dot{E}_{\text{total}}$ is the rate of change in total energy of the system, T_L is the net force (given by Eq. (2.7)) drawing out the thread at a peeling velocity V, and $F_{\text{P}}(V)$ is a velocity-dependent peeling force acting at the peeling site. Neglecting the inertia and changes to the

elastic energy of the peeling thread gives

$$T_L = F_{\mathrm{P}}(V), \qquad V = \dot{L}\,. \tag{2.13}$$

A natural dimensionless quantity that will determine the dynamics of the unraveling process is given by the ratio of the net viscous drag force on the thread and the resisting peel force, each of which depends on a characteristic velocity U:

$$\wp := F_{\mathrm{D}}(U)/F_{\mathrm{P}}(U)\,. \tag{2.14}$$

The functional form of the peeling force, $F_{\mathrm{P}}(V)$, in general is dependent on parameters such as the chemistry of peeling surfaces, velocity of peeling, etc. In the absence of a known functional form for hagfish thread peeling, we use a simple constitutive form of peeling force that includes a wide range of behavior, given by

$$F_{\mathrm{P}}(V) = \alpha V^m, \qquad 0 \le m \le 1, \tag{2.15}$$

for constant $\alpha > 0$ and m. Such a power-law form of peeling force has been observed in several engineered and biological systems [45, 46, 18, 47, 48]. Several other parametric forms of velocity-dependent peeling force exist that are functionally more complex [49, 50]. However, to obtain simple and insightful solutions, we use the power-law form defined above. The form (2.14) allows for the limiting case $m = 0$, a constant peeling force, e.g. to simply counteract van der Waals attractions at the peel site.

For $m > 0$, we can rearrange equation (2.13) for the velocity, $V = \dot{L} = (T_L/\alpha)^{1/m}$. Using (2.9) we can then obtain a solution for the case where the tension at the peeling point, T_L, is constant:

$$\tfrac{4}{3}(R_0^3 - R^3) = (T_L/\alpha)^{1/m}\, r^2 t/\eta\,, \tag{2.16}$$

where $R_0 = R(0)$. From (2.16) we can easily extract the 'depletion time' or 'full-unraveling time' t_{dep} by setting $R = 0$:

$$t_{\text{dep}} = \frac{4\eta R_0^3}{3r^2}\,(T_L/\alpha)^{-1/m}\,. \tag{2.17}$$

In the next section we compute this timescale when the skeins are subjected to different hydrodynamic flow scenarios, which cause different time histories of tension, $T_L(t)$.

2.4 Skein in One-dimensional Flow

Having described the unraveling dynamics in Sec. 2.3.2 for the case of constant tension, T_L, we now consider a skein in a hydrodynamic flow where generally T_L varies in time as the thread-skein geometry changes during unraveling. In physiological scenarios the flow can arise from the hagfish-predator motion, or the suction feeding of the predator, or a combination of both. To simplify the problem we assume an incompressible flow of the form

$$\boldsymbol{u}(x, y, t) = (u(x, t), -yu_x(x, t)). \tag{2.18}$$

The thread will be assumed to lie along the x axis. We solve for the depletion time for four relevant cases: Pinned thread in uniform flow (Sec. 2.4.1); Pinned skein in uniform flow (Sec. 2.4.2); Free skein and thread in extensional flow (Sec. 2.4.3); and Free skein splitting into two smaller skeins in extensional flow (Sec. 2.4.4).

2.4.1 Pinned Thread

The simplest case to consider is the thread pinned at $s = 0$ in Fig. 2.3, with a uniform flow to the right, $u(x, t) = U$. This situation can arise in a controlled experiment if the thread is pinned down, or in the physiological unraveling process if the end of the thread is caught in the network of other threads, or stuck on the mouth of a predator.

The tension in the thread at $s = L$ balances the Stokes drag on the skein of radius R, $T_L = T(L(t), t) = 6\pi\mu R\,(u(L, t) - \dot{L})$. Using (2.13) and (2.15), we obtain the governing equation for unraveling as

$$(\dot{L})^m = 6\pi\mu\alpha^{-1}R(L)\,(u(L, t) - \dot{L}). \tag{2.19}$$

From (2.9), since $\dot{L} > 0$ (the thread never 're-spools'), the unspooling speed satisfies $\dot{L} \leq u(L, t)$, i.e. the thread cannot unspool faster than the ambient flow speed. The radius $R(L)$ is given by (2.10).

We nondimensionalize (2.19) using a characteristic length scale R_0 and flow speed U which gives

$$(\dot{L}^*)^m = \wp\, R^*(L^*)\,(u^*(L^*, t^*) - \dot{L}^*) \tag{2.20}$$

where $\dot{L}^* = \dot{L}/U$, $R^* = R/R_0$ and $u^*(L^*, t^*) = u(L, t)/U$ are the nondimensional unraveling rate, skein radius, and flow rate, respectively. The nondimensional timescale naturally results from these choices as $t^* = t/(R_0/U)$. The dimensionless quantity $\wp$ on the right

hand side of (2.20) is given by

$$\wp = \frac{6\pi\mu R_0\, U}{\alpha U^m} = 6\pi\mu R_0\, U^{1-m}\alpha^{-1}\,. \tag{2.21}$$

This is the ratio of characteristic drag to peeling force, as defined in (2.14). If $\wp$ is large (e.g. zero resistance to peeling), then (2.19) implies $\dot{L} \approx u(L,t)$, that is, in this drag-dominated limit the drag force so easily unravels the skein that it advects with the local flow velocity. In the opposite limit of small $\wp$, we get $\dot{L} \approx 0$ and the skein cannot unravel. Hence, we require $\wp \gg 1$ for a fast unravel time.

To achieve the criterion $\wp \gg 1$, at a flow of speed $U = 1\,\mathrm{m/s}$ and a skein of initial radius $R_0 = 50\,\mu\mathrm{m}$, we require the peeling resistance at this velocity to satisfy $F_{\mathrm{P}}(1\,\mathrm{m/s}) \ll 1.4\times10^{-6}\,\mathrm{N}$. The estimated van der Waals peeling force is much lower than this threshold, $F_{\text{vdW}} \sim 10\,\mu\mathrm{N}$. At such a flow speed a skein containing $16.7\,\mathrm{cm}$ of thread (an upper bound physiological value) will unravel affinely (kinematically matching the flow speed) in roughly $167\,\mathrm{ms}$. This lower bound estimate is commensurate with the rapidity with which hagfish slime is created (100–400 ms).

In Fig. 2.4 we show a numerical solution of (2.19) with a uniform flow for some typical physical parameters values, and assuming a moderately-large force ratio $\wp = 10$. (Equation (2.19) is an implicit relation for $\dot{L}$ which must be solved numerically at every time step; it is a Differential-Algebraic Equation rather than a simple ODE [49].) For these parameters, the kinematic lower bound on the depletion time is $L_{\text{max}}/U \approx 167\,\mathrm{ms}$, and the numerical value is $t_{\text{dep}} \approx 194\,\mathrm{ms}$.

There is a mathematical oddity where the skein might not get depleted in finite time, depending on the exponent m. To see this, consider a skein close to depletion, $L = L_{\text{max}} - U\tau$, where $\tau > 0$ is small. The equation for τ is

$$(-\dot{\tau})^m = \wp\left(\frac{U\tau}{L_{\text{max}} - L_0}\right)^{1/3}(1+\dot{\tau}), \qquad \dot{\tau} < 0. \tag{2.22}$$

Since τ is small and we expect the thread to be drawn out slowly as it is almost exhausted, we take $1 + \dot{\tau} \approx 1$. Hence, we have the approximate form

$$(-\dot{\tau})^m \approx \mathrm{C}^m\,\tau^{1/3}, \qquad \mathrm{C}^m := \wp\,(U/(L_{\text{max}} - L_0))^{1/3} \tag{2.23}$$

for some constant $\mathrm{C} > 0$, with solution

$$\tau(t) \approx \left[\tau_0^{1-\frac{1}{3m}} - \left(1-\tfrac{1}{3m}\right)\mathrm{C}\,t\right]^{\frac{3m}{3m-1}}. \tag{2.24}$$

The behavior of this solution as the skein is almost depleted depends on m. For $m > 1/3$, the exponent $3m/(3m-1)$ in (2.24) is greater than one, so $\tau(t) \to 0$ as t approaches the depletion time, with $\tau'(t_{\text{dep}}) = 0$ so that $L(t)$ has slope zero when the skein is depleted (as can be seen at the very end in Fig. 2.4). We can thus rewrite (2.24) as

$$\tau(t) \approx \left[\left(1 - \tfrac{1}{3m}\right) \mathrm{C}\,(t_{\text{dep}} - t)\right]^{\frac{3m}{3m-1}}, \qquad m > 1/3, \quad t \nearrow t_{\text{dep}}. \tag{2.25}$$

For $m < 1/3$, the exponent $3m/(3m-1)$ is negative, but the factor $1 - \frac{1}{3m}$ inside the brackets is also negative, so that $\tau(t)$ asymptotes to zero as $t \to \infty$ and the skein never gets fully depleted. In that case we write (2.24) as

$$\tau(t) \approx \left[\left(\tfrac{1}{3m} - 1\right) \mathrm{C}\, t\right]^{-\frac{3m}{1-3m}}, \qquad m < 1/3, \quad t \to \infty. \tag{2.26}$$

Physically, for $m < 1/3$ the drag force ($\sim \tau^{1/3}$) is decreasing faster than the peeling force ($\sim (\dot{\tau})^m$).

In practice, it is difficult to see the difference between $m \lessgtr 1/3$ numerically. The thread appears to get depleted even for $m < 1/3$ because of limited numerical precision as L approaches L_{max}. The symptom of a problem is that the depletion time starts depending on the numerical resolution for $m < 1/3$. Of course, the skeins in the hagfish slime do not need to get fully depleted to create the gel, so a power $m < 1/3$ is still applicable. When comparing the different flow scenarios we will explore a range of m and define an "effective deployment" time $t_{\text{dep},50\%}$, when 50% of the thread length is unraveled.

2.4.2 Pinned Skein

When the skein is pinned and the thread is free at the other end, the tension arises from hydrodynamic drag on the thread. Such a scenario can arise if the skein is arrested in the network of other fibers or in a mucus network.

Consider a free thread ending at $s = 0$ and a pinned skein at $s = L(t)$ (Fig. 2.3), so that the Eulerian skein position X is fixed and is thus not a function of time. Unlike the pinned thread case in Sec. 2.4.1, where a shrinking skein led to a decreasing drag, here the tension *increases* with time as the extended thread provides more drag.

We formulate the problem by imposing boundary conditions at the free end, $T_0 = T(0,t) = 0$, and pinned end, $x(L(t),t) = X$. From (2.7) with $T_0 = \dot{X} = 0$ and $T_L = \alpha\,(\dot{L})^m$, the equation for the growth of the thread is

$$(\dot{L})^m = -4\pi\mu\,\alpha^{-1} L\,\delta(L)\left(\dot{L} + \bar{u}(L,X,t)\right). \tag{2.27}$$

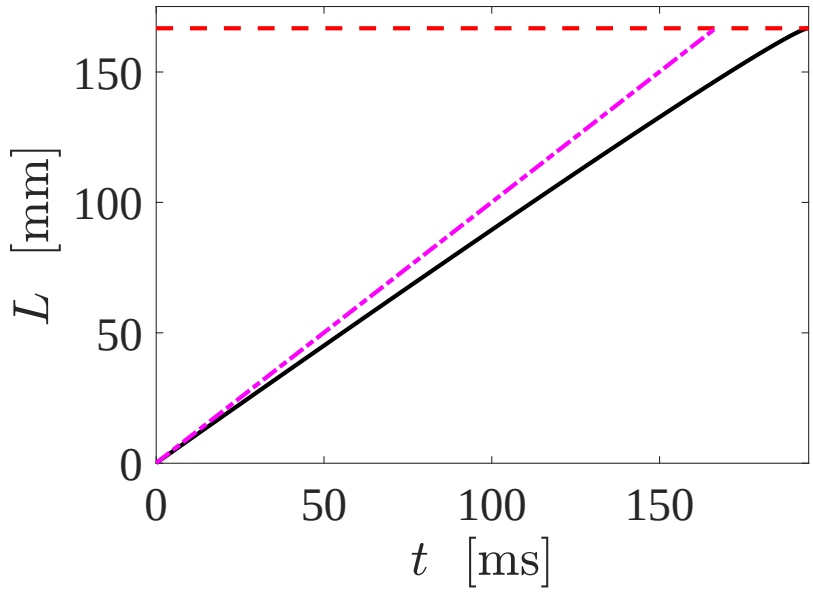

Figure 2.4: Numerical solution (solid line) of (2.19) for the parameter values $R_0 = 50\,\mu\mathrm{m}$, $L_0 = 2R_0$, $\wp = 10$, $m = 1/2$, $U = 1\,\mathrm{m/s}$. The – — line is the upper bound $L = L_0 + Ut$. The horizontal dashed line is at $L = L_{\max}$, when the skein is fully unraveled. Even for such a moderate force ratio $\wp = 10$ the thread unravels almost as fast as the upper bound.

The slenderness parameter δ depends on L through its definition (2.2). Because the thread extends to the left in Fig. 2.3, we must have $\bar{u}(L, X, t) < 0$ to avoid unphysical respooling. The pinned thread equation (2.19) and the pinned skein equation (2.27) have a very similar form, though the drag in the former ($\sim R(L)$) decreases with L and that in the latter ($\sim L\delta(L)$) increases with L.

Using a characteristic velocity U and a characteristic length scale L_0, we obtain the nondimensional form of (2.27) as

$$(\dot{L}^*)^m = -\wp L^* \delta(L^*)(\bar{u}^*(L^*, X^*, t^*) + \dot{L}^*), \tag{2.28}$$

where $\dot{L}^* = \dot{L}/U$, $L^* = L/L_0$, and $u^*(L^*, t^*) = u(L, t)/U$ are nondimensional unraveling rate, unraveled length and flow rate, respectively. The natural dimensionless force ratio (2.14) is

$$\wp = 4\pi\mu\, L_0\, U^{1-m}\, \alpha^{-1}. \tag{2.29}$$

This differs from $\wp$ in (2.21) by replacing R_0 with L_0. It is sensible in this pinned skein case to use the initial thread length L_0, since drag on the thread controls the unraveling rate.

Figure 2.5 shows a numerical solution of (2.27) for our reference parameter values using a constant velocity field, $u(L, X, t) = -U = -1\,\mathrm{m/s}$. As before, the lower bound on the

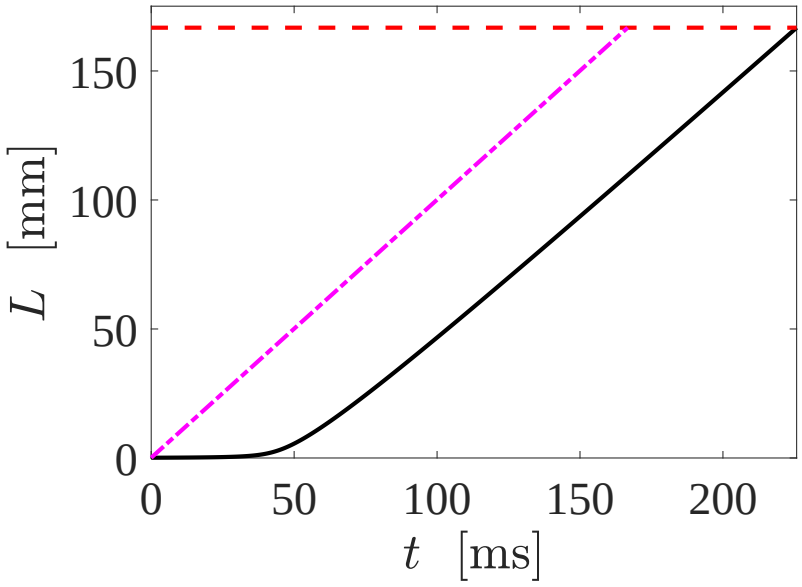

Figure 2.5: Numerical solution (solid line) of (2.27) for the parameter values $R_0 = 50\,\mu\text{m}$, $L_0 = 2R_0$, $\wp = 1/2$, $m = 1/2$, $U = 1\,\text{m/s}$. The – — line is the upper bound $L = L_0 + Ut$. The horizontal dashed line is at $L = L_{\text{max}}$, when the skein is fully unraveled. Even for such a small force ratio $\wp$ the thread unravels almost as fast as the upper bound.

depletion time is $L_{\text{max}}/U \approx 167\,\text{ms}$, and now the numerical value is $t_{\text{dep}} \approx 226\,\text{ms}$. This is slower than what we observed in the pinned thread case ($t_{\text{dep}} \approx 194\,\text{ms}$), but here we are using the much smaller force ratio $\wp = 1/2$. This shows that the pinned skein case can unravel almost as fast as the lower bound for a much smaller value of $\wp$, since the drag on the thread increases with L, as reflected by the accelerating speed $\dot{L}$ in Fig. 2.5. This is in contrast to the deceleration in Fig. 2.4 for the pinned thread, where drag decreases as the skein radius diminishes.

2.4.3 Free Skein and Thread

In the previous two cases, we took either the thread or skein to be pinned; here we consider the case where neither is pinned, and both are free to move with the flow. This scenario is possible if both the thread and the skein are not stuck to the existing fibrous network, or at the beginning of the slime formation when none of the skeins have unraveled to a significant extent.

The force at the peeling point $x(L(t), t) = X(t)$ is then determined by the balance of two forces: Stokes drag on the spherical skein, $F_1 = 6\pi\mu R\,(u(X,t) - \dot{X})$, and drag on the thread, $F_2 = -4\pi\mu L\delta\,(\dot{L} - \dot{X} + \bar{u}(L, X, t))$. The latter is obtained from (2.7)

with $T_L = F_2$ and $T_0 = 0$. Since both the skein and thread are free and we have neglected inertia, $F_1 + F_2 = 0$, which we can use to solve for $\dot{X}$, the velocity of the peeling point in the Eulerian (lab) frame. Coupling this with the peel force constitutive model (2.13)–(2.15), the unspooling rate equation is then $\alpha(\dot{L})^m = F_1 = -F_2$. The dynamics of this scenario are governed by the system

$$(\dot{L})^m = -\frac{12\pi\mu\alpha^{-1}RL\delta}{2L\delta + 3R}\,(\dot{L} + \bar{u}(L, X, t) - u(X, t)), \tag{2.30a}$$

$$\dot{X} = \frac{2L\delta}{2L\delta + 3R}\,(\dot{L} + \bar{u}(L, X, t)) + \frac{3R}{2L\delta + 3R}\,u(X, t), \tag{2.30b}$$

where $\bar{u}(L, X, t)$ is the thread-averaged velocity (2.8). The velocity (2.30b) for the thread-skein system is the average of a velocity $\dot{L} + \bar{u}(L, X, t)$ arising from drag on the thread and a velocity $u(X, t)$ arising from drag on the skein, weighed by the relative strength of the drags.

The difference $\bar{u}(L, X, t) - u(X, t)$ that appears in (2.30a) implies that adding a constant to the velocity field does not change the unspooling dynamics, as expected since the thread-skein system is freely advected by the flow, and only relative velocities generate drag. Hence, unlike our previous two cases in Secs. 2.4.1–2.4.2, a spatially-varying flow field is required for unraveling. For a linear velocity field $u(x, t) = \lambda x$, i.e. uniaxial extensional flow with extensional strain rate λ, we have $u(X, t) - \bar{u}(L, X, t) = \frac{1}{2}\lambda\, L$ independent of X, so that we can solve the $\dot{L}$ equation (2.30a) by itself:

$$(\dot{L})^m = \frac{6\pi\mu\alpha^{-1}RL}{L + (3R/2\delta)}\,(\tfrac{1}{2}\lambda\, L - \dot{L}). \tag{2.31}$$

The mass conservation equation (2.10) then relates R to L, and the slenderness parameter (2.2) relates δ to L.

To define a characteristic length scale for this problem, should we use R_0 or L_0 as a length scale? Both are important for the unraveling process to start quickly, but typically L_0 is a bit larger than R_0. A compromise is to use R_0 as the viscous drag length scale and $U = \lambda L_0$ as the velocity scale. The choice of R_0 emphasizes the magnitude of the drag on the skein, and λL_0 reflects the amplitude of velocity gradients over the longer length L_0. We thus obtain the dimensionless form of (2.31) as

$$(\dot{L}^*)^m = \wp\,\frac{R^* L^*}{L^* + (3R^*/2\delta)}\,(\tfrac{1}{2}L^* - \dot{L}^*) \tag{2.32}$$

where $\dot{L}^* = \dot{L}/\lambda L_0$, $R^* = R/R_0$, and $L^* = L/R_0$ are nondimensional unraveling rate,

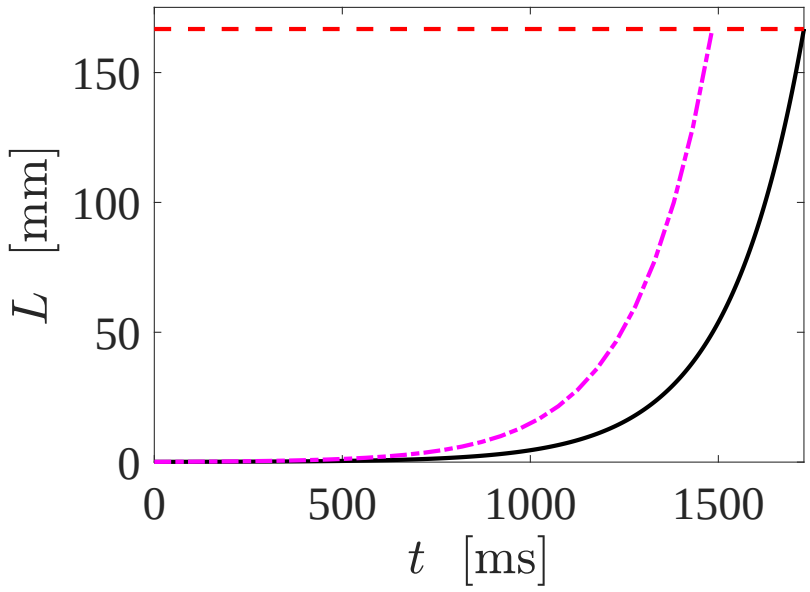

Figure 2.6: Numerical solution (solid line) of (2.31) for the parameter values $R_0 = 50\,\mu\text{m}$, $L_0 = 2R_0$, $\wp = 10$, $m = 1/2$, $\lambda = 10\,\text{s}^{-1}$. The – — line is the upper bound $L_0 \exp(\frac{1}{2}\lambda t)$. The horizontal dashed line is at $L_1 = L_{\text{max}}$, when the skein is fully unraveled.

skein radius and unraveled length, respectively. The natural dimensionless number in this case is

$$\wp = \frac{6\pi\mu\, R_0\, U}{\alpha\, U^m} = 6\pi\mu\, R_0\, (\lambda\, L_0)^{1-m}\, \alpha^{-1}. \tag{2.33}$$

Assuming as before that $\dot{L} \geq 0$ (the thread doesn't 're-spool'), the right-hand side of (2.31) implies $\dot{L} \leq \frac{1}{2}\lambda\, L$, which gives the constraint that $L(t) \leq L_0\, \text{e}^{\frac{1}{2}\lambda t}$. This constraint is the kinematic limit where the thread extends at a rate dictated by the strain rate in the flow. This implies that the depletion time satisfies

$$t_{\text{dep}} \geq 2\lambda^{-1} \log(L_{\text{max}}/L_0). \tag{2.34}$$

In the two pinned cases we considered before, the lower bound on the depletion time was of the form $t_{\text{dep}} \geq L_{\text{max}}/U$, *independent of* L_0. The lower bound (2.34) depends explicitly on the ratio L_{max}/L_0, so a very short initial thread length will take a long time to unravel, even if $\wp$ is large.

When the thread is almost depleted, the unspooling rate decreases due to the factor of R in (2.31). To see this explicitly, put $L = L_{\text{max}} - U\tau$ in (2.31) and assume τ and $\dot{\tau}$ are small:

$$(-\dot{\tau})^m \approx \tfrac{1}{2}\wp \left(\frac{U\tau}{L_{\text{max}} - L_0}\right)^{1/3} \frac{L_{\text{max}}}{L_0}, \qquad \tau \ll 1. \tag{2.35}$$

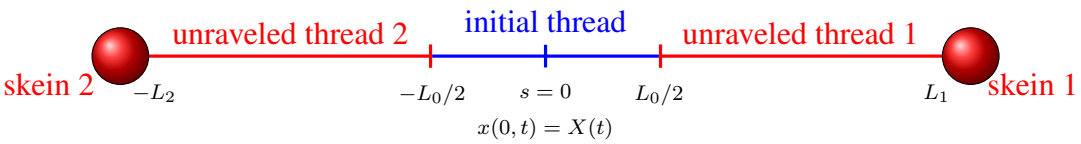

Figure 2.7: Thread being drawn from two skeins.

This is exactly the same form as (2.23), with a different constant C. We conclude that once again the criterion for finite-time complete unraveling is $m > 1/3$, as it was for the pinned thread case (Sec. 2.4.1). But as before this is not very physically consequential, as it only applies to the last phase of unspooling when the skein is almost completely unraveled.

Figure 2.6 shows a numerical solution of (2.31) for our reference parameter values and with a strain rate $\lambda = 10\,\mathrm{s}^{-1}$ for $\wp = 10$. (We choose λ such that $\lambda L_{\max}$ is of the same order of magnitude as $U = 1\,\mathrm{m/s}$ in the pinned cases.) The lower bound (2.34) on the depletion time is $1.48\,\mathrm{s}$, and the numerical value is $t_{\mathrm{dep}} \approx 1.73\,\mathrm{s}$. This is slower than what we observed in the two pinned cases ($t_{\mathrm{dep}} < 1\,\mathrm{s}$), due to the factor $2\log(L_{\max}/L_0) \approx 14.8$. The slowdown due to the short initial thread length is thus considerable in this case. A longer initial length or a higher strain rate would be needed to make the times comparable.

2.4.4 Two Free Skeins (Skein Splitting)

Another scenario of unraveling is when a skein splits into smaller connected fractions, which then unravel. This scenario is possible since the hagfish ejects the skein through its slime gland and the resulting shear forces (from the ejection process and fluid's viscous drag) can break the skein into two.

Here we consider the simple case of a skein breaking into two halves. The unraveling may be faster since the initial viscous drag is dominated by two skeins, rather than a skein and a small initial length of thread. A diagram of this configuration is show in Fig. 2.7: we model the broken skein as two spheres, of radius R_1 and R_2 respectively, connected by an unraveled length of thread, which can unspool at both ends. We fix a reference point $s = 0$ between the two skeins such that $x(0,t) = X(t)$. The thread then extends a length $L_1(t)$ towards the first skein (right) and $L_2(t)$ towards the second skein (left), with $L = L_1 + L_2$ the total unraveled length. Without loss of generality we take $L_1(0) = L_2(0) = \frac{1}{2}L_0$. The peeling force at the first skein ($s = L_1$, $x = X + L_1$) is the sum of the drag forces due to the second skein ($s = -L_2$, $x = X - L_2$) and drag on the thread:

$$T|_{s=L_1} = -6\pi\mu R_2(u(X - L_2, t) - (\dot{X} - \dot{L}_2)) - 4\pi\mu L\delta\,(\bar{u}(L, X, t) - \dot{X}) \qquad (2.36)$$

where now $\bar{u}(L,X,t) \coloneqq \frac{1}{L_1+L_2}\int_{X-L_2}^{X+L_1} u(x,t)\,\mathrm{d}x$. Since the thread and skeins are free, the peeling force at $s = L_1$ (2.36) must balance the viscous drag force on the first skein:

$$T|_{s=L_1} = 6\pi\mu R_1(u(X+L_1,t) - (\dot{X}+\dot{L}_1)). \tag{2.37}$$

Equating (2.36) and (2.37), we can solve for $\dot{X}$:

$$\dot{X} = \frac{3R_1(u(X+L_1,t)-\dot{L}_1) + 3R_2(u(X-L_2,t)+\dot{L}_2) + 2L\delta\,\bar{u}(L,X,t)}{3(R_1+R_2)+2L\delta}. \tag{2.38}$$

We use this to eliminate $\dot{X}$ from (2.37):

$$\begin{aligned} T|_{s=L_1} = \frac{6\pi\mu R_1}{3(R_1+R_2)+2L\delta}(&3R_2(u(X+L_1,t) - u(X-L_2,t) - \dot{L}) \\ &+ 2L\delta(u(X+L_1,t) - \bar{u}(L,X,t) - \dot{L}_1)). \end{aligned} \tag{2.39}$$

We can then also carry out the same calculation for the second skein, at $s = -L_2$, and find

$$\begin{aligned} T|_{s=-L_2} = \frac{6\pi\mu R_2}{3(R_1+R_2)+2L\delta}(&3R_1(u(X+L_1,t) - u(X-L_2,t) - \dot{L}) \\ &- 2L\delta(u(X+L_2,t) - \bar{u}(L,X,t) + \dot{L}_2)). \end{aligned} \tag{2.40}$$

Now it is a matter of solving the coupled peeling equation $\alpha(\dot{L}_1)^m = T|_{s=L_1}$, $\alpha(\dot{L}_2)^m = T|_{s=-L_2}$. To keep things simple, let us take a symmetric configuration centered on $x = X = 0$ where the two skeins are initially of equal size. (Unequal splitting would result in a depletion time in between this case of even splitting and the free skein-thread of Sec. 2.4.3.) We take an antisymmetric velocity field $u(x,t) = -u(-x,t)$ that pulls apart the skeins, such as for an extensional flow $u = \lambda x$. Then $R_1 = R_2$ and $L_1 = L_2$ for all time, and $\bar{u} = 0$. The tensions (2.39) and (2.40) are then equal and greatly simplify to $T|_{s=L_1} = T|_{s=-L_2} = 6\pi\mu R_1\,(u(L_1,t) - \dot{L}_1)$. Thus, the dynamics for this case is governed by

$$\alpha(\dot{L}_1)^m = 6\pi\mu R_1\,(u(L_1,t) - \dot{L}_1). \tag{2.41}$$

The drag force on the thread has dropped out, since the antisymmetric velocity field leads to canceling forces on the thread. Another way to think of (2.41) is to observe that in making a symmetric configuration, with the two skeins being pulled apart by a straining flow centered on the origin, we have effectively 'pinned' the thread at $x = 0$. We have thus recovered our pinned thread equation (2.19) from Sec. 2.4.1, with the notable difference that now we cannot use a constant velocity field U, but must resort to a straining flow λx

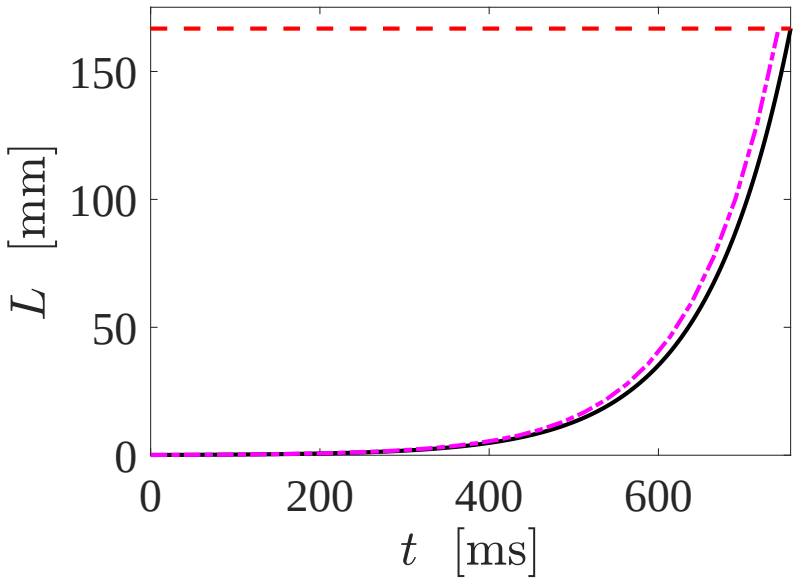

Figure 2.8: Numerical solution (solid line) for the thread half-length $L_1(t)$ using the force for two symmetric free skeins (Eq. (2.41)) for the parameter values $R_1(0) = 50\,\mu\text{m}$, $L_1(0) = 2R_1(0)$, $\wp = 10$, $m = 1/2$, $\lambda = 10\,\text{s}^{-1}$. The – — line is the upper bound $L_1(0)\exp(\lambda t)$. The horizontal dashed line is at $L_1 = L_{1\max}$, when the skein is fully unraveled.

or some other nonuniform flow.

We nondimensionalize (2.41) using a characteristic length scale R_0 and obtain

$$(\dot{L}_1^*)^m = \wp R_1^* \,(u^*(L_1^*, t^*) - \dot{L}_1^*), \tag{2.42}$$

where $\dot{L}^* = \dot{L}/\lambda R_0$ and $R^* = R/R_0$ are the nondimensional unraveling rate and skein radius, respectively. The natural dimensionless number in this case is

$$\wp = \frac{6\pi\mu\,\lambda\,R_0^2}{\alpha\,(\lambda\,R_0)^m} = 6\pi\mu\,R_0^{2-m}\,\lambda^{1-m}\,\alpha^{-1}. \tag{2.43}$$

Figure 2.8 shows the unraveling dynamics associated with a split skein using parameter values similar to the free configuration of Sec. 2.4.3 and Fig. 2.6. The free skein unravels faster when split, as expected ($0.756\,\text{s}$ vs $1.73\,\text{s}$), owing to a stronger effective drag force and a kinematic upper bound with a rate λ rather than $\frac{1}{2}\lambda$. There is an important difference between using the free thread-skein equation (2.30) and the free split-skein equation (2.41): the former has a drag slaved to a short initial thread length, whereas for the latter the drag depends on the initial radius of the split skein, which can easily be larger.

In addition to the four cases discussed in this section, we also analyzed a slightly more

realistic scenario of suction flow where velocity decays away from the mouth of the predator and we consider a pinned skein at different locations away from the mouth. We use an approximate flow profile from the experimental data available in the literature (Appendix A.3). In general, such a flow profile is both spatially and temporally varying, but we neglect time-dependent variations for our analysis. The peak velocity (at the mouth of predator) was chosen to match the characteristic velocity ($U = 1\,\mathrm{m/s}$). The velocity decays over a characteristic length scale on the order of the gape size (e.g. opening size of the mouth). We estimate gape size from the video evidence [23] of slime deployment, resulting in extensional strain rates between 0.28–$2.2\,\mathrm{s}^{-1}$), with the rate being highest at the predator mouth. These are smaller extension rates than considered in the earlier cases of this section. The choice of pinning location drastically affects the unraveling time. A depletion time of $\sim 0.4\,\mathrm{s}$ was obtained for the case where the skein is pinned at a distance equal to 1/3 of the gape size of the predator. This is longer than the unravel time we found for the pinned skein in a uniform flow ($\approx 0.22\,\mathrm{s}$), due to the decaying velocity away from the predator's mouth, but the unraveling time still falls close to natural unraveling time scales. More complicated spatially and temporally varying flow fields can be treated in a similar way; we expect the timescales in such cases to be on the order of those we found, given that in real scenarios the thread-skein system can be very close to or in the mouth of the predator, and the nondimensional quantity $\wp$ is likely to be sufficiently large.

2.5 Discussion

2.5.1 The Role of the Dimensionless Parameters $\wp$ and m

The unraveling times for various cases discussed in Sec. 2.4 depend on the dimensionless quantity $\wp$, but also separately on the model parameter m in the peeling force law. This is clear from the dimensionless governing equations in Sec. 2.4 that depend on these two dimensionless parameters separately, although m also appears in the definition of $\wp$. The power-law exponent m determines the peeling force dependence on the unraveling rate. Such a rate dependence exists in peeling scenarios due to the viscoelastic nature of adhesion at the peeling site. In the case of hagfish thread peeling from the skein, the dependence can possibly arise from viscoelastic timescales involved in the deformation of mucous vesicles or the polymeric solution of mucus [35], or the protein adhesive between the loops of thread [32]. The peeling resistance also depends on the dimensional constant factor, α, but its influence on unraveling is built into the dimensionless factor $\wp$, for which $\wp \sim \alpha^{-1}$.

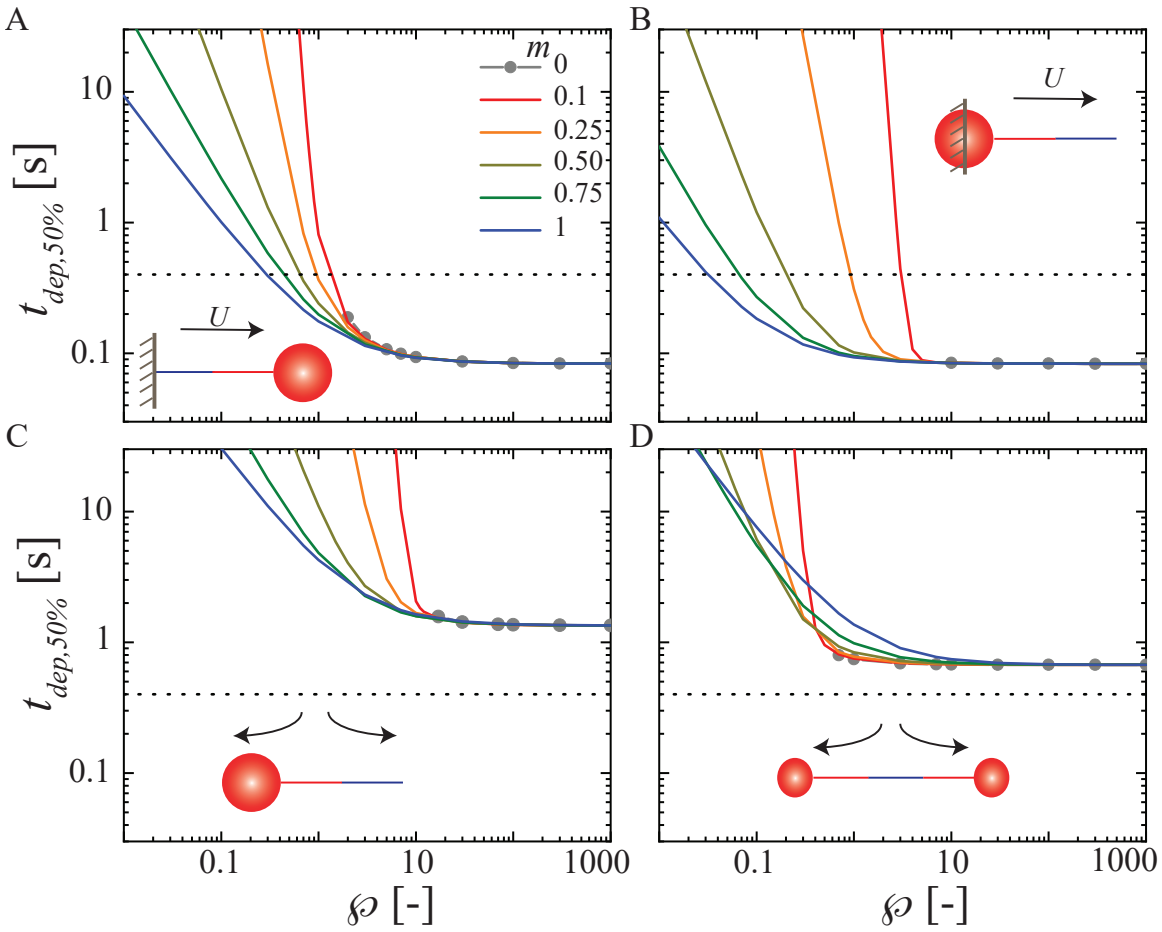

Figure 2.9: Parameter dependence of "effective" unraveling. Comparison of timescale $t_{\mathrm{dep},50\%}$ for unraveling half the total length of the fiber for different values of m, as the dimensionless quantity $\wp$ is varied in different unraveling scenarios. (A) pinned thread in uniform flow, (B) pinned skein in uniform flow, (C) free thread and skein in straining flow, and (D) symmetric free skeins in straining flow. Other parameters used are $r = 1\,\mu\mathrm{m}$, $R_0 = 50\,\mu\mathrm{m}$, $L_0 = 2R_0$, $U = 1\,\mathrm{m/s}$, and $\lambda = 10\,\mathrm{s}^{-1}$. The dotted horizontal line represents the physiologically observed timescale ($= 0.4\,\mathrm{s}$).

Figure 2.9 compares all four flow scenarios of Sec. 2.4 as a function of $\wp$ and m in terms of the effective deployment time, i.e. the time to unravel half of the thread length, $t_{\mathrm{dep},50\%}$. (This effective time is used because some flows cannot fully deplete the skein in finite time for $m < 1/3$, as discussed in Sec. 2.4. Moreover, in practice the threads do not need to be fully unraveled to create slime.) The flow parameters are identical to those previously described. For all cases, the limit of high drag and low peel resistance, $\wp \gg 1$, converges to the kinematic limit of unraveling where unconstrained portions of the skein-thread system exactly advect with the local flow velocity. At the other extreme, viscous drag is weak compared to peel resistance and for some small value of $\wp$ unraveling is too slow to match

physiological timescales.

The power-law exponent m is a secondary effect compared to $\wp$. In general, for $\wp > 10$, m has negligible effect on unraveling times. For $\wp < 10$, the dependence on m is case-specific. For the cases of pinned thread (Sec. 2.4.1), pinned skein (Sec. 2.4.2), and free skein-thread (Sec. 2.4.3), a larger value of m leads to a smaller unraveling time (while keeping the same value of $\wp$). For the case of skein splitting in an extensional flow (Sec. 2.4.4), such a monotonic trend is not observed and above a critical value of $\wp$ the unraveling is faster for small values of m. This presumably arises from the nonlinearity in the peel force constitutive equation. For example, taking $m = 1$ as a reference case, making $m < 1$ *increases* the dimensionless peel resistance for $\dot{L}^* < 1$, but *decreases* the peel resistance for $\dot{L}^* > 1$. As such, whether the unraveling rate is $\dot{L}^* \gtrless 1$, the exponent m can accelerate or decelerate the unraveling process.

The value of m affects the minimum required $\wp_{\text{min}}$ to achieve unravel times comparable to physiological timescales (i.e. $t_{\text{dep},50\%}$ at or below the dotted lines in Fig. 2.9). For the uniform velocity field cases ($U = 1\,\text{m/s}$), $\wp_{\text{min}}$ is a weaker function of m for the pinned thread case, $\wp_{\text{min}} = 0.29$–1.32, compared to the pinned skein case, $\wp_{\text{min}} = 0.03$–3. For the cases of a free skein-thread in extensional flow, even with splitting, $t_{\text{dep},50\%}$ never falls below $400\,\text{ms}$ even at high $\wp$. That is, $t_{\text{dep},50\%}$ is higher than the physiological unravel timescales by a factor of 2 or 3. However, as stated earlier, the timescales in such cases are determined by the specific choice of strain rate, λ, and the initial unravel length L_0. Such kinematic and geometric parameters are certainly variable in reality, and small changes could easily decrease the unravel timescales, as previously discussed. In any case, m becomes important only when depletion timescales are much larger than the kinematic limit, clearly showing that m is of secondary concern compared to $\wp$.

An important caveat to the $m = 0$ case of $F_{\text{P}} = \alpha =$ constant is that peeling cannot occur ($\dot{L} = 0$) if the viscous drag falls below a critical value. For example, if either the initial skein radius R_0 or thread length L_0 is too small, the viscous drag force is less than F_{P} and unraveling cannot occur. Thus, in Fig. 2.9 a minimum value of $\wp$ is needed for the $m = 0$ cases. The minimum values ranges from about 1–10, depending on the case and the corresponding definition of $\wp$ for the flow and geometry. In three cases, the viscous drag can potentially increase during unraveling as the thread elongates (Fig. 2.9B–D). In these cases, the minimum $\wp$ is associated with initiating the peeling process. For the other case of the pinned thread, Fig. 2.9A, the viscous drag decreases during unraveling, since it is slaved to the skein radius which decreases in size during the process. Unraveling here will eventually stop at a critical value of R. This therefore feeds back to requiring a larger critical initial value of $\wp$ to unravel by 50%, and is used in Fig. 2.9A to determine the

domain of $\wp$ for the $m = 0$ case.

2.5.2 Estimating the Parameter $\wp$

A key question remains: what is $\wp$ in physiological scenarios? For this we must know the peeling force parameters in the constitutive model, and no direct experimental measurements are yet available. Here we make estimates for the two extreme conditions of $m = 1$ and $m = 0$, i.e. a linear dependence on velocity (akin to a constant viscous damping coefficient) and a constant peel force, respectively.

For the $m = 1$ case, we consider viscous resistance acting at the peel site with stress $\sigma = \mu_u \dot{\epsilon}$, where μ_u is the uniaxial extensional viscosity between the separating thread and the skein (related to shear viscosity as $\mu_u = 3\mu$), and $\dot{\epsilon} = \dot{L}/L_c$ is the local extensional strain rate that depends on the peel velocity $\dot{L}$ and the characteristic velocity gradient length L_c. The stress acts over the characteristic thread-thread contact area, which we assume scales as $A \approx d^2$, i.e. contact across the diameter and the length of contact along the thread also scales with the diameter. The peel force is then

$$F_{\mathrm{P}} \approx \mu_u \big(\dot{L}/L_c\big) d^2. \tag{2.44}$$

Comparing to the peeling law in (2.15), $F_{\mathrm{P}} = \alpha \dot{L}^m$, we get

$$\alpha = \mu_u d^2/L_c; \qquad m = 1. \tag{2.45}$$

Substituting this into $\wp = F_{\mathrm{D}}/F_{\mathrm{P}}$, and considering the majority of cases where drag is set by the skein radius R_0, i.e. equations (2.21), (2.33), (2.43), we obtain

$$\wp = \frac{6\pi\mu R_0\, U}{\mu_u \big(\dot{L}/L_c\big) d^2} = 6\pi \frac{\mu}{\mu_u} \frac{U}{\dot{L}} \frac{R_0 L_c}{d^2} \tag{2.46}$$

where important ratios have been grouped. The simplest case is peel viscosity arising from the surrounding viscous liquid at the peel site. In other words, the viscosity causing drag is also resisting peeling, and to cast in terms of extensional viscosity we take $\mu_u = 3\mu$, a result for a Newtonian fluid. The viscosity μ may be that of sea water, or a surrounding mucous vesicle solution with higher viscosity, but under these assumptions the ratio μ/μ_u is still the same. Furthermore, typically $U/\dot{L} \gtrsim 1$, and the velocity gradient length scale is likely set by the thread radius, $L_c \approx r$. Then (2.46) dramatically simplifies to

$$\wp = 2\pi R_0/d \tag{2.47}$$

which clearly estimates $\wp \gg 1$, or more specifically for $R_0 = 50\,\mu\mathrm{m}$ and $d = 2\,\mu\mathrm{m}$, $\wp \approx 160$. If drag is instead dominated by the thread length L_0, e.g. for the pinned skein case of Sec. 2.4.2, then the numerator in (2.46) would be modified by replacing $6\pi R_0$ with $4\pi L_0$. We expect L_0 to be the same order as R_0, e.g. a single curl in the coil. But if L_0 is smaller, it would decrease $\wp$ accordingly.

Our specific assumptions can modify the details, but in general we estimate that physiological conditions for $m = 1$ would give $\wp > 1$, if not $\wp \gg 1$. The velocity gradient length scale L_c could be smaller than the thread radius r. A decrease in L_c/r makes $\wp$ proportionally smaller, but it is difficult to imagine this being more dramatic than, say, a factor of 10. The velocity ratio $U/\dot{L}$, if anything, will be larger than 1, and this proportionally increases the estimate of $\wp$. The viscosity ratio μ/μ_u could be smaller, e.g. if the viscosity of proteins between thread wrappings is larger than the surrounding viscous liquid. However, we note that the surrounding viscous liquid can have a very large viscosity, e.g. the measured extensional viscosity of hagfish mucous vesicle solutions obtained by Böni et al. [35] is $\mu_u \approx 10\,\mathrm{Pa}\cdot\mathrm{s}$. This is much higher than water, $\mu_u \approx 3\,\mathrm{mPa}\cdot\mathrm{s}$. An additional mechanism of increasing drag, and $\wp$, is for mucous vesicles to bind on the thread during the unraveling process (Fig. 2.10), which would transmit additional forces to the drag term, as suggested by Winegard et al. [42]. Such a scenario is possible since mucous vesicles and threads cells are densely packed inside the slime glands and are released simultaneously. For all of these variations, $\wp > 1$ seems very likely for physiological conditions in this constant viscosity estimate for $m = 1$.

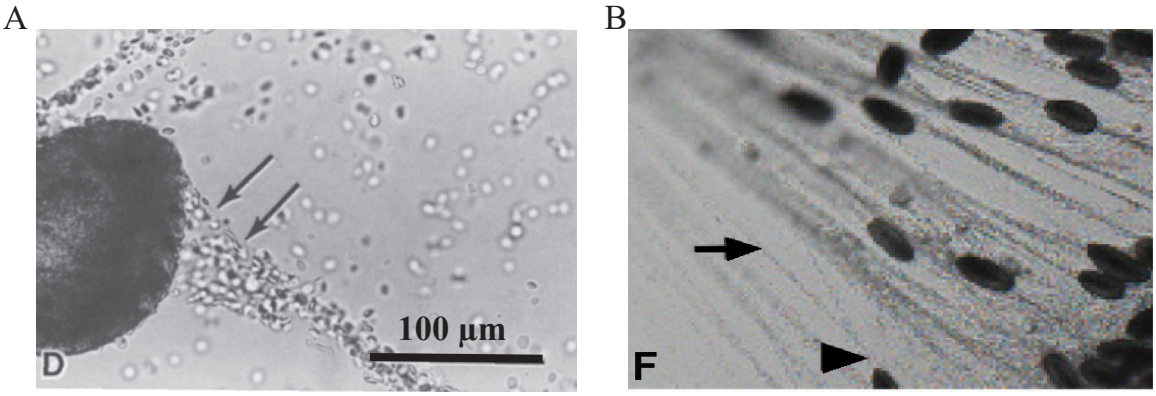

Figure 2.10: (A) Mucous vesicles aggregating on unraveling thread (adapted from Koch et al. [41], by permission from SpringerNature). (B) Mucous vesicles aggregated on unraveling thread elongated along with the fiber under the flow (adapted from Winegard et al. [42], by permission from The Journal of Experimental Biology).

To estimate physiological $\wp$ for $m = 0$, the other extreme of a constant force resisting peel, we consider peel strength interactions between the skein fibers solely due to van der

Waals forces. We estimate $F_{\mathrm{P}} = \alpha \approx 10^{-7}\,\mathrm{N}$ (see Appendix A.2). Substituting into $\wp = F_{\mathrm{D}}/F_{\mathrm{P}}$, and considering cases where drag is set by the skein radius, i.e. Eqs. (2.21), (2.33), (2.43), with $R_0 = 50\ \mu\mathrm{m}$, water viscosity $\mu = 1\,\mathrm{mPa}\cdot\mathrm{s}$, and $U = 1\,\mathrm{m/s}$, gives $\wp \approx 90$. We see that $\wp \gg 1$ with these assumptions. Even if the force resisting peeling is larger by a factor of 10 or 100, still $\wp \gtrsim 1$ and viscous hydrodynamics can provide rapid unraveling that can be very close to the kinematically-derived lower bounds on unraveling time.

2.6 Conclusion

Our analysis shows that, under reasonable physiological conditions, unraveling due to viscous drag can occur within a few hundred milliseconds and is accelerated if the skein is pinned at a surface, such as the mouth of a predator. A dimensionless ratio of viscous drag to peeling resistance, $\wp = F_{\mathrm{D}}/F_{\mathrm{P}}$, appears in the dynamical equations and is the primary factor determining unraveling timescales. Large $\wp$ corresponds to fast unraveling that approaches a kinematic limit wherein free portions of the thread-skein system directly advect with the local flow velocity. For characteristic velocity U, the bound is $t_{\text{dep}} \geq L_{\text{max}}/U$, whereas for extensional flows with strain rate λ, $t_{\text{dep}} \geq \lambda^{-1}\log(L_{\text{max}}/L_0)$, where L_0 is the initial thread length.

The modeling approach captures essential features and insight by considering a single dilute skein unraveling in idealized flow fields. Future modeling efforts could build on our work by expanding and detailing several aspects, primarily with new experimental measurements of peel strength for skein unraveling, but also details of physiological flow fields including characteristic velocities and strain-rates. Real physiological scenarios are more complex due to chaotic flows and multi-body interactions (multiple skeins, mucous vesicles). Our model does not consider such interactions, or the important feature of unraveled threads interacting to create a network. At leading order, we expect such modeling to require more complex flow fields that create extension (to unravel fibers) but also bring different fibers together. Mixing flows would be excellent candidates for theoretical analysis, and any experimental characterization of physiological flow fields should keep this perspective in mind, e.g. simple suction flow with extension, but no mixing, may not be sufficient to create a network of unraveled threads.

Although the physiological flow fields may be different from the ones that were used in the analysis, our results underline the importance of viscous hydrodynamics and boundary conditions on the process. Recent work [32] found that Pacific hagfish skeins undergo

spontaneous unraveling in salt solution. However, the unraveling timescales ($\sim$ min) are much larger than the in physiological timescales ($\sim 0.4\,\mathrm{s}$) during the attack. It is possible that ion transport to the peeling site may help in peeling the adhesive contacts, which may be diffusion-limited without flow. Although it is known that flow is required to accelerate unraveling to $t_{\mathrm{dep},50\%} < 1\,\mathrm{s}$, it is not yet clear whether flow-enhanced ion transport may also contribute to a faster unraveling, in addition to the drag effects. The effects of various salt ions on the swelling and rupture of mucin vesciles have been studied in the past [38, 39], but the influence of such ionic effects on the skeins and their deployment is not yet known. If ion transport and chemistry are important, this would modify the F_{P} behavior and require modeling of transport at the peel site due to flow. Our results do not rule out the possibility of ion-mediated unraveling but provides an alternate mechanism of unraveling which may be occurring alone or in conjunction with a multitude of other processes.

Acknowledgment

We thank Prof. Douglas S. Fudge (Chapman University, CA, USA) for providing the hagfish exudate and for many helpful discussions. GC and RHE are grateful to the National Science Foundation for supporting their contributions to this research under grant number CBET-1342408.

CHAPTER 3

CONCENTRATION-INDEPENDENT MECHANICS AND STRUCTURE OF HAGFISH SLIME

3.1 Introduction

Many species of animals have evolved mechanisms for defending themselves against predators. One such strategy utilized by the deep-sea dwelling hagfishes involves the production of a large volume of a gel-like material, commonly known as hagfish slime or defense gel. Hagfish slime is known to clog the gills of fish predators and threaten them with suffocation [22, 23]. It is different from many other animal secretions in the sense that its rheological complexity is vital to its function, unlike many other secretions where typically the toxicity/ chemical deterrence of the secretion is important e.g. in several arthropods [51, 52], molluscs [53, 54, 55, 56] and mammals [57, 58]. Rheological complexity is also known to influence the physiological performance of several other animal secretions e.g. snail slime [59], frog saliva [60] and coral mucus [61]. Interestingly, unlike most other secretions that are ejected/secreted from an animal's body, hagfish slime is not fully formed until outside the body of the animal in the surrounding water. A very small quantity of biomaterial (exudate) is secreted from hagfish slime glands (Figure 3.1 A-B), which then expands in sea water achieving expansion ratios up to 10,000 [21]. This process occurs within a fraction of a second ($\approx 100 - 400$ ms) [22, 23]. Exudate contains two primary components: thread cells and mucin vesicles [40]. A thread cell is made up of an intermediate filament-based fiber coiled into an ovoid (~ 150 μm) [40]. Mucin vesicles ($\sim 5 - 7$ μm) are glycoprotein containing membrane-bound vesicles. Once the exudate is ejected into the sea water, advective mixing causes thread cells to unravel into long fibers [22], up to $10 - 15$ cm in length and $1 - 3$ μm in diameter, and mucin vesicles swell and rupture [39], to set up a fibrous network [21]. The fiber intermediate-filaments are composed of α and γ proteins

This chapter appeared in the following peer-reviewed publication: Chaudhary, G., D. S. Fudge, B. Macias-Rodriguez, and R. H. Ewoldt, "Concentration-independent mechanics and structure of hagfish slime," Acta Biomaterialia, 79, 123-134 (2018),doi: https://doi.org/10.1016/j.actbio.2018.08.022

[62, 63] and undergo an $\alpha \leftrightarrow \beta$ transition at large strains [64]. The composition of hagfish mucus resembles that of mucin glycoproteins but the relative composition of components, namely: protein, carbohydrates, sulfate and lipids, is different [65]. Recent work focused on exploring the effect of the relative concentration of mucus and thread cells [41, 42] found that mucus is essential for slime formation although its detailed role in slime production and functioning remain to be discovered. Several other works have explored the roles of organic and inorganic ions and compounds on slime production [38, 39].

Recent work [33, 35, 66] on the mechanics of hagfish slime suggests that this material has predominantly elastic properties with a very low elastic modulus(~ 0.01 Pa). A very narrow range ($0.01 - 0.08$ wt $\%$) of concentration was considered in these studies. However, hagfish exudate is ejected into a comparably infinite sea of water and the animal itself cannot directly control the concentration of the resulting network nor its mechanical properties. It is thus vital to understand how the concentration of slime affects its properties and the resulting performance of this material. A recent work [67], focused on water retention in slime over the concentration range of $(0.005 - 0.1)$ wt$\%$, but many questions about the mechanics are yet to be answered.

In this paper, we focus on the viscoelastic shear rheology of this gel over two orders of magnitude variation in its concentration a much wider range compared to our own prior work [33] and those of others [35, 66]. We found that irrespective of concentration, the gel has similar viscoelastic time-dependent properties with constant power law exponent ($n = 0.18 \pm 0.01$), a constant ratio $\tan\delta = G''/G'$, and varying overall stiffness that scales exactly linearly with the concentration ($\sim c^{0.99\pm0.05}$). The power-law creep compliance, with an exponent that is independent of concentration, suggests an underlying self-similar structure at all concentrations. We consider constitutive modeling to understand the time-dependent material properties and find that a three-parameter fractional Kelvin-Voigt model has an excellent agreement with the linear creep response for all concentrations. We gain insights into the structure-property relationship based on the mechanics of an individual fiber and develop a scaling estimate for the bulk response that agrees with our experimental observation.

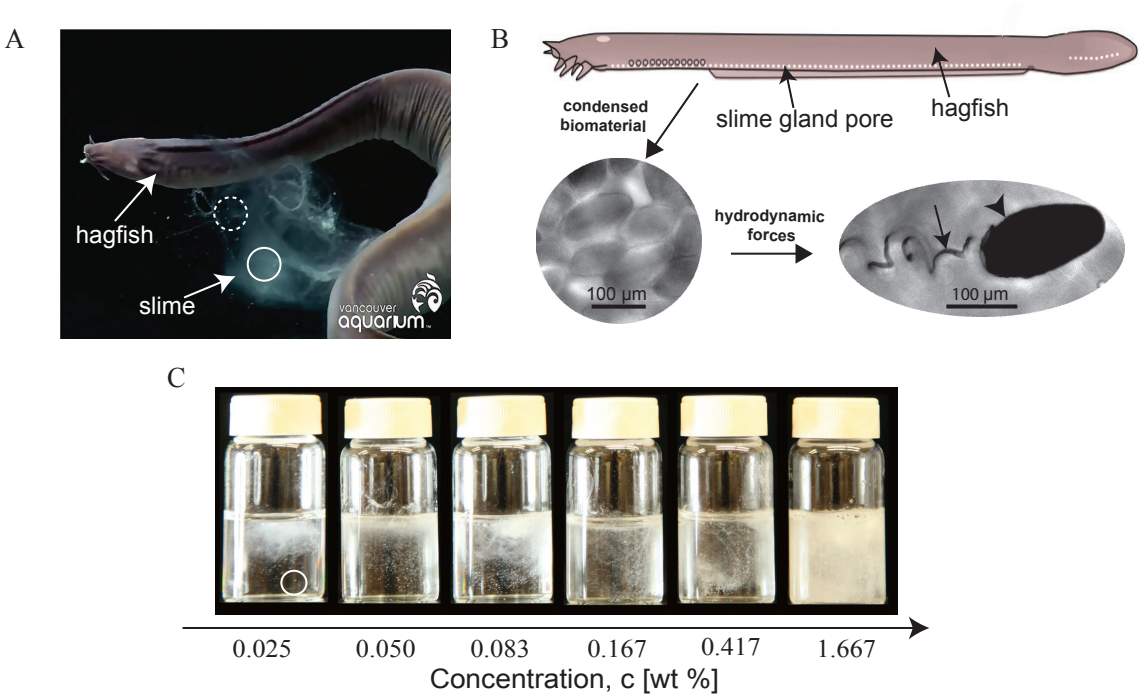

Figure 3.1: Hagfish slime is produced *ex vivo* with an uncontrolled concentration.(A) Hagfish producing slime in a large tank of sea water. Since the exudate is released into a large volume of water, its concentration dependent properties become vital for its functional requirements. Even in the released slime the concentration can vary as apparent from the image (dashed circle corresponds to low concentration, solid circle corresponds to high concentration) (image adapted with permission from Vancouver Aquarium YouTube channel). (B) Hagfish (image adapted [39] with permission) locally ejects a small quantity of biomaterial from its specialized slime pores near the site of stimulus. Thread cells and mucus are major components of the secreted biomaterial, which under the hydrodynamic forces produce slime within a fraction of a second. The fibrous component in slime comes from the Gland Thread Cells that are ovoids of coiled intermediate filament-based fiber (arrowhead) and unravel into long fibers (arrow) when mixed in sea water. These fibers have a diameter of $1-3$ μm and have length up to $10-15$ cm [64]. (C) Hagfish slime samples of varying exudate concentrations (wt $\%$) prepared in the lab by mixing fresh exudate with sea water. Samples with apparent concentration 0.025 wt $\%$ and 0.050 wt $\%$ have significant sol fraction (circle) in them while samples with concentration 0.083 wt $\%$ or greater appear to have a sample spanning network with negligible sol fraction.

3.2 Materials and Methods

3.2.1 Sample Preparation

Pacific hagfish (*Eptatretus stoutii*) were maintained at the University of Guelph as previously described [42]. All housing, feeding, and experimental conditions were approved by the University of Guelph Animal Care Committee (Animal Utilization Protocol 2519). Hagfish were anesthetized before the extraction of exudate. Electrical stimulation near the slime glands resulted in the secretion of the exudate locally near the site of stimulation [42]. The exudate was collected directly from multiple fish using a spatula, stored in a microcentrifuge tube at 10° C (no buffer or oil was used to stabilize) and used within 2-5 hours from the time of extraction to ensure sample viability. A precise volume of exudate was pipetted out and introduced into a larger Falcon tube containing artificially prepared sea water (prepared using commercially available marine salt mix from Coralife, Energy Savers Unlimited, Inc., Carson, CA, USA) at 10°C and the contents were sloshed back and forth in the closed falcon tube six times, similar to prior work [33]. For microscopy studies, smaller volumes (1 ml) of sample were prepared in 1.5 ml microcentrifuge tubes using a similar protocol. Following this, the sample appeared to be a fibrous cohesive mass. Samples with varying concentration of exudate were prepared using this protocol. A few such samples are shown in Figure 3.1 C. Samples with concentrations 0.025 wt $\%$ and 0.05 wt $\%$ had a significant quantity of free solvent present (sol fraction), since the network could not span the entire solvent volume. Only the samples with a volume spanning network were tested in experiments (0.083 wt $\%$ and above). We note that the concentration range tested in this work is higher than the estimates of natural slime concentration [21]. However, as the images of physiologically produced slime (Figure 3.1 A) suggest, the concentration varies spatially in the same sample and hence the local concentration can be very different from the reported physiological concentration.

3.2.2 Microscopy

Gel samples of various exudate concentrations were transferred to glass slides with small wells. A Nikon 90i Eclipse microscope was used to visualize the network with differential interference contrast (DIC).

3.2.3 Rheometry Methods

The viscoelasticity of hagfish slime was probed using rotational rheometers (model AR2000 from TA instruments and model MCR302 from Anton Paar). These are both torque-controlled instruments (a.k.a. combined-motor-transducer type). A single gap concentric-cylinder geometry with fixed outer measuring cup and torque controlled inner bob (with a conical bottom) was used in all experiments. The inner cylinder radius $R_i = 14$ mm and length $L = 41.5$ mm for the AR2000. For the MCR302, $R_i = 13.33$ mm and $L = 40.01$ mm. The gap between the two cylinders was 1 mm and 1.13 mm for the AR2000 and MCR302, respectively. It should be noted that the gap of the rheometer is much smaller than the total contour length of the fibers, which may be up to (10-15) cm [22]. This may raise questions about the continuum assumptions of the material within this confinement. Except for the lowest concentration (0.08 wt%), we note that the typical mesh size of the network is actually much smaller than the millimetric gap, as suggested by DIC images (Figure 3.2). This supports a continuum perspective of the material response. Sample volume was chosen so as to "overfill" above the thin gap region, thus reducing the surface tension effects [68]. This is important since water alone may appear elastic due to surface tension artifacts [69]. As a control experiment, we measure water alone. All tests were done at 10 °C and a solvent trap (a two-piece metal cover) was used to minimize evaporation. Compression and pre-stress of the material may also be a concern. Since the bob is lowered into the gelled material, it may cause deformation and alignment of the fibrous structure. We had no method of assessing the isotropic structure of the network, but we note that we allowed the sample to relax after loading, the moduli we obtain here are comparable with earlier published literature from our group and others [33, 35, 66], and we do not observe normal forces which may be caused by confinement and penetration of the bob. We therefore interpret our measurements as continuum properties of the material. Studies of confinement effects or sample pre-stress are outside the scope of our work here.

Two types of rheological characterizations were performed: creep-relaxation and oscillatory shear. In creep-relaxation tests, the input torque (stress) is a step function up from zero (creep) and then back to zero (relaxation) and the resulting strain was measured as a function of time. In oscillatory shear experiments, sinusoidal deformations of various strain amplitudes and fixed frequency were applied to the sample and the resulting torque signals measured. The tests provide observations of the time-dependent and deformation amplitude-dependent viscoelastic properties of the gel.

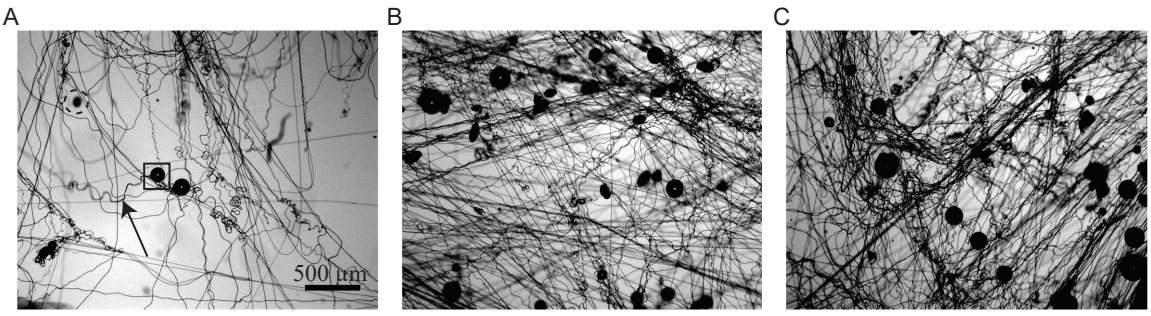

Figure 3.2: Microstructure of hagfish slime. Differential interference contrast (DIC) images of hagfish slime at three concentrations: (A) 0.08 wt $\%$,(B) 0.4 wt $\%$ and (C) 0.8 wt $\%$. Threads (solid arrow) assemble into a network as a result of advective mixing of released exudate with sea water. The network also has packed thread cells (inside dashed circle) which are not fully unraveled. Air bubbles (inside solid square) are entrapped during mixing. Mucus, although present, cannot be seen at this scale.

3.3 Results

3.3.1 Microscopy

Advective mixing of exudate with sea water creates a fibrous gel network. Figure 3.2 shows DIC images of gel networks at three different concentrations: 0.08 wt $\%$, 0.4 wt $\%$ and 0.8 wt $\%$. A network of unraveled fibers can be seen in the images. The fiber density increases with concentration as expected and the topology of the network appears essentially the same. Contacts between fibers are also evident which may be physical junctions. Some intact thread cells can be seen, which are perhaps due to inefficient mixing from our protocol compared to what hagfish can achieve naturally. A few air bubbles are present in the sample, which get entrapped during mixing. It is worth noting that we are not able to see mucus in these images which would need some other imaging technique such as fluorescent labeling [42].

3.3.2 Linear Oscillatory Shear

Linear viscoelastic moduli are shown in Figure 3.3 as a function of the concentration of exudate. A fixed angular frequency $\omega = 0.2$ rad/s was used for all the tests, for which elasticity dominates dissipation. Amplitude sweep data for all the concentrations are shown in the Appendix Figures B.4 A-C, which show that $\gamma_0 = 10\%$ is reasonably in the linear regime (i.e. less than 20% change). Only the first-harmonic response is shown which represents the average energy storage and loss [70, 71]. As expected, the moduli increase

with the concentration. Consistent with the literature [72, 35, 66]; G' has an extremely low value $G' = 0.02$ Pa, at the lowest concentration of 0.083 wt $\%$.

The linear viscoelastic moduli, G' and G'', corresponding to $\omega = 0.2$ rad/s, show a power-law dependence ($G \sim c^k$) on the concentration, with exponents 1.12 ± 0.04 and 1.28 ± 0.11, respectively. This approximate linear dependence is different from many other biopolymer networks [73, 74, 75, 76, 77]. A comparison with some common biological materials is given in the Table 3.1. Consequently, the loss tangent, $\tan\delta = G''/G'$, is independent of the concentration and has values in a very narrow range, $\tan\delta = 0.2 - 0.3$, in the linear regime. More insights into this unique linear concentration dependence of moduli will be provided in the later discussion based on a network model.

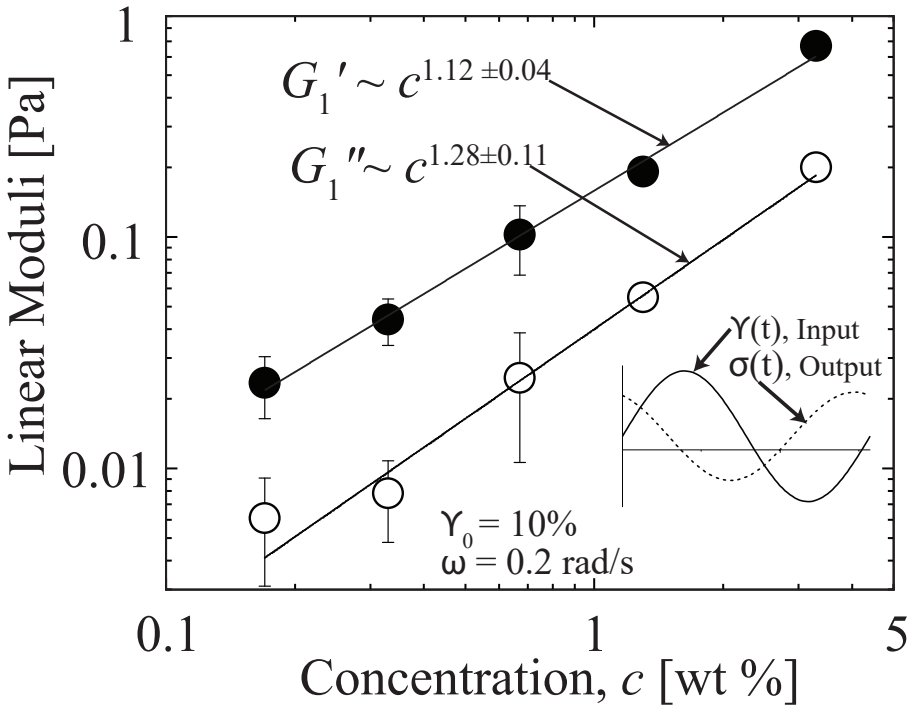

Figure 3.3: Viscoelastic properties vary linearly with concentration. The average elastic (G_1') and viscous (G_1'') moduli extracted from the linear regime ($\gamma_0 = 10\%$, $\omega = 0.2$ rad/s) of oscillatory shear deformation follow a power-law dependence of 1.12 ± 0.04 and 1.28 ± 0.11 respectively. The inset shows the input and output signals for the concentration, 0.67 wt$\%$, processed in MITLAOS [71].

From the nonlinear amplitude sweeps (Appendix Figures B.4 A-B), the strain dependence is similar over the range of concentrations probed i.e. data appears to be vertically shifted for subsequent concentrations. Similar responses are also evident in the raw oscillatory waveform, e.g. shown as parametric Lissajous curves (Appendix Figures B.5-B.6). The average network response softens above a critical strain $\gamma_{critical} \sim 20\%$ and the loss

Table 3.1: Concentration dependence ($G' \sim c^k$) for various biomaterial gels

Material	k
Semi-flexible networks [73, 74]	2-2.5
Methylcellulose [75]	2.27
Hagfish gel	**1.1**
Desmin [76]	0.71
Vimentin [76]	0.48
Human Keratin K8/K18 [77]	0.53

tangent increases due to increasing dissipation at higher strains (Appendix Figures B.4 C). Although the material shows an average softening response (decreasing G_1') with increasing strain, intracycle stiffening can be observed from the Lissajous curves before the sample fails (Appendix Figures B.5-B.6). This indicates that more elasticity is lost at strain $\gamma = 0$ than is lost at the extremes $\gamma = \pm\gamma_0$.

The material being very soft presents several challenges in its rheological characterization [68] on commercial rheometers due to several experimental artefacts. Our control experiments on water agree well with the theoretical predictions for water (Appendix Figures B.4 B). We did not observe any apparent dominant elastic response from water [35] arising from surface tension artifacts [69]. We also estimate and avoid the effects of low torque, instrument inertia, and sample inertia on the measurements [68]. Hence, we believe our measurements have negligible contributions from experimental limits and represent the true material response from the hagfish slime.

3.3.3 Time-Dependent Viscoelasticity

We use creep-relaxation tests to understand the time-dependent viscoelastic properties of hagfish slime. Figure 3.4 shows the observed strain in the samples when a step shear stress of 0.01 Pa is applied for 90 s followed by stress free relaxation (repeat measurements in Appendix Figure B.7). As expected, the samples become stiffer with increasing concentration, i.e. deform less, consistent with the viscoelastic moduli results in Figure 3.3. Upon careful inspection, the strain evolution has a power-law response at longer times rather than a solid-like plateau response described in the literature for hagfish slime [33, 35]. Such a power-law response is observed for several other systems such as foams [78], microgels [79, 80], biopolymer networks [81, 82, 83], gelling suspensions [84], physically cross-linked polymers [85], and protein gels [86, 87]. It is generally believed to originate from the fractal nature of the underlying microstructure [85, 88, 89, 90]. In creep, there is a monotonic dependence on concentration (wt $\%$). However, this is not observed in relax-

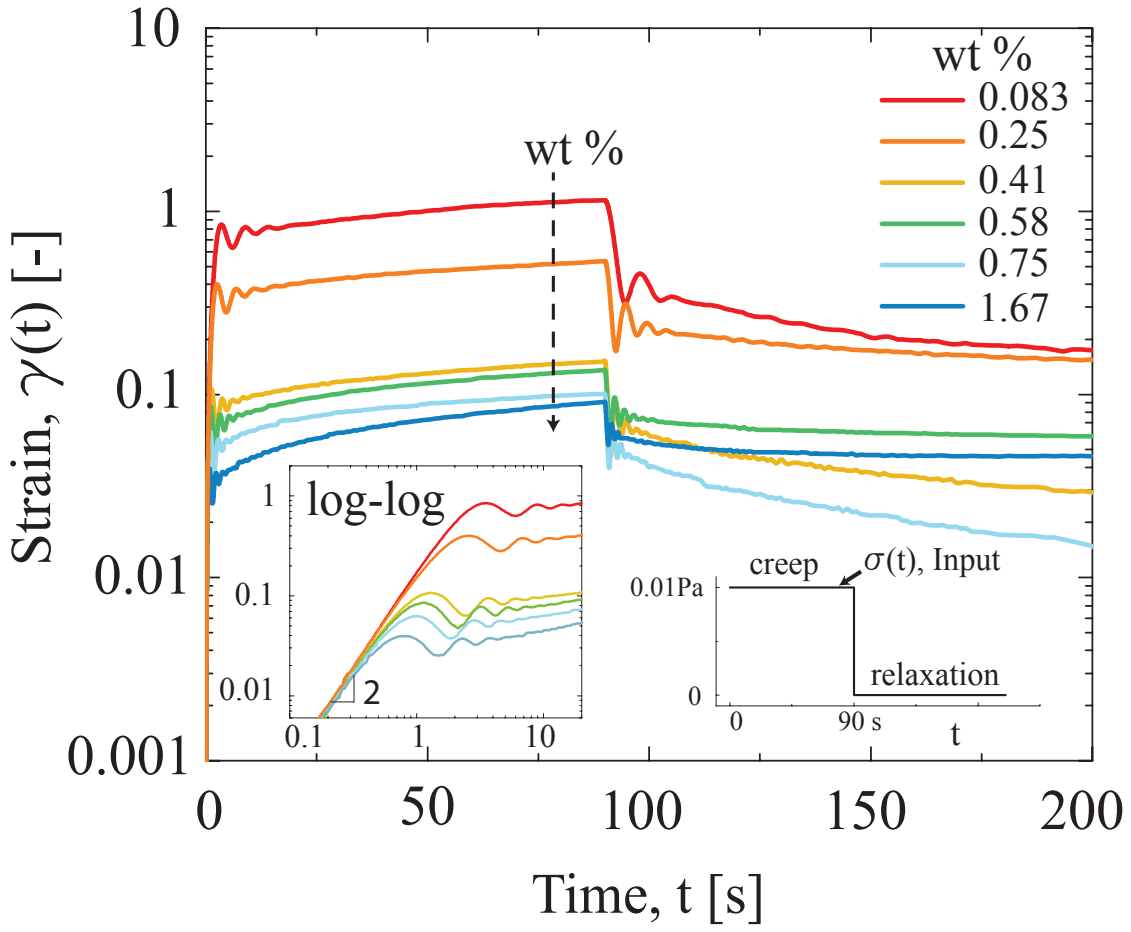

Figure 3.4: Linear viscoelastic creep-relaxation. Material deformation, strain $\gamma(t)$, is observed under an applied shear stress, σ_0 (0.01 Pa in this case) for 90 s. The stress is then removed and the material is allowed to relax. The materials stiffen as the concentration is increased. (Inset) at very short times inertio-elastic ringing is observed as a result of coupling between instrument inertia and material elasticity.

ation. Such a response might arise due to non-linear effects which are easily achieved in such soft samples even at very low stress.

We observe oscillations in the strain response at shorter time scales, which can be seen more clearly in the inset of Figure 3.4 when the same data are shown on a log-log scale. It is well established that such damped oscillations arise following a coupling between instrument inertia and sample elasticity [91, 92, 33]. The power-law scaling $\gamma \sim t^2$ at very short times is due to instrument inertia [91, 68]. Such effects limit our understanding at very short time scales, which is very relevant to the functional properties of this material, considering the short duration of predator attacks. Hence, to reveal short time material properties we use constitutive model fits to the inertio-elastic ringing [91, 92, 33, 93] (de-

tails in Appendix B.4.). The linear-viscoelastic information we obtain at short timescales from creep-ringing analysis, namely the tangent storage and loss moduli, K' and K'', have a near linear dependence on concentration, i.e. $K' = c^{0.91\pm0.08}$, $K'' = c^{0.92\pm0.08}$ (Appendix Figure B.8). This is consistent with the results from linear oscillatory experiments, Figure 3.3. In a later section, we will describe a constitutive model to compare the viscoelastic creep data across all tested time scales.

3.3.4 Nonlinear Creep

Increasing the stress in creep compliance tests probes the nonlinear properties of hagfish gel, and are relevant to understand the large deformations of the material during a predator attack. A similar approach was followed in prior work [33] but was limited to a single concentration. Figure 3.5 A shows a representative result for concentration $c = 0.25$ wt $\%$. For all concentrations (Appendix Figure B.9), we perform creep tests similar to those in Figure 3.5 A. The nature of the response is remarkably similar over the range of concentrations tested.

At low applied stresses, the creep compliance, $J(t) = \frac{\gamma(t)}{\sigma_0}$, is linear viscoelastic; as discussed it follows a power-law solid-like response. A small increase in the input stress results in a very similar material response, though slightly stiffer (lower compliance).

As the applied stress is increased further, the creep compliance shows a clear transition from a power-law solid-like response to a liquid-like behavior. We refer to this transition as material failure. When failure occurred, we could not distinguish if the observed failure was the yielding of the material itself (cohesive failure), or material slipping at the surface of the geometry (adhesive failure), since the sample is not directly visible during the experiment. Either case could be important for the physiological function of the slime. Here, adhesive failure is more likely because the failure stresses only range from 0.1–13 Pa whereas video observations of actual attacks [23] seem to imply that the slime remains cohesive under larger stresses. With further increase in the stress, $J(t)$ varies linearly with time, i.e. a viscous response with a steady shear viscosity. The creep response is very similar to typical yield stress fluids [77], some of which also have power-law creep behavior instead of a solid-like response [94]. We did not systematically check for recovery of solid-like behavior after failure, which would be expected for a yield-stress fluid, though our prior work observed partial recovery [33]. It was also outside the scope here to assess other questions of yielding, such as the dependence of the failure stress on fatigue history, or if delayed failure may occur at smaller stresses. We did run some creep tests for longer times, up to 600 s, and did not observe delayed failure.

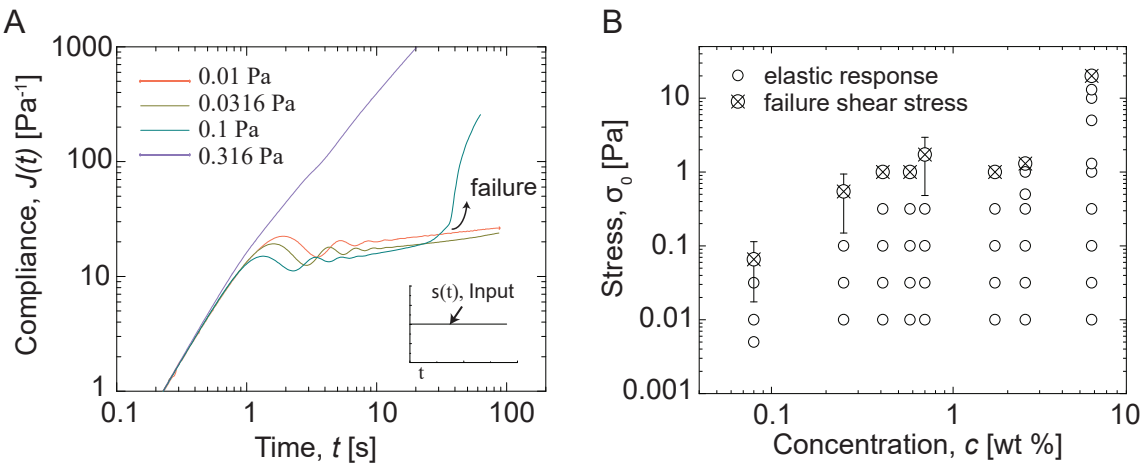

Figure 3.5: Nonlinear shear properties of Hagfish slime. (A) Constant step stress was applied at $t = 0$ to the sample (0.25 wt $\%$). Three distinct responses can be observed as the applied stress amplitude is increased. The material showed a power-law response for low stresses (up to 0.0316 Pa), followed by material failure which is evident from the transition of a power-law response to liquid-like response at a higher stress value (0.1 Pa) and a further increase in the applied stress (0.316 Pa) causes the material to flow as a viscous liquid. (B) For all concentrations, the range of stress where material exhibits a power-law creep response (unfilled circle) and the material failure stress(crossed circle) are shown. The failure stress increase is increases with the concentration of exudate (see Appendix Figure B.9) for full details of nonlinear creep tests at other concentrations.

The threshold shear stress at failure is a function of concentration as shown in Figure 3.5 B. It should be noted that since we are increasing the stress input in a discrete manner, we may not resolve the exact failure stress. In Figure 3.5 B, we indicate failure as the stress at which the material failure was first observed. Failure stress varied between 0.1–13 Pa for the concentrations tested and generally increased with concentration. These failure stresses are consistent with those observed in oscillatory amplitude sweep tests (Appendix Figure B.4 A-B). Stiffening before failure is also consistent across several test protocols. The tangent moduli obtained from creep-ringing analysis shows stiffening as the stress is increased (Appendix Figure B.10), agreeing with the observations made from the raw stress-strain Lissajous curves from the oscillatory shear experiments (Appendix Figure B.5-B.6).

3.3.5 Fractional Constitutive Model for Linear Viscoelasticity

The material functions used to describe the concentration dependence in earlier sections, G', G'' and K', K'', are insufficient for describing the full linear viscoelastic material re-

sponse, since they only provide information about a fixed time scale (frequency). To quantitatively compare the linear viscoelastic response across the range of concentrations and timescales, we use a fractional constitutive model. A brief overview of fractional constitutive models is given in Appendix B.6. For more details on fractional constitutive models we refer readers to other literature [95, 96, 97, 98, 99, 100]. Simply put, fractional time derivatives represent a continuous relaxation spectrum with a power-law distribution of timescales [100]. A major benefit is a small number of model parameters. Here we utilize a special case of a three-parameter fractional Kelvin-Voigt model which has a dashpot (η) in parallel with a spring-pot (α, G). The governing differential equation for such a model is given by

$$\sigma(t) = \Big[\eta\frac{d}{dt} + G\frac{d^\alpha}{dt^\alpha}\Big]\gamma(t) \tag{3.1}$$

where $0 \leq \alpha \leq 1$ is the fractional order of the derivative and G is a quasi-property which describes the strength of a spring-pot (i.e. the strength of the power-law relaxation spectrum).

Since the instrument inertia effects are prevalent in creep measurements at short times, to extract the viscoelastic information at such time scales we solve the equation of motion for the spindle of a stress controlled rheometer, given by

$$\frac{I}{b}\frac{d^2}{dt^2}\gamma(t) = H(t)\sigma_0 - \sigma(t) \tag{3.2}$$

where I is the total moment of inertia of the rheometer spindle with measuring system attached and b is a geometric factor dependent on the instrument and geometry used. The values obtained from rheometer calibration are $I = 19.593$ μN ms^2 and $b = 8.026 \times 10^{-4}$ m^3. σ_0 is the applied stress and $H(t)$ is the Heaviside step function. The stress response from the sample, $\sigma(t)$, is modeled by a fractional Kelvin-Voigt model as described by Eq.3.1. Hence, a coupled fractional order initial value problem can be obtained from Eq.3.1 and Eq.3.2

$$\Big[\frac{I}{b}\frac{d^2}{dt^2} + \eta\frac{d}{dt} + G\frac{d^\alpha}{dt^\alpha}\Big]\gamma(t) = H(t)\sigma_0. \tag{3.3}$$

Since the material has no deformation at $t = 0$, the initial conditions are $\gamma(t = 0) = \dot{\gamma}(t = 0) = 0$. The initial value problem in Eq.3.3 is numerically solved using a method previously described [101]. The constitutive model predictions are compared to the experimental data over the entire concentration range with η, G and α as fit parameters. The best fits were obtained by minimizing the residual sum of squares in MATLAB. The fitting results are shown in Figure 3.6. It is evident that a 3 parameter fractional Kelvin-Voigt

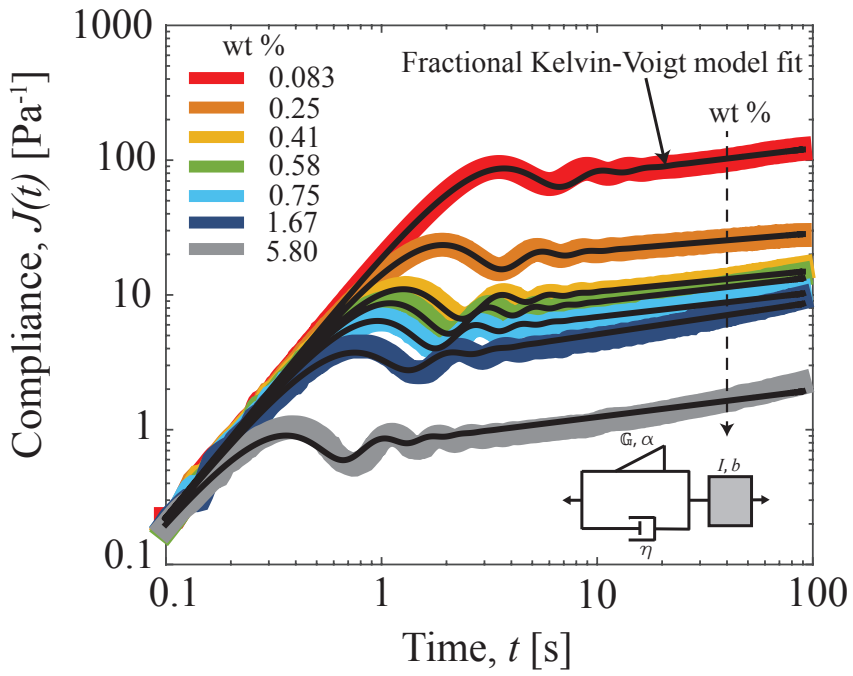

Figure 3.6: Three-parameter fractional Kelvin-Voigt model describes the linear viscoelastic creep response at all time scales. Different colors show varying sample concentration and the black curves are the fractional Kelvin-Voigt fits to the experimental data. Constitutive model fits have an excellent agreement with the creep data across all concentrations. Distinct regimes in the creep data, namely instrument inertial response at the start, creep ringing at shorter time scales and power-law response at longer times, are described using only three parameters (η, $\mathbb{G}$, α).

model fits the data reasonably well at all timescales and, remarkably, all concentrations. Very slight disagreement can be seen during the oscillatory ringing for the extremes of concentration, but for our purposes it is unnecessarily complex to add additional model parameters to improve this aspect of the fit.

The dependence of the fit parameters on concentration is shown in Figure 3.7. Appendix table B.1 lists the fit parameters and associated fit uncertainty for all cases.

3.4 Discussion

3.4.1 Interpreting Fractional Model Fit Parameters

The springpot strength parameter G does not directly represent any physical property [102, 98]; this is evident from its dimensions which have non-integer powers of time. However,

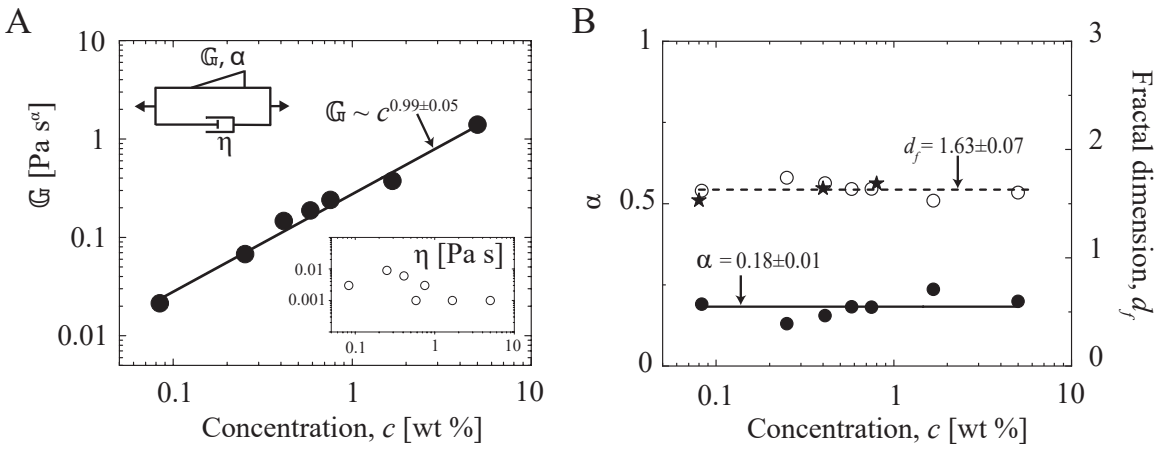

Figure 3.7: Constitutive parameters also highlight the self-similar response. (A) Parameter G, a quasi-property, varies linearly with the exudate concentration, this parameter is analogous to gel strength S. (inset) the parameter η does not show a monotonic trend with concentration, its values take a narrow range ($0.001 - 0.01$ Pa.s). (B) Fractional order (solid circles), α, is nearly constant with an average value of 0.18 ± 0.01, indicating a self-similarity in the structure across the wide range of tested concentrations. A constant fractal dimension (open circles), d_f, of 1.63 ± 0.07 extracted from the fractional order is consistent with the observation of fractal microstructure using a box-counting method (solid stars, details in Appendix B.1), though a direct numerical comparison cannot be made.

this quantity is analogous to gel stiffness, S, which describes the “strength" of a critical gel ($J(t) = \frac{1}{S\Gamma(1-n)\Gamma(1+n)}t^n$) [85]. G combines information about the elastic strength of the material with a time scale and the fractional order, α.

Across the concentration range, α has a very narrow range (0.13 - 0.24) with an average value of 0.18. This implies that the relative elastic and viscous contributions from the spring-pot stay nearly the same over the concentration range tested [99]. This was also observed in our oscillatory shear experiments where $\tan\delta = G''/G'$ has values in a narrow range ($0.2-0.3$) in the linear regime (Appendix Figure B.4 C). Moreover, the near constant value of fractional order, α, allows for the comparison of G across the concentration range. Remarkably, the quasi-property, G, shows a power-law dependence on concentration ($G \sim c^k$) with an exponent $k = 0.99 \pm 0.05$, essentially unity, consistent with linear oscillatory experiments and viscoelastic information extracted from creep-ringing. This is the most conclusive evidence for linear scaling of the gel strength with concentration. Unlike G' which was measured at a single frequency (Figure 3.3), G represents gel strength across the entire range of viscoelastic time scales. The three different measures for the concentration dependence of hagfish slime are compared in the Table 3.2.

The fractional order, α, has been associated to the critical gel relaxation exponent or critical scaling, n, which in turn can be related to the fractal dimension of the network [103,

Table 3.2: Comparison of different measures of concentration dependence

Measure	Concentration dependence
Linear oscillatory shear	$G' \sim c^{1.12\pm0.04}$, $G'' \sim c^{1.28\pm0.11}$
Creep ringing	$K' \sim c^{0.91\pm0.08}$, $K'' \sim c^{0.92\pm0.08}$
Fractional Kelvin-Voigt	$G \sim c^{0.99\pm0.05}$

104, 105, 106, 90] α is the the power-law exponent at long times in the creep test, identical to n). Many theoretical relations linking the fractal dimension, d_f, of the gel network and the exponent, n, have been proposed depending on several factors, e.g. monodispersity/polydispersity [85]. One such relation has been derived for a fractal network with arbitrary mechanical network of springs with the same spring constant [103]. It has been shown that for the networks whose stress-strain relation can be described by a spring-pot or with a fractional equation, $\sigma(t) = G\frac{d^\alpha}{dt^\alpha}\gamma(t)$, the fractal dimension, d_s, of the network at larger times is related to the observed power-law scaling, α, as

$$\alpha = 1 - \frac{d_f}{2}. \tag{3.4}$$

We use this relation to obtain the fractal dimension, d_f, for different concentrations of hagfish slime. We find the fractal dimension has a nearly constant value of $d_f = 1.64 \pm 0.07$.

We also use a box-counting method to evaluate a 2D fractal dimension from the DIC images for slime samples (details in Appendix B.1). There are limitations with the box-counting approach that require caution when interpreting the numerical result or attempting to compare to the result from viscoelastic measurements. Notably, only a limited 2D section of the 3D sample is used and only the fibers (not mucin) are visible in the images. Additional limitations of the box-counting approach are discussed in the (details in Appendix B.1). Despite these limitations, the box-counting fractal dimension is valuable because it identifies a fractal dimension that is almost independent of concentration or fiber number density. This helps show a possible rheology-to-structure connection and supports the observation of a constant fractal dimension suggested by the viscoelastic power law exponent. It has been shown that given constant stoichiometry of a single polymer network (ratio of polymer to crosslinker), the fractal dimension should not change [105]. Hence, the concentration-independence of the fractal dimension might be attributed to the constant ratio of mucus to thread cells (stoichiometry) in the hagfish exudate [64], but moreover suggesting that the flow-induced structural connectivity in the hagfish slime networks stays

similar at all concentrations.

It should be noted that several other theoretical models that describe relations between relaxation exponent (α) and structural properties (d_f) are found in literature which may give different numerical value of fractal dimension, d_f e.g. $\alpha = \frac{d(d+2-2d_f)}{2(d+2-d_f)}$ gives $d_f = 2.33 \pm 0.01$ for a polydisperse fractal with full screening of excluded volume [88, 105, 107] where $d = 3$ for three-dimensional space. Regardless, the fractal dimension following any such relation will be nearly constant since the power-law exponent of hagfish slime has a near constant value. Hence, we interpret the self-similar viscoelasticity in hagfish slime as having its origins in a self-similar material structure. Figure 3.8 shows the comparisons of various materials adapted from the literature [108, 109, 110, 75, 111, 112, 113, 114, 115, 116, 117, 118, 119, 120, 121] and the concentration dependence of their power-law relaxation exponents. Appendix table B.2 provides the data used in this figure. All the materials in Figure 3.8 can be described by a single viscoelastic relaxation exponent, α. For most materials α decreases with increasing concentration, which is consistent with the common intuition of increasing solid-like character of the materials. However, some materials like κ-carrageenan [118] and gelatin [122] are known to show concentration independence across a certain (narrow) range. Such universality in the concentration dependence is related to the self-similar global structure of the material.

The parameter η, which represents the viscosity in parallel with the gel network, has best fit values between $(1-10)$ mPa.s, consistent with very weak concentration of polymer suspended in water. This non-monotonicity suggests that the amount of free polymer (e.g. mucus and intact thread cells) in the solvent may be variable. We find that this parameter has negligible effect in fitting the power-law creep data, but is included here to make the fractional model thermodynamically valid [97].

3.4.2 A Structure-Rheology Model

The ultrasoft mechanics of hagfish slime is attributable to the underlying dilute network of very long fibers as shown in Figure 3.2. Understanding the network mechanics of hagfish gel requires an understanding of the mechanics of individual fibers. Although an attempt has been made to relate the fiber mechanics to the underlying molecular structure and arrangement of intermediate filaments [64], here we focus on the mesoscale structure of the fibrous network. Unraveled fibers have natural bends in them likely due to their previously coiled state inside the thread cell [123, 124]. Here, we treat the individual fibers as cylindrical elastic rods of radius, a. The bending rigidity of a fiber is given by $EI = \frac{\pi}{4} E_f a^4$, where E_f is the Young's modulus, reported to be $E_f = 6.8$ MPa [64]. We treat the fibers as

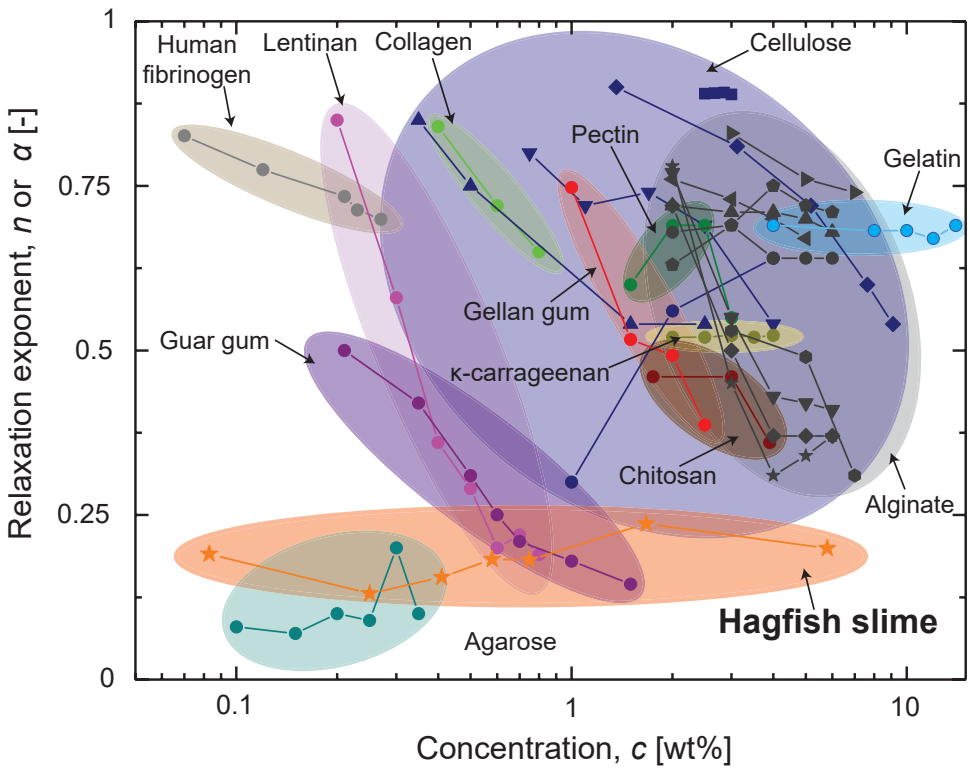

Figure 3.8: Comparison of concentration dependence of the relaxation exponent (n or α) for various materials that show a power-law response. Unlike various other materials where the solid-like nature of the material dominates with increase in concentration, evident by the decreasing relaxation exponent, n or α; hagfish slime has nearly constant relative viscous/solid-like properties. The data sets for materials other than hagfish slime are obtained from literature (Appendix table B.2).

athermal elastic rods and neglect any thermal energy changes during deformation. Under an applied deformation, the bends in a fiber tend to straighten out. Due to its geometry, the fiber will be nearly inextensible and experience negligible physical stretch (lengthening) unless nearly all the bends are straightened out [125].

The resulting shear modulus can be derived by considering the elastic energy of the deformed fiber network. The energy involved in deforming an inextensible fiber of total length L from its natural curvature κ_0 to a new curvature $\kappa(\gamma, s)$ can be expressed as $E_{fiber} = \int_0^L ds \frac{EI}{2}(\kappa(\gamma, s) - \kappa_0)^2$, s is the curvilinear distance along the fiber [126]. We approximate $\kappa(\gamma, s)$ as a Taylor series expansion about the natural curvature κ_0 , $\kappa(\gamma, s) = \kappa_0 + \frac{d\kappa}{d\gamma}\big|_{\gamma=0}\gamma + O(\gamma^2)$. Hence, we can write the bending energy per unit volume from all the fibers as $e_{network} = \rho\frac{EI}{2}\langle(\frac{d\kappa}{d\gamma}\big|_{\gamma=0})^2\rangle\gamma^2$, where ρ is the total length of all fibers per unit volume.

Under a small deformation, the deformation energy per unit volume due to a differential applied shear strain γ is given by $w = \frac{1}{2}G\gamma^2$, where G is elastic shear modulus. Assuming negligible dissipation and a purely elastic response, an energy balance in the system gives $e_{network} = w$. Hence, we obtain the shear modulus as

$$G = \rho EI\langle(\frac{d\kappa}{d\gamma}\big|_{\gamma=0})^2\rangle. \tag{3.5}$$

We evaluate the terms in angular brackets in Eq.3.5 using purely geometric arguments utilizing the inextensiblity of the fibers and in the limit of zero strain. The details are given in the Appendix B.8. We have assumed an isotropic distribution of fibers to evaluate the bulk response per unit volume. This however may not be true in general considering some of the microstructural images where the threads appear to align roughly orthogonal to each other. However, estimating a fiber orientation function is beyond the scope of present work. Here, we directly use the final expression for shear modulus

$$G = \rho EI\frac{\left(3 + 20(\frac{h}{l})^2\right)^2}{64h^2\left(1 + 4(\frac{h}{l})^2\right)^4} \tag{3.6}$$

where l is defined as the end-to-end length of a curl in fiber i.e. the half-wavelength of naturally curved fiber, and h is the amplitude of the curl from the end-to-end vector (inset Figure 3.9). ρ is evaluated from the concentration (wt%). It is evident from Eq.3.6 that for $\frac{h}{l} \ll 1$, $G \sim \frac{\rho EI}{h^2}$, implying that it is more difficult to bend fibers as amplitude of curl, h, decreases. That is, straighter fibers cause higher stiffness of the network, all else being equal. The sensitivity to h is more extreme at increasing values of h/l, e.g. $G \sim \rho EI\frac{l^4}{h^6}$ for $h/l \gtrsim 1$.

We also observe (shown in Appendix B.8) that as long as the ratio $\frac{h}{l} \ll 1$, the contribution from the term involving $\frac{h}{l}$ changes narrowly. This gives $G \sim \rho$, a linear dependence on total fiber length concentration, which agrees remarkably with our experimental observations discussed earlier.

The linear dependence of concentration is a direct consequence of the following assumptions: (i) The deformation of each length of fiber is assumed affine, independent of connectivity. (ii) We assume the effective spring constant of each fiber is set by its material and geometric properties, and these are independent of concentration. For example, l and h are independent of concentration (as a consequence of their packing inside the thread cells) and the spring constant does not depend on the distance between crosslinks. This in general may not be true for other networks which are chemically or physically cross-linked or where the monomers polymerize to form a volume spanning network [127]. In such cases, unlike the hagfish slime, the mesh size or the distance between cross-links sets up the curvature of the fiber hence this mesh size and concentration play a stronger role in the mechanics of the network. (iii) We assume the fiber network orientation, even if anisotropic, is independent of concentration. Even for an anisotropic network, the linear dependence on concentration would also appear if the same anisotropy exists for each concentration.

Contrary to a pure bending response from the fibers, we also evaluate the modulus arising from pure stretching of fibers (details in Appendix B.8.). The modulus obtained from such a response is orders of magnitude higher that the experimentally measured results. This is expected, since it is more difficult to physically stretch the fibers than bend them. We also neglected any irreversibility (e.g. dissipation) during the deformation. We argue that such effects primarily come from the weak cross-link connections between the fibers and mucus-like molecules and the frictional interactions between the fibers, which have been shown to be weak [33, 125]. Although individual fiber hysteresis effects were observed in single fiber studies [64], we neglect such effects here in the structure-rheology modeling, since we focus our understanding to small deformations and the overall elastic strength of the network. We also show (in Appendix B.8) that the mucus component in the hagfish slime at the probed concentrations cannot form a volume spanning network of their own. This is consistent with prior work in the literature [21, 35]. Yet, the mucus component can affect the mechanics of the slime by forming local networks within the fibrous mesh [42]. Such effects are beyond the scope of the present model. Hence, the mesoscale model we described serves as a leading-order model for hagfish slime.

Figure 3.9 shows the comparison between the modulus evaluated using Eq.3.6 and the experimental measurements. Eq.3.6 fits to the experimental data using just a single fit parameter as front factor i.e. $G_{fit} = \beta G$ and minimizing the residual sum of squares, while

fixing the values of Young's modulus E and fiber geometric parameters a, h, and l to values known from the literature or microstructural images. The best fit value of $\beta = 0.37 \pm 0.03$ gives an excellent agreement with the experiments. The most sensitive parameter for this estimate is the radius a, given the sensitivity of Eq.3.6 to the fiber radius a through the second moment of area $I \sim a^4$. The fit parameter β can show wide variation, $(0.0728 - 10)$, considering the full range of radius for slime threads reported in the literature, $(0.4 - 1.5)$ μm [21, 31]. In the absence of a more precise average radius of the fibers, we assume a uniform average radius, $a = 1$ μm, which reasonably captures the average radius of fibers in the network. Other sources of uncertainty include the fiber Young's modulus and curvature length scales l and h. There is an expected spread in the values of l and h since the packing of canonical loops of fiber inside a thread cell will produce a distribution of these length scales. For simplicity, we use average values obtained from microscopic images of $l = 121 \pm 32\,\mu$m and $h = 23 \pm 3.7\,\mu$m, that is, $h/l = 0.17 \pm 0.04$. Nevertheless, the agreement between the model prediction and experimental data, using an average value of fiber radius, supports our assumption of pure bending response from the fibrous network. We see the slight disagreement between the model and experimental result at the highest concentration, we attribute this mismatch to the contribution from mucus networks, as the highest concentration is close to the overlap concentration for the hagfish mucus component (details in Appendix B.8.5).

3.5 Summary

We studied the concentration-dependent shear rheology of hagfish slime to understand how the concentration of slime influences its physiological function, especially given that the process of slime formation is very fast $\sim 100 - 400$ ms [22, 23] and the concentration is uncontrolled in an "infinite" sea of water. We did not explicitly test this material in an "infinite" solvent scenario. Our mixing protocol was in a finite volume of water, and our results must be interpreted within the limits of this protocol. Nonetheless, our concentration-dependent results have strong implications for the uncontrolled, concentration-dependent gel structure that forms under physiological conditions in the ocean. Contrary to the recent proposition that the linear viscoelastic moduli remain largely constant with the concentration of exudate [35], our experiments show that the linear viscoelastic moduli of hagfish slime have a linear dependence on the exudate concentration. Both the linear oscillatory shear and creep measurements agree well with each other.

Notably, such a linear concentration dependence has not been observed in other interme-

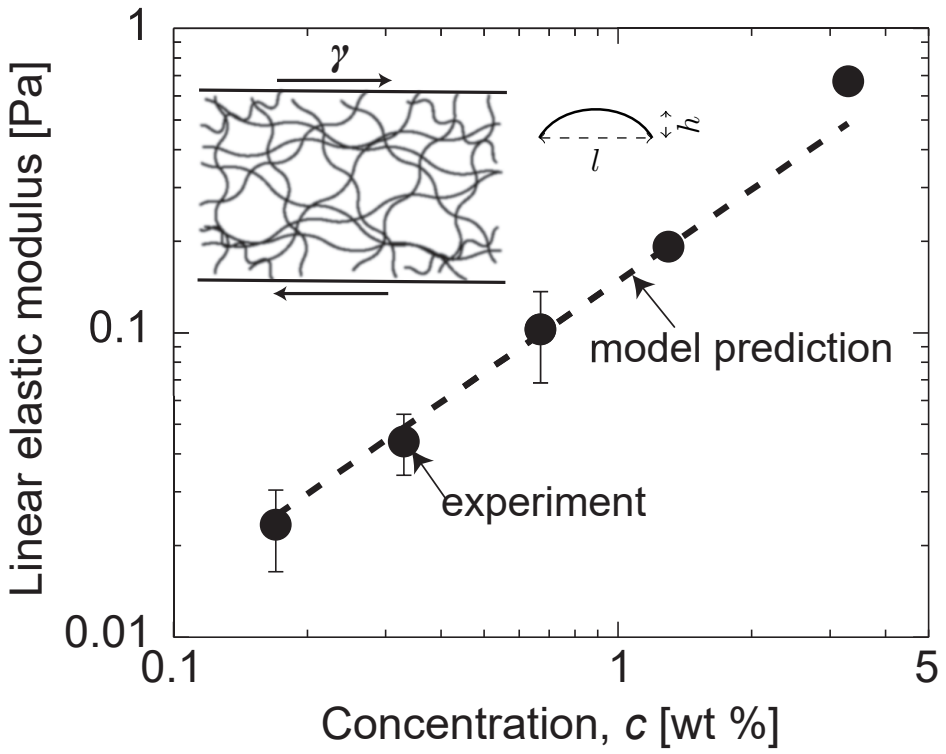

Figure 3.9: Bending-dominated response leads to the ultra-soft mechanics of hagfish slime. The shear elastic modulus measured via oscillatory rheology in the linear regime agrees well with the linear elastic shear modulus predicted using purely bending response from the curved fibers. A single fit parameter, $\beta = 0.37 \pm 0.03$, is used as a proportionality constant between the modulus evaluated from Eq.3.6 and the fit value. (Inset) A schematic of structural elements (fibers) of the hagfish slime arranged in a random order. The length of fibers is comparable to the sample length. The two parameters h and l which represent the height and chord length of a bent fiber are obtained from the microscopic images.

diate filament (IFs) based fibrous networks [128, 76, 129, 130]. IFs in hagfish threads are bundled intracellularly with a high degree of axial alignment into thick ($\sim 2\ \mu$m) and very long fibers (~ 10 cm) [131, 63]. The thread is produced and organized into canonical loops within the thread cell [123]. We hypothesize that this unusual organization of thread (i.e. canonical loop packing [123]) sets up characteristic length scales in hagfish slime threads, which determine the thread's mechanical response and lead to a distinct mechanical response of the network.

We explain our experimental observations through a mesoscale network model and demonstrate that as the elastic elements (i.e. the fibers) in the slime increase in concentration, the elastic modulus increases proportionally. Interestingly, the ultra-soft mechanics arise from a bending-dominated response from underlying fibers. Although the gel strength (or linear modulus) is not constant with concentration, we find that the time-dependent viscoelastic response is similar for all the concentrations tested, with a nearly constant power-law relaxation exponent. We relate this observation to the underlying fractal nature of slime based on a simple fractional constitutive model.

We conclude that hagfish slime is concentration-independent in its normalized viscoelastic time-dependent response and its self-similar structure. This is a rather unique feature of hagfish slime compared to a wide range of other material systems.

We hypothesize that like many other naturally occurring fractals, self-similar structure in hagfish slime arises due to its uncontrolled production governed by several underlying physical phenomenon like convective mixing, diffusion, swelling, unraveling etc [132]. We speculate that the fractal structure might have certain robust and functional advantages as is the case in many other biological system [133, 134]. Such an investigation is beyond the scope of current work. Remarkably, the fractal dimension is constant across concentrations, unusual in most materials. We hypothesize that the relative concentration of mucus and threads in the slime might play a role in maintaining the constant fractal dimension of hagfish slime.

There are potential physiological implications of our results. The viscous and elastic properties of hagfish slime are comparable and their relative contribution in dissipating and storing an applied deformation, respectively, is also constant over the range of concentration explored ($\tan\delta = G''/G' \approx 0.2-0.3$). Being a very soft material ($G' \approx 0.02$ Pa) slime is compliant and easily conforms to surfaces, e.g. mouth/gills of the predator. The creep experiments show that it does not flow under small enough stress and relaxes following a weak power law, thus allowing it to persist on gills and continue its clogging function. The huge stretch ratios that hagfish slime can withstand without failure understandably makes it difficult for the predator to remove the gel adhered to its gills (as evident from video evi-

dence [23]). We speculate that the extremely soft mechanics enables it to make contact with the substrate at molecular dimensions, necessary for adhesive bond formation between gel and substrate [135]. We propose that such features are possibly provided by the dissipative mucus networks [136, 137, 138, 139, 140], which are known to be much smaller in length scale compared to threads. Thus the invariant dissipation ratio $\tan\delta$ makes slime robust with respect to its adhesive properties.

Our observations present several novel findings and are a significant advance in understanding the behavior of this unique material system. The research will impact not only the design of bioinspired materials with a clogging/entangling functionality, but provide new design paradigms for polymeric and fibrous materials in general. This new understanding could bring about radical changes in materials available for personal defense, oil-drilling leakage safeguards, or fibrous cell cultures. For bioinspired design of ultra-soft materials like hagfish slime, Eq.3.6 provides the design guidelines. The aspect ratio $\frac{h}{l}$ and ρ in a synthetic material can be tuned to get an ultra-soft gel from a given material, i.e. a given EI. The quantity l is very low for many rubber-like materials but ρ is much higher in those cases compared to hagfish slime. Hence, at low concentration i.e. a low ρ, such materials are unlikely to show solid-like behavior since a volume spanning network cannot be formed. Therefore, another necessary characteristic is the length of fibers. Fibers with length scales comparable to that of the bulk sample will more easily form a connected network. It will be interesting to know if the slime achieves a constant expansion ratio regardless of its concentration. Such efforts were limited by the mixing protocol adopted here. Nevertheless, our results highlight the rather unique features of this material and offer a new target for bioinspired design of materials aimed at achieving robust concentration-independent structure and mechanical properties.

Acknowledgement

We are grateful to the National Science Foundation for supporting this research under grant number CBET-1342408 to RHE. We thank Prof. Alejandro G. Marangoni (Food Science, University of Guelph) for providing access to rheometers in immediate proximity to the hagfish and Evan McKenzie, Sarah Schorno and Dr. Atsuko Negishi (Integrative Biology, University of Guelph) for assistance in collecting the samples. We also thank Lukas Böni and Prof. Peter Fischer (ETH Zürich) for helpful discussions.

CHAPTER 4

LARGE DEFORMATION AND PERMEABILITY OF HAGFISH SLIME

4.1 Introduction

Building on the work described in Chapter 3, we further explore the mechanics of hagfish slime. Most studies on slime mechanics [33, 35, 66] focused on the shear rheology limited to small deformations. It is reasonable to assume that in case of predator attacks, the large deformation properties of slime are critical for performance. Probing large deformation response of slime is challenging due to its ultra-soft nature. Additionally, the roles of individual components, i.e. mucus and threads, and there contribution towards the overall mechanics of slime remains to be discovered. Understanding of the large deformation mechanics and the roles of individual components will elucidate the bioinspired design of materials similar to hagfish slime.

In this work, the extensional properties of slime under very large deformations are reported for the first time, and comparisons the mechanical properties of slime in shear and extension. Slime is found to be significantly stiffer in extension than in shear. The mesoscale network model based on the mechanics of an individual fiber as described in Chapter 3 is extended to explain the distinct modes of deformation in shear and extension. It is shown that varying the relative composition of mucus to threads in slime compared to the physiological composition drastically affects the mechanics.

Additionally, a concentration-dependent permeability study is utilized to further investigate the roles played by individual components of slime, namely, thread cells and mucus. Our results provide vital insights into the roles of individual components, and it is evident from our observations that mucus networks play a vital role in significantly reducing the permeability of the fibrous network formed by threads.

Dr. Atsuko Negishi, Evan McKenzie and Dr. Douglas Fudge (Integrative Biology, University of Guelph) provided slime exudate and filtered mucin vesicles used in the experiments.

4.2 Materials and Methods

4.2.1 Sample Preparation and Microscopy

The sample preparation protocol adopted here is same as the Sec. 3.2.1.

4.2.2 Mechanical Characterization

The viscoelasticity of hagfish slime was probed using a rotational rheometers (model MCR302 from Anton Paar). This is a torque-controlled instruments (a.k.a. combined-motor-transducer type). A single gap concentric-cylinder geometry with fixed outer measuring cup and torque controlled inner bob (with a conical bottom) was used in all experiments. The inner cylinder radius $R_i = 13.33$ mm and length $L = 40.01$ mm for the AR2000. The gap between the two cylinders was 1.13 mm. Sample volume was chosen so as to "overfill" above the thin gap region, thus reducing the surface tension effects [68]. This is important since water alone may appear elastic due to surface tension artifacts [69]. As a control experiment, we measure water alone. All tests were done at 10 $^{\circ}C$ and a solvent trap was used to minimize evaporation. Oscillatory shear experiments were performed, in which sinusoidal deformations of various strain amplitudes and fixed frequency were applied to the sample and the resulting torque signals measured.

For probing the extensional properties, we used an Instron Universal Testing machine (model 3343) with a 5 N static load cell (equipment courtesy: Fudge lab, University of Guelph). All experiments were done in a bath (BioPlus Temperature Controlled Bath) at room temperature, with same solvent as used for preparing slime samples. Custom made plates (37 mm in diameter) were used to sandwich the slime samples. An adhesive backed 80 grit sand screen provided sufficient adhesion to hold the sample in contact with the plates during stretching. Sample was left in the unstretched position, for 5 min before stretching to allow it to equilibrate in the sample. All experiments were done at a constant stretching rate of 0.1 1/s, with a moving upper plate and a fixed bottom plate. To ensure that the force measurements are not influenced by the varying bouyant force on the upper plate, the rod which was used to attach the upper plate with the load cell was made very thin (1.5mm). The measured response with and without the slime sample are different by at least an order of magnitude. Hence, our experimental measurements the actual response from the sample and free from any other effects/artefacts.

The permeability was measured by a custom-built set up shown in Fig. 4.2. A pressure holder (XX4004740, EMP Millipore co., MA) fitted with a pressure filter was used to hold

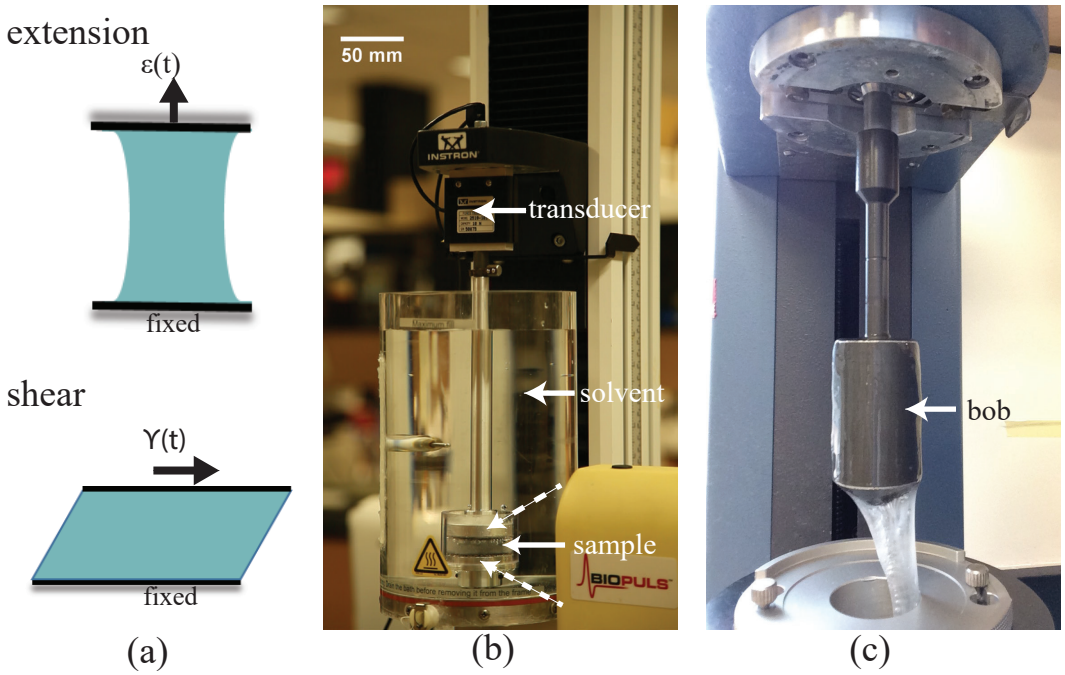

Figure 4.1: Mechanical characterization. (a) Properties were probed by deforming the sample in two different deformation modes. Extension: sample is sandwiched between two parallel plates which separate at a set rate. Shear: slime is sandwiched between two parallel plates held at fixed distance and one plate moving parallel to the other. (b) Experimental set up used for extensional test. Experiments were performed in a water bath filled with artificial sea water. A transducer attached to the top plate provides the axial force as the sample is stretched. (c) A commercial rheometer (AR2000, TA Instruments), with a cup and bob set up, was used to probe the shear properties of slime.

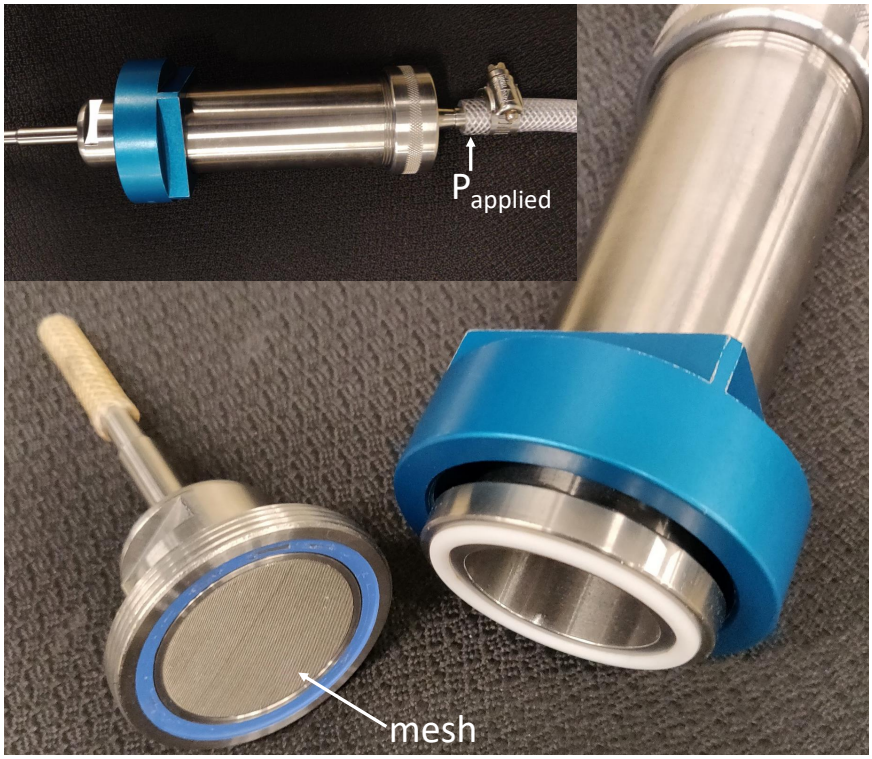

Figure 4.2: Experimental set up used to measure Darcy permeability.

a fixed volume of sample. The liquid column was then allowed to flow through the sample under an externally applied pressure from a compressed nitrogen reservoir. The outflow from the filter was collected and weighted as a function of time using a mass balance.

4.3 Results

4.3.1 Exudate Concentration Effects

Figure 4.4 shows the images of slime being stretched at an engineering extension rate of 0.1 1/s. It is evident that slime can easily undergo very large stretched without breaking. In most of the extension experiments, the sample did not break or separated any of the two plates. The length of water bath limited the maximum stretch ratio that could be reached. The engineering stress-strain curves for various exudate concentrations are shown in Fig. 4.5 A. As the concentration of exudate in the sample is increased, sample stiffens. The trend at all the concentrations are similar. A monotonic increase in stress with strain is observed initially, followed by a maximum in the stress, which corresponds the yielding. Post yielding, the stress monotonically decreases with increasing strain. We extract an

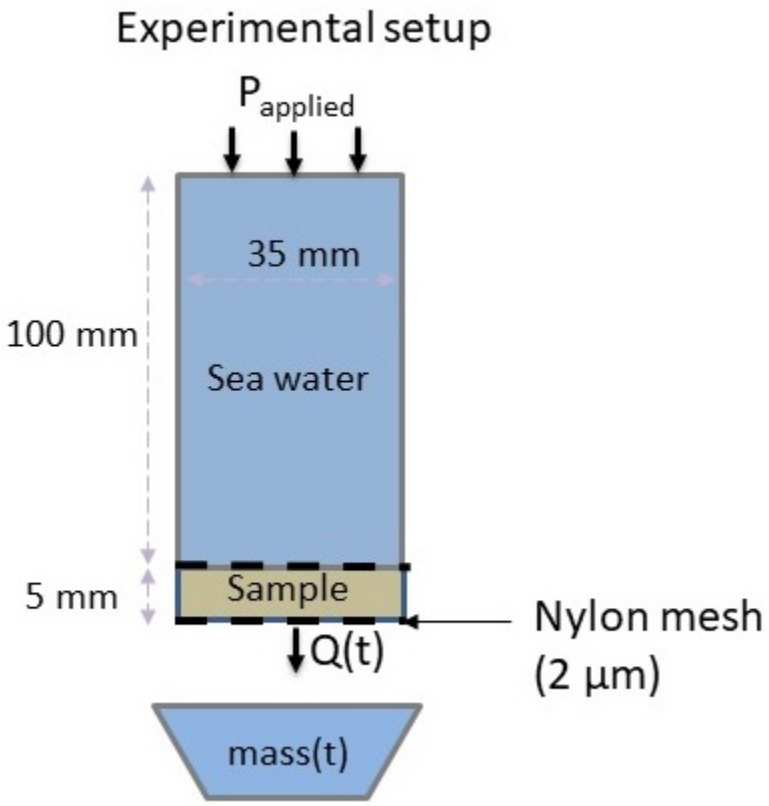

Figure 4.3: Permeability measurements. Custom-built set up used for permeability measurements. The solvent flows through the slime sample under an applied pressure. The outflow is recorded as a function of time.

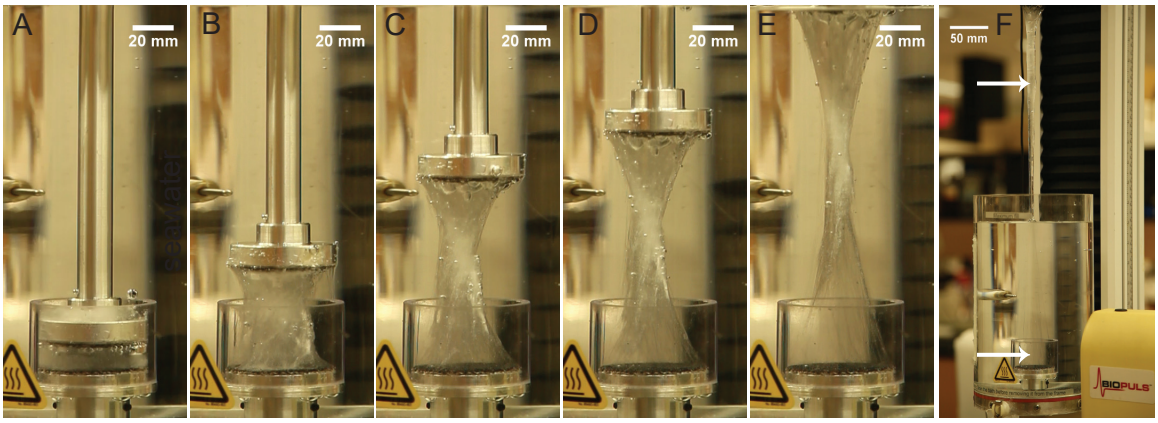

Figure 4.4: Extensional experiments on slime. (A-E) Images from extensional experiment at different extensional strains. Slime is stretched between two plate by moving the top plate at a fixed extensional rate (0.01/s) while holding the bottom plate fixed. (F) Sample can withstand extreme extensional deformation (stretch ratio > 100) without breaking.

effective extension modulus (Fig. 4.6 a) from the slope of stress strain curve below $\gamma \leq 5$ (best fits by minimizing the residual sum of squares). The extension modulus shows a power-law dependence on concentration, the power law exponent close of unity, $E \sim c^{0.90\pm0.10}$. The area under the stress-strain curves, $W_e = \int \sigma d\gamma$, is interpreted as extension work, which increases with increasing exudate concentration (Fig. 4.6 c.). The yield stress, corresponding to the yielding point, is plotted in Fig. 4.6 b. In Fig. 4.6, the results from shear rheology from Chapter 3. The properties in uniaxial extension are significantly higher than in shear.

4.3.2 Pure Mucus

Linear viscoelasticity of pure mucus, probed by oscillatory shear at a fixed angular frequency, $\omega = 1$ rad/s and strain amplitude, $\gamma = 2.5\%$ is shown in Fig. 4.7. At all the concentrations, the pure mucus solutions show a dominant elasticity, $G'' > G'$. This is consistent with literature [35]. Both G' and G'' increase with concentration, $G' \sim c^{0.41\pm0.09}$ and $G'' \sim c^{0.44\pm0.05}$. An apparent viscosity is extracted from the linear loss modulus $\eta = G''/\omega$. Inset of Fig. 4.7 shows the relative viscosity, $\eta_r = \eta/\eta_s$, where η_s is the solvent viscosity. The relative viscosity has a power-law dependence on concentration, $\eta_r \sim 0.44 \pm 0.04$. Such a power-law concentration dependence is very close to the theoretical predictions for polyelectrolyte solutions in the dilute and semi-dilute limit (Fuoss law) [141, 142]. The concentration dependence in G' is very different from dilute polyelectrolyte solutions. Although, we see a dominant elastic response in pure mucus rheology, we note that the the value of elastic moduli are significantly smaller than the elastic modulus on slime samples.

4.3.3 Varying Mucus Concentration in Slime

To probe the effects on varying mucus in slime samples. We vary the relative concentration of mucus to threads from the physiological concentration in exudate. First, we increase the concentration of mucus while holding the concentration of slime fixed. Fig. 4.8 A shows the linear viscoelastic moduli at $\omega = 1$ rad/s and $\gamma = 2.5\%$. Increasing the concentration of mucus, has a very weak effect on the elasticity of slime, $G' \sim c^{0.18\pm0.03}$. This is consistent with the observation that the elasticity of pure mucus networks is weaker compared to slime. Thus, the dominant component of elasticity in hagfish slime comes from the threads. The loss modulus shows a stronger dependence on concentration, $G'' \sim 0.55 \pm 0.12$. This is similar to the concentration dependence of G'' for pure mucus solutions (Fig. 4.7). We also decreased the mucus concentration in slime compared to physiological concentrations

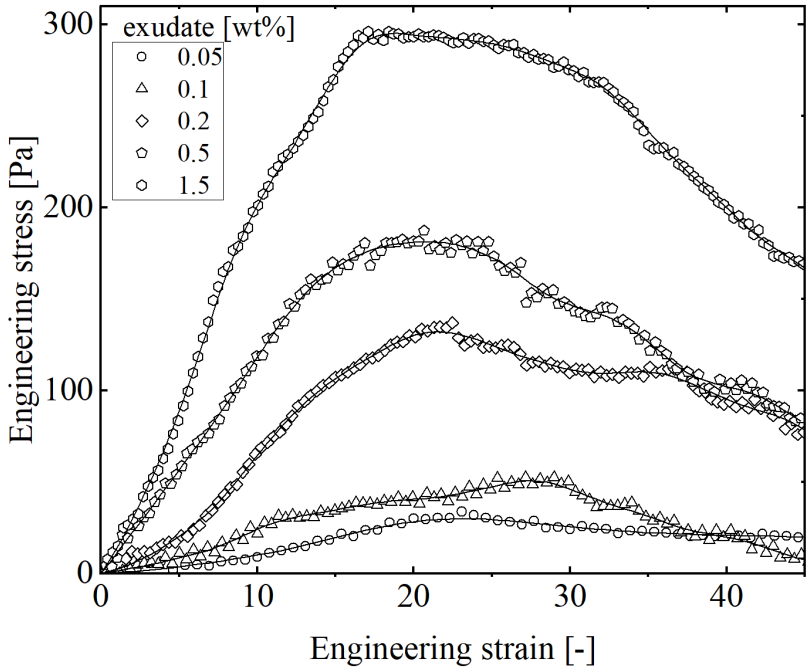

(a)

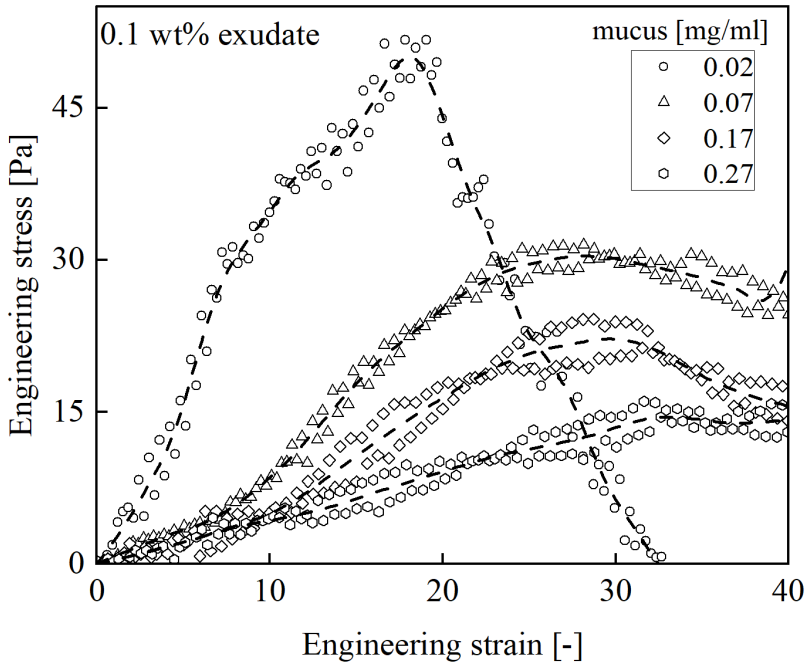

(b)

Figure 4.5: Extensional testing of hagfish slime. (a) Engineering Stress vs strain data for the samples with varying exudate concentration. The highest reported strain corresponds to the deformation when the upper plate is totally submerged in the solvent. Data at all the concentration follow similar trend, the stress increases with strain followed by a yield point, post which stress decreases with any increase in the strain. (b) Stress-strain curves for samples with varying mucus content while holding the concentration of threads fixed. At same applied strain, sample with more mucus content tend to soften.

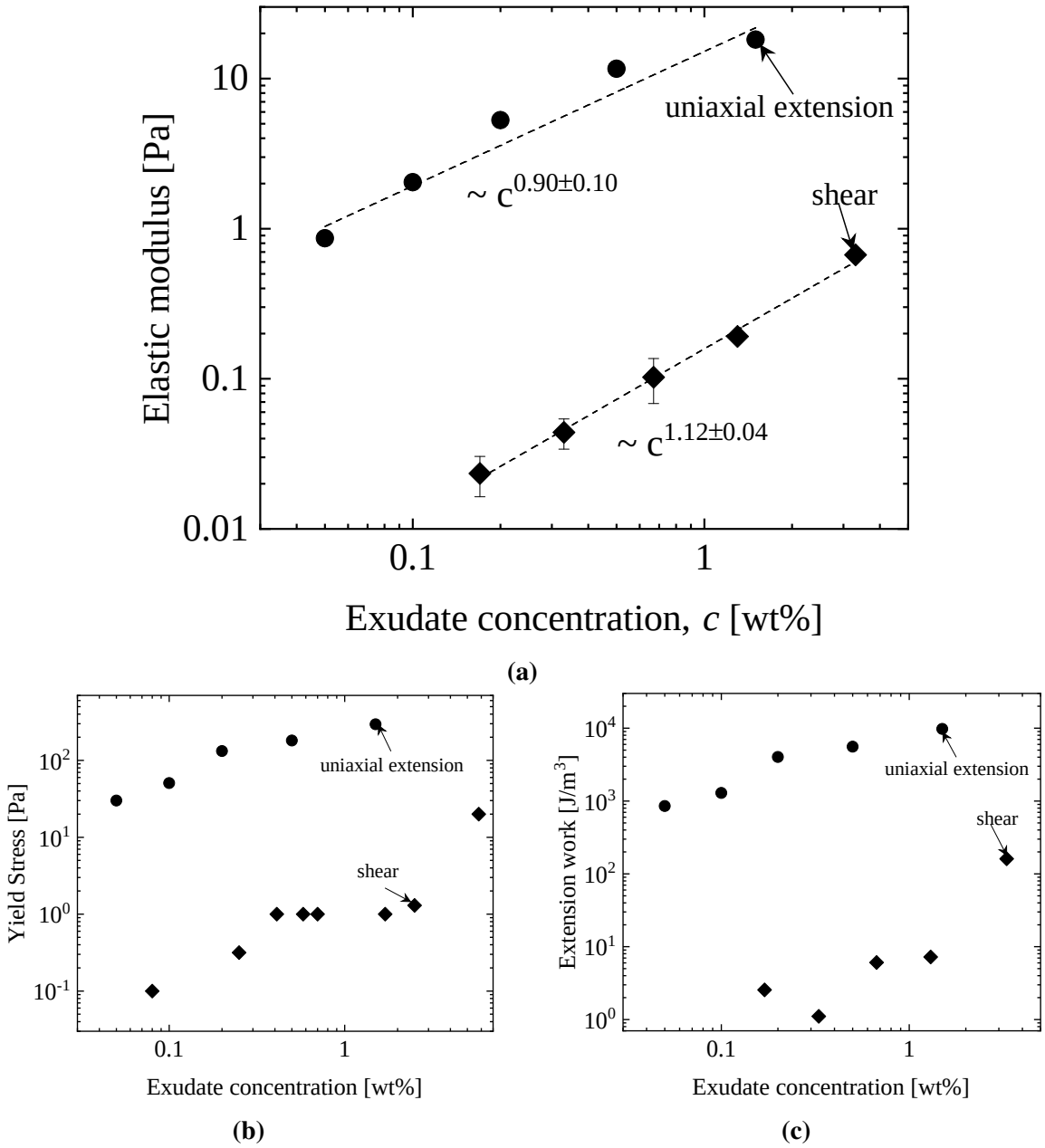

Figure 4.6: Hagfish slime is stiffer in extension than shear. (a) Comparison of elastic modulus of slime in shear and extension. The extension modulus is roughly 2 orders of magnitude larger than the shear modulus. Both extension and shear elastic moduli show an approximate linear dependence on the exudate concentration. (b) Increasing concentration of slime increases its yield strength both in shear and extension, but the yield strength in extension is roughly two orders of magnitude higher than in shear. (c) Comparison between the work done in extending and shearing the sample shows that it is much easier to shear the sample than stretch it.

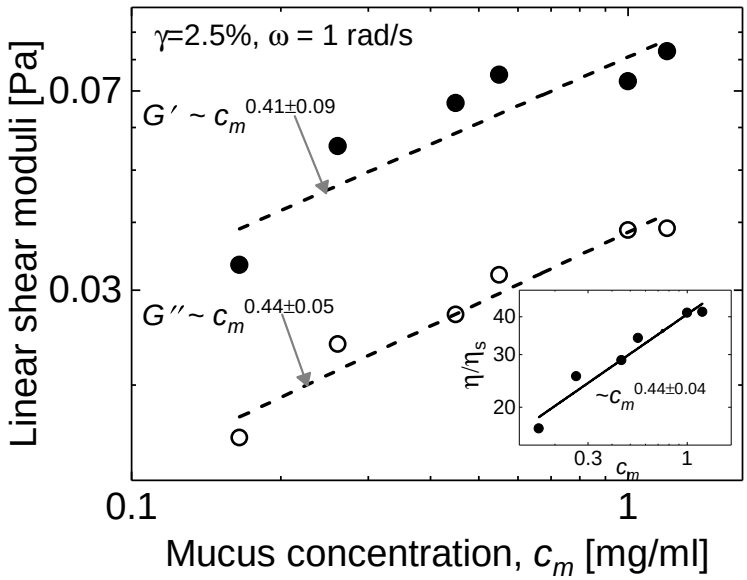

Figure 4.7: Hagfish mucus shear properties. The linear shear moduli of pure mucus samples (no threads) as a function of mucus concentration show a very weak power-law dependence on concentration. The rheological response shows a weakly dominant elastic character. (Inset) Relative viscosity of pure mucus samples closely agree with the Fuoss law for dilute/semidilute polyelectrolyte solutions.

by adding varying concentrations of dithiothreitol (DTT). DTT is known to disrupt the disulfide bonds in mucus networks. Fig. 4.8 B shows the linear viscoelastic moduli for a fixed concentration of exudate as the concentration of DTT is varied. As expected, the linear viscoelasticity decreases with increasing DTT. This is consistent with the results observation of reduced slime volume in presence on DTT [41, 42]. It is important to note that disulphide bonds are also present with in several intermediate filament dimers [143, 144] which may as well get affected by the DTT addition.

Figure 4.5 B shows the engineering stress-strain curves in uniaxial extension when the concentration of mucus in varied increased while holding the concentration of threads fixed. Contrary to what was observed in the cases of increasing exudate concentration, Fig. 4.9 A, adding more mucus, makes slime more compliant. Similar trend is observed in the extension work. It is also observed that although the yield stress decreases with increasing mucus, corresponding yield strain increases, Fig. 4.9 B. Thus, the effect of increasing relative mucus to thread concentration in slime results in different properties in shear and extension.

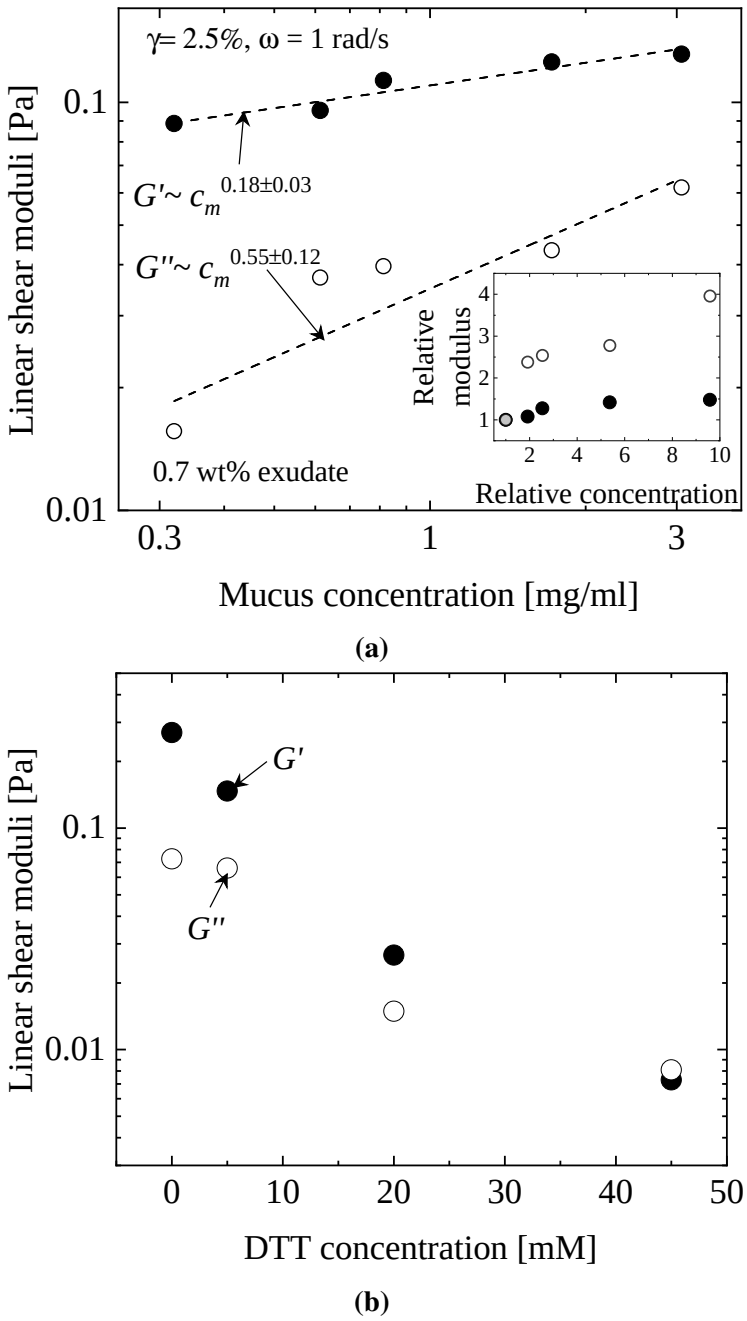

Figure 4.8: Effect of varying mucus concentration on shear properties of slime. (a) Increasing mucus content in slime while holding the thread concentration fixed has a weak effect on the shear elastic properties. Loss modulus has a stronger dependence on increasing mucus concentration, the power-law dependence of loss modulus closely follows Fuoss law. Inset shows same data normalized by the modulus (vertical axis) and mucus concentration (horizontal axis) of the samples formed at physiological exudate concentration. (b) Disrupting the mucus networks using varying concentration of DTT (dithiothreitol) has a detrimental effects on both elastic and viscous properties of slime.

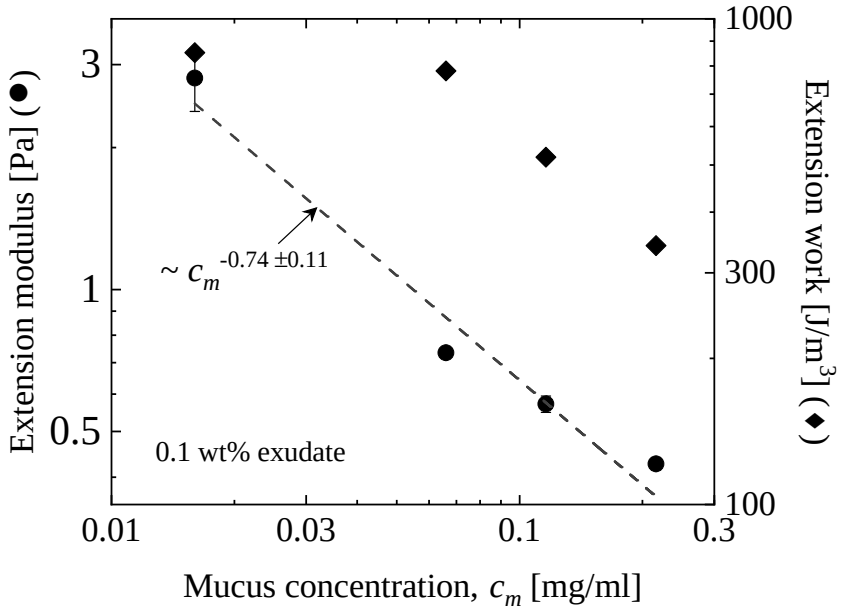

(a)

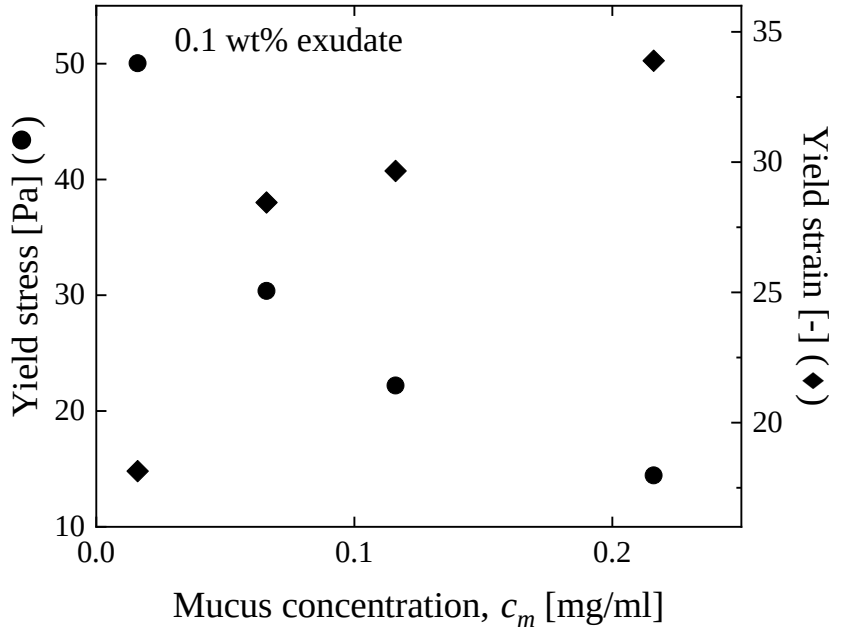

(b)

Figure 4.9: Mucus content affects the extensional properties of slime. (a) Extension modulus of slime samples with increasing mucus content while holding the concentration of threads fixed, decreases contrary to the results in shear rheology, where elasticity weakly increase with mucus concentration. Correspondingly, the work done in stretching the samples decreases. (b) The yield stress, extracted as the topmost point in stress-strain curves, decreases with the increasing mucus content. However, the yield strain, increases for samples with more mucus content. The slime becomes more softer and ductile with increasing mucus content.

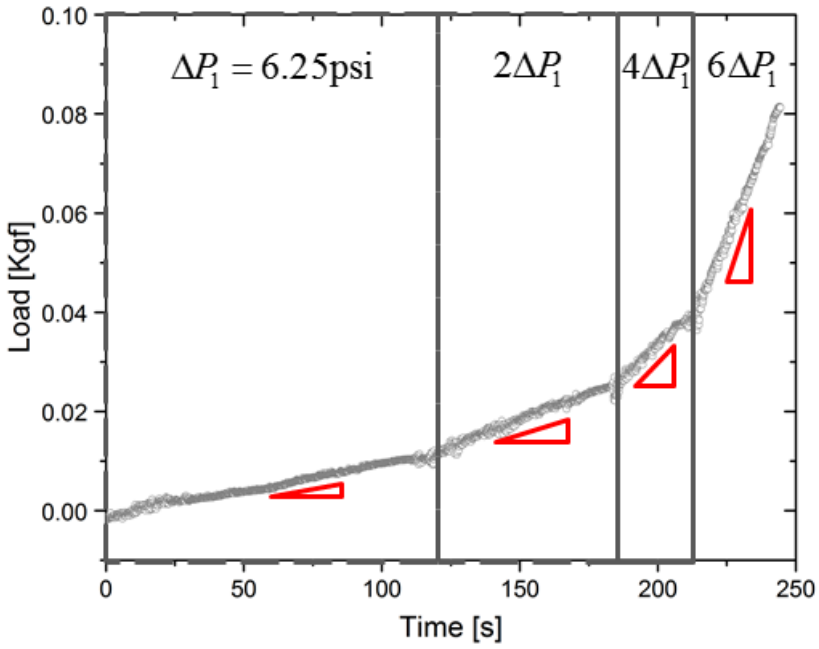

Figure 4.10: The mass of the solvent that flows through the slime sample under pressure is plotted as a function of time for different applied pressures.

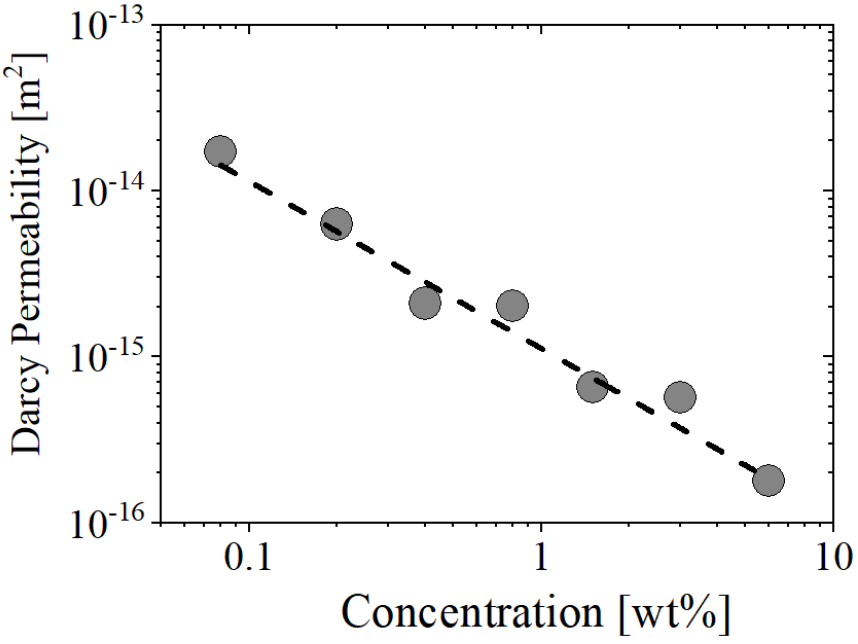

Figure 4.11: The Darcy permeability of hagfish slime as its concentration is varied. The dashed line shows the best-fit power-law dependence of permeability on concentration, $\kappa \sim c$. The permeability of slime is much lower than the characteristic permeability of fish gills ($O(10^{-13}$ m^2))

4.3.4 Permeability Measurements

Figure 4.10 shows the raw-data from the experiments that was used to calculate the permeability of hagfish slime. A constant pressure is applied to maintain the flow, and since the gravitation head is negligible compared to the applied pressure, we assume that the pressure difference, ΔP, deriving the flow is constant for a P_{applied}. The mass of solvent that is collected on a weighing scale is used to calculate the volume flow rate Q of the solvent. The calculated volume flow rate is roughly constant in the duration of experiments (although some deviations as observed, but the load-time curve is linear to the leading order). An apparent Darcy permeability κ can be calculated as

$$\kappa = \frac{Q}{A}\frac{\mu}{(\Delta P)/L} \tag{4.1}$$

where A is the cross-sectional area of the setup and L is the thickness of the slime sample. It is trivial to note from Fig. 4.10 that the flow rate ($\sim$ as the slope of the load vs time curve) increases as the pressure is increased. The apparent Darcy permeability for slime at various concentrations is plotted in Fig. 4.11. The apparent permeability follows a inverse relation with the concentration of exudate. Following this power-law trend, we estimate the permeability of hagfish slime at its physiological concentrations to be $O(10^{-13})$ m^2. This value of permeability is significantly lower than the representative value of permeability of the interlamellar structures in fish gills ($O(10^{-6})$ m^2), hence is consistent with the idea of slime choking the predators. Note that, we verified that the permeability of the set-up without slime is orders of magnitude higher than the the values shown in Fig. 4.11 hence our measurements should be representative of the intrinsic permeability of slime. Fig. 4.12 shows the effects of varying the pressure difference on the measurements. We find that the flow rate weakly increases with the applied pressure. For an undeformed structure (constant permeability), a linear relationship between the flow rate and pressure difference is expected. However, since slime is very soft and easily deformable, we expected the effective permeability to decrease as the pressure is increased.

4.4 Discussion and Modeling

4.4.1 Structure-Property Relationship in Uniaxial Extension

From the experimental observation, it is apparent that elasticity of hagfish slime is attributable to the underlying dilute network of very long fibers as shown in Figure 4.13 a.

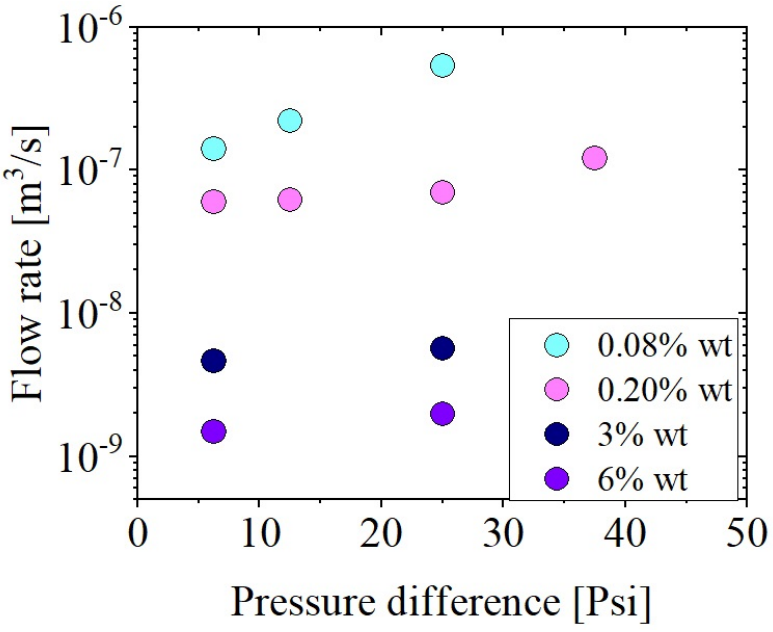

(a)

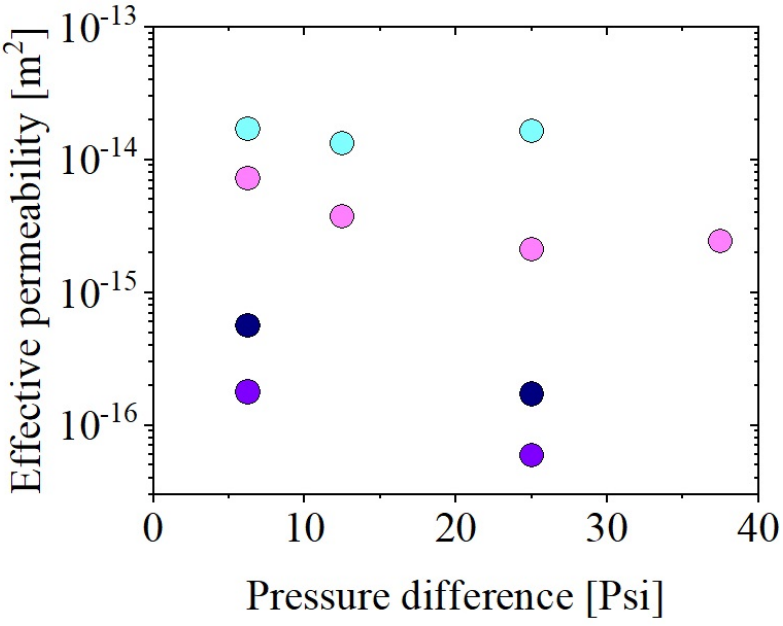

(b)

Figure 4.12: (a) Flow rate as the applied pressure is varied for different concentrations of slime. (b) Effective permeability decreases with the applied pressure.

Here, we extend the network model from section 3.4.2. Contrary to the case of small applied deformation, where we showed that the bending/unbending of fibers dominates the mechanical response of the network Fig. 4.13 b, we hypothesize that under large deformations remove all the athermal bends in the fibers and the fiber stretches as shown in

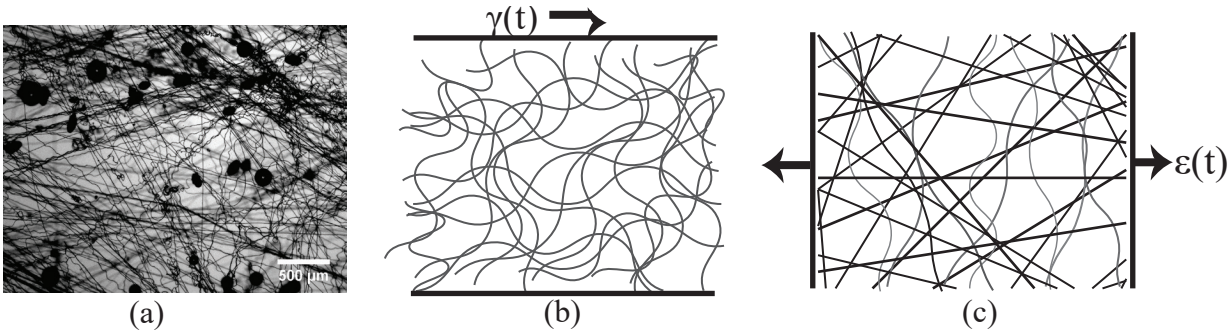

Figure 4.13: (a) DIC image of hagfish slime showing the network of threads. (b) Under small shear deformations the bending-unbending of fibers gives relatively soft mechanics. (c) When deformed with large extensional strain, all the athermal bends are pulled out and the stretching of fibers provides a stiffer response.

Fig. 4.13 c. To evaluate the modulus in extension, we consider the pure stretching of fibers. Fibers are essentially randomly oriented straight rods. Extension will lead to an increase in the length of individual rods in the direction of stretch. A rod at oriented at an angle, α, w.r.t. the direction of extension, stretches by $\Delta L = \epsilon \cos^2 \alpha$ under an extension, ϵ. Hence the work done in stretching the rod is given by $dW_{extension} = \frac{1}{2} E a^2 (\epsilon \cos^4)$. To sum over such contribution from fibers oriented in all directions is given by $W_{extension} = \frac{2}{\pi} \int_0^{\pi/2} dW_{extension} d\alpha$ or $W_{extension} = \frac{3}{16} \rho E a^2 \epsilon^2$. Hence, the extension modulus can be obtained by energy balance as,

$$Y = \frac{3}{8} \rho E a^2 \tag{4.2}$$

In section 3.4.2, we found that the linear shear modulus $G \sim EI/h^2$. Thus the ratio of shear modulus in extension to bending modulus, Y/G scales as $h^2/a^2 \sim O(10^2)$. This is expected, since it is more difficult to physically stretch the fibers than bend them. We neglected any irreversibility (e.g. dissipation) and alignment during the deformation. Although individual fiber hysteresis effects were observed in single fiber studies [64], we neglect such effects here in the structure-rheology modeling, since we focus our understanding to small deformations and the overall elastic strength of the network.

So far, we have not considered the effect of mucus. We argue that effective elasticity produced from mucus if significantly lower than that by threads. However, when we increase the concentration of mucus while holding the concentration of threads fixed, we see different effects in shear and extension as shown in Figs. 4.8 and 4.9. This is can be explained by the different experimental conditions in shear and extension. In both cases, sample preparation involves, mixing threads and mucin vesicles in fixed volume of solvent. Thus, with increasing mucin vesicles, the swelling ratio of mucus network will decrease (because the total solvent volume is fixed). This explains why the shear elastic modulus

increases (number density of mucus fibers increases). However, the extension experiments are performed inside a solvent bath containing same solvent as the sample. Thus there is possibility of mucus swelling and the extent of network swelling will be determined by the equilibrium thermodynamics. Mucus swelling will result in increasing the overall volume of slime. Thus the thread length per unit volume, ρ, will decrease as more mucus is added in abundance of solvent. Thus, the extension modulus decreases.

4.4.2 Interpretation of the Permeability Measurements

The permeability of hagfish slime is remarkably low, considering the large pore size structure of the network of threads inside the slime. In general, the permeability (κ) of a medium is related to the total solid fraction (ϕ), and a characteristic length scale (a), and can be expressed as $\kappa = a^2 f(\phi)$. For a random isotropic fibrous network [145],

$$\kappa_2 = a_2^2 \left[\frac{1}{2} \left(\frac{\pi}{\phi} \right)^{1/2} - 1 \right]^2 [0.71407 \exp(-0.51854\phi_2)] \tag{4.3}$$

This provides an estimate of the contribution of threads in the slime network in its permeability. For the fibrous network of slime, $a \approx 2$ μm is the fiber diameter and in the range of concentrations that we studied, $\phi \approx 10^{-4} - 10^{-2}$. This gives $\kappa \approx 10^{-9} - 10^{-7}$ m^2. We conclude that the low permeability of hagfish slime cannot arise from pure thread network. Hence, the mucus component that coexists with the thread network in slime must have a drastic impact on the overall permeability.

Inspired by the work done by White et al. [146], we propose three possible microstructures for slime. Fig. 4.14 a shows an interpenetrated network of thread and mucus. The threads form the larger pores, and the mucus form the smaller pores. The overall permeability κ of the network is related to the permeability κ_1 and κ_2 of the individual components (if the fiber radii are not very different), and their volume fractions, ϕ_1 and ϕ_2,

$$\frac{1}{\kappa} = \frac{\phi_1}{\phi_1 + \phi_2} \frac{1}{\kappa_1(\phi_1)} + \frac{\phi_2}{\phi_1 + \phi_2} \frac{1}{\kappa_2(\phi_2)} \tag{4.4}$$

For hagfish slime, we expect if the mucus exists in a network, the fiber diameter is likely much smaller than that of thread. Under such conditions, the microstructures in Fig. 4.14 a and b are essentially the same and the overall permeability can be described as [146]

$$\frac{\kappa}{\kappa_2} = 1 - \frac{5}{3}\phi_1 + O(\phi_1^2) \tag{4.5}$$

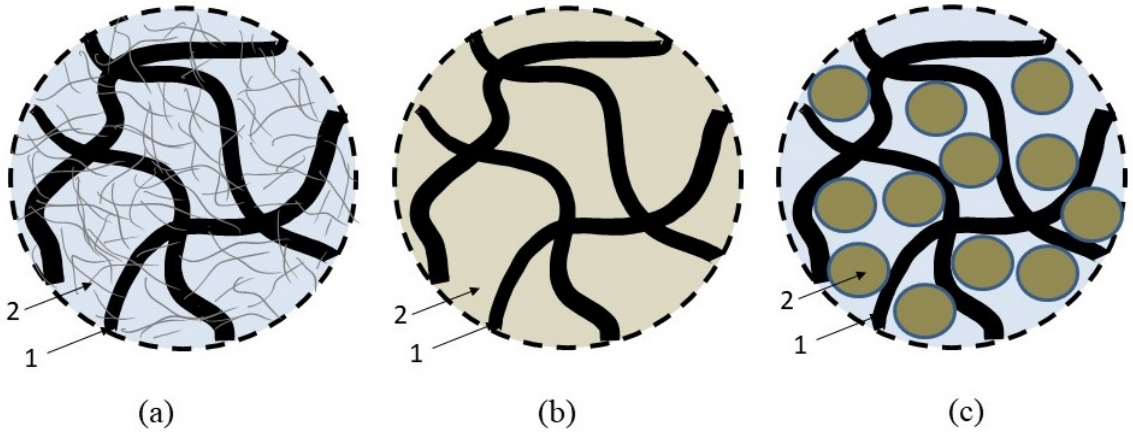

Figure 4.14: Proposed microstructures for hagfish slime. (a) an interpenetrating network of threads (thicker, longer fibers) and mucus network (thinner, shorter fibers). (b) A homogeneous mucus solution filling the pores of network formed by threads. (c) Swollen mucus blobs in the pores of thread network.

The scenario presented in Fig. 4.14 c depicts the scenarios of swollen mucin vesicles inside the thread network. The contribution from the swollen vesicles can be expressed as $\kappa_2 = \frac{2a^2}{9\phi_2}$, where a is the radius of the swollen vesicle [147]. Fig. 4.15 shows the predictions of the microstructural hypothesis. For the scenarios in Fig. 4.14 c, the the predictions are based on assuming the swollen blob size of 15 μm. It is evident that such a microstruture cannot provide the low permeability that is experimentally observed. The hypothesis described in Fig. 4.14 a/b, shows a good agreement with the experiments. In this case, the fiber diameter in the mucus diameter is assumed to be 4 nm. Such a value is close to the ones reported for different mucus networks [148]. This indicates that the characteristic mesh size in hagfish slime is set by the mucus networks. And the characteristic mesh size can be estimated as $\sim \sqrt{\kappa} = 10 - 100$ nm. Such a mesh size is consistent with the mucus networks studied in the literature [149]. Mucus networks can either exist as volume spanning networks or local networks in the interstitial spaces of the thread network. The ability of small amounts of fine fibers to greatly reduce the permeability of a fiber matrix has been demonstrated for synthetic systems [146]. Slime appears to utilize similar principle.

4.4.3 Material Performance

An obvious objective of hagfish slime is to clog the gills of predators. Such a functional requirement requires the material to be compliant (to easily contact the surface), posses a low permeability (reduced water flow), high adhesion (stick to the gills/surfaces), and large expansion ratios (evident from the videos). A qualitative comparison of Darcy permeability

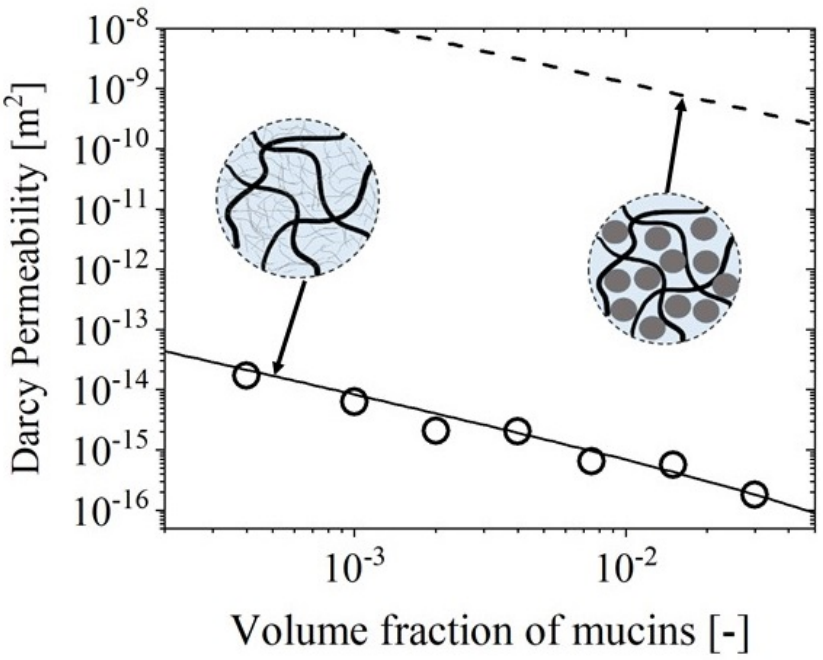

Figure 4.15: Comparison of predictions using the hypothesized microstructures (Fig. 4.14) versus the experimental measurements. The hypothesis presented in Fig. 4.14 c, predicts significantly higher permeability while the predictions Fig. 4.14 a, shows a good agreement with the experiments (assuming 5 nm thick mucus fiber diameter).

versus volume fraction for various soft materials is given in the Ashby plot (Fig. 4.16). It is evident that hagfish slime provides very low permeability at a very low volume fraction of its constituent material. Fig. 4.17 is shown for the elastic modulus versus permeability. It is evident that the slime is much compliant comparable to other common biomaterials, which makes it easy to deform, and yet maintain relatively low permeability. Such a feature is potentially a result of its structure where the bends in thick threads provide it a low modulus thus making it compliant while the swollen mucus potentially lower its permeability.

4.5 Summary

A comparison of shear and extensional properties of hagfish slime and the effects of varying the relative composition of constituents in slime is reported for the first time. Our results suggest that slime is significantly stiffer in extension than in shear and can undergo huge extensional deformations before failure. Varying the relative composition of mucus (M) to threads (T) in slime compared to the physiological composition drastically affects the mechanics: lowering M/T, decreases the shear viscous and elastic properties while increasing

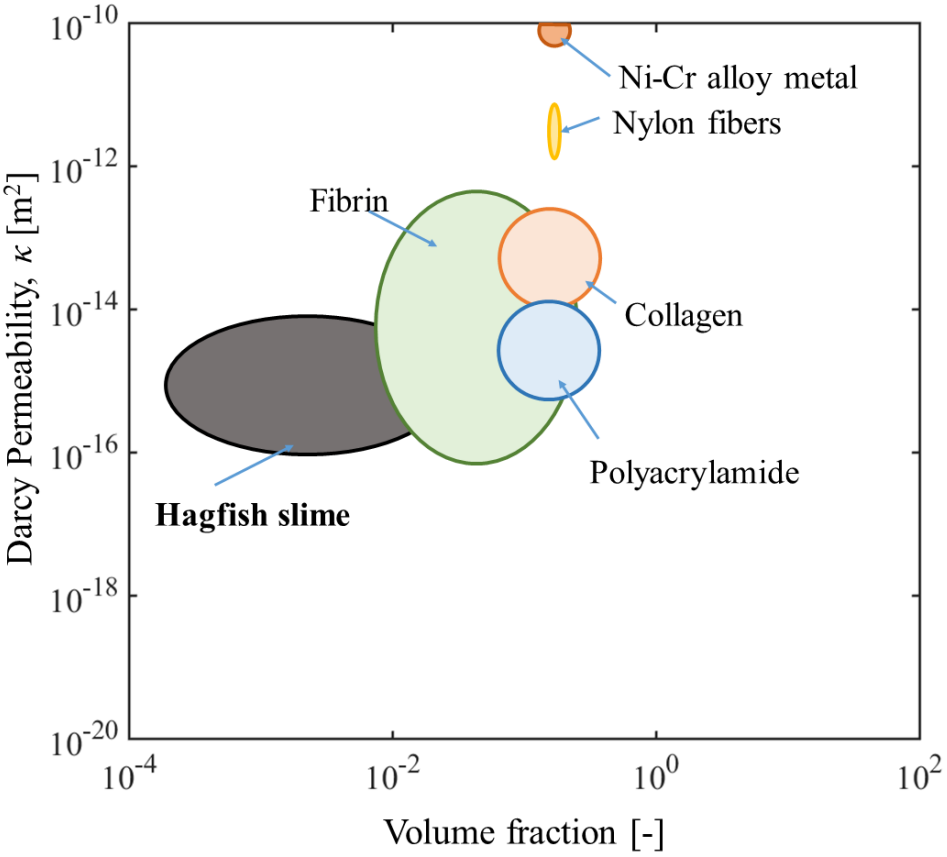

Figure 4.16: Ashby diagram showing Darcy permeability for some common materials as a function of volume fraction. The properties measured in this work indicate that hagfish slime achieves remarkably low permeability at very low volume fraction of its constituents.

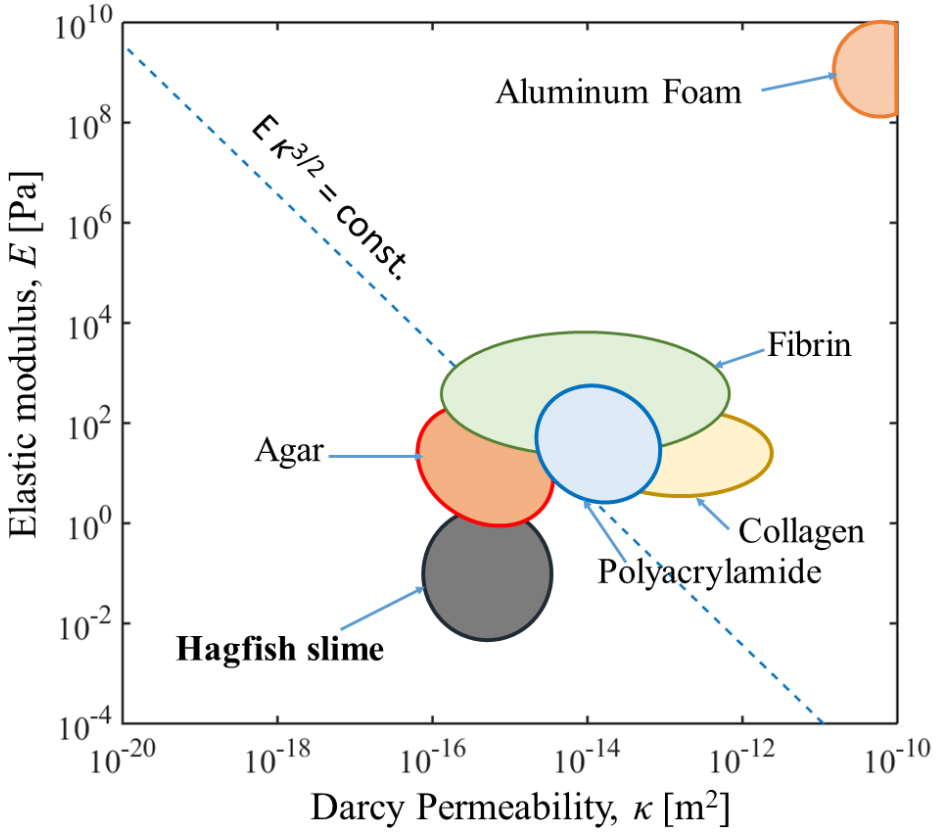

Figure 4.17: Ashby diagram showing Elastic Modulus for some common materials versus their Darcy permeability. The dashed blue line is the scaling prediction using the rubber elasticity idea $E \sim 1/\xi^3$ and the Darcy permeability scales as $\kappa \sim \xi^2$, where ξ is the characterisitic mesh size.

M/T weakly increases the shear elastic and viscous properties and drastically reduces the extensional properties, while increasing the ductility of slime.

Acknowledgement

We are grateful to the National Science Foundation for supporting this research under grant number CBET-1342408 to RHE. We also thank Prof. Alejandro G. Marangoni (Food Science, University of Guelph) for providing access to rheometers in immediate proximity to the hagfish and Evan McKenzie, Sarah Schorno and Dr. Atsuko Negishi (Integrative Biology, U Guelph) for assistance in collecting the samples.

CHAPTER 5

LINEAR AND NONLINEAR RHEOLOGY OF SOFT REPULSIVE PNIPAM MICROGEL SUSPENSIONS

5.1 Introduction

Colloidal suspensions have been a major area of interest in the soft matter community for decades. Much fundamental research has been done with model hard-sphere colloids, with or without small polymer depletants, which have elucidated the understanding of physical phenomenon such as crystallization, phase separation, glassy dynamics, and nonlinear rheology [150, 151, 152]. Other widely studied systems are dense suspensions of soft colloids [153, 154]. However, they bring additional complexities since the particles are deformable with a fluctuating internal polymeric microstructure, which can lead to their size and even shape becoming a function of thermodynamic state (volume fraction, temperature, ionic strength) and deformation. Most microgels are charged and can be created with diverse chemistry, which introduces concentration-dependent complexities associated with osmotic decompression, the poorly known internal density profile (often core-shell), and variable single particle mechanical stiffness. Hence, the effective interaction potential between microgel particles is a complex issue, consistent with a lack of universal signatures in their rheology [155, 156]. Moreover, microgels can exist as dense Brownian suspensions that can form kinetic glasses or gels, or at ultra-high concentration as paste-like materials characterized by literal contacts between deformed particles. If the latter exist, the system is typically viewed as in a "soft jammed" regime. However, whether the physics in this regime is entirely akin to granular materials where large scale motion requires the application of external mechanical energy is not well understood, and the answer may depend on

This chapter appeared in the following peer-reviewed publication: Ghosh*, A., G. Chaudhary*, J. G. Kang, P. V. Braun, R. H. Ewoldt, and K. S. Schweizer, "Linear and nonlinear rheology and structural relaxation in dense glassy and jammed soft repulsive microgel suspensions," Soft Matter, 15, 1038-1052 (2019), doi: 10.1039/C8SM02014K (*equal contribution)
Ashesh Ghosh made equal contribution towards this chapter. Gaurav Chaudhary led the experimental work (Figs. 5.1-5.5) and Ashesh Ghosh led the theoretical work (Figs. 5.6-5.14).

system and thermodynamic state.

In this chapter, we perform a coordinated experimental and theoretical study of the dynamics and rheology of soft, thermoresponsive poly(N-isopropylacrylamide) (pNIPAM) based microgel suspensions under conditions where they are swollen in a good solvent and repel. There have been extensive prior studies of similar systems [154, 157, 158, 159, 160], albeit mainly in the soft jamming regime with ionic microgels which are chemically crosslinked and can osmotically de-swell with changing concentration [154, 157, 158]. Such microgel pastes are generally viewed as effectively athermal or granular.

Our study has several not very common features: (a) there is no chemical crosslinking via added molecules of the microgel particles, (b) the microgels are only slightly charged, and (c) experiments are performed over an exceptionally wide range of concentration that spans the low viscosity fluid, glassy Brownian, and soft jammed regimes. These aspects distinguish our experimental system from most others, and isolates particle compression as solely due to many body steric effects with negligible ion-induced deswelling. We will show that points (a) and (b) lead to mechanical behavior with features significantly different than prior studies. Point (c) is also a strong focus of this work where in the first two concentration regimes there are no literal inter-particle "contacts" and the mechanical response is influenced by Brownian caging processes driven by thermal fluctuations and external stress [161, 162, 163]. The possibility that the ultra-dense regime is not granular-like is also explored.

The remainder of this chapter is structured as follows. In section 5.2 we describe the experimental materials and methods. Our key experimental results for the linear and nonlinear rheology are presented in section 5.3. Section 5.4 presents the basics of our theoretical modeling of single microgel structure, and the equilibrium and dynamical statistical mechanical tools we employ to make predictions for collective packing structure, linear elasticity, structural relaxation, and aspects of nonlinear rheology. Quantification of microgel effective volume fraction is discussed in section 5.5, and predictions made for the linear dynamic shear modulus and packing structure, with the former compared with our measurements. Theoretical results for the equilibrium structural relaxation time, its variation with deformation, and yielding properties are presented in section 5.6, with some comparison to experiment. The paper concludes with a discussion in Section 5.7. Additional experimental characterization and rheological results are presented in the Appendix C.

5.2 Materials and Methods

5.2.1 Microgel Synthesis and Characterization

Slightly charged self-crosslinked pNIPAM microgels were synthesized under a 'crosslinker free' condition following the protocol described in literature [164] with modifications. 100 ml of Type I water (18.2 MΩ cm) was filtered through a 0.2 μm Acrodisc syringe filter. Then, 146 mM (1.65 g) of N-isopropylacrylamide (NIPAM, 99 %, Acros) monomer was dissolved in filtered water. The monomer solution was again filtered through a 0.2 μm Acrodisc syringe filter into a 3-neck round bottom flask. The solution was stirred at 500 rpm, purged with nitrogen, and heated to 68°C in a temperature-controlled oil bath until the temperature of the solution became stable (1 hour typically). We then injected a solution of 2.8 mM (80 mg) potassium peroxodisulfate (KPS, 99 %+, Sigma-Aldrich) dissolved in 1 ml of the pre-filtered Type 1 water through a 0.2 μm Acrodisc syringe filter to initiate the polymerization. The mixture was left to react under continuous stirring at 500 rpm in nitrogen atmosphere overnight. This leads to the formation of stable nanospheres instead of linear chains if the solution is incubated at temperatures well above the lower critical solution temperature (LCST) of PNIPAM ($\sim 32^{\circ}$C. The formation of gel nanospheres is attributed to self-crosslinking by chain transfer reaction during and after polymerization [165]. Microgels prepared with a similar preparation protocol have been referred to as neutral in their charge [164, 166]. Here, we refer to such microgels as 'slightly charged', because the initiator used may possibly leave some charge on the colloids. After the polymerization, the solution was cooled down to the room temperature and filtered with a glass wool five times to remove large particulates. The microgel particles were then thoroughly purified via five cycles of a centrifuge/dispersion process. The centrifugation was done at 15000 x g of relative centrifugal force (RCF), and the dispersion was enabled by a mixed process of the ultrasonication followed by the magnetic stirring. The cleaned particles were then lyophilized for further characterization. A stock solution of c=9 wt% was then diluted with deionized water to achieve the desired concentration of the slightly charged microgel suspension.

The particle radius was determined by dynamic light scattering (DLS) (Zetasizer Nano ZS, Malvern) and a Helium-Neon gas laser emitting at 632.8 nm on a very dilute suspension (0.04 wt%) with a beam diameter of 0.63 mm (see Appendix Fig. C.1). The present work focuses on the lower temperature regime where microgels are swollen and interact via repulsive forces. In dilute solution, the microgel particles have a mean diameter of $2R = 551 \pm 71$ nm at 10°C.

5.2.2 Rheological Characterization

Rheological experiments are performed over a very wide range of microgel concentration from 0.03 to 9 wt%. Viscoelasticity was probed using a rotational rheometer (model Discovery Hybrid 3, TA instruments and model MCR 702 from Anton Paar) with plate-plate geometry. These are both torque-controlled instruments (a.k.a. combined-motor-transducer type). A 600 grit, adhesive-back sand paper (Norton Abrasives) was adhered to the contact surfaces to suppress wall slip. The plate diameter was varied depending on the sample concentration to obtain a measurable response higher than the minimum torque resolution. A 60 mm plate was used for dilute samples 0.03-0.25 wt%, 40 mm plate for 0.25-1.5 wt%, 20 mm for 0.5-4.5 wt% , and 8 mm for 4.5-9 wt% samples. The typical gap in all experiments was between (550-750) μm, far larger than the particle size, thus eliminating confinement effects. A solvent trap, with a wet-tissue adhered to its interior, was used to minimize solvent evaporation during the measurements. The temperature of the bottom plate was controlled using a Peltier-system. To suppress sample aging effects and erase any history, all samples were rejuvenated by shearing at 50 1/s for 60 s and then allowed to relax for 12 min before taking measurements [154].

Two types of rheological characterization were performed: oscillatory shear and steady shear. To probe the linear response, frequency sweeps were performed from $\omega = (0.03 - 100)$ rad/s at a strain amplitude of 1% at 10°C. To probe the nonlinear response, strain sweeps of amplitude $\gamma_0 = (0.1 - 300)\%$ at a fixed frequency of 1 rad/s were performed. In the steady shear experiments, shear rates were typically varied from (300-0.01) 1/s while waiting for the system to reach an apparent steady state as deduced by $< 5\%$ variation in torque over a period of 30 s.

5.3 Experimental Results

5.3.1 Linear Rheology

Figure 5.1 shows the frequency-dependent linear storage, G', and loss, G'', moduli as a function of frequency. One sees a nearly frequency independent G', with a smaller G'' that also is weakly frequency-dependent. Hence, $G'' < G'$ for all concentrations above 0.4 wt% and the response is predominantly solid-like with the structural or flow relaxation time obeying $\tau_\alpha > \omega_{low}^{-1} \approx 100$ s. No crossover between G' and G'' was observed in the range of frequencies probed, indicating the microgels do not show significant diffusion or structural relaxation on the probing time scales.

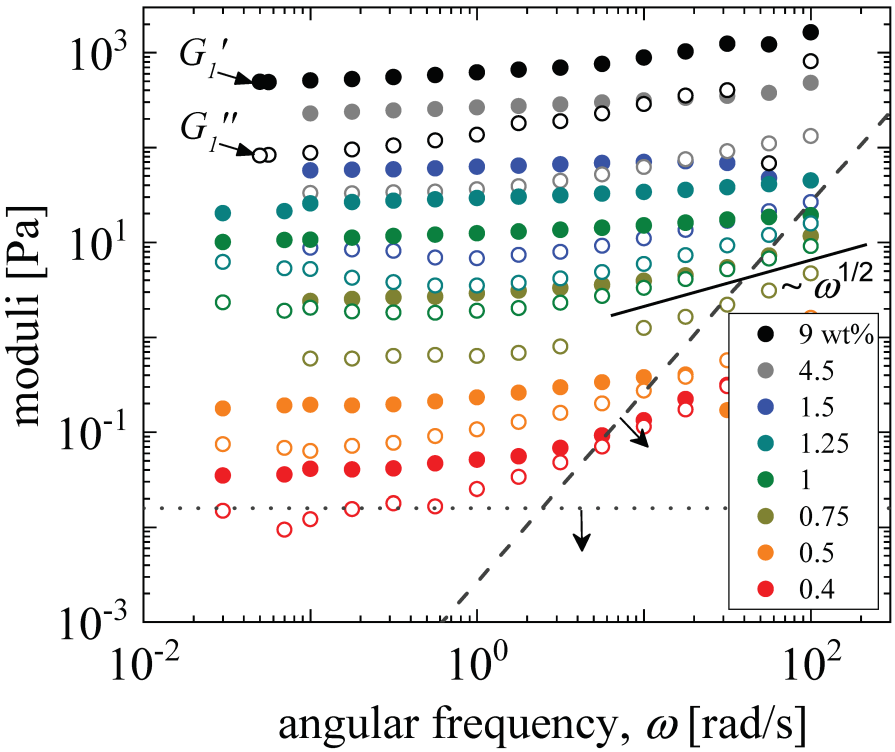

Figure 5.1: Linear rheological response (G' closed symbols, G'' open symbols) of the slightly charged, self-crosslinked microgel suspensions. Frequency dependence at $\gamma_0 = 1\%$. Suspensions at $c > 0.4$ wt% do not flow on the longest probed time scales (~ 100 s). Experimental limits shown by the dotted horizontal line (minimum torque limit) and the dashed line (instrument inertia limit) [68].

At higher frequencies, the commonly observed frequency dependence of G'' $\omega^{1/2}$ for a loosely and randomly packed emulsion is very roughly observed for the 0.75 wt% and 1 wt% samples [167]. However, there are systematic deviations – power laws are often not well developed, and apparent scaling exponents, if force fit, can be larger or smaller than 0.5, and tend to decrease as concentration grows. For concentrations below 1 wt%, the inertia of the measuring system influences the torque measurements significantly and makes it difficult to observe any reliable signatures [68] for high frequency measurements.

The linear storage modulus at a fixed frequency of $\omega = 1$ rad/s and a strain amplitude of $\gamma_0 = 1\%$ is shown in Fig. 5.2. It monotonically grows with increasing concentration (as also found at slightly higher temperatures, see Appendix Figure C.3). Three distinct regimes of behavior are observed. For concentrations below $c = 0.4$ wt%, no measurable elastic modulus is detected above the minimum torque limit of the instrument. This seems consistent with measurements of the high shear rate viscosity (Appendix Figure C.2), where an excellent agreement with the Einstein prediction of the dilute intrinsic viscosity is ob-

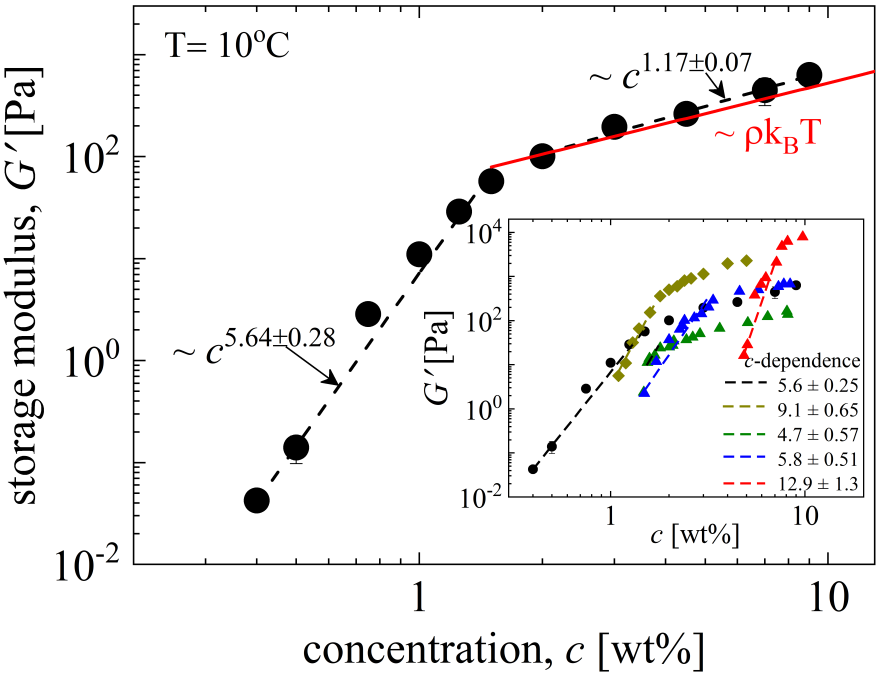

Figure 5.2: Concentration dependence of linear storage modulus, G'. For low concentrations ($c < 1.5$ wt%), G' varies over 3 orders of magnitude and roughly follows a power law concentration dependence, $G' \sim c^{5.68\pm0.28}$. Above $c = 1.5$ wt%, the concentration dependence changes to a roughly linear relation, $G' \sim c$. The red line shows a fit using the classic rubber elasticity model (with monomer molecular weight of 113.6 g/mol and 3903 monomer units each polymer chain) discussed in the text. (inset) Comparison of the concentration dependent storage modulus as observed in the current work that employs self crosslinked slightly charged microgel suspensions (black circles) and prior studies of crosslinked ionic microgels (yellow diamonds [160] and blue, green and red triangles [154]). A wide concentration range spanning the glassy and "soft jammed" regimes is shown for all the data with different concentration dependencies of shear modulus in the glassy regime. A qualitative universality exists for soft microgels in the sense that, independent of chemistry, all soft particles show a stronger concentration dependence in the glassy regime and roughly linear growth in the "soft jammed" regime. However, the apparent power laws and soft jamming crossover points are highly variable, depending on microgel chemistry, preparation protocol, their internal crosslink density, and the nature of the steric and/or ionic driven deswelling behavior.

served in the concentration range (0.03-0.35) wt%, beyond which the viscosity strongly grows. Since the microgels are only slightly charged, the latter is presumably due to repulsive inter-microgel forces and transient caging in the suspension. Such a fundamental change in the concentration range (0.4-0.5) wt% is consistent with a dynamic crossover to a regime where there is little particle motion on the experimentally probed time scales

[160, 168]. In hard sphere glasses the characteristic modulus scale is set by the thermal energy per particle volume [153, 163], $G \sim k_B T/(2R)^3$, where k_B is Boltzmann constant, T is temperature, and R is the particle radius, which for our system is $G' = 0.024$ Pa for $2R = 550$ nm. This estimate is fairly close to when we first observe a solid-like response: $G' = 0.04$ Pa and $G' = 0.14$ Pa for 0.4 wt% and 0.5 wt% concentrations, respectively.

In the intermediate concentration range, defined as (0.4-1.25) wt%, the elastic modulus shows a dramatic dependence on microgel concentration. A variance weighted fit of all data yields $G' \sim c^{5.64\pm0.28}$, but it seems clear the effective exponent weakly decreases with concentration. Similar observations have been made in literature [154, 160], but the apparent power law exponent in Fig. 5.2 is generally very different for previous work using pNIPAM based suspensions. For example, Menut et al. [154] observed power law exponents of 4.4, 6.1 and 14, respectively, for three p(NIPAAm-co-AAc) ionic microgel suspensions of increasing single particle stiffness as synthesized by precipitation polymerization with varying cross-linker concentration. Pellet and Cloitre [160] observed a power-law exponent of 9.1 for a suspension of polyelectrolyte microgels synthesized by emulsion polymerization. Given the narrow range of data in the "glassy regime" of that study, such a high apparent exponent may simply indicate exponential growth.

In the highest concentration range of our experiments, defined as (1.5-9) wt%, the elastic response again qualitatively changes. The modulus now grows weakly in a nearly linear manner with concentration (variance weighted fit, $G' \sim c^{1.17\pm0.07}$. How to interpret this solely from mechanical data is neither obvious nor unique. We can envision three possibilities. (1) It could indicate a transition to what is usually called a "soft jammed" state where microgels are in literal contact, particles may deform and form facets, and elastic energy is stored in a granular manner. This scenario predicts $G' \propto (\phi - \phi_{\text{jam}})$ [160], which to be consistent with our data seems to require the effective volume fraction grows linearly with microgel concentration (which is *a priori* unclear). (2) Discrete microgel particles could somehow effectively "fuse" in the practical sense that the suspension behaves as a connected macroscopic network of flexible "elastically active chains or strands". From the classical theory of rubber elasticity, this scenario implies elasticity is fundamentally of single strand (conformational) entropic origin, with $G' \sim \rho_x kT$, where ρ_x is the polymer concentration divided by the number of monomer units in each polymer strand, N_x [154, 169]. A comparison between our experimental data and the rubber elasticity model [170] is given by the red line (variance weighted fit parameter, $N_x = 3903$) in Fig. 5.2. (3) A third scenario is the change in concentration dependence of G' reflects a crossover from sterically-induced weak compression of core-shell microgels to a regime where the microgels isotropically shrink in a manner that keeps its effective volume fraction fixed.

This scenario retains the discrete picture of microgel particles, does not invoke facets or literal interparticle contacts, and posits an interparticle collective origin of stress storage. It will theoretically be developed in section 5.4, and shown to also lead to a linear growth of G' with microgel concentration. While we cannot completely rule out there might be components of scenario (1) or (2) that contribute to the observed linear growth of elastic modulus of our system, in this article we take a minimalist approach of exploring a Brownian glassy suspension scenario for the entire concentration regime without invoking athermal soft jamming.

The inset of Fig. 5.2 shows elastic modulus data from other labs for different types of microgels, all of which are ionic. Clearly, one sees that at fixed concentration in wt%, different microgel samples display a wide variety of modulus levels and sensitivity to concentration. This emphasizes that our present self-crosslinked slightly charged microgel system with different chemistry does display a distinct elastic response. It also emphasizes the far larger range of concentration probed in our study (factor ~ 25) versus prior studies (typically factor of 3-10). However, these prior studies all observe, to varying degrees, a stronger growth of G' at lower concentration followed by a much weaker growth at very high microgel concentrations.

5.3.2 Nonlinear Rheology

Our nonlinear oscillatory shear measurements are shown in Fig. 5.3. Only the first-harmonic responses are plotted, representing the average storage and loss of mechanical energy, here indicated as G'_1 and G''_1, respectively. The response at all concentrations is similar. At low strains, the response is in the linear regime, with roughly a constant value of G'_1 and G''_1 and $G'_1 > G''_1$. At large strains, the response becomes nonlinear with G'_1 showing a monotonic decrease while G''_1 exhibits a maximum. An increasing G''_1 indicates more dissipation presumably due to deformation-induced microgel motion which can be qualitatively viewed as a stress driven solid-to-fluid like transition or yielding [154, 163]. One measure of the latter is the strain at which $G'_1 = G''_1$, which occurs at rather high strain values of $\sim 25 - 50\%$ with systematic variation with concentration difficult to discern. More precise definitions and analysis of yielding will be given in section 5.6.

Figure 5.4 shows the steady state flow curve of the microgel suspensions. Below c=0.4 wt%, the response resembles a shear thinning fluid at high shear rates. At higher concentrations, $c > 0.4$ wt%, the stress-strain rate response resembles that of a yield-stress fluid, although for most samples there is no rigorous low shear plateau and the degree to which the data is flat does not vary systematically with concentration. Such a response can be adequately

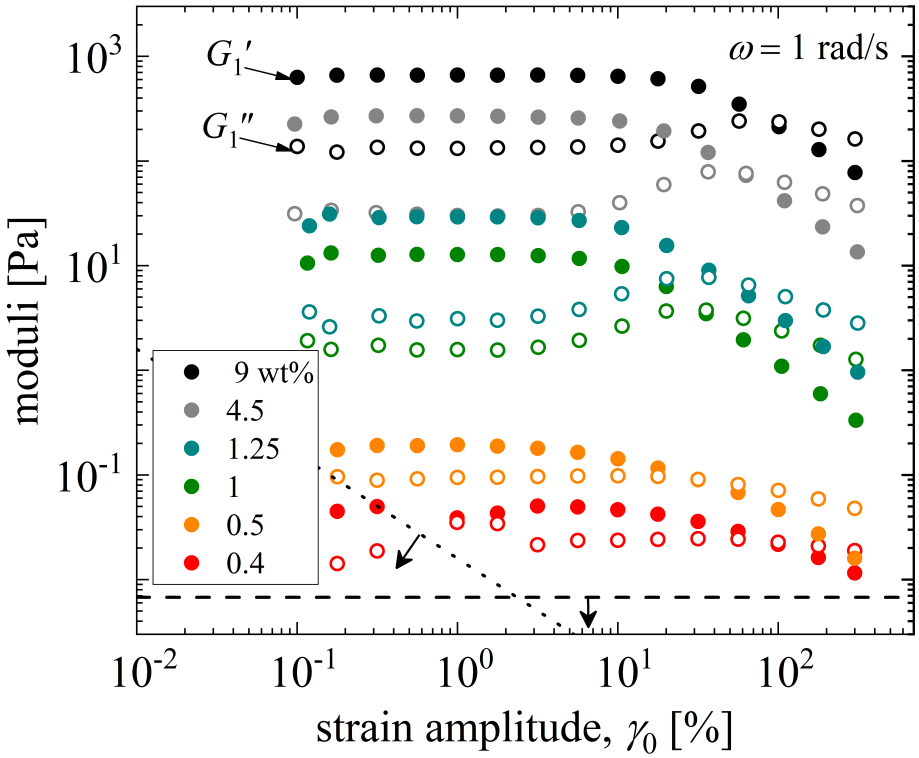

Figure 5.3: Nonlinear viscoelastic moduli (first harmonic G_1' closed symbols, G_1'' open symbols) measured at varying strain amplitudes at a fixed frequency $\omega = 1$ rad/s. At low strains, the response is predominantly elastic, $G_1' > G_1''$ and $G_1' \sim$ constant. Beyond the linear regime, G_1' monotonically decreases, while G_1'' achieves a maximum value as the material undergoes yielding. With further increase in strain, suspensions at all concentrations have a dominant liquid-like response, with both G_1' and G_1'' showing a monotonic decrease and $G_1' < G_1''$. The dotted line shows the minimum torque limit of the instrument and the dashed line shows the instrument inertia limit [68].

captured by the empirical Herschel-Bulkley (HB) model given by: $\sigma(\dot{\gamma}) = \sigma_y^{HB} + K(\dot{\gamma})^n$, where σ_y^{HB} is the apparent yield strength, n is the flow index, and $K(\dot{\gamma})^n$ describes the shear-thinning behavior at high shear rates for $n < 1$ [163]. The parameter K has dimensions that depend on n and does not represent a physical quantity. However, we can instead use a modified form of the HB model [171],

$$\sigma(\dot{\gamma}) = \sigma_y^{HB}\left(1 + \frac{\dot{\gamma}}{\dot{\gamma}_c}\right) \tag{5.1}$$

where the characteristic shear rate, $\dot{\gamma}_c = \left(\frac{\sigma_y^{HB}}{K}\right)^{1/n}$, is associated with a crossover from rate-independent plastic flow to rate-dependent viscous flow. Eq. 5.1 is used to fit the experimental data which directly yields the parameter $\dot{\gamma}_c$.

The HB fits to the data (assuming constant error weighting) and corresponding fit pa-

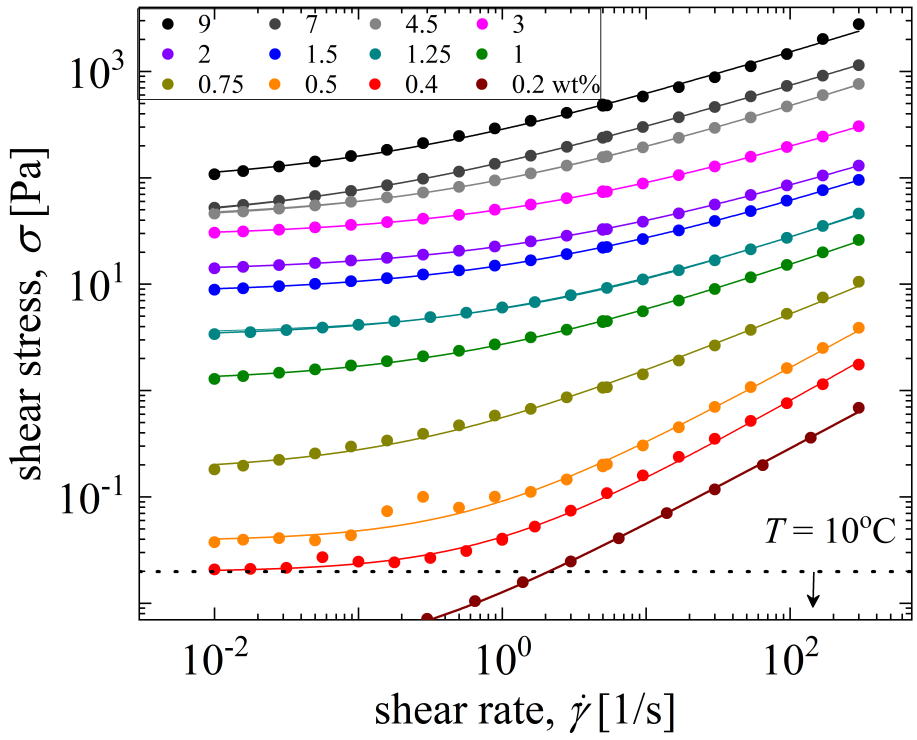

Figure 5.4: Steady state shear flow curves for various suspension concentrations. For $c \geq 0.4$ wt%, all suspensions show an apparent yield stress response, achieving a near plateau at low shear rates. For $c < 0.4$ wt%, the response closely resembles a shear thinning fluid (power law stress-rate scaling with an apparent exponent smaller than 1) in the range of shear rates probed. The solid curves are the Herschel-Bulkley model fits. The dotted horizontal line shows the minimum torque limit of the instrument [68].

rameters ($\sigma_y^{HB}, \dot{\gamma}_c, n$) are shown in Fig. 5.5. Similar to the observations made earlier for the linear elastic modulus, we find a strong concentration dependence of $\sigma_y^{HB} \sim c^{4.5}$ in the intermediate concentration regime, which is however clearly weaker than that of the G' data in Fig. 5.3. We will refer to such behavior as indicating the "glassy regime". At higher concentrations the yield stress grows roughly linearly with concentration, which for descriptive purposes we refer to as the "soft jamming" regime. The flow index, n, decreases monotonically with the concentration in the glassy regime, $n \sim c^{-0.48}$, followed by a nearly constant value of 0.41 in the soft jamming regime. The lower inset of Fig. 5.5 shows that the characteristic shear rate ($\dot{\gamma}_c$) is roughly constant in the glassy regime and follows a power law relation, $\dot{\gamma}_c \sim c^{-2.5}$, in the soft jammed regime. As true of the linear elastic modulus, Fig. 5.5 shows that the yielding properties of our microgel suspensions follow quite different trends from previous studies [160] of different ionic microgel systems. Specifically, the yield stress in the soft jamming regime displays a stronger concentration dependence ($\sim c^2$), the exponent n values are generally larger, and $\dot{\gamma}_c$ increases with the concentration

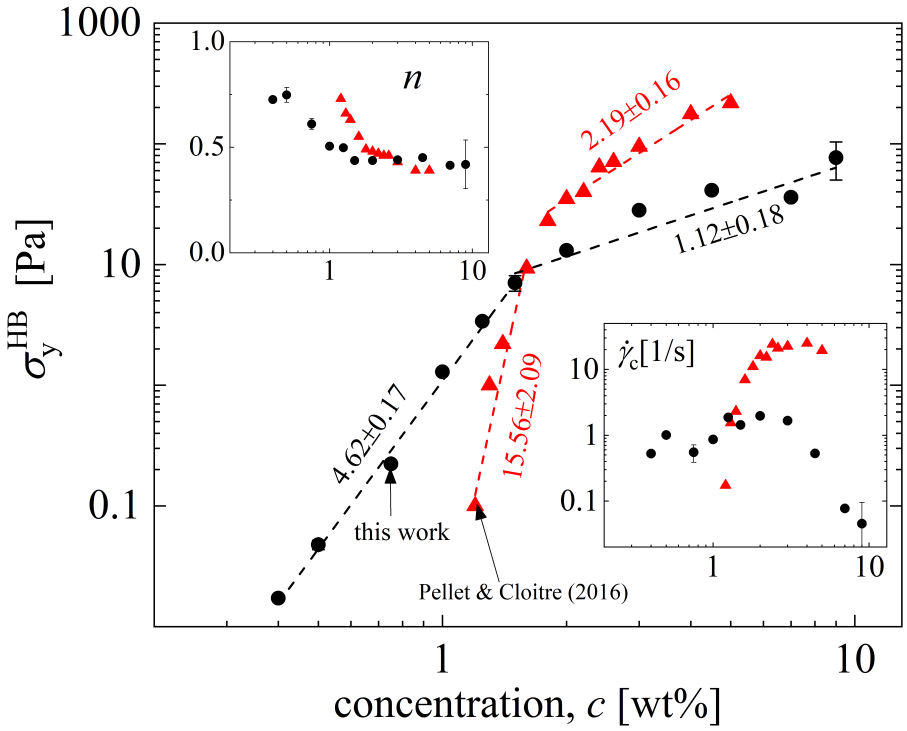

Figure 5.5: Concentration dependence of the Herschel-Bulkley model fit parameters, Eq. 5.1, for our slightly charged microgel suspensions (black circles, from data in Fig. 5.4). Data for the ionic microgel suspensions [160] are shown as red triangles. Power-law scaling exponents are indicated for each fit line. (Inset) Corresponding characteristic shear rate data.

in the glassy regime until appearing to plateau in the soft jamming regime.

5.4 Theoretical Approach: Microgel Model, Packing, Elasticity, Dynamics, and Rheology

5.4.1 Overview and Modeling of Single Microgel Structure in the Condensed Phase

Much theoretical progress has been made in recent years by many workers [172, 173, 174, 175] for understanding the slow dynamics and rheology of simple colloidal particles which can be treated as soft or hard spheres that interact via a central pair potential, $V(r)$.

Ashesh Ghosh, Chemistry, University of Illinois, led the theoretical work

If $V(r)$ is known, then one can use a litany of statistical mechanical methods to analyze their collective structure, equilibrium dynamics under Brownian conditions, and nonlinear rheology. The approach Schweizer and co-workers have developed and widely applied in prior work [176] is used here and proceeds in a series manner as follows. (1) Construct a single particle model and $V(r)$. (2) Use liquid state integral equation methods to predict the intermolecular pair correlation function, $g(r)$, and its Fourier space collective structure factor, $S(k)$. (3) Use (1) and (2) to construct predictive dynamical theories of thermally activated equilibrium structural relaxation dynamics and mechanical properties, and (4) combine (1)-(3) to construct a theory for the effect of deformation on non-equilibrium dynamics and mechanics.

The daunting difficulty to quantitatively carryout such a program for microgels is that they are soft fluctuating polymeric particles with many internal degrees of freedom. Quantitative knowledge of their internal structure in dense suspensions, as a function of thermodynamic state variables (concentration, temperature), is scarce. This renders an *a priori* theoretical analysis at the monomer level very difficult or impossible. It has led to almost all theoretical and simulation studies adopting a coarse-grained center-of-mass (CM) level description of the polymer microgel which interacts via a pair decomposable isotropic soft repulsive potential where the influence of all internal degrees of freedom are effectively pre-averaged. This corresponds to $V(r)$ becoming a free energy or potential-of-mean force (PMF) quantity. But an *a priori* quantitative theoretical construction of such a PMF for real chemical systems is extremely difficult since it requires the following information. (i) How a global measure of mean size (radius, R) of a single microgel changes as a function of concentration and temperature, i.e. what is (c, T) ? (ii) What is the functional form of $V(r)$ and how does it change with thermodynamic state? (iii) Even for a simple $V(r)$ such as the Herztian contact model (see below), the single particle modulus is variable, depending on chemistry, preparation method, and crosslink density, and is *a priori* unknown. (iv) How does the experimental concentration variable (weight percent) map to an effective volume fraction as a function of concentration and temperature, i.e. $\phi_{eff}(c, T)$? The inability to *a priori* answer the above questions forces one to adopt models constrained by incomplete knowledge. Physical ideas must be invoked, and parameters introduced, with the goal of retaining some predictive power. Here we outline our approach, which is summarized in Fig. 5.6.

Soft microgels are generally globally compact and compressible objects that are swollen in a good solvent but have a (dense) core - (more dilute/hairy) corona structure [174, 177]. We take a microgel to be, on average, a spherical soft object. Its internal density $\rho(r)$ decreases continuously in a non-universal manner upon transitioning from its center to

edge, ultimately becoming effectively zero at $r = R_{eff}$. In the dilute low concentration regime the microgel size is fixed and one can define a volume fraction $\phi = \frac{4\pi}{3}\rho R^3$ which grows linearly with concentration. As suggested by experiments of Schurtenberger et. al. [156, 178], in an intermediate concentration regime of $c_1 < c < c_2$ (per the notation of Fig. 5.6) the microgels begin to de-swell due to steric repulsions between particles, in a manner that experiments suggest is initially weak. Crudely, experimental data in the latter regime can be modeled as a power law, $R \sim c^{-1/x}$ where $x > 3$, implying an effective volume fraction that scales as $\phi \sim c^{1-3/x}$. Motivated by the experimental data of Figure 5A of Conley et al. [178], we estimate $x = 6$. Beyond a "high enough" $c \geq c_2$, one expects the more fuzzy "corona" of the microgel is largely squeezed out, leaving a dense core which further decreases in size as concentration grows due to isotropic compression in the sense that $x = 3$, as again suggested previously [178]. This leads to $\phi \sim c^0$ where the linear growth of microgel particle number density (ρ) with concentration is perfectly compensated by their shrinking size. Ultimately, beyond an even higher concentration c_3, the internal concentration of microgels presumably saturates at a maximum value akin to a collapsed molten globule with radius $R_{collapsed}$.

Quantitative knowledge of such a complex, continuous, and material-specific variation of microgel size with concentration is unknown for our system. Thus, we adopt the model of Fig. 5.6 which has 3 crossover concentrations, one exponent parameter "x", and 3 characteristic sizes. The crossover concentrations are determined using our elastic modulus data and theory as explained in detail in section 5.4. Here we summarize the model adopted there.

We assume that the lowest concentration regime extends up to $c = 0.4$ wt% and the microgel size is constant and the same as in the $c \to 0$ dilute limit as determined from our DLS measurements, $2R = 2R_0 = 551$ nm. A second regime is defined starting at c_1 (0.4 wt%) and ending at $c_2 = 1.5$ wt% (onset of "soft jamming" behavior of G'). Here we assume the microgels begin to weakly contract and employ $x = 6$ as suggested in Conley et al. [178]. This implies at c_2 the microgel diameter is $2R = 442$ nm. Beyond c_2 a third regime is entered and we adopt the 3 exponent to describe microgel shrinkage. This implies at the highest concentration we study (9 wt%) one has $2R \approx 244$ nm. Interestingly, as Fig. S1 shows, this is roughly the size of dilute microgels at high temperature beyond the LCST where they undergo an enthalpy-driven collapse. Although a collapsed microgel driven by poor solvent conditions need not be exactly the same size as what can be attained via interparticle steric repulsion, it is not unreasonable they could be similar. Hence, in terms of the scenario of Fig. 5.6 we deduce as a rough approximation $c_3 \sim 9$ wt%, and our present measurements do not probe the ultra-high concentration fourth regime which may

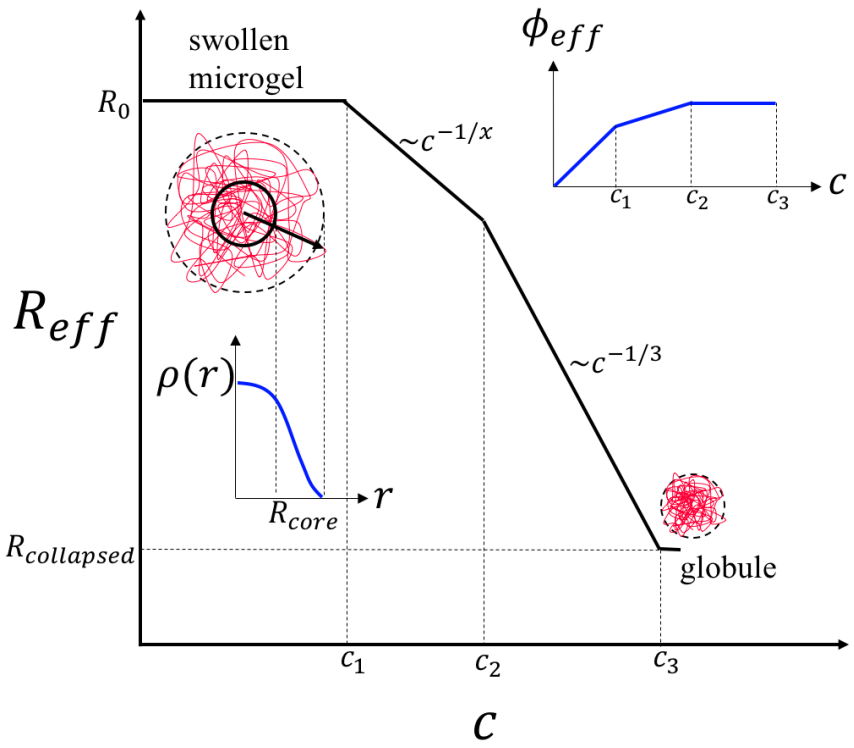

Figure 5.6: Schematic of our model for microgel radius as a function of concentration. In principle, there can be four regimes. At low concentration, the size is fixed at its $c \to 0$ dilute limit value as measured by DLS. Two intermediate regimes have different concentration dependences in the glassy and "soft jammed" regimes which we envision as physically indicating first compression of the corona and then stronger shrinkage of the core due to interparticle steric repulsions. The final, perhaps not observable, regime is when the core is maximally compressed and microgel size saturates.

be impossible to explore in practice.

We employ a suite of older and recently developed theoretical tools to model our system. The rest of this section provides a brief summary without derivation of these methods. All details can be found in original papers, and for consistency we employ the same notation developed in these prior theoretical works. Our present work is the first time the new activated dynamics (ECNLE) theory in equilibrium and under deformation has been employed to study soft colloids.

Finally, for clarity we again emphasize that our goal is to attempt to understand all concentration regimes (fluid, glassy suspension, so-called "soft jammed") for our lightly crosslinked polymeric microgel based on the assumption of thermal equilibrium in the Boltzmann sense. No athermal granular jamming or contact mechanical force network concepts are invoked. This does not contradict the fact that the interparticle soft repulsive interaction and the corresponding forces (modeled via the elastic Herztian model described

below) are very strong compared to the thermal energy scale. Our goal is to predict the equilibrium structure and relate it using statistical dynamical ideas to intermolecular stress storage, the dynamic plateau shear modulus, and relaxation.

5.4.2 Center-of-Mass Hertzian Repulsion Model

The vast majority of modeling studies of soft microgels has employed the repulsive Hertzian contact or harmonic interaction model. We adopt the former which is given by [172, 173],

$$\beta V(r) = \begin{cases} \frac{4E}{15}\left(1-\frac{r}{d}\right)^{5/2} & \text{if } r < d = 3R_{eff} \\ 0 & \text{if } r \geq d \end{cases} \tag{5.2}$$

where $\beta = (k_B T)^{-1}$ is the inverse thermal energy, r is the interparticle separation, and d is the particle diameter. The front factor $\frac{4E}{15}$ is the inverse dimensionless temperature that controls the elastic stiffness of a particle and hence repulsion strength. E is *a priori* unknown for our system, and $d \approx 2R$ where $R \approx R_g$ of the core-corona particle. From its mechanics derivation, E is related to the sphere diameter d, Young's modulus Y, and Poisson ratio ν, as:

$$E = \frac{Yd^2}{3k_B T(1-\nu^2)}. \tag{5.3}$$

Depending on the magnitude of the dimensionless temperature, the Hertzian potential can describe ultra-soft microgels ($E \leq 10^3$), intermediate soft microgels ($10^3 \leq E \leq 10^6$), and effective hard spheres ($E \geq 10^6$). The literal hard sphere limit is smoothly obtained as $E \to \infty$. Very recent simulations of soft microgel suspensions that explicitly considered the polymeric internal degrees of freedom found the Hertzian pair potential to work fairly well [179]. Again, no ionic interactions are taken into account in our modeling.

5.4.3 Equilibrium Packing Structure

We use the standard Ornstein-Zernike (OZ) integral equation [180, 181] approach to compute the inter-particle pair structure. The OZ equation relates the non-random part of the interparticle pair correlation function, $h(r) = g(r) - 1$ (where $g(r)$ is the pair correlation or radial distribution function), and the direct correlation function, $c(r)$ via [180, 181],

$$h(r) = c(r) + \rho \int c(|\vec{r} - \vec{r}'|)h(r')d\vec{r}' \tag{5.4}$$

where ρ is the particle number density. Collective density fluctuations are controlled by the static structure factor which in Fourier space is

$$S(k) = 1 + \rho h(k) = \frac{1}{1 - \rho C(k)}. \tag{5.5}$$

Numerical solution of the OZ equation requires a closure approximation that relates $c(r)$, $g(r)$, $V(r)$, and thermodynamic state (density, temperature). For soft colloids the hypernetted chain closure (HNC) relation works well and is given by,

$$c(r) = -\beta V(r) - \ln(g(r)) + h(r). \tag{5.6}$$

5.4.4 Dynamic Localization and Elasticity: Naive Mode Coupling Theory

The starting point for describing the dynamics of a tagged particle in a liquid is the Generalized Langevin Equation (GLE) for its position and velocity [180, 181],

$$m\frac{d}{dt}\vec{V}(t) + \zeta_s\vec{V}(t) = \frac{\beta}{3}\int_0^\infty d\tau \langle \vec{f}_\alpha(t).\vec{f}_\alpha(t-\tau)\rangle + \delta\vec{f}_\alpha(t) + \xi(t) \tag{5.7}$$

where ζ_s is a short time friction constant, $\vec{f}_\alpha(t)$ is the force on a tagged particle due to the surrounding particles, and $\delta\vec{f}_\alpha(t)$ and $\xi(t)$ represent the random white noise (Gaussian) force associated with the short time process. The naive ideal Mode-Coupling Theory (NMCT) of single particle dynamics calculates the force-force time correlation function or memory function by quantifying dynamical constraints at the pair structural level as [176]:

$$K(t) = \langle \vec{f}_\alpha(0).\vec{f}_\alpha(t)\rangle = \frac{-\beta^2}{3}\int_0^\infty \frac{d\vec{k}}{(2\pi)^3}\rho|\vec{M}_{NMCT}(k)|^2 S(k)\Gamma_s(k,t)\Gamma_c(k,t) \tag{5.8}$$

where $\vec{M}_{NMCT}(k) = kC(k)\hat{k}$ is the wave vector resolved effective force on a tagged particle, and the "dynamic propagators" $\Gamma_s(k,t)$, $\Gamma_c(k,t)$ are the $t = 0$ normalized single and collective dynamic structure factors (decay to zero in a fluid phase, non-zero for solids). At long times, localized states can exist and the Gaussian Debye-Waller factors are non-zero, $\Gamma_s(k, t \to \infty) = \exp(-\frac{k^2 r_L^2}{6})$, where r_L is the dynamic localization length associated with a kinetically arrested state. The collective propagator is accounted for in a de Gennes

narrowing manner as [176],

$$\Gamma_c(k, t \to \infty) \equiv \Gamma_s(\frac{k}{\sqrt{S(k)}}, \infty) = \exp(-\frac{k^2 r_L^2}{6}). \tag{5.9}$$

A self-consistent equation in the long time limit for the particle displacement can be derived and is given by: $\langle \vec{f}_\alpha(0).\vec{f}_\alpha(t \to \infty)\rangle \frac{r_L^2}{2} = \frac{3k_BT}{2}$. From this, the ideal NMCT self-consistent localization equation is [182]

$$\frac{1}{r_L^2} = \frac{\rho}{18\pi^2} \int_0^\infty C(k)^2 s(k) \exp(-\frac{k^2 r_L^2}{6}(1 + S^{-1}(k))). \tag{5.10}$$

One can also compute the elastic shear modulus associated with such an ideal glass state. The calculation is relevant in practice if the product of the frequency of the measurement and structural relaxation time obeys $\omega\tau_\alpha >> 1$. A standard statistical mechanical formula for the dynamic elastic shear modulus, based on projecting microscopic stress onto a bilinear product of the collective density fields followed by factorization of multi-point correlations to the 2-point level, is [180]:

$$G' = \frac{k_BT}{60\pi^2} \int_0^\infty dk[k^2 \frac{d}{dk} ln(S(k))]^2 \exp(-\frac{k^2 r_L^2}{3S(k)}) \approx a\phi \frac{k_BT}{dr_L^2} = a(\rho k_BT) \left(\frac{d}{a_L}\right)^2 \tag{5.11}$$

where "a" is a numerical prefactor. The final approximate "microrheology-like" relation can be analytically derived for hard spheres and works well for Hertzian spheres [161, 162]. Tighter dynamic localization (smaller r_L) leads to higher mechanical stiffness. We comment that one might interpret Eq. 5.11 as suggesting an apparent equivalence of the basic mathematical form of the "microrheology-like" relation to that of classic rubber elasticity, $G' \sim \rho_x k_BT$. But, there is no conceptual correspondence since ρ is the number of microgels per unit volume in Eq. 5.11 and not the crosslink number density as in rubber elasticity. Moreover, the localization length is an emergent dynamic quantity associated with kinetic trapping of particles due to interparticle forces and is a strong function of the thermodynamic state variables. Most fundamentally, the basis of Eq. 5.11 is the spatial correlation in a (transiently in practice) kinetically arrested state of collective interparticle microscopic stress defined by particle positions and interparticle forces, not the intra-strand entropic stress per rubber elasticity.

5.4.5 Quiescent Activated Structural Relaxation

To go beyond ideal MCT to treat thermally activated events that lead to slow structural relaxation, the nonlinear Langevin equation (NLE) theory has been developed. It is based on the scalar displacement of a tagged particle, $r(t)$, as the central dynamic variable. In the overdamped limit, the stochastic NLE for a particle trajectory is [176, 182]

$$\Gamma_s \frac{d}{dt} r = -\frac{\partial}{\partial r} F_{dyn}(r) + \xi(t) \tag{5.12}$$

where $\xi(t)$ is a Gaussian white noise and the key quantity is the dynamic free energy, F_{dyn}. The gradient of the latter determines the instantaneous force on a moving tagged particle due to its near neighbors and is given by [182]

$$\beta F_{dyn}(r) = \frac{3}{2} ln(\frac{3d^2}{2r^2}) - \frac{\rho}{2\pi^2} \int_0^\infty dk \frac{k^2 c(k)^2 S(k)}{1 + S^{-1}(k)} \exp(-\frac{k^2 r_L^2}{6}(1 + S^{-1}(k))) \tag{5.13}$$

The first contribution is an ideal entropy like term that favors the delocalized fluid state, and the second interaction free energy like term favors dynamic localization. The dynamic free energy is constructed to recover NMCT per $\frac{\partial}{\partial r} F_{dyn}(r)|_{r=r_L} = 0$. At and above a critical volume fraction $\phi > \phi_c$ (≈ 0.43 for hard spheres [182]) a barrier in $F_{dyn}(r)$ emerges at $r = r_B$ of height F_B with a corresponding transient localization length r_L; see Fig. 5.7 for an example. The liquid structural relaxation time is estimated from the Kramers' mean barrier hopping time as [182]

$$\frac{\tau_\alpha}{\tau_s} = 1 + \frac{2}{d^2} \int_{r_L}^{r_B} \exp(\beta F_{dyn}(x)) \int_0^x dy \exp(-\beta F_{dyn}(y)) \approx 1 + \frac{2\pi}{K_0 K_B} \exp(\beta F_B) \tag{5.14}$$

where τ_s is a short time process relaxation time and K_0 and K_B are positive local curvatures of free energy at r_L and r_B, respectively. The approximate relation in Eq. 5.13 holds when $\beta F_B \gtrsim 1 - 2$. The short time scale is [183]:

$$\tau_s = g(d) \frac{d^2}{D_{DE}} [1 + \frac{1}{36\pi\phi} \int_0^\infty dQ \frac{Q^2 (S(Q) - 1)^2}{S(Q) + b(Q)}] \tag{5.15}$$

where D_{SE} is the Stokes-Einstein (SE) diffusivity in dilute solution. One can define a short time friction constant $\zeta_s = \zeta_0 [1 + \frac{d^3}{36\pi\phi} \int_0^\infty dQ \frac{Q^2 (S(Q)-1)^2}{S(Q)+b(Q)}]$ where for a colloidal suspension $\zeta_0 = \zeta_{SE} g(d)$. In the above equation $\tau_0 \equiv \frac{d^2}{D_0}$, $D_0 = \frac{k_B T}{\zeta_0}$, $Q = kd$, and $b^{-1}(k) = 1 - j_0(k) + 2j_2(k)$ where $j_n(x)$ is the spherical Bessel function of order n.

The above NLE based theory only captures the consequences of the local cage on tagged particle hopping. Most recently, the "Elastically Collective NLE" theory (ECNLE) has

been developed, widely applied, and quantitatively validated for dense suspensions of hard sphere colloids, cold molecular liquids, and polymer melts [184, 183]. It includes a longer range cooperative motion aspect of structural relaxation based on the idea that the fluid surrounding a particle cage must elastically dilate by a small amount (via a spontaneous thermal fluctuation) to accommodate large amplitude hopping. This elastic energy contributes an extra barrier to the activated hopping process given by: $\beta F_{el} = 2\pi K_0 \int_{r_{cage}}^{\infty} dr r^2 \rho g(r) u(r)^2$, where K_0 is the harmonic spring constant of the dynamic free energy which sets the energy scale of the elastic barrier, $u(r)$ is the elastic displacement field at a scalar distance r from the cage center $u(r) = \Delta r_{eff}(r_c/r)^2$, $r > r_c \sim 1.5d$, and the amplitude $\Delta r_{eff} \leq r_L$ the explicit formula for which is given elsewhere [184, 183]. Physically, the local and elastic barrier are additive, so the hopping time is modified as a multiplicative factor $\exp(\beta F_{el})$ in the Kramers time as $\beta F_{Total} = \beta F_B + \beta F_{el}$ [184].

The conceptual ideas of ECNLE theory, key length and energy scales, and a representative dynamic free energy are shown in Fig. 5.7 for the Hertzian model. The location of the maximum cage restoring force (r^*) obeys $\frac{\partial^2}{\partial r^2} F_{dyn}(r) = 0$, and the barrier location (r_B), jump distance ($\Delta r = r_B - r_{loc}$), and local barrier (βF_B) are also indicated.

5.4.6 Rheology

The NLE and ECNLE theories can be extended to treat non-equilibrium materials under deformation. Extensive applications to hard sphere colloids, polymer-colloid depletion systems, polymer glasses, molecular colloids, and nanoparticle gels have been made [161, 162, 185, 186]. The approach assumes the dominant effect is the direct consequence of applying stress to the material, which leads to an effective force on each particle in a micro-rheological spirit. Technically, a stress ensemble (creep) is adopted to formulate the basic ideas. It is asserted that a macroscopic stress manifests itself locally as a scalar applied force on any tagged particle given by [185]

$$f = ad^2\sigma \tag{5.16}$$

where $a = \pi 6\phi^{\{} - 2/3\}$. Stress then modifies the dynamic free energy as [185]

$$\beta F_{dyn}(r, \sigma) = \beta F_{dyn}(r, \sigma = 0) - \beta \frac{\pi}{6} \phi^{-2/3} d^2 \sigma r. \tag{5.17}$$

External forces are assumed to not modify structural correlations on the local length scales dynamically relevant in the theory, nor the short time relaxation process in τ_s. Increasing the applied stress weakens the localizing constraints of the dynamic free energy,

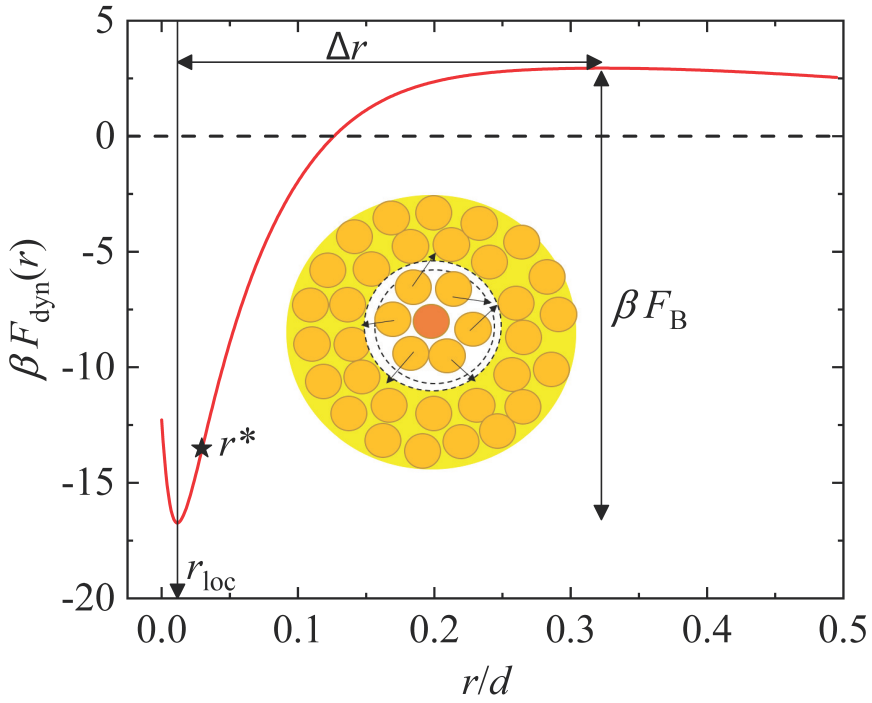

Figure 5.7: A representative plot of the dynamic free energy in thermal energy units as a function of dimensionless single particle displacement from its initial position for a dense suspension. Here $\phi = 0.70$ and $E = 30000$, with all important length scales and the cage local barrier height indicated. The local minimum of the dynamic free energy, r_{loc}, defines the transient localization length, $r = r^*$ is the particle displacement where the cage restoring force is a maximum, and the particle hop or jump distance is Δr. The schematic indicates a tagged particle at the center of a cage composed of its nearest neighbors, all of which undergo large amplitude hops. To allow the latter, particles outside the cage region undergo a long-range collective elastic radial dilational displacement of small amplitude which results in an elastic contribution to the total dynamic activation barrier.

and hence reduces the barrier and can mechanically drive a glass-to-liquid transition. At a critical value of stress, called the "absolute yield stress", σ_{abs}, the barrier is completely destroyed, indicating an athermal type of solid-to-liquid transition. With increasing force or stress below its absolute yield value, the localization length grows and the elastic shear modulus decreases continuously. A simple nonlinear elastic mechanical equation-of-state (relevant in practice at times short compared to stress relaxation times) previously adopted implicitly defines strain as [161, 162, 185]:

$$\sigma = G'(\sigma)\gamma \tag{5.18}$$

This equation can be used to define an "absolute yield strain"

$$\gamma_{y,abs} = \frac{\sigma_{y,abs}}{G'(\sigma_y, abs)} \tag{5.19}$$

Other types of yield strains such as a "dynamic yield strain" can also be defined as the strain at which G'' has a maximum within the framework of a one structural relaxation time model which is a function of applied deformation. The nonlinear loss modulus is modeled as [184, 186]:

$$G'' = G\frac{(\omega\tau_\alpha(\gamma))^2}{1+(\omega\tau_\alpha(\gamma))^2}. \tag{5.20}$$

"Mixed" yield strains can also be defined as [161, 162, 185]:

$$\gamma_{y,mix} = \frac{\sigma_{y,abs}}{G'(0)}. \tag{5.21}$$

The stress dependent relaxation time follows from the same Kramers' hopping time expression but where all dynamic free energy quantities are now stress-dependent,

$$\frac{\tau_\alpha(\sigma)}{\tau_s} = 1 + \frac{2\pi}{\sqrt{K_0(\sigma)K_B(\sigma)}}\exp(\beta(F_B(\sigma)+F_{el}(\sigma))). \tag{5.22}$$

A predictive theory for the full stress-strain response, time-dependent creep, steady shear flow curve, etc. can be constructed [187] but this is beyond the scope of the present work.

5.5 Model Calibration, Glassy Shear Modulus, and Collective Structure Predictions

In this section, we employ the microgel model of section 5.4.1 to determine the effective volume fraction for our microgel suspensions. We then use this knowledge to perform theoretical calculations of the linear elastic shear modulus and compare to experiment.

5.5.1 Effective Microgel Radius and Volume Fraction in Dense Suspensions

The effective volume fraction ($\phi_{eff} = \frac{\pi}{6}\rho d^3$) depends on concentration via the microgel diameter, $d(c)$. As discussed in section 5.4 and Fig. 5.6, experiments suggest there are two regimes where the microgel radius first decreases weakly ($R_g \sim c^{-1/6}$) starting at 0.4 wt% whence $\phi \sim c^{1/2}$, which then changes beginning at 1.5 wt% to a stronger shrinkage

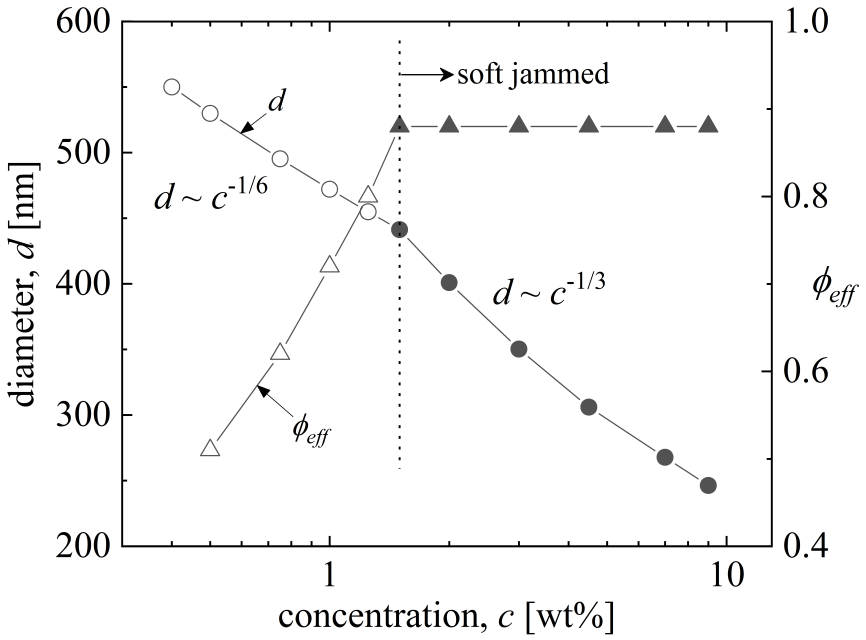

Figure 5.8: Quantitative model employed for the microgel diameter (circles) and effective volume fraction (triangles) as a function of concentration (i.e., quantitative realization of the schematic of Fig. 5.6). Open symbols indicate the glassy regime while solid symbols indicate the "soft jamming" regime. Here $d = 550$ nm in dilute solution and we assume microgel compression starts at 0.4 wt%.

$R_g \sim c^{-1/3}$ and hence $\phi_{eff} \neq f(c)$. The chosen crossover concentration is motivated by our physical hypothesis that the sharp change of the elastic modulus data in Fig. 5.2 is an indication of a change of the scaling of microgel size with concentration. Fig. 5.8 presents the quantitative model employed for microgel size and effective volume fraction as a function of concentration. The latter ranges from ~ 0.5 to 0.88. As an independent estimate of the effective volume fraction for our 0.5 wt% sample, we have applied our approach to data from literature [140] for a similar microgel system and find it gives $\phi = 0.45 \sim 0.55$ for $c = 0.5$ wt%, consistent with Fig. 5.8.

The one remaining unknown in our model is the dimensionless strength of the Hertzian repulsion, the parameter E in Eq. 5.2. For simplicity, and to avoid introducing an adjustable function, we assume this is a material constant invariant to concentration. This simplification seems consistent with the very recent simulation study [179] that included the internal polymeric degrees of freedom of a microgel. We can then apply the theory ideas of section 5.4 to calculate the dynamic elastic shear modulus. We ask the question whether it is possible to theoretically predict the entire set of linear elastic modulus data in both the glassy and soft jamming regimes of Fig. 5.2 based on a single constant value of varying E. There is no guarantee the answer is yes.

5.5.2 Linear Elastic Modulus: Theory versus Experiment

The inset of Fig. 5.9 shows model calculations of the dimensionless linear shear modulus, $G'/(k_BT/d^3)$, over a wide range of E values. Recall that the data of Fig. 5.2 in the glassy regime covers almost ~ 3 decades of modulus variation. Given the theoretical model calculations and experimental data, this places a constraint on possible values of E. Values of E lower than those shown in the inset of Fig. 5.9 cannot possibly account for our observations. Based on these considerations, and visual comparison of the theory and experimental results for the elastic modulus, we choose $E = 30,000$ to explore the ability of the theory to account for the entire G' data set. This E value corresponds to a single particle Young's modulus of $Y \approx 1.5$ kPa ($\nu = 0.5$), which seems a reasonable value for our lightly self-crosslinked and slightly charged microgels.

Before quantitatively confronting theory with experiment, we note that the NMCT-based theory of the elastic shear modulus that employs the approximation of Eq. 5.11 is, of course, not exact. It has been successfully employed to understand how particle and thermodynamic state variables determine dependencies and trends of the elastic modulus in diverse colloidal glass and gel forming suspensions [161, 162, 185, 188, 189, 185, 190, 191, 192] and molecular and polymeric liquids [36,42]. However, concerning the absolute magnitude of the dynamic modulus, multiple previous studies and comparisons with diverse experimental systems (colloids, molecules, polymers) have consistently shown that NMCT quantitatively overestimates particle localization and hence G', which is at least partially likely a consequence of its formulation at the single particle dynamics level [161, 162, 185, 188, 189, 185, 190, 191, 192, 184]. Specifically, Eq. 5.10 has been found to generically overpredict G' by roughly one order of magnitude. Thus, we introduce a numerical 'fudge-factor' to empirically rescale the theoretical result for all microgel concentrations, $G' = 0.1G_{NMCT}$.

To compare theory with experiment, we use the model of Fig. 5.8 for the effective microgel diameter and volume fraction and $(k_BT)/(10\,\text{nm})^3 = 4.2$ Pa at room T. The results are shown in absolute units in the main frame of Fig. 5.9, and the corresponding dimensionless unit comparison in its inset. We first discuss the glassy regime. One sees from the main frame that, rather remarkably and non-trivially, all the experimental data points essentially fall onto the theoretical curve based on using $E = 30,000$. Considering the high uncertainties of the data for the lowest microgel concentration $c = 0.4$ wt%, we have chosen to ignore this data point for the purpose of assessing the quality of the theoretical analysis. The last data point in the glassy regime ($c = 1.5$ wt%) corresponds to $\phi = 0.88$. As discussed in the next section, this is very close to where structural "soft jamming" is predicted based on our calculations of the equilibrium structure of the suspension where the

volume fraction at which the cage peak of $g(r)$ is a maximum is the metric [193] adopted to operationally define the soft jamming crossover.

The sensitivity of our elastic modulus predictions to the value of E is illustrated in Fig. 5.9. The blue solid curve is for $E = 30,000$, while the gray band covers results over the range of $E = 20,000$ to $40,000$. Red and black points show experimental data below and beyond the onset of "soft jamming". The blue theory curve follows well a power law concentration dependence of $G'(c) \sim c^{5.65}$ in the glassy regime, very similar to experiment. Our calculations agree well with the data in the glassy regime for this relatively narrow range of E, but not outside of it.

At concentrations beyond $c = 1.5$ wt%, the effective volume fraction is fixed per the isotropic microgel compression idea discussed in section 5.4.1. Thus, this idea alone, in conjunction with Eq. 5.11, immediately predicts a crossover of G' to a linear growth with concentration since the dynamic shear modulus scales as $G' \sim k_BT/d^3 \sim c$ and the ratio r_L/d is a constant if the effective volume fraction is constant. The blue line in Fig. 5.9 beyond the soft jamming onset is the predicted linear $G'(c) \sim c$ dependence, and agrees rather well with the data. We emphasize that our theoretical analysis in the very high concentration regime is not in the spirit of granular jamming and a literal force contact network, nor the idea that the suspension acts as a homogeneous rubber network, scenarios (1) and (2) discussed in section 5.3. Effectively we retain a discrete particle picture with stresses of interparticle Brownian origin due to caging. The "soft jamming crossover" in Fig. 5.2 is thus interpreted as a consequence of the particle size decreasing as the $1/3$ root of concentration, which implies a constant effective volume fraction, but a shear stress scale of k_BT/R^3 that grows linearly with concentration.

Finally we briefly note that the trends of our experimental shear modulus data in Fig. 5.2 and our corresponding theoretical calculations are both in qualitative accord with the micromechanical model simulations in literature [194]. Quantitative comparison is not appropriate given the sensitivity to system details as illustrated in the inset of Fig. 5.2, use of a measure of volume fraction in the theory work not identical to that of the simulations, and most importantly that the simulations employ the essentially infinite frequency or equilibrium formula for the shear elastic modulus of Zwanzig and Mountain [195]. The latter is in conceptual contrast to our statistical dynamical theory which analyzes a dynamically relaxed plateau shear modulus at finite frequency which is the emergent consequence of particle localization.

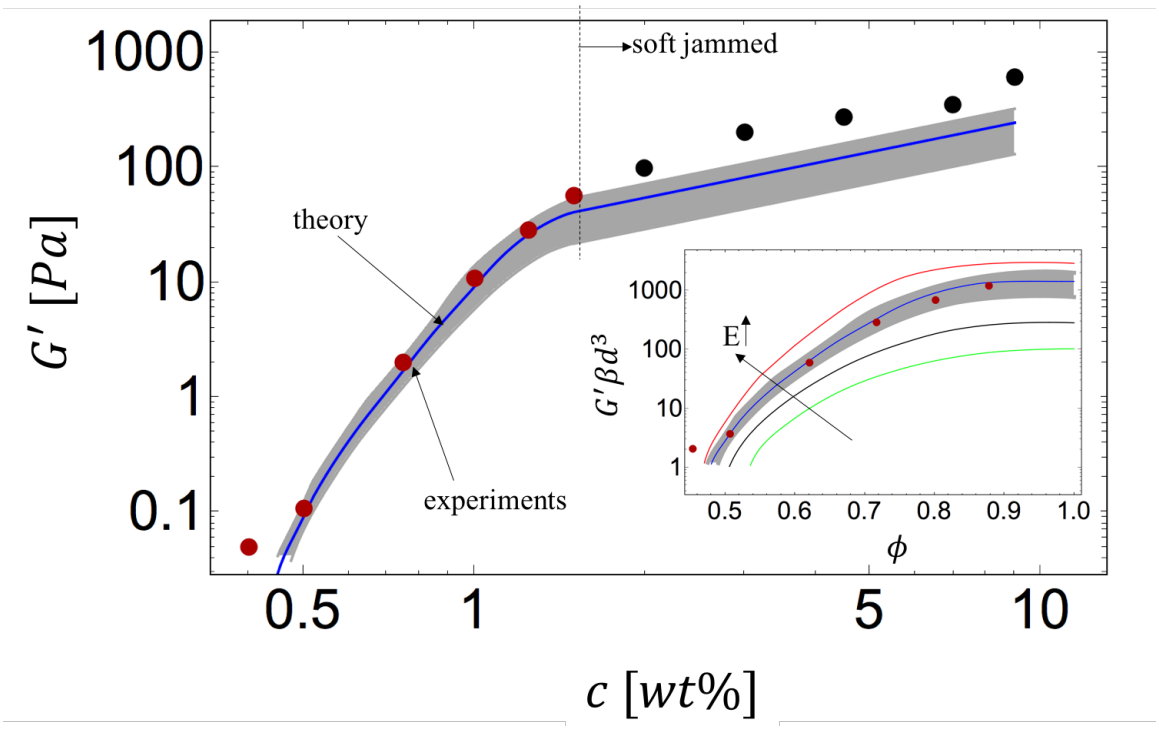

Figure 5.9: Linear elastic shear modulus in Pascals as a function of concentration. Points indicate experimental data and curves are theoretical calculations using $E = 30,000$. Beyond $c = 1.5$ wt%, volume fraction is constant and $G' \sim c$, which agrees well with the experimental results. (Inset) Dimensionless modulus versus volume fraction ϕ for $E = 5000, 10000, 30000$ and 10^5 (bottom to top). At high ϕ beyond soft jamming, the theoretical G' results tend to saturate or very weakly decrease, trends that are consistent with previous findings for soft microgel potentials [161, 162]. After the last experimental data point in inset, the volume fraction of the system is essentially constant as described in Fig. 5.8. The gray bands in the main frame and inset indicate the range of variation of the predicted elastic modulus as the repulsion strength in the Hertzian potential varies over the range of $E = 20000$ to 40000.

5.5.3 Predicted Intermolecular and Collective Equilibrium Structure

Given the apparent success of our single microgel model for predicting the dynamic shear modulus of our system, we now use it to explore its consequences for measurable aspects of equilibrium structure. Fig. 5.10 shows predictions for the real and Fourier space pair structure using the "best fit" value of $E = 30,000$ over a wide range of volume fractions. Fig. 5.11 quantifies various metrics of the structural correlations in wave-vector and real space. Fig. 5.10 and Fig. 5.11 show that as the effective volume fraction grows, the "contact value" (local maximum) of $g(r)$ (crucial for transmitting repulsive forces between microgels) first grows but then goes through a maximum at a volume fraction of ≈ 0.85 and decreases beyond that; there is also a splitting of the second peak. This behavior was previ-

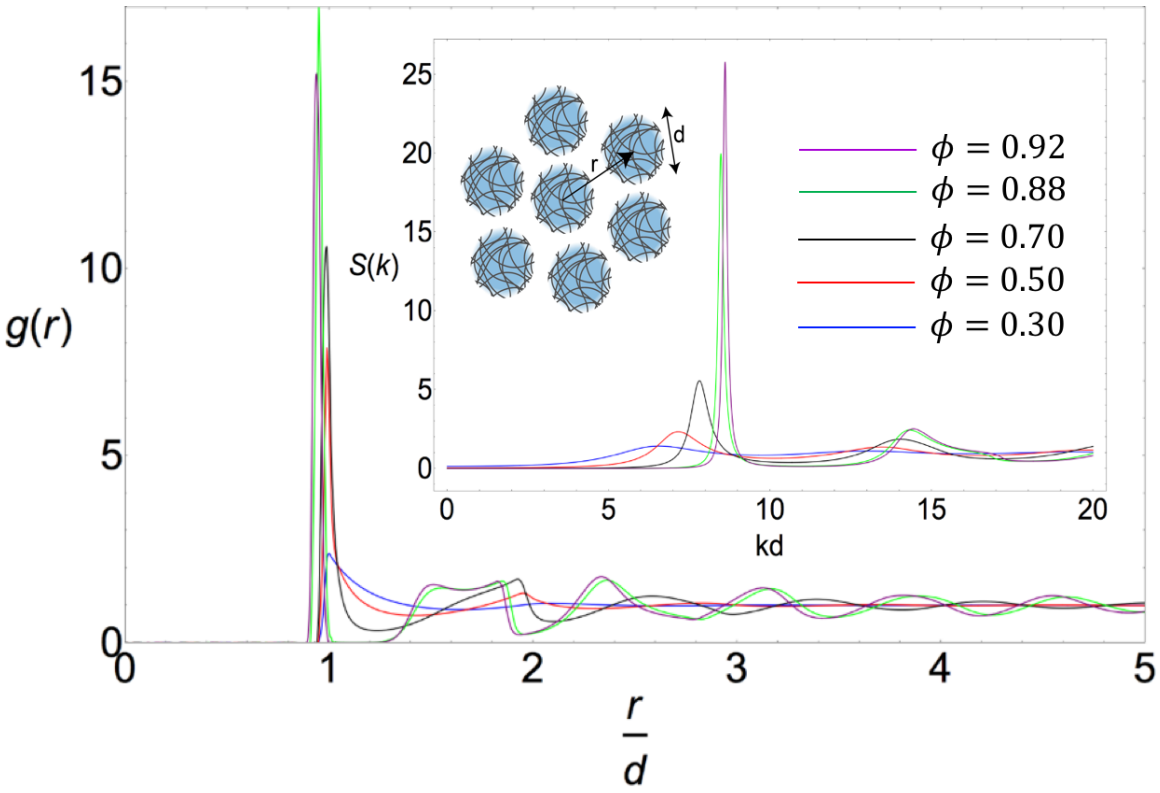

Figure 5.10: Equilibrium pair correlation function as a function of reduced interparticle separation for a fixed repulsion strength of $E = 30,000$ over a wide range of indicated volume fractions. (Inset) Static collective structure factor, $S(k)$, for the same value of E and volume fractions. The cartoon shows soft microgels in a transiently kinetically arrested state which are modeled here as Hertzian elastic spheres.

ously found theoretically [161, 162], and in the simulations and experiments of Liu, Yodh and coworkers [193]. The maximum of the contact value was taken to be an empirical measure of the "soft jamming crossover" by the latter workers. The emergence of a split second peak occurs at essentially the same value of volume fraction $\phi_J \approx 0.85$ as where the first peak is a maximum, which is far beyond $\phi_{rcp} = 0.64$ of jammed hard sphere suspensions. We note in passing that our calculations based on OZ-HNC integral equation theory are in qualitative accord with the simulations in the literature [194, 196], as also previously discussed by Yang and Schweizer [161, 162]. On the other hand, $S(k)$ shows a monotonic growth of cage coherence defined as the amplitude of the first peak of the static structure factor, $S(k^*)$, with increasing volume fraction. The inset of Fig. 5.10 presents calculations of the zero wave-vector value of $S(k)$, $S_0 = \rho k_B T \kappa_T$, which is a dimensionless measure of the osmotic compressibility of the suspension. It decreases strongly and monotonically with increasing volume fraction. Integration over concentration of the inverse of this quantity provides the osmotic pressure [197]. In principle the results of Fig. 5.9 and 5.10 can be

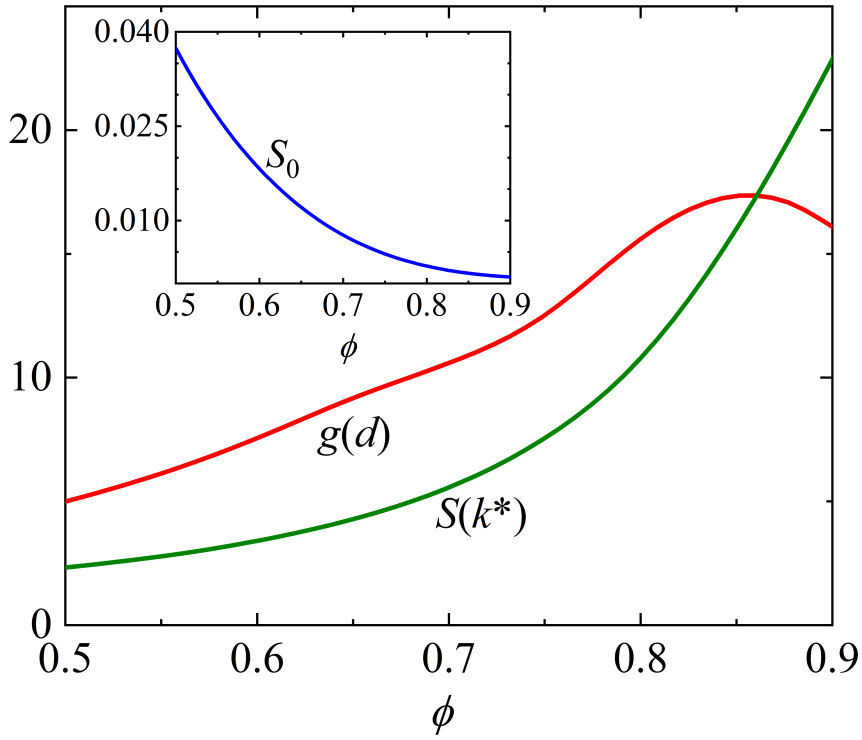

Figure 5.11: Characteristic structural features as a function of volume fraction ϕ for Hertzian spheres at a fixed repulsion strength of $E = 30,000$. Amplitude of the first peak of $g(r)$, denoted as $g(d)$, is a measure of the degree of real space short range order between nearest neighbors in the liquid. Amplitude of the first peak of the collective static structure factor as defined in section VC, $S(k^*)$, which quantifies the collective coherence of cage packing associated with the nearest neighbors. (Inset) Zero wave-vector value of the collective static structure factor, $S_0 \equiv S(k = 0) = \rho k_B T \kappa_T$, which is a dimensionless osmotic compressibility.

tested via new experiments on our microgel samples such as confocal imaging, scattering, and thermodynamic measurements. We now use the obtained structural knowledge to make further dynamical and rheological predictions in the next section.

5.6 Dynamics and Rheology Predictions and Comparison to Experiment

To convert our dimensionless theoretical time scales into absolute time scales relevant to our system, we estimate the short relaxation time of Eq. 5.15 and find $\tau_s \geq 200$ s since the peak value of $g(r)$ obeys $g(d) \geq 4$, and the factor in square brackets in Eq. 5.14 is ~ 100 at the high effective volume fractions of interest. This estimate also employed the

experimental particle radius, the SE diffusivity $D_{SE} = (k_B T)/(6\pi\eta R)$, a water viscosity of 10^{-3} N.s/m^2, and $T = 10$°C. We note $\tau = d^2/D_{SE} = 0.4$ s for a $d = 550$ nm diameter particle.

5.6.1 Quiescent Relaxation

To test if our theoretical approach is consistent with the nearly flat frequency dependence of the shear modulus observed experimentally (Fig. 5.1), we consider a simple Maxwell model defined as

$$G'(\omega) = G' \frac{(\omega\tau_\alpha)^2}{1 + (\omega\tau_\alpha)^2} \tag{5.23}$$

where G' is given by Eq. 5.11. A flat frequency dependence requires $\omega\tau_\alpha \geq 1$. In the experiments the lowest frequency probed is $\sim 10^{-2}$ rad.s^{-1}. Using this and our calculation of the short time scale $\tau_s \geq 200$ s, we find $\omega\tau_s \geq 2$. Indeed, the actual structural relaxation time, estimated here as the Kramers time, is much larger than τ_s. Since we interpret in a Maxwell model spirit the structural and longest stress relaxation times to be essentially the same to leading order, the inequality $\omega\tau_\alpha >> 1$ applies and thus the dynamic theory is consistent with the observation of no terminal flow on the experimental time scale under quiescent conditions.

As discussed in section IVE, the dynamic free energy has several key length scales per Fig. 5.7 shows examples using $E = 30,000$. All length scales are $1-2$ decades smaller than the particle size. The transient localization length (r_{loc}) and location of maximum force (r^*) monotonically decrease (initially strongly) with volume fraction, and then tend to saturate as the soft jamming point is approached. The jump distance grows monotonically. Our predictions of localization length can potentially be tested using confocal microscopy or simulations. Calculations of the local cage, collective elastic, and total barriers discussed in section section 5.4 are shown in Fig. 5.14a. All grow monotonically and strongly with volume fraction over the range shown. The collective elastic barrier increases more strongly with concentration, as also true for hard spheres and other glass forming liquids [184]. The elastic and local barriers cross at a much higher volume fraction than for hard spheres, and the crossing point decreases as E grows (not shown).

5.6.2 Nonlinear Response

With increasing deformation or stress, both dynamical barriers decrease and the structural relaxation time strongly decreases. Figure 5.13 B shows this is an extremely dramatic effect

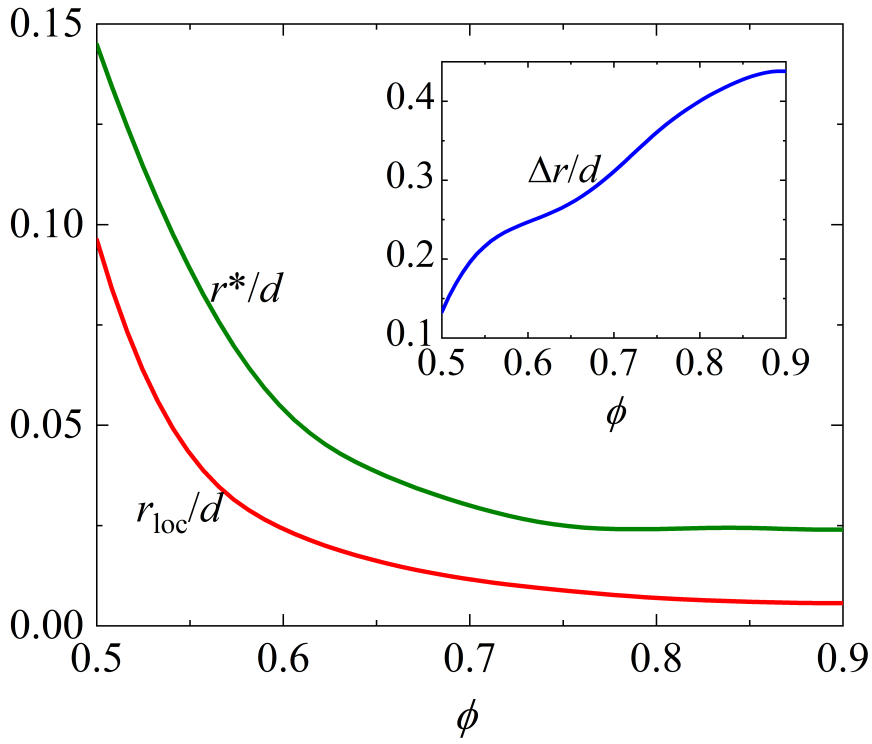

Figure 5.12: Characteristic length scales of the dynamic free energy (c.f. Fig.5.7) as a function of volume fraction for fixed $E = 30,000$. Dimensionless dynamic localization length, r_{loc}/d (red), and location of maximum cage restoring force, r^*/d (green). (Inset) Particle jump distance, $= r_B - r_{loc}$.

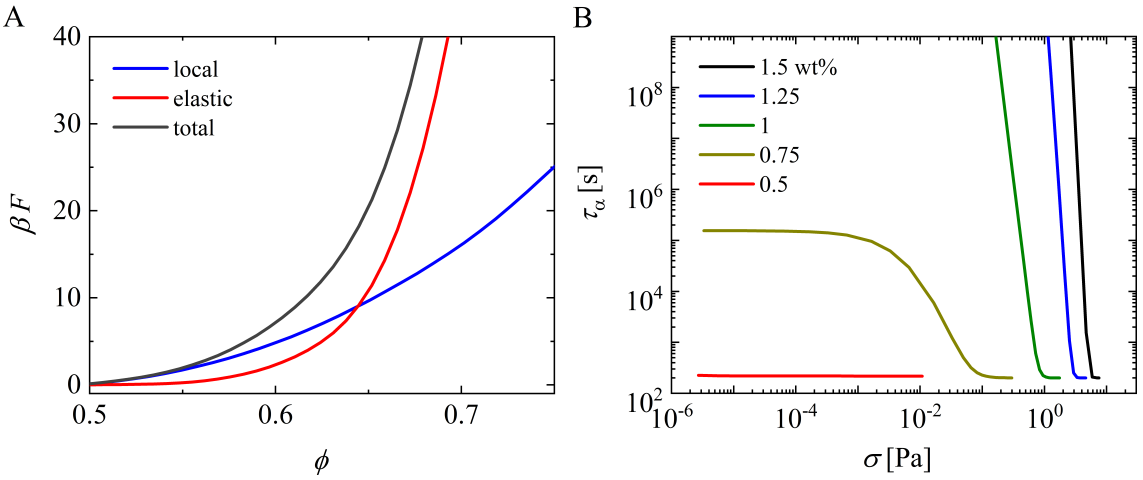

Figure 5.13: (A) Dimensionless dynamic free energy barriers (c.f. Fig. 5.7) for E = 30,000. The local, elastic, and total dynamic barriers discussed and defined in section 5.4 are shown as a function of volume fraction. (B) Alpha relaxation time (in seconds) for five microgel concentrations in wt% as a function of stress in Pascals.

for five different concentrations below the soft jamming threshold. The last point in each plot corresponds to when the localized form of the dynamic free energy is first destroyed (and hence the total barrier vanishes), which signals the absolute yield stress.

Figure 5.13 B can also be used to operationally define a dynamic yield stress in the spirit of a mechanically-driven glass to liquid transition. Typically, the kinetic criterion used is set by the maximum experimental observation time. For example, the dynamic yield stress could correspond to the stress value when $\tau_\alpha = 10^x$ s where $x \sim 2 - 4$. But here we choose to do a simpler analysis by defining [161, 198, 185] a dynamic yield stress as $\sigma_{y,dyn} = \gamma_{y,dyn}\, G'(\gamma_{y,dyn})$ in analogy with Eq. 5.18, where $\gamma_{y,dyn}$ is the dynamic yield strain defined at the maximum of the strain dependent loss modulus, $G''(\gamma)$ of Eq. 5.20. Another way of defining yield strain is where the strain dependent storage and loss moduli cross, $G''(\gamma) = G'(\gamma)$. Within the simple nonlinear Maxwell model framework of Eq. 5.20, these two definitions are the same. Experimentally, these two criteria may be different. We take the peak in G'' as the dynamic yield strain and the crossover as the absolute yield strain for comparison to theory. Figure 5.14 presents our theoretical results for the dynamic and absolute yield stresses and strains, and compares them in a no adjustable parameter manner to experiment.

Figure 5.14 shows rather good agreement between different theoretical measures of the yield stress (smooth curves) and experimental data analyzed in 3 different ways (data points) in both the glassy and soft jamming regimes (except for the lowest concentration sample for which the data is most uncertain). The inset compares yield strains from theory and experiment. Overall, the agreement is good in the glassy regime where the system has yield strains of modest magnitude, $\sim 10 - 20\ \%$. Agreement between theory and experiment is not very good beyond the putative "soft jamming" crossover. While theory predicts $\gamma_y \sim c^0$, experiment suggests a strong yield strain dependence on concentration at very high concentrations, leading to a large yield strain value of $\sim 72\%$ for the 9 wt% sample. This is much larger than the theoretical predictions and may reflect the arbitrariness of defining yield strains from real experimental data. Using a different definition, the mixed yield strain (defined in Eq. 5.21) evaluated using our experimental data as the ratio of the HB yield stress to plateau modulus ($\gamma_y^{mix} = \sigma_y^{HB}/G_0$), results in a nearly constant yield strain $\gamma_y^{mix} \sim c^0$ in the highest concentration regime.

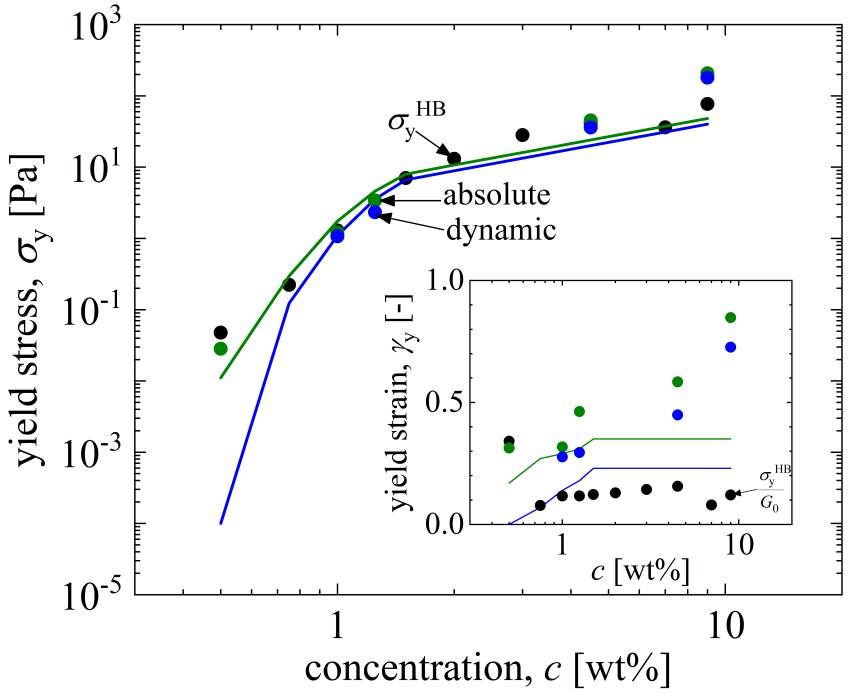

Figure 5.14: Comparison of the yield stress and yield strain from experiment (symbols) and theory with no additional fit parameters (solid curves). Experimental Hershel-Buckley (black), dynamic (blue), and absolute (green) yield stresses as defined in Sec.VI B (from data in Fig. 5.3, Fig 5.4 and Fig. S4). (Inset) Experimental yield strain values (points) and the predicted theoretical dynamic and absolute yield strains as defined in Sec.VI B. These theoretical results are based on the parameters deduced by aligning theory and experiment for the linear shear modulus and involve no horizontal or vertical shifts.

5.7 Summary and Conclusions

We have presented an integrated experimental and quantitative theoretical study of the linear and nonlinear rheology of self-crosslinked, slightly charged pNIPAM microgel suspensions at low temperatures where they repel. An exceptionally wide range of concentrations were studied that span the fluid, glassy and so-called "soft jammed" regimes. In the intermediate glassy regime, we measured over 3 orders of magnitude an apparent power law dependence of the elastic shear modulus on concentration, $G' \sim c^{5.64}$. This variation appears distinct compared to prior studies of crosslinked ionic microgel suspensions. At high enough concentrations, there is a rather sharp crossover to a nearly linear growth of the dynamic shear modulus. To theoretically understand these quiescent observations within a single framework we constructed a minimalist model of single microgel size as a function of concentration that includes steric de-swelling effects (neglecting any ion-induced deswelling) which differ in the so-called glassy and highest concentration or soft jammed

regimes. Using a Hertzian repulsion interparticle potential and a suite of statistical mechanical theories, we made quantitative predictions for the microgel collective structure, dynamic localization length, and elastic shear modulus. Based on a constant Hertz repulsion strength parameter (E), determined by requiring the theory to reproduce the measured elastic modulus over the entire concentration regime studied, we demonstrated good agreement between theory and experiment for $E \approx 30,000$. The various parameters used in theory are summarized in Appendix table C.1. Experimentally testable predictions were made for the structure of the suspensions.

We also measured several nonlinear rheological properties with a focus on the yield stress and strain. Again significant differences of our data compared to published studies using crosslinked ionic microgels were found [154, 157, 158, 159, 160]. A theoretical analysis was also performed (now with no adjustable parameters) to predict the structural relaxation time in equilibrium, how it changes under deformation, and the yield stress and strain as a function of microgel concentration. Reasonable agreement with our observations was obtained. To the best of our knowledge, this is the first theoretical attempt to quantitatively understand structure, quiescent relaxation and shear elasticity, and yielding of dense microgel suspensions using microscopic force based methods that include activated hopping processes.

We expect the ideas and approach presented here will be useful for other realizations of microgel suspensions based on different chemistries and also other types of soft polymeric particles in the core-shell family. A key input to the modeling is knowledge of the interparticle pair potential and the microgel size and effective volume fraction as a function of concentration. Given these, the statistical mechanical theories discussed in this article can be employed to predict packing structure in real and Fourier space, the shear elastic modulus, structural relaxation time, and nonlinear rheological properties. Our integrated experimental-theoretical approach will be applied in a future article to study how heating induced changes of microgel size and stickiness impact linear and nonlinear viscoelasticity.

Acknowledgement

This work was performed at the University of Illinois and supported by DOE-BES under Grant No. DE-FG02-07ER46471 administered through the Materials Research Laboratory. RHE thanks Anton Paar for providing the rheometer MCR702 which was used for some of the rheology experiments.

CHAPTER 6

LINEAR AND NONLINEAR VISCOELASTICITY OF DENSE ATTRACTIVE MICROGEL SUSPENSIONS

6.1 Introduction

Colloidal suspensions show diverse dynamical behavior with externally controllable parameters such as volume fractions, interparticle interaction potential and external applied stress. A wide range colloidal systems have been explored in the literature and phase diagrams have been proposed for the jamming transition in such systems. While for purely repulsive interparticle pair potentials between the particles, crowding of colloidal particles leads to the formation of colloidal glasses which do not relax on the observational timescales in the absence on an external stress, a fundamentally different state is realized when the particles interact via attractive interparticle pair potential. For attractive colloidal suspensions, the particles can form aggregations, and provide solid-like characteristics if a volume spanning network is formed. Efforts have been made in the past to develop a theoretical understanding for such systems. Additional complications in the understanding of such systems are introduced while dealing with the suspensions made from soft, deformable particles. Suspensions formed with soft microgels are one such systems. Microgel particles are formed from crosslinked polymer chains which can imbibe solvent. Such particles can change their volume (hence the effective volume fraction of suspension) depending on several factors such as polymer-solvent interactions and osmotic pressure. Additionally, the fluctuating internal polymeric structures in the microgels, their chemistry, and internal density profile result in additional complexity in developing a theoretical understanding of suspensions formed with microgels particles.

Microgels synthesized from Poly(N-isopropylacrylamide) (pNIPAM) have widely employed to study the dynamics of soft particle suspensions. The temperature-sensitivity of such particles allows for the *in situ* control of the particle size and interparticle-pair po-

Ashesh Ghosh made equal contribution towards this chapter. Gaurav Chaudhary led the experimental work (Fig. 6.1-6.5) and Ashesh Ghosh led the theoretical work (Fig. 6.5-6.10).

tential which affects structural and dynamical features of such suspensions. Previous work with such suspensions have focused both on the low-temperature dynamical behavior of such systems, where the particles interact via repulsive interactions. Others have also studied the transition in the dynamical behavior from a repulsive glass-like to attractive colloidal gel-like state as the temperature of highly packed pNIPAM microgel suspension is changed beyond the Lower Critical Solution Temperature (LCST) of pNIPAM polymer.

Our prior work with purely repulsive slightly charged pNIPAM microgel suspensions at low temperature has focused on understanding both linear and nonlinear rheological response from experimental and theoretical point of view. In the linear viscoelastic regime our experiments have suggested concentration-dependent power-law growth of elastic shear modulus with concentration at low temperature. At low concentrations $G' \sim c^x, (x > 1)$ have been observed that changes at a critical concentration (we call it c_{sj} for reasons explained later) to a linear growth i.e. $G' \sim c$. We also observed similar trends in the yield stress of the suspensions . Based on the recent experiments [178] focused on understanding the concentration-dependence of microgels particle size at low T, microgel effective radius (R_g) was modeled to have distinct power-law concentration-dependence above (strong concentration dependence $R_g \sim c^{-1/3}$) and below (much weaker concentration dependence $R_g \sim c^{-1/6}$) the critical concentration (c_{sj}). Using a suit of liquid state structure and statistical mechanical theories and modeling the microgel particles as soft repulsive Hertzian spheres, a good agreement between experiment and theory was demonstrated. Theoretical predictions for equilibrium pair structure of the microgels and alpha relaxation time we also made. The central findings are described in Chapter 5.

Building on our prior work in this paper we focus on understanding the role of temperature on the linear and nonlinear viscoelastic properties of similar slightly charged pNIPAM microgel suspensions. We experimentally study the dynamical behavior of such suspensions over a wide range of concentration and temperature. Varying the temperature of the suspension has two salient effects on the suspensions: (1) microgel particles continuously de-swell as a function of temperature below the LCST with a sharp decrease in the size across the LCST, and (2) the interparticle-pair potential function changes from purely repulsive below the LCST to an additional attractive potential. Detailed discussion are provided in subsequent sections. We extend our theoretical model [199] to understand the wide range of temperature-dependent behavior with primarily focused on relative change in linear shear elastic modulus below the LCST and, modulus dependence on concentration at temperatures greater than the LCST.

The rest of the chapter is structured as follows. Section 6.2 describes materials and methods used for preparation and characterization of pNIPAM microgel suspensions. Key

experimental results in both linear and nonlinear regime are presented in section 6.3. A brief review of statistical mechanical theory to understand colloidal suspensions is provided in section 6.4, before moving onto specific modeling of microgels below and above LCST in section 6.5 and 6.6. Comparisons with experimental findings has also been done in corresponding places. Finally, the article concludes with a detailed discussion and summary of key findings of our research. Additional details can be found in the Appendix D.

6.2 Materials and Methods

6.2.1 Microgel Synthesis and Characterization[1]

Slightly charged self-crosslinked pNIPAM microgels were synthesized under a 'crosslinker free' condition following the protocol described in literature [164] with modifications. 100 ml of Type I water (18.2 MΩ cm) was filtered through a 0.2 μm Acrodisc syringe filter. Then, 146 mM (1.65 g) of N-isopropylacrylamide (NIPAM, 99 %, Acros) monomer was dissolved in filtered water. The monomer solution was again filtered through a 0.2 Âţm Acrodisc syringe filter into a 3-neck round bottom flask. The solution was stirred at 500 rpm, purged with nitrogen, and heated to 68°C in a temperature-controlled oil bath until the temperature of the solution became stable (1 hour typically). We then injected a solution of 2.8 mM (80 mg) potassium peroxodisulfate (KPS, 99 %+, Sigma-Aldrich) dissolved in 1 ml of the pre-filtered Type 1 water through a 0.2 μm Acrodisc syringe filter to initiate the polymerization. The mixture was left to react under continuous stirring at 500 rpm in nitrogen atmosphere overnight. This leads to the formation of stable nanospheres instead of linear chains if the solution is incubated at temperatures well above the lower critical solution temperature (LCST) of PNIPAM ($\sim 32^{\circ}$C). The formation of gel nanospheres is attributed to self-crosslinking by chain transfer reaction during and after polymerization [165]. Microgels prepared with a similar preparation protocol have been referred to as neutral in their charge [164, 166]. Here, we refer to such microgels as 'slightly charged', because the initiator used may possibly leave some charge on the colloids.

After the polymerization, the solution was cooled down to the room temperature and filtered with a glass wool five times to remove large particulates. The microgel particles were then thoroughly purified via five cycles of a centrifuge/dispersion process. The centrifugation was done at 15000 x g of relative centrifugal force (RCF), and the dispersion was enabled by a mixed process of the ultrasonication followed by the magnetic stirring.

[1] contributed by Jin Gu Kang and Paul Braun

The cleaned particles were then lyophilized for further characterization. A stock solution of $c = 9$ wt% was then diluted with deionized water to achieve the desired concentration of the slightly charged microgel suspension.

The particle radius was determined by dynamic light scattering (DLS) (Zetasizer Nano ZS, Malvern) and a Helium-Neon gas laser emitting at 632.8 nm on a very dilute suspension (0.04 wt%) with a beam diameter of 0.63 mm. DLS was performed at varying temperatures between $10 - 40^{\circ}$C in both heating and cooling cycles.

6.2.2 Rheological Characterization

Rheological experiments are performed over a very wide range of microgel concentration from 0.03 to 9 wt%. Viscoelasticity was probed using a rotational rheometer (model Discovery Hybrid 3, TA instruments and model MCR 702 from Anton Paar) with plate-plate geometry. These are both torque-controlled instruments (a.k.a. combined-motor-transducer type). A 600 grit, adhesive-back sand paper (Norton Abrasives) was adhered to the contact surfaces to suppress wall slip. The plate diameter was varied depending on the sample concentration to obtain a measurable response higher than the minimum torque resolution. A 60 mm plate was used for dilute samples 0.03-0.25 wt%, 40 mm plate for 0.25-1.5 wt%, 20 mm for 0.5-4.5 wt%, and 8 mm for 4.5-9 wt% samples. The typical gap in all experiments was between (550-750) μm, far larger than the particle size, thus eliminating confinement effects. A solvent trap, with a wet-tissue adhered to its interior, was used to minimize solvent evaporation during the measurements. The temperature of the bottom plate was controlled using a Peltier-system. To suppress sample aging effects and erase any history, all samples were rejuvenated by shearing at 50 1/s for 60 s and then allowed to relax for 12 min before taking measurements [154].

Two types of rheological characterization were performed: oscillatory shear and steady shear. To probe the linear temperature dependent response, samples were probed at $\omega = 1$ rad/s at a strain amplitude of 1 % while the temperature was varied from $10 - 40^{\circ}$C. In the steady shear experiments, shear rates were typically varied from (300-0.01) 1/s while waiting for the system to reach an apparent steady state as deduced by < 5 % variation in torque over a period of 30 s at fixed temperatures.

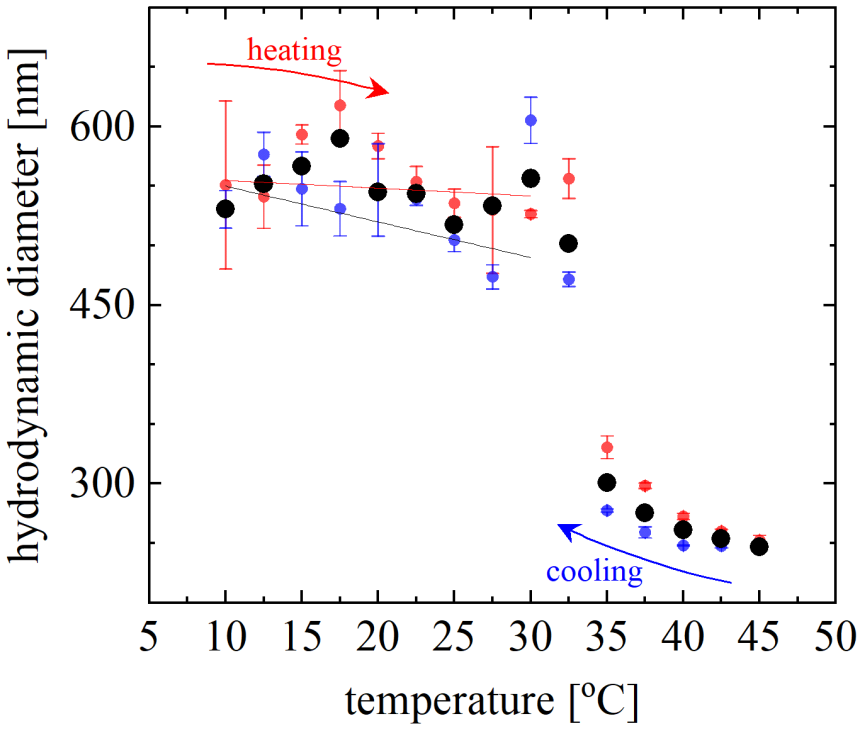

Figure 6.1: Temperature dependence of the hydrodynamic diameter of pNIPAM microgel particle measured using dynamic light scattering of an aqueous suspension of microgels. The "intramolecular" phase transition of the pNIPAM polymer across the LCST leads to a drastically change in the particle size. (DLS data courtesy: Jin Gu Kang and Paul Braun)

6.3 Experimental Results

6.3.1 Temperature-Dependent Particle Volume

In dilute suspensions (0.04 wt%) the microgel particles have a mean diameter of 550 nm at $10 - 40°$C. The dependence of hydrodynamic diameter of the suspension temperature is shown in Fig. 6.1. In both heating and cooling cycles, we observe a sharp change in the size of the microgel across the LCST ($\sim 32°$C). The particle size reduces to a mean diameter of 250 nm at $45°$C. Such a large variation in size is attributed to the "intramolecular" phase transition in pNIPAM polymer chains at the LCST due to the changing solvent quantity. As a result the volume of solvent a 'free' microgel can imbibe in the equilibrium configuration changes drastically [200]. A modest hysteresis in the hydrodynamic diameter while cooling and heating the suspension is observed and is consistent with the prior studies [201, 202]. Microgels prepared by such a crosslinker free preparation protocol are known to be highly deformable and ultra soft [164]. Our estimates for the individual particle modulus is around 1.5 kPa in the fully swollen state based on our previous work [201, 199].

6.3.2 Temperature-Dependent Linear Rheology

At low temperature ($10°$C) the microgel suspensions for $c > 0.4$ wt% exhibit a predominant solid-like response with the linear storage modulus G' larger than the linear loss modulus G'' in the probed frequency range. G' is nearly frequency-independent (Fig 5.1). We also found that the response at different temperatures (above and below the LCST) is nearly frequency-independent for selected concentrations (Appendix Figure D.2). The linear moduli (G', G'') at a fixed angular frequency of $\omega = 1$ rad/s and a strain amplitude of $\gamma_0 = 1$ %, as a function of the temperature are shown in Fig. 6.2 in the concentration range ($0.4 - 9$ wt%). We note that the $c = 0.4$ wt% gives a very weak torque response at all probed temperatures which can be clearly observed as the noise in the sinusoidal response of the material. Above this concentration, the torque signals are significantly larger that the instrument specified low torque limit (below the LCST) and hence can be reliably resolved [68].

The diverse rheological response of suspensions at various concentrations to the temperature can be observed from Fig. 6.2 as the temperature is raised up to and beyond the LCST. Experimentally, visible changes in the transparency and color of the suspension were observed. Local microgel aggregation was also observed at low concentrations as the attractive intra- and interparticle interactions emerge across the LCST. In the entire concentration regime, the temperature-dependence of the linear viscoelastic response can be broadly divided into three categories: weak softening, strong softening-to-stiffening and stiffening.

In the concentration range 0.4-1.25 wt%, the moduli monotonically decrease as the temperature is raised from 10 to $30°$C. From our prior work [199], we conclude that the suspension in this concentration regime at $10°$C behaves as glassy liquid with repulsive interparticle interaction pair potentials. In the physical sense, each microgel particle is entrapped in a cage formed by its neighbors. Such cages store elastic energy under small deformations, and provides a dominant elastic nature to the suspension. The time scale of collective relaxation of such cages under small deformations is generally much larger than the experimental time scales, and hence the suspension behaves as a predominant solid ($G' > G''$) on the observational time scales. From 10 to $20°$C, similar physics appear to be the determining the overall dynamics. A weak softening in the shear moduli can be observed which is seemingly related to the decreasing effective volume fraction of particles as they weakly deswell in this temperature regime (Fig. 6.1). Weak temperature dependence of the interaction potential between the microgel particles can be another reason for such a response. A rather sharp decrease in the values of moduli is observed between 20 to $30°$C at concentrations: 0.75, 1 and 1.25 wt%; while the concentrations: 0.4, 0.5 and 0.75 wt% show less

drastic change. A further increase in the temperature 30 to 40°C leads to non-monotonic tends in the shear moduli both with temperature and concentration. The non-monotonic trends in this concentration regime can be attributed to the spatially heterogeneous clustering of deswollen microgel particles, as the attractive interactions between the particles emerge across the LCST.

The suspensions in the concentration regime 1.5-4.5 wt% at low temperatures (10 to 20°C) shows a similar weak softening response similar to $c < 1.5$ wt%. The softening effect weakens with the increasing concentration in this regime. Increasing the temperature from 20 to 32°C leads to drastic softening in the linear moduli but the suspension maintains a predominant elastic response ($G' > G''$). A further increase in the temperature above the LCST, i.e. in the range 32-40°C, a monotonic increase in the linear moduli with the temperature is observed. Such a softening-to-stiffening trend in the linear moduli is hypothesized to be a consequence of two effects: (1) changing effective volume fraction of particles across the LCST, and (2) the emergence of attractive interactions between the particles across the LCST. Our expectation is that, well above the LCST, the effective volume fraction of suspension should be approximately constant (since the DLS data in Fig. 6.1 suggests fairly weak dependence of particle size on temperature above the LCST) and the increase in the moduli is directly related to the increasing attractive interactions between the particles. It is well established in the literature that the attraction strength between the pNIPAM polymers increase with the temperature above the LCST, and the formation of particle networks provide a dominant solid-like response. At the lower concentrations, ($0.4 - 1.25$ wt%), even though the interactions between the particles switch from repulsive to attractive, we suspect that the volume fractions of the particles at high temperatures in this regime is low enough, and hence a volume spanning (percolated) particle network cannot be formed in the explored temperature regime.

Finally, at the $c = 7$ and 9 wt%, the linear moduli does not shown any apparent softening below the LCST, rather the moduli show a very weak stiffening as the temperature of the suspension is increased from $10 - 32^{\circ}$C. A further increase in the temperature leads to a drastic stiffening in the moduli, and the stiffening effect is more prominent at 9 wt% compared to 7 wt%. The trends above the LCST can be attributed to the emergence of attractive interactions between the particles in highly crowded suspensions. Below the LCST, the weak increase in the moduli is suggestive of the weak dependence of the interaction potential on the temperature. At such high concentrations, the microgels are highly compressed close to their collapse size due to steric effects[199, 201, 178], hence we expect the temperature changes may not have as drastic effect on the effective volume fraction contrary to the lower concentration regimes. Such ideas will be quantitatively explored in

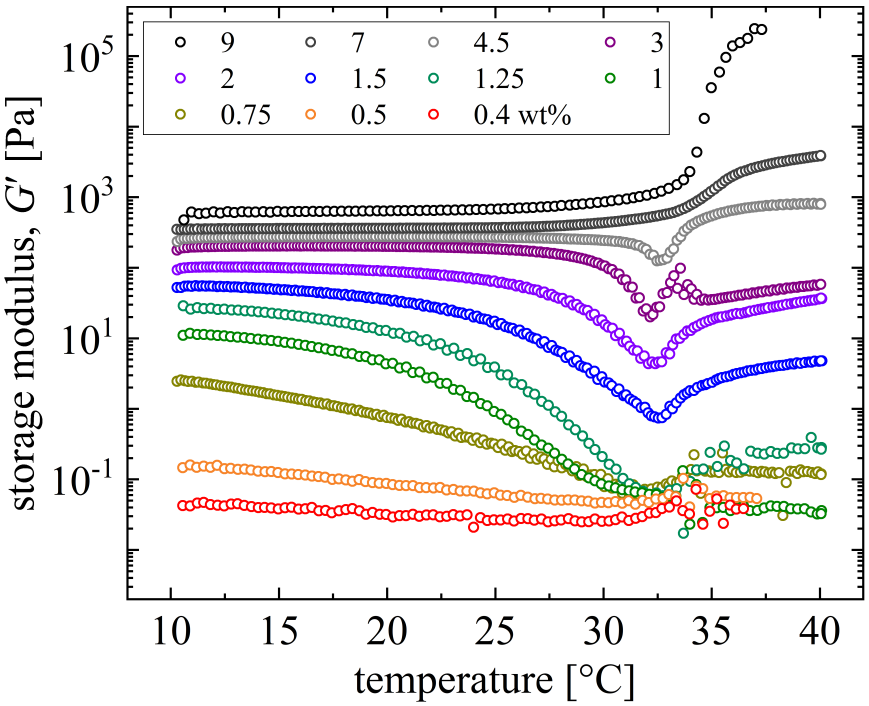

Figure 6.2: Linear storage modulus, G' for various concentrations of pNIPAM microgel suspensions as a function of temperature at an angular frequency of 1 rad/s. The suspensions show a rich dependence on the temperature. At each concentration (wt%), changing temperature affects both the effective volume fraction since the microgel particles swell/deswell, and the interparticle interactions (repulsive to attractive across the LCST) that exist between the particle.

a later sections.

In an earlier work on similar pNIPAM microgel suspension system [203], it was shown that at an intermediate temperature between the repulsive glassy and attractive particle-gel state, the interparticle potential vanishes and a liquid-like state is achieved (also called reentrant glass melting regime). However, in the concentrations range of 1.5-9 wt%, we do not observe such response and the samples remain predominantly elastic, ($G' > G''$), in the entire temperature range. Below 1.5 wt% it is not clear from the experimental data whether such a liquid state is realized due to instrument low torque limitations. Another difference that we observe is in the frequency dependence of linear viscoelastic moduli above the LCST. The previous work shows a weak power-law dependent viscoelastic moduli. We do not explore the frequency dependence systematically at all concentrations and temperatures, but our frequency-dependent experiments (Fig. D.2) at selected concentrations and temperatures, do not establish clear power-law dependence. Several limitations on the experimental artifacts render the measurements impossible over wide range of frequencies.

The linear moduli at all temperatures show a monotonic increase with the concentra-

tion. Fig. 3 shows the concentration dependence of G' at various temperatures. The measurements at low concentrations (0.4 –0.5 wt%) at 10 and $20°$C show a good agreement the characteristic modulus scale for thermal hard-sphere suspensions in glassy state, $G' \sim k_B T/(2R)^3$, where k_B is the Boltzmann constant, T is the temperature, and R is the radius of the suspension. For our microgel system such a scaling estimates gives a value of $G' = 0.024$ Pa for $2R = 550$ nm. At 10, 20 and $30°$C the elastic modulus shows a dramatic dependence on concentration ($G' \sim c^n, n > 1$) in the range (0.4 - 1.25 wt%) followed by a weaker concentration dependence ($G' \sim c$) in the range (1.5 - 9 wt%). Such a trend has also been observed in several other studies on related systems with different power-law exponents n which depends on several aspects such as stiffness, chemistry of the particles among other factors [154, 160, 199, 201]. The power-law fits for various temperatures are shown in the Fig.3. The power-law exponent n increases with increasing temperature below the LCST. This is likely a consequence of increasing particle stiffness as the particle volume decreases with increasing temperature and is consistent with prior literature [154] We note that at 30 and $40°$C, the measurements at low concentration are influenced by the low torque limit in the rheometer and the apparent plateau-like response at these temperatures is likely a consequence of such an experimental artifact and is not the true rheological response of suspension. The transition in the power-law response at 10, 20 and $30°$C has been attributed to the 'soft jamming' crossover transition in repulsive soft glasses in several studies in the literature. The "soft jamming" crossover transition takes place at a higher concentration as the suspension as the temperature is raised from 10 and $30°$C. Because of the discrete concentrations chosen in experiments, we cannot establish the "soft jamming" transition concentration as a function of temperature. However, it is apparent from the experimental trends that such a trend persists. This is because of the temperature induced particle de-swelling, and hence a higher particle number density (concentration) is required to reach the effective volume fraction necessary for such transition. In our prior work [199], we estimate that such a transition occurs at an effective volume fraction of 0.88. We also attributed the linear relationship of elastic modulus with the concentration above the "soft jamming" crossover transition to the isotropic shrinking of the cores of repulsive microgel particles which results in a constant effective volume fraction, and the modulus grows linear with number density of particles as the concentration is increased. At $40°$C, a "soft jamming" crossover transition is not observed rather the modulus shows a strong dependence on the suspension concentration, which is attributable to increasing attractive interactions at higher concentrations. More quantification will be made in a following section.

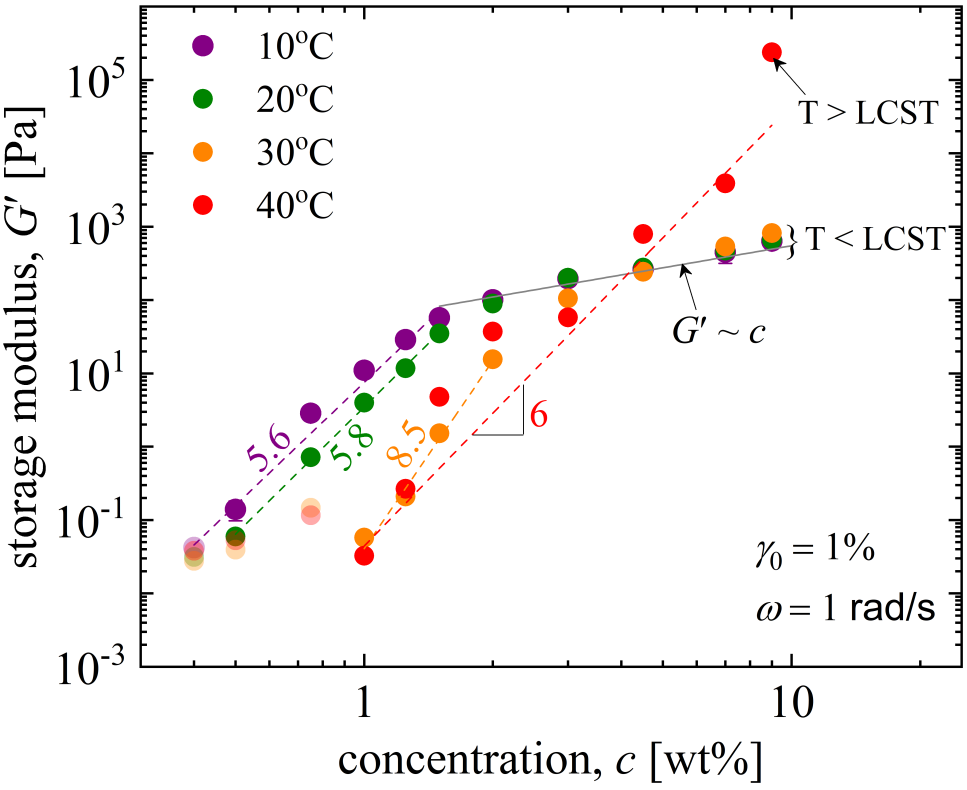

Figure 6.3: Concentration dependence of linear elastic shear modulus, G', at various temperatures. At temperatures below the LCST, i.e. 10, 20 and 30°C, G' shows two regimes of concentration dependence: a strong apparent power-law dependence on concentration ($G' \sim c^n, n > 1$) followed by a roughly linear concentration dependence. Above the LCST (40°C), the modulus monotonically increases with the concentration due to increasing strength of attractive interactions between the microgel particles.

6.3.3 Nonlinear Rheology

Figure 6.4 shows the steady state flow curves for the suspensions at two concentrations (3 and 7 wt%) probed at various temperatures. The response at these temperatures resembles that of a yield-stress fluid for both the concentrations with the stress value reaching an apparent plateau value at low shear rate. At $c = 3$ wt% the flow curves appear to shift vertically downwards at higher temperatures. Such a trend is not observed for $c = 7$ wt% with the flow response showing a non-monotonic temperature-dependence. We could not explore the flow response at temperatures above the LCST due significant evaporation issues, but the high shear rate viscosity at all the concentrations above the LCST was significantly lower than the corresponding values below the LCST. The response in the concentration regime of interest and probed temperature range is sufficiently captured by a Herschel-Bulkley (HB) model given by[171]

$$\sigma(\dot{\gamma}) = \sigma_y^{HB}\left(1 + \frac{\dot{\gamma}}{\dot{\gamma}_c}\right)^n \tag{6.1}$$

where σ_y^{HB} is the apparent yield strength and n is the flow index. The characteristic shear rate, $\dot{\gamma}c$ is interpreted as a crossover shear rate for the transition between the rate-independent plastic flow to a rate-dependent viscous flow. For $c = 3$ wt%, σ_y^{HB} decreases with increasing temperature below the LCST, similar to the trends of decreasing G' at this concentration while $\dot{\gamma}_c$ shows a monotonic increase as shown in Fig. 6.4 a inset. n increases with temperature with its values varying from 0.43 to 0.56 which can be attributed to the increase in the fluidity of the suspension at high shear rates and temperatures. For $c = 7$ wt%, Fig. 6.4 b, such a trend is not followed. σ_y^{HB} initially stays nearly independent of the concentration but then increases to reach a maximum value (at $\approx 25°$C), followed by a weak decrease at the highest probed temperature ($30°$C). Note that the change in the flow curves and hence the HB fits parameters is very subtle with temperature. Similar non-monotonic trends were also observed at $c = 4.5$ and 9 wt% (see Appendix Fig. D.4). We attribute such non-trivial effects in the nonlinear rheology to the complex nature of inter-particle interaction potential and the varying effective volume fraction of the suspension with the temperature.

Figure 6.5 shows the Herschel-Bulkley fit parameters as a function of suspension concentration at two temperatures: 10 and $25°$C. Full range of flow curves at all concentrations and corresponding HB fits are given in Appendix Fig.D.3. Similar to the observations made earlier for G' at the temperatures below the LCST, follows a strong apparent power-law concentration dependence below the "soft jamming" crossover transition, followed by a weak

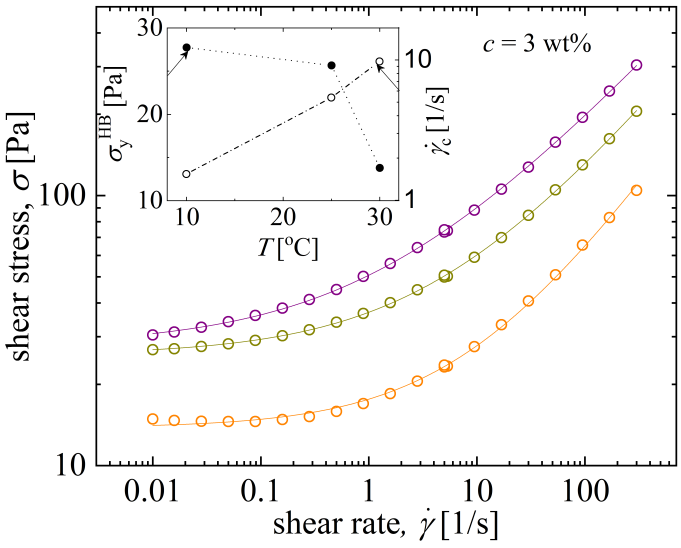

(a)

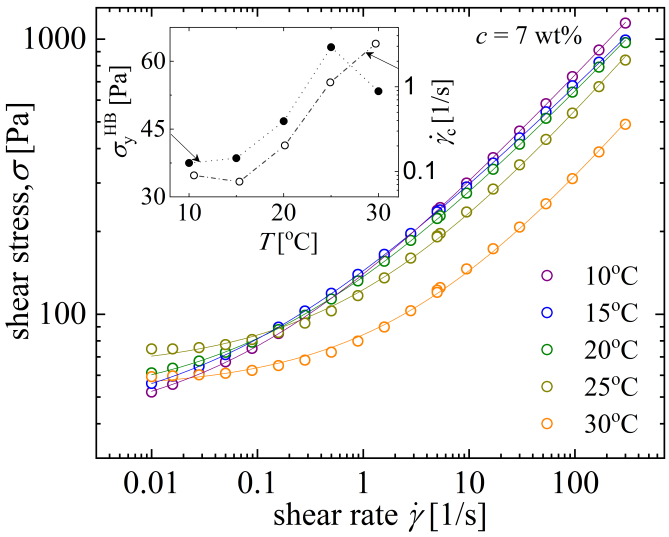

(b)

Figure 6.4: Steady state shear flow curves at different temperatures. (a) For c = 3 wt%, increasing the temperature monotonically shifts the flow curves vertically downwards attributable to the temperature-dependent effective volume fractions and interparticle interaction potential. Open symbols are the experimental data and the solid lines are the variance weighted fits of Herschel-Bulkley (HB) model . (inset) HB fit parameters are plotted as a function temperature. The yield strength (σ_y^{HB}) shows a monotonic decrease with increasing temperature while the characteristic shear rate ($\dot{\gamma}_c$) increases monotonically. The flow index (n), not shown here, increases with temperature, indicating increasing fluidity at higher temperatures at 3 wt%. (b) For $c = 7$ wt%, flow curves show non-monotonic temperature-dependent trends. (inset) The yield strength (σ_y^{HB}) initially increases with temperature, and then drops, hence showing a contrasting behavior to $c = 3$ wt%. The characteristic shear rate ($\dot{\gamma}_c$) shows a weak temperature-dependence decay initially followed by a monotonic increase similar to $c = 3$ wt%. The flow index (n), not shown here, shows similar trends as $\dot{\gamma}_c$

concentration dependence at both the temperatures. Power-law indices in the different concentration regimes are also temperature-dependent. σ_y^{HB} at $25°$C is lower than that at $10°$C below a certain concentration followed by a opposite trend beyond it. Above the "soft jamming" transition, both linear elastic shear modulus G' and show a nearly linear dependence on concentration at $10°$C while at $25°$C power-law concentration dependence of deviates from linearity different unlike G'. Such differences further exemplify the complex effects in the dynamics due to coupled effects from varying interparticle interactions and effective volume fraction with temperature. Differences can also be observed in the trends in $\dot{\gamma}c$ shown in the inset of Fig. 6.3. However, clear trends cannot be established from the experimental data. The flow index, n, shows similar trends at both the temperatures. n decreases monotonically with the concentration below the "soft jamming" transition, followed by a nearly constant value of 0.41 in the jammed regime. The values of n are marginally higher at $25°$C at all concentrations indicating an increased fluid-like nature of the suspension at high temperature undergoing deformation at large shear rates.

6.4 Theoretical Background[2]

Equilibrium pair structure, equilibrium Brownian dynamics, rheology, barrier hopping and related dynamical problems of a system of particles is intricately related to the knowledge of central potential of the system. Given the central potential of interaction, one can use Liquid State Ornstein-Zernike (OZ) theory along with either Percus-Yevick (PY), or, hypernetted chain closure (HNC) relation to determine pair level structure of the system of particles. Thus, we get interparticle pair correlation function, $g(r)$, static structure factor in fourier space, $S(k)$, and, direct correlation function $c(r)$ from OZ theory given a closure and pair potential of the system.

Structural information at the pair level is tied to dynamical phenomena at the ideal naive mode coupling theory (NMCT) level. The position and velocity of a tagged particle can be given by the Generalized Langevin Equation (GLE) where the central quantity to be determined is the force-force time correlation function. The NMCT description for force-force time correlation function projects dynamical correlations at the pair level. Non-zero gaussian Debye Waller (DW) factors consistent with the existence of a localized state alongside deGennes narrowing accounting for local and coupled channels of force relaxation gives

[2]Ashesh Ghosh (Chemistry, University of Illinois) led the theoretical work

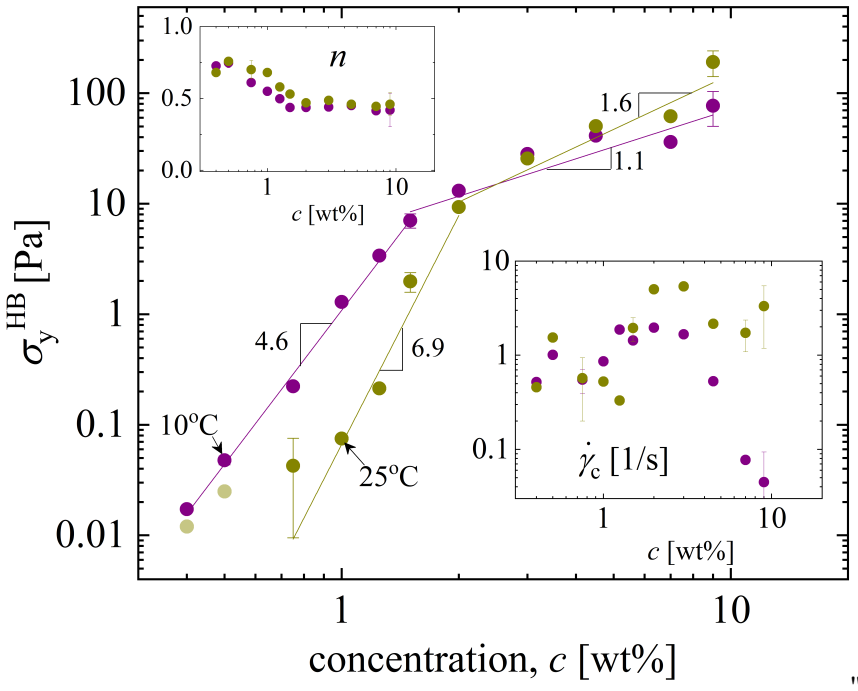

Figure 6.5: The Herschel-Bulkley fit parameters ($\sigma_y^{HB}, \dot{\gamma}_c$ and n) obtained from fits to the steady shear data for various concentrations at $10°$C (purple) and (yellow). The solid lines are the least squares power-law fits. Power-law exponents vary with the concentration regimes and the temperature. σ_y^{HB} shows a strong concentration dependence below the "soft jamming transition", past which the dependence weakens at both temperatures. (inset–n) Flow index are marginally higher at $25°$C compared to $10°$C below the "soft jamming" crossover transition implying increasing fluid-like nature at $25°$C. Above the "soft jamming" transition, n reaches a constant value of roughly 0.41 in both cases. (inset–$\dot{\gamma}_c$) Characteristic shear rate at $10°$C has a nearly constant value below the "soft jamming" transition followed by a decreasing trend above it. At $25°$C, no specific trends could be observed in $\dot{\gamma}_c$. Raw experimental data and HB fits are shown in the Appendix Fig. D.3.

the self-consistent NMCT dynamic localization equation, as,

$$\frac{1}{r_L^2} = \frac{\rho}{18\pi^2}\int_0^\infty C(k)^2 S(k)\exp(-\frac{k^2 r_L^2}{6}(1+S^{-1}(k))). \tag{6.2}$$

where r_L is the dynamic localization length, ρ is the particle number density, $C(k)$ is the direct correlation function in Fourier space and, $S(k)$ is the static structure factor. Existence of a solution to the localization equation predicts a localized state where particles are trapped within their neighboring cages under interparticle caging forces. One can derive a dynamic elastic modulus formula in ideal NMCT limit starting from stress-stress correlation functions, as,

$$G' = \frac{k_B T}{60\pi^2}\int_0^\infty dk[k^2\frac{d}{dk}ln(S(k))]^2\exp(-\frac{k^2 r_L^2}{3S(k)}) \approx a\phi\frac{k_B T}{dr_L^2} = a(\rho k_B T)\left(\frac{d}{a_L}\right)^2 \tag{6.3}$$

where a is a pre-factor. We note that elastic shear modulus goes inversely with dynamic localization length.

Beyond ideal NMCT localization transition, we can consider a dynamic free energy, $F_{dyn}(r)$ that controls the force on a tagged particle, and the particle moves under the influence of the force in presence of random noise, $\xi(t)$, as,

$$\zeta_s\frac{d}{dt}r = -\frac{\partial}{\partial r}F_{dyn}(r) + \xi(t) \tag{6.4}$$

Expression for the dynamic free energy is given as,

$$\beta F_{dyn}(r) = \frac{3}{2}ln(\frac{3d^2}{2r^2}) - \frac{\rho}{2\pi^2}\int_0^\infty dk\frac{k^2 c(k)^2 S(k)}{1+S^{-1}(k)}\exp(-\frac{k^2 r_L^2}{6}(1+S^{-1}(k))) \tag{6.5}$$

where d is the particle diameter. Dynamic free energy has a minimum at $r = r_L$ and a maximum at $r = r_B$ with a barrier height of F_B for volume fractions higher than mode coupling crossover transition. Collective elasticity can be taken into account by considering cage scale hopping requires cage expansion that costs energy to the system, giving rise to an elastic barrier $F_{elastic}$ on top of local cage scale F_B. Liquid structural relaxation time can be calculated as the Kramers time required to hop barrier of height ($F_B + F_{elastic}$).

The theory above in extendable to consider the effect of external deformation, where, an externally applied deformation is thought to manifest itself as microscopic stress altering the dynamic free energy. With the assumption that structural correlations remain unaltered at their equilibrium values, it is possible to calculate a local barrier, elastic barrier, elastic modulus and hopping times. With increasing stress, dynamic free energy liquifies or, the

barrier height decreases as a continuous function of increasing stress. The critical stress where $F_B = 0$, is termed as the absolute yield stress (σ_{abs}). Similarly, an absolute yield strain can be defined from the implicit stress strain relation, $\sigma = G'(\sigma)\gamma$ with γ being the strain.

6.5 Temperature-Dependence in Repulsive Regime

6.5.1 Modeling Microgels in Repulsive Regime

Simulations and theory have modeled the core-shell microgels as a central Hertzian contact potential before. Based on pair potential information, one can determine structural correlations at the pair level that can eventually be tied to dynamical problems of interest using sophisticated statistical mechanics based theories as sketched in the previous section. Low temperature behavior of microgels have been studied systematically under the assumptions mentioned in the introduction where microgel concentration dependence at low temperature is modeled with different qualitative regimes and shown to produce good agreements with experiments. Microgels below LCST are modeled with Hertzian pair potential [172, 204], given as,

$$\beta V(r) = \begin{cases} \frac{4E}{15}\left(1 - \frac{r}{d}\right)^{5/2} & \text{if } r < d = 2R_{eff} \\ 0 & \text{if } r \geq d \end{cases} \tag{6.6}$$

where $\beta = (k_B T)^{-1}$ is the inverse thermal energy, r is the interparticle separation, and d is the particle diameter. The front factor $4E/15$ is the inverse dimensionless temperature which controls the elastic stiffness of a particle. Structural correlations of soft microgels are better modeled using HNC closure in OZ theory, thus HNC closure relation is used. Comparison to low T experiments have provided $E = 30,000$ for the microgels studied here. Thus, we will use the same E to understand T dependence.

Temperature sensitive pNIPAM microgels show a strong temperature dependent coil to globule transition as it goes through LCST around 31-33°C. With increasing temperature, the microgels expel more amounts of water to reach a collapsed globule state at higher temperatures. The diameter of microgels change linearly until very close to LCST, as understood from dynamic light scattering measurements of the size of microgels as a function of temperature. Close to LCST, we see a rather abrupt change in diameter and finally it has a fixed size that correspond to the fully collapsed state that can expel no more water. Initial

linear diameter dependence can be modeled by the following equation,

$$d(c,T) = d(c,T_0) - \alpha(c)(T - T_0) \tag{6.7}$$

where diameter of microgels is a function of both concentration and temperature. To note, temperature dependent de-swelling is different from concentration dependent one and happen because of qualitatively different reasons, the latter one being purely steric de-swelling. As the concentration grows, the soft microgels jam against each other and this jamming causes the water to expel out. In previous work, we have provided a prediction of how the size of the particles at low T change as concentration goes higher. The different regions with pre-jammed and post jammed concentration dependence has been discussed before in detail.

For the pNIPAM system considered here, we find $\alpha = 3$ for dilute suspensions as per Eq. 6.7. It should be noted that concentration dependent steric de-swelling puts the higher concentration ($c > 4.5$ wt%) microgels at such an initial size that is already collapsed and cannot expel more water with increasing temperature. From the storage modulus data, we see at and after a certain concentration of microgels, storage modulus is independent of temperature for T <LCST. We hypothesize that, for these concentrations, steric de-swelling causes the particles to have similar size of a collapsed globule and small temperature dependent size change can be ignored ($d(T) = d(T_0)$) for T <LCST for $c > c_{threshold}$, thus volume fraction of the microgels remain constant. Hence, we see for low concentrations ($c = 0.5$ wt%), $\alpha(c) = 3$ and for $c > c_{threshold}$, we have $\alpha(c) = 0$. Consistent with the storage modulus data, we assume $\alpha(c)$ vanishes at a concentration of $c = 5.5$ wt%. Looking at the storage modulus response this seems reasonable since intermediate of concentrations of 4.5 wt% and 7 wt% we see ($G'(10°\text{C})$)$G'(32°\text{C})$) goes to 1 that can be taken as a signature of non-changing size of the microgels within the temperature range $10 - 32°$C. As a simple model in conjunction with experimental observations, we thus assume $\alpha(c)$ decays linearly with increasing concentration from 3 to 0, given as, $\alpha(c) = \alpha_0 - 0.6(c - 0.5)$ where $\alpha(c = 0.5 \text{ wt}\%) = \alpha_0 = 3$. To note, we understand that the precise concentration where $\alpha(c) \to 0$ can be taken anywhere in the range $5 - 6$ wt%, results based on them differ so little compared with the choice of 5.5 wt%, decision has been made to only look at 5.5 wt%.

We consider Hertzian repulsive pair potential, to calculate temperature dependent change in storage modulus with repulsion parameter, $E = 30000$. Here E is in units of k_BT and can be related to single particle modulus via, $E = \beta Y d^3/2(1 - \nu^2)$. As T increases the diameter of microgels change as per equation 6.7, where $d(c, T_0) = d(c, 10°\text{C})$ is set by

the models adopted before for change of size of microgels at low T. Considering this, temperature dependence of the volume fraction for T <LCST accounts for changing size of microgels as a function of T for fixed concentrations,

$$\phi_{c;T} = \phi(c; T = 10^{\circ}\mathrm{C}) \left(\frac{d(c;T)}{d(c;10^{\circ}\mathrm{C})} \right)^3 \tag{6.8}$$

The conversion factor for storage modulus from dimensionless units to Pa also follow a similar relation due to changing size and volume fraction, where with increasing T, non-dimensional parameter increases as d decrease.

6.5.2 Comparison to Experiments

Considering the above-mentioned factors, we can calculate theoretical plots for storage modulus for all concentrations that show drop in storage modulus with T. But given the complex de-swelling behavior and size change of microgels at different concentrations we decide to only look at the ratio of low temperature to around LCST elastic storage modulus. We see for all concentrations; theoretical calculation provides the same order of magnitude decay in storage modulus with a difference by a factor of 2-5 for certain concentrations. This suggest the actual size of particles might be decreasing more than as calculated by our simple model and the precise nature of size decay might not be linear as assumed by our simple model. We also note that, mode coupling based elastic shear modulus exist above the NMCT crossover and thus, for $c < 0.75$ wt%, high T, we do not have any number from theory.

Fig. 6.6 looks at the ratio of storage modulus at low temperature at 10°C to a high temperature value at LCST where $G'(T)$ shows a minimum. Qualitatively theory and experiment show the same trend even though the numbers differ. At low concentration, since the volume fraction to begin with at high temperature is low, states are very close to mode coupling crossover point and thus theory might not predict a ratio of modulus. At higher concentrations, $c > 5.5$ wt%, since there is no temperature dependent de-swelling, the ratio is trivially same as 1, since both size and volume fraction becomes temperature independent. One interesting observation is, both theoretical predictions and experimental observations predict the ratio ($G'(10^{\circ}\mathrm{C})/G'(32^{\circ}\mathrm{C})$) maximizes around jamming concentration, presumably due to change in volume fraction between high and low T maximizes around jamming point as shown in the inset.

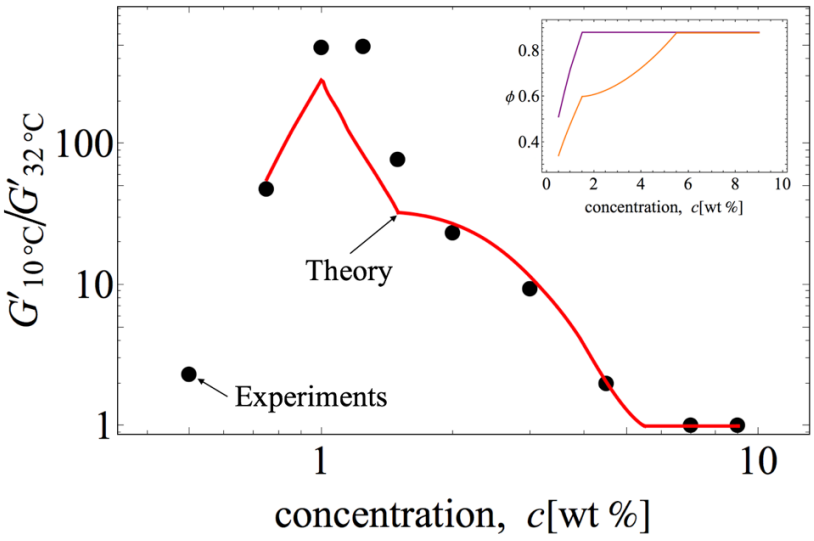

Figure 6.6: Comparison of the relative change of modulus at low temperatures compared to its value at the LCST. The theoretical predictions (red) captures the trends observed in the experiments (blue). (Inset) shows the change in volume fraction as a function of concentration at two temperatures, 10°C (Purple) and 32°C (Orange).

6.6 Theoretical Analysis of Temperature Dependence above LCST: Attractive Regime

6.6.1 Model at T >LCST

pNIPAM microgels undergo a coil to globule collapse beyond LCST and interactions between microgels become attractive in a smooth temperature dependent fashion. Keeping in mind an effective pair potential that works for the entire range of temperature where microgel swelling de-swelling behavior takes place is yet to be developed, we try to model the attraction at high temperature by the following attractive potential,

$$\beta V(r) = \begin{cases} -\epsilon + \frac{4E}{15}\left(1 - \frac{r}{d}\right)^{5/2} & \text{if } r < d = 2R_{eff} \\ -\epsilon \exp\left(-\frac{r-d}{a}\right) & \text{if } r \geq d \end{cases} \tag{6.9}$$

where $\beta = (k_B T)^{-1}$ is the inverse thermal energy, r is the interparticle separation, d is the particle diameter, a is the range of interaction and ϵ is the strength (amplitude) of attraction. Hydrophobic force law is seen to follow exponential decay with distance between surfaces where average decay length is of the order few water diameter ($d_{H_2O} = 0.3$ nm) for micrometer sized surfaces. Considering this, we take the range of attraction to be $a = 0.01d$

given at high T, $d = 250$ nm. To keep in mind, we do not know how to turn on attraction as a continuous and smooth function of temperature as the systems swiftly transitions through LCST, thus, we analyze only the highest T behavior studied in experiments where $T >$LCST and there is much experimental evidence supporting particles behave attractively.

6.6.2 Effect of Attraction on Structural Correlations and Dynamic Free Energy

As a short-range attraction is introduced on top of repulsive center of mass potential, structure of the system changes; reflected through equilibrium pair correlation functions (not shown here). Liquid state OZ equation with HNC closure can again be used to understand dynamical correlations at the pair structure level, and structure can be related to dynamics as per the theory briefly mentioned in section 6.4. As strength of attraction grows, peak of radial distribution function $g(r = d)$ increases indicating more ordering at contact. In the given example below, we look at $g(r)$ for $\phi = 0.60$ at range of attraction $a = 0.01d$ for three strengths of attraction of 0, 1.0 and 2.5 k_BT. $g(d)$ is seen to increase from 7.6 to 10.3 to 14.6 as one moves from attraction strength of 0 to 2.5. Similarly, we can look at the static structure factor, where the peak value of $S(k = k^*)$ goes from 3.40 to 3.06 to 2.81 by going from 0 to $2.5k_BT$ attraction. The softening of cage coherence as a function of strength of attraction for short range attractive potentials is intricately related to phenomenon such as 'glass-melting' and 're–entrant glass transition' and beyond the scope of discussion in this paper.

Strength of attraction increases bonding forces acting between the particles on top of increasing caging forces. Since NMCT motivated dynamic free energy depends on changing structural correlations and caging forces, we can expect dynamic free energy to change as a function of attraction strength where range of attraction is kept fixed. Here we show one example of how dynamic free energy changes as strength of attraction is increased at a fixed volume fraction and fixed range of attraction. The important length scales associated with dynamic free energy such as, localization length (r_L), barrier location (r_B) and location of maximum force (r^*) are shown in inset figure as well as the local barrier (F_B). We see from the following figure, the local barrier grows a lot (goes from $5k_BT$ to $16k_BT$) with strength of attraction for the model system shown.

From Fig. 6.8, some interesting features should be noted, as, (i) Location of the minimum of free energy or the localization length r_L decreases gradually as the strength of attraction is increased. r_L/d values for the system given above is found to be, 0.024 (blue),

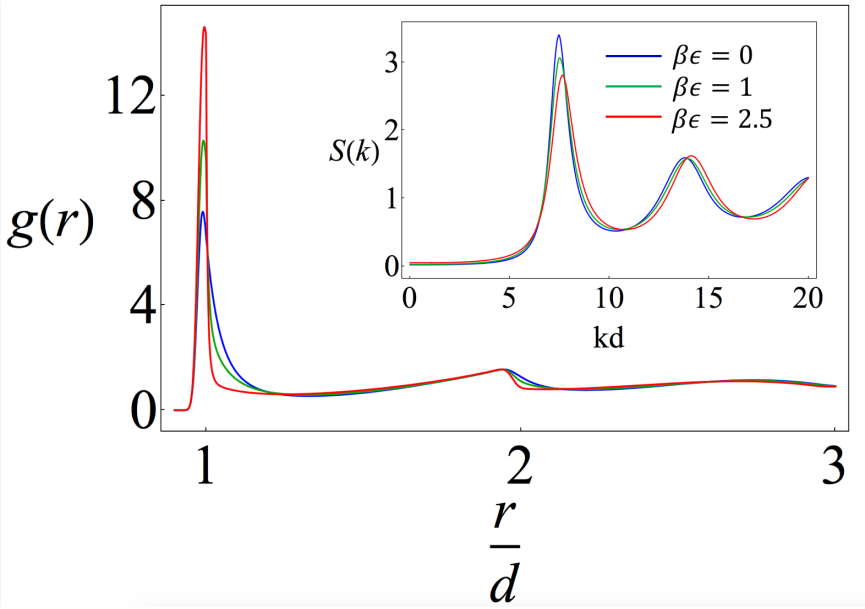

Figure 6.7: Equilibrium pair structure for a volume fraction of $\phi = 0.60$, and range of attraction $a = 0.01d$. (Inset) shows static structure factor for the same system parameters at three different strengths of attraction.

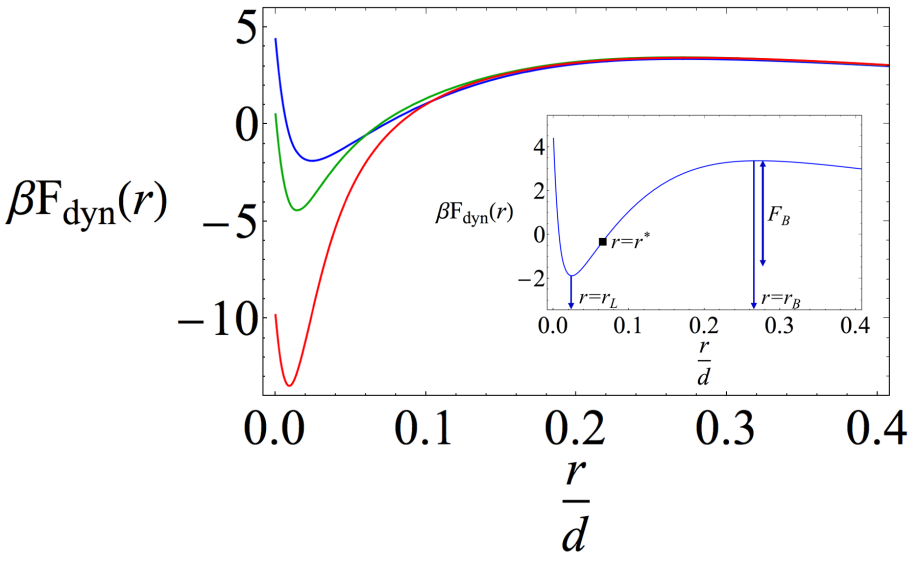

Figure 6.8: Examples of dynamic free for a given volume fraction of $\phi = 0.60$ with range of attraction $a = 0.01d$ and strengths of attraction $0k_BT$ (pure Hertzian repulsive case, blue), k_BT (green) and $2.5k_BT$ (red). (Inset) shows the important length scales associated with dynamic free energy and the local barrier.

0.014 (green), and, 0.009 (red), respectively. We already know $G' \propto \frac{\phi}{r_L^2}$, which means as strength of attraction increases, elastic shear modulus grows for a fixed volume fraction and fixed range of attraction. (ii) Location of maximum force (r^*, where $\partial^2 F_{dyn}(r)/\partial r^2 = 0$) moves inwards as strength of attraction grows and slope of dynamic free energy at $r = r^*$ increase with increasing $\beta\epsilon$. Maximum force in the dynamic free energy (f_{max}) in units of k_BT/d are given as, 46 (blue), 110 (green), and, 332 (red) respectively. This quantity correlates directly with absolute yield stress and thus we can safely say yield stress grows with increasing $\beta\epsilon$ for a fixed volume fraction and range of attraction. (iii) Barrier location r_B moves inward and local barrier height increases with growing $\beta\epsilon$, indicating stronger localized state. Increasing jump distance of states obtained at higher attraction strength increases the collective elastic barrier which leads to higher alpha relaxation times.

6.6.3 Comparison with Experimental Observations

Looking at Fig. 6.1 and Fig. 6.2 we can say that, concentration dependent de-swelling at low T puts the microgel size comparable to high T collapsed state (In other words, within the studied temperature and concentration space, concentration dependent de-swelling and temperature dependent de-swelling has similar effect on the particle diameter).

From Fig. 6.2 in experiments, we can safely say, for lowest concentrations up-to 1.25 wt%, storage modulus for $T >$LCST does not show a gradual increase in modulus presumably due to very low volume fraction of the samples as we estimated as per inset of Fig. 6.9. Starting from 1.5 wt% to the highest concentration of 9 wt%, we see a gradual increase of storage modulus as temperature grows. Due to our inability to fully understand, (i) how to switch from repulsive to attractive interaction continuously as a function of temperature, or, in other words a singular potential that works for all temperature ranges is yet to be developed and (ii) the growth of $\beta\epsilon(T)$ as a function of T in the post LCST region, we have decided to understand the concentration dependence of storage modulus at highest $T = 40°$C. We note that within the given range of concentration, G' grows by almost ~ 5 orders of magnitude. Fig. 6.9 shows the experimental data at $T = 40°$C along with theoretical attempts to understand the data.

Given the step like increase in storage modulus data (black points), we consider the least square fit to be the best representation of concentration dependence of experimental G' which goes as, $G' \approx 1.21 \exp(1.33c)$ where c is the concentration in wt%. Our theoretical attempts to understand the experimental results is thus aimed to look at the trend in modulus growth given by black dotted line rather than the precise black points. Theory calculations are done exactly the same way as sketched in Section 6.4, where G' is given. To convert the

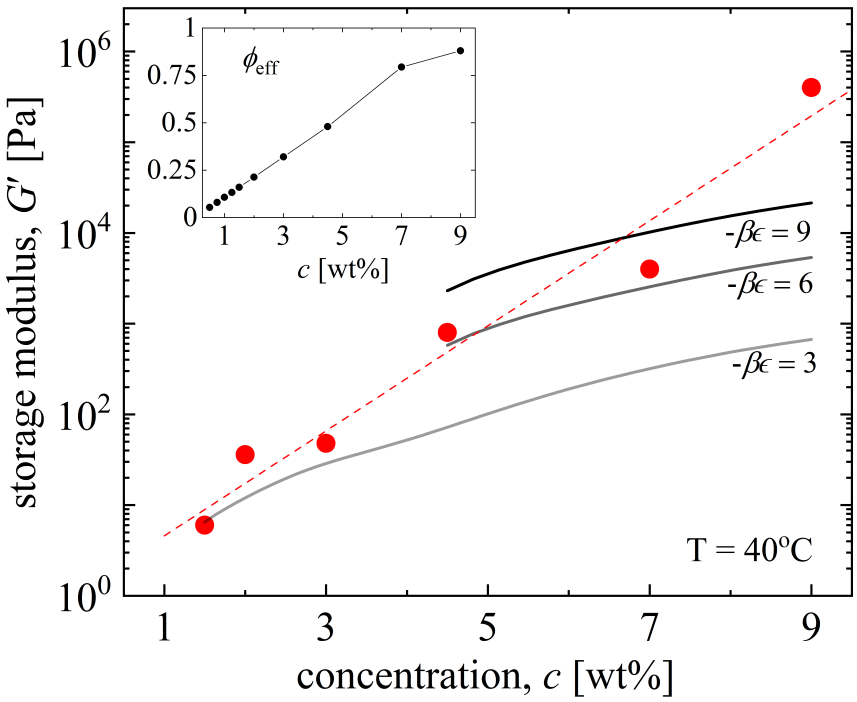

Figure 6.9: Storage Modulus at $40°$C. Black dots represent experimental points and black dotted line is the exponential fit to the data. Blue, Green and Red lines are theoretical calculations done with $-\beta\epsilon = 3, 6 \,\&\, 9$ and fixed range of interaction $a = 0.01d$. (Inset) shows estimates of effective volume fractions as a function of concentration at high T. (inset) shows effective volume fraction estimated at high temperature as a function of concentration.

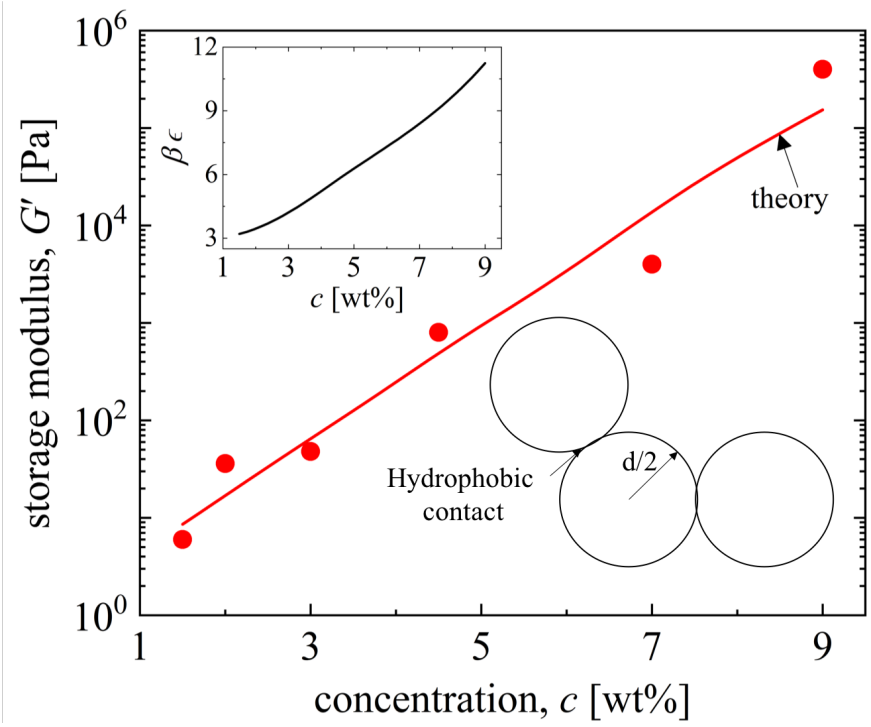

Figure 6.10: Theoretical linear elastic Shear Modulus (red) at $40°$C as a function of concentration. Black points are experimental observations. (Inset) shows concentration dependence of strength of attraction that produces the correct shear modulus.

theoretical G' into an experimentally verifiable number, (i) we use the 'fudge-factor' of 0.1 to compensate for the overestimation in MCT results the same way it was used to analyze low temperature concentration dependence and (ii) non-dimensional $k_BT/\ d^3$ is converted to Pa units using $k_BT\ /(250\text{ nm})^3 \approx 0.256$ Pa. Hertzian model parameter E relevant with the given potential in Eq. 6.9 is taken to be unchanged, i.e. $E = 30000$. Calculations are presented in Fig. 6.9 for given attraction strengths of $-\beta\epsilon = 3$ (red), 6 (magenta) and 9 (green) for given range of attraction $a = 0.01d$. Thus, we note, to produce experimental G' the strength of attraction must increase as a function of concentration. Explanation for this is provided later. We have also studied other ranges of attraction (not shown for the purpose of this paper), that does not change the numbers much (has to do with how MCT deals with attractive forces, detailed discussion on this is beyond the scope of the paper). An estimate of volume fractions at highest $T = 40°$C is given in inset of Fig. 6.9 where the collapsed size is taken to be $2R_{collapsed} = 250$ nm and Eq. 6.8 is used to determine temperature dependent volume fraction. We note that, unlike the low T case, at high temperature, microgel volume fraction grows linearly with concentration.

In Fig. 6.10 we look at how theoretical linear elastic shear modulus changes with concentration and inset shows concentration dependence of the attraction strength required

to produce sensible theory-experiment agreement. The black points are experimental observations at respective concentrations for $40°$C. Red solid line corresponds to theoretical calculations that are all done for range of attraction $a = 0.01d$. To note, for all the concentration considered here, theoretical alpha relaxation time is "high" compared to 100 seconds. Strength of attraction is seen to grow from $3k_BT$ to $11k_BT$ over the concentration range of 1.5 to 9 wt%.

To understand the concentration dependence of strength of attraction, we consider the nature of attractive interactions as hydrophobic. Interaction strength per unit area between two identical hydrophobic surfaces at a distance D is given by,

$$W_h = 2\gamma H_y \exp(-D/D_h) \tag{6.10}$$

where W_h is the hydrophobic energy per unit area, γ is the inter-facial energy of hydrocarbon in water, H_Y is the hydrophobicity parameter (=1 for perfectly hydrophobic surface, taken to be the case at $40°$C), D is the distance between two surfaces and D_h is the hydrophobic decay length (usually 0.3-1 nm or, 1-3 d_{H_2O}). Interfacial energy of hydrocarbon in water is taken to 50 kJ/mol at $25°$C . Now as concentration goes up, the surface area of contact grows and as a result, the total interaction energy (can be calculated by $W_h A_c$, where A_c is the area of contact) increases. Theoretical prediction for area of hydrophobic interaction considering $D = D_h$ or $D = 0$ gives the contact area for Hertzian particles to be 0.25-1.5 nm^2 where we consider the same value for interfacial energy.

We can calculate absolute yield stress and absolute yield strain as a function of concentration (strength of attraction increases with concentration) which is shown in Fig. 6.11. We see the growth of absolute yield stress is linear similar to increase in elastic shear modulus both of which change roughly exponentially with concentration. Here, absolute yielding is related to maximum force on the dynamic free energy or where barrier goes to zero. For the absolute yield strain, measured as $\sigma^y_{abs}/G'(\sigma = 0)$ decreases with concentration. For the purpose of this work, a predictive plot for dynamic yield stress/strain is not shown but as discussed for pure repulsive case at low T, both absolute and dynamic criteria follow same qualitative trend.

6.7 Conclusions and Summary

We studied the dynamical response of suspensions made from thermoresponsive pNIPAM microgel particles experimentally and theoretically. The particles used in this study are slightly charged and self-crosslinked, distinct from ionic microgels that have been utilized

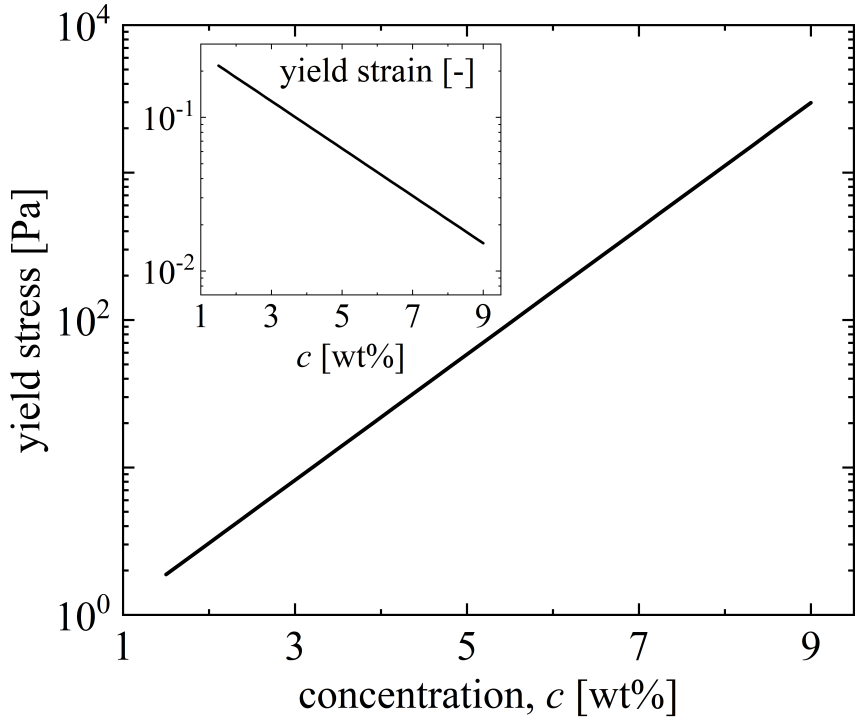

Figure 6.11: Prediction for absolute yield stress as a function of concentration. (Inset) shows absolute yield strain as a function of concentration

in prior studies, a feature that we have demonstrated in our prior work [199] leads to several key distinct features in the rheology. The particular focus of this work is on the temperature induced effects on the dynamics of such suspensions. Temperature change has two key effects: (1) size of individual microgel particle is a function of temperature, hence the effective volume fraction of suspension varies with the temperature in addition to the concentration-dependent steric effects, and (2) the interparticle interaction pair-potential changes from repulsive to attractive as the temperature is raised beyond the LCST. While a few previous studies have experimentally studied the response of such thermoresponsive suspensions in highly packed state, our work provides insights into the coupled concentration and temperature-dependent dynamics of in these systems over a very wide range.

The concentration regime that we have explored spans the low viscosity liquid, glassy and "soft jammed" regimes at low temperatures (below the LCST) where the microgels interact via repulsive pair potential. In the entire concentration regime, we performed a systematic study of the effect of temperature on the linear and nonlinear rheological properties of the suspensions. The coupled effect of (1) and (2) results in a diverse set of dynamical behavior, which to the best of our knowledge has not been explored in the previous studies. In addition to the experiments, we also gain insights into the underlying

physics by theoretical modeling the suspensions and their dynamics. We use a suite of existing statistical mechanical theories, along with the knowledge of single microgel particle size, and simple approximations for interparticle particle pair-potential functions to make quantitative predictions for several structural and rheological properties. We used the temperature-independent Hertzian potential function to model the repulsive-glassy behavior of the suspension below the LCST. The interactions were modeled via an exponentially decaying attractive potential in addition to the Hertzian repulsion above the LCST. The theoretical prediction show close agreement to the linear elastic shear modulus and the yield stress of the suspensions in the entire concentration regime. Additionally, we make testable predictions for several other structural and rheological properties that will be a subject of our future experimental efforts.

We believe the ideas presented in this work are applicable (with modifications) to diverse range of suspensions, both repulsive and attractive. Our approach also establishes the ways to design the key rheological properties of the suspensions from the parameters such as individual particle stiffness, polymer-solvent interactions, and interparticle interactions, all of which in principle can be controlled independently.

Acknowledgement

This work was performed at the University of Illinois and supported by DOE-BES under Grant No. DE-FG02-07ER46471 administered through the Materials Research Laboratory. RHE thanks Anton Paar for providing the rheometer MCR702 which was used for some of the rheology experiments.

CHAPTER 7

THERMORESPONSIVE STIFFENING WITH MICROGEL PARTICLES IN A SEMIFLEXIBLE FIBRIN NETWORK

7.1 Introduction

Stimuli responsive materials are important for diverse applications including actuators, sensors, tissue engineering, drug delivery, and soft robotics where they provide functionalities difficult to obtain by using passive materials [205, 198, 206, 207]. Our interest here is in stimuli-responsive particle-filled polymer composites [18, 208]. Such systems typically consist of a dense flexible chain polymer matrix (e.g., crosslinked elastomer) that exhibits a broad linear elastic regime and a mean physical mesh size that is small compared to the added rigid particles. Here we consider a different polymer-particle composite scenario based on semiflexible biopolymer networks, which exhibit strong elastic nonlinearities, and particles that are soft and comparable in size to the network mesh.

We report fabrication, characterization, and modeling of a two-component stimuli-responsive particle-biopolymer composite in an aqueous suspension which responds to increasing temperature by stiffening, even though the two components independently soften under the same conditions. Biopolymer networks are ubiquitous in living organisms, present as both intracellular scaffolds and extracellular matrices which are vital for the structural integrity of biological structures [209, 210, 211], and play key roles in physiological processes such as cell migration, cytokinesis, and mechano-responsiveness [212, 213, 214, 215]. A key feature is that their mechanical properties are dependent not only on dynamic biochemical processes, but also on applied deformation. Biopolymer networks are well known for their distinctive nonlinear stiffening response under deformation (stress or strain), which distinguishes them from flexible polymeric networks (such as crosslinked elastomers) which

This chapter appeared in the following peer-reviewed publication: Chaudhary, G., A. Ghosh, N. A. Bharadwaj, J. G. Kang, P. V. Braun, K. S. Schweizer, and R. H. Ewoldt, "Thermoresponsive stiffening with microgel particles in a semiflexible fibrin network," Macromolecules, 52 (8), 3029-3041 (2019), doi: doi.org/10.1021/acs.macromol.9b00124

generally show softening at large strains and overall are not nearly as deformation responsive [216, 217, 218]. The nonlinear strain-stiffening behavior is a direct consequence of the stiffness and large persistence length of underlying polymer filaments which constitute these networks [74, 219, 220, 127, 221]. Such biopolymers are classified as semiflexible due to their large bending stiffness, and do not form random coils [127]. The semiflexible nature also strongly modifies the nature of physical entanglements and influence of chemical crosslinking on the mechanical response, resulting in structural and dynamical length scales which are very different from their flexible counterparts [222]. From a property perspective, using a large mesh semiflexible polymer network presents several opportunities for novel material design [223, 224, 225] and have already found applications in tissue-engineering and cell culture scaffolds [226, 227] because of such distinctive structural and dynamic-mechanical properties, and offer new mechanisms of developing stimuli-responsive systems which are fundamentally different from the flexible polymer based composite systems.

In the current work the biopolymers and corresponding network architecture is formed via in situ polymerization around a pre-existing dispersion of temperature-sensitive Poly(N-isopropylacrylamide) (pNIPAM)-based microgel particles. In dilute solution, pNIPAM particles collapse at temperatures above the lower-critical solution temperature (LCST) of $\sim 32^{\circ}$C [228]. We employ a very large volume fraction of microgels (32-78 %) in contrast to an earlier study [229] on a microgel-containing fibrin composite where the microgel volume fraction was less than 17 %. Moreover, this earlier study [229] did not focus on stimuli-responsive stiffening, but rather examined cell mobility through fibrin networks, showing that a composite of fibrin with microgel particles had enhanced cell mobility via the formation of colloidal tunnels compared to typical high density fibrin networks. Here, we show that at these large microgel volume fractions there is a near negligible modification of elastic stiffness of the composite network below the pNIPAM LCST where the microgels are swollen. Upon increasing temperature above the LCST, the composite controllably stiffens which we hypothesize is due to microgel collapse modifying the fibrin network structure. A key idea is that a very small amount of local stretch in the fibrin network can lead to noticeable stiffening. This functional response was not present in the previous work on fibrin containing low volume fractions of microgels [229]. Furthermore, the mechanical behavior of our system is potentially richer at large microgel volume fractions since they can in principle form soft glass or gel-like states in the composite in a manner which could be modified by geometric or other fiber-induced physical factors. With growing efforts towards the development of synthetic semiflexible polymer networks [230, 231, 232], our efforts provide novel design principles for realizing new classes of

smart responsive materials.

7.2 Materials and Methods

7.2.1 Microgel Synthesis and Characterization[1]

Ultra-low crosslinked pNIPAM microgels were synthesized under a 'cross-linker free' condition following a published protocol [164]. Free-radical polymerization of NIPAM (Sigma-Aldrich) in water was initiated using potassium persulfate at $45°$C and the temperature was gradually increased to $65°$C in the absence of added cross-linker. The formation of microgel particles is attributed to self-crosslinking by chain transfer reaction during and after polymerization [165]. Typically, such microgels have a dense core and a more dilute/hairy corona structure which we assume to be, on average, a spherical soft object. The internal density ρ decreases continuously in a non-universal manner as one transitions from its center to edge.

As shown elsewhere [164], initiating polymerization at low temperature leads to a lower radical concentration in the solution and hence a low concentration of particle nuclei. Particle growth is achieved via favorable radical propagation relative to the nucleation of new particles process because of the higher concentration of monomer compared to nuclei. With a gradual increase in temperature more radicals are generated while monomer is consumed [164]. A detailed preparation protocol is provided in the Appendix E.1. A stock solution of 9 wt% polymer microgel particles was then diluted with Type 1 water to achieve the desired concentrations of the uncharged microgel suspension.

The particle radius as a function of temperature was determined by dynamic light scattering (DLS) (Zetasizer Nano ZS, Malvern) with a Helium-Neon gas laser emitting at 632 nm on a very dilute suspension (0.04 wt%) with a beam diameter of 0.63 mm. The temperature of the samples was controlled with a step size of $2.5°$C by the automated heating/cooling module built in the instrument. The equilibration time at each temperature was 150 s.

7.2.2 Sample Preparation

The aqueous buffer used in all the samples was produced by mixing 25 mM HEPES, 150 mM NaCl, and 20 mM $CaCl_2$ in type 1 water and adjusting the pH to 7.4. Pure microgel suspensions were produced by diluting the stock solution of microgels with an

[1] contributed by Jin Gu Kang and Paul Braun

estimated mass of aqueous buffer. Bovine fibrinogen (free of plasminogen and fibronectin) and thrombin were acquired commercially (Enzyme Research Laboratories, South Bend, IN, USA) and stocked at -70°C. Prior to composite preparation, fibrinogen was thawed at 37°C and diluted to the required concentration with the aqueous buffer. To prepare pure fibrin hydrogels, predetermined volumes of solutions of fibrinogen and thrombin were mixed in a centrifuge tube and immediately loaded between the plates on the rheometer. For preparing composites, a predetermined mass of pNIPAM microgels was added to the diluted fibrinogen solution in a microcentrifuge tube and the contents were mixed using a vortex mixer at 1000 r.p.m until the microgels were well dispersed visually. The solution was kept on ice and diluted thrombin was added to the fibrin-microgel solution to initiate gelation. The sample was quickly loaded between the rheometer plates and allowed to gel at a constant temperature of 25°C for an hour while probing its viscoelasticity using a very low oscillatory strain (1 % strain amplitude). This was done to ensure that the sample gels to a stable shear modulus before any temperatures ramps are applied. The small strains applied during network formation do not have a significant effect on rheological properties, as evidenced from our pure fibrin rheological properties being similar to those reported throughout the literature [233, 224].

7.2.3 Rheological Characterization

Viscoelastic properties of all materials were probed using a torque controlled rotational rheometer (model Discovery Hybrid 3, TA instruments and MCR702, Anton Paar) using a plate-plate geometry. A 20 mm diameter steel plate was used in all experiments with a 600 grit, adhesive-back sand paper (Norton Abrasives) adhered to the contact surfaces to suppress wall slip. A fixed gap setting was used in each experiment. Typical gaps varied between $750 - 1100\,\mu$m, significantly large compared to the microgel or polymer pore size, thus eliminating any confinement effects. The reported nonlinear measurements are without any parallel plate corrections. A solvent trap with a wet-tissue adhered to its interior was used to minimize water evaporation. The temperature of the bottom plate was controlled using a water-cooled Peltier system. For the pure microgel suspension experiments, all the samples were rejuvenated by shearing at 50 1/s for 60 s, and then relaxed for 12 min before taking data to suppress sample aging effects and erase any history [154]. For the pure fibrin and composite rheology, fibrinogen was allowed to polymerize for an hour while probing its viscoelasticity at an oscillatory strain with small amplitude (in the linear regime) and an angular frequency , after which time approximately constant plateau values of linear moduli were observed as a function of time. Temperature sweeps from $25 - 35^{\circ}$C

(up and down) were performed at a constant rate of 25°C/min while probing the linear viscoelasticity of the samples. Strain amplitude sweeps were also performed on the pure fibrin hydrogels and fibrin-microgel composites to probe the strain dependent viscoelasticity at a fixed angular frequency of 1 rad/s.

7.2.4 Microscopy

Two-color fluorescence microscopy experiments were performed on the composite using a laser scanning confocal microscope (LSM 700, Zeiss, Germany). A 63x oil-immersion objective lens (NA 1.4) was used. The microgels were labeled with rhodamine green (Invitrogen, USA) and fibrinogen was labeled with TAMRA-SE red (Thermofisher Scientific, USA) with excitation/emission wavelength of 504/535 nm and 547/576 nm respectively. The temperature of the sample was controlled using a heated stage (Delta T, Bioptechs, USA).

7.3 Results

7.3.1 Microgel Characterization

In dilute solution (0.04 wt%), the size of microgels strongly depends on temperature. Fig. 7.1 shows the average hydrodynamic diameter of the microgels measured via DLS. More details about the intensity distribution and polydispersity in size are provided in the Appendix E.2. The averaged hydrodynamic diameter varies roughly from 2 to 0.6 μm as the temperature is varied between $25 - 35^{\circ}$C at 1°C/min with an abrupt decrease around the LCST of pNIPAM. This is attributed to an intramolecular "phase transition" of the pNIPAM polymer across the LCST and hence the volume of solvent the microgel can imbibe changes abruptly to achieve an equilibrium configuration [234, 200]. Hysteresis is observed in the hydrodynamic diameter while cooling and heating the suspension which is consistent with other studies in the literature [235]. Microgels prepared by such a crosslinker-free preparation protocol are known to be highly deformable and ultra soft [164]. We did not explicitly measured the microgel stiffness, but our estimates using the Flory-Rehner theory [169, 234] (see Appendix E.4) yields an elastic shear modulus of 1.6 kPa at 25°C and 4.6 kPa at 35°C. This is consistent with our earlier work, where we have estimated a similar particle stiffness based on an independent statistical mechanical analysis [199].

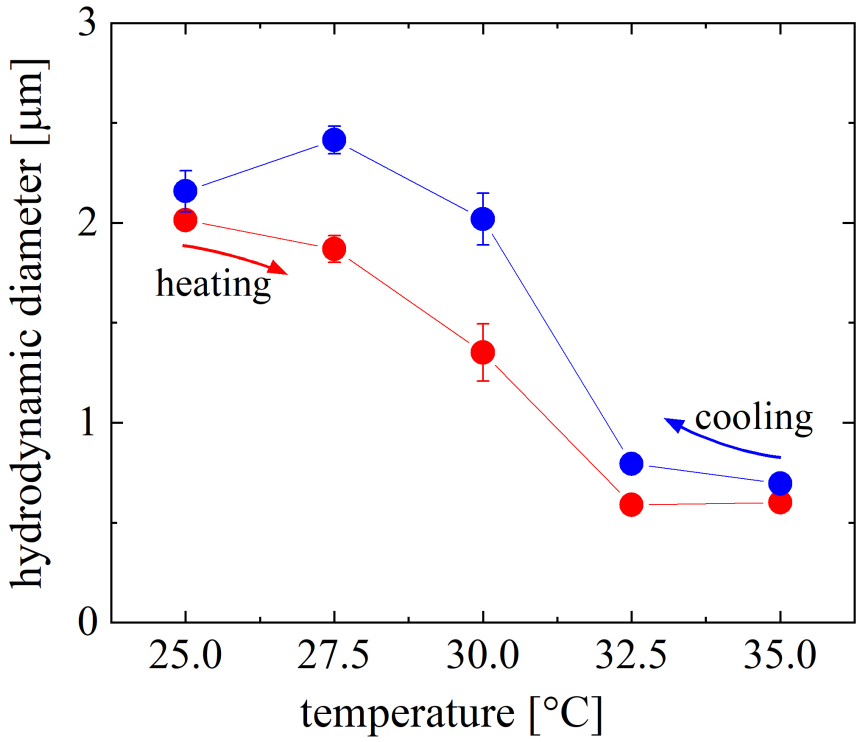

Figure 7.1: Hydrodynamic diameter of self-crosslinked pure pNIPAM microgels, measured using dynamic light scattering, as a function of temperature. The "phase transition" in pNIPAM across the LCST leads to the sharp change in the volume of the microgel particles (data courtesy: Jin Gu Kang and Paul Braun).

7.3.2 Pure Microgel Suspension Rheology

The linear elastic shear modulus G' for pure microgel suspensions at various concentrations is shown in Fig. 7.2 as temperature is varied from 25 to $35°$C. At all concentrations, the response is predominantly elastic ($G' > G''$) in the probed temperature range at 1 rad/s (G'' data is shown in Appendix Fig. E.3). At low temperature, G' monotonically increases with suspension concentration, owing to an increasing volume fraction of swollen microgels which are known to interact via repulsive pair potentials [199, 194, 192]. A linear concentration dependence ($G' \sim c_P$) is expected in the ultra-high volume fraction soft jamming regime and a stronger concentration dependence has been observed below it in the glassy fluid regime in earlier studies on similar microgel suspensions [154, 199, 160]. The observed scaling of ($G' \sim c_P^{2.65}$) in the glassy regime is slightly lower than other microgel systems with different chemistry and synthesis procedures where power laws ranging from 4-12 have been observed [154, 199, 160].The power law dependence in the glassy fluid regime does not follow a universal scaling with concentration since it is dependent on microgel softness, chemistry, synthesis, etc. [154, 199, 160]. Based on the concentration dependence of G' (Fig. 7.3), we conclude that the explored concentration regime of pure microgels is in the glassy fluid regime, well below the soft jamming crossover. The origin of elasticity in such suspensions is associated with a kinetically arrested/caged state of microgels which do not relax on the observation time scales [163, 199].

With increase in temperature (but below the LCST), the microgels undergo continuous and modest de-swelling, reducing the effective volume fraction of the suspension which results in a lower G'. Across the LCST ($\sim 32°$C), the microgels shrink abruptly accompanied by the emergence of attractive interactions between the microgels which leads to the formation of local aggregates of de-swollen particles. We observe a non-monotonic trend in G' versus concentration at temperatures close to the LCST. This may be attributable to the inhomogeneity in the suspension that has low effective volume fraction of aggregated de-swollen microgels. The repeat measurements are shown in Appendix E.4. A key point to note is that G' drops by nearly an order of magnitude as the temperature is increased from $25 - 35°$C in the glassy fluid regime. Unlike previously published literature on pNIPAM based microgel suspensions, which stiffen across the LCST due to attractive interactions between the microgels [203], we observe no re-emergent stiffening in G' above LCST. We attribute this lack of stiffening to the lower concentrations (well below soft jamming) and the different chemistry of the microgels used in the current work.

A major challenge in working with suspensions of soft microgels is determining the effective volume fraction. The compressible microgels can swell/de-swell depending on osmotic pressure which is as a function of concentration. We do not have *a priori* informa-

tion about the size of microgels as a function of varying concentration or osmotic pressure. Hence, to estimate the volume fraction of microgel suspensions at low temperature, we adopt an approach suggested by recent experiments on similar microgels [178]. In the dilute low concentration regime, the microgel size is fixed and one can define an effective (hydrodynamic) volume fraction by determining an intrinsic viscosity $[\eta]$ from the steady shear experiments with very dilute suspensions (Appendix E.10). From this, we obtain a volume fraction $\phi = 0.22$ at $c_p = 0.25$ wt%. In an intermediate concentration regime of $c_{p1} < c_p < c_{p2}$ per Fig. 5.6, the microgels begin to de-swell due to steric repulsions between particles, in a manner that experiments suggest is initially weak. Crudely, experimental data (of microgel radius R) in the latter regime can be modeled as a power law of $R \sim c_p^{-1/6}$, implying an effective volume fraction that scales as $\phi\, c_p^{1/2}$. Beyond some "high enough" $c_p > c_{p2}$, one expects that the more fuzzy "corona" part of the microgel is largely squeezed out, leaving a dense core which at yet higher concentration undergoes isotropic compression in the sense that $R \sim c_p^{-1/3}$, as again suggested in literature [178]. This leads to $\phi \sim c_p^0$ where the linear growth in microgel concentration is perfectly compensated by their shrinking size. Ultimately beyond an even higher concentration c_{p3}, the internal concentration of microgels presumably saturates at a maximum value similar to that of a collapsed globule with radius $R_{collapsed}$. In our experiments we always remain below, i.e. in the glassy fluid regime. Hence, for the range of concentration $0.3 - 3$ wt% that we have used in preparing composites, the volume fraction at $25°$C varies from $\phi = 0.28 - 0.78$ as shown in Fig. 7.3. We can also estimate an effective volume fraction (a lower bound) at temperatures beyond the LCST assuming all the microgels shrink to the same collapsed size as indicated by the DLS experiments. The volume fraction in the deswollen state $35°C$ varies from $\phi = 0.012 - 0.072$.

7.3.3 Pure Fibrin Hydrogel Rheology

Fibrinogen polymerizes into a polymer network of fibrin filaments in the presence of thrombin following a cascade of events [236]. Pure fibrin networks have a viscoelastic solid-like response in the linear response regime. The concentration dependence of the linear elastic shear modulus G_0 (Fig. 7.5) follows a power-law dependence on the concentration of fibrinogen; here we observe $G' \sim c_f^{2.1\pm0.1}$. The power-law exponent is close to the theoretical scaling exponent of 2.2 for semiflexible polymer networks at low-strains due to an entropic single fiber stress storage [74, 237]. Fig. 7.5 shows the nonlinear shear strain-stiffening response of pure fibrin networks at various concentrations (at $25°$C) when probed with an oscillatory strain of increasing strain amplitude . The stiffening, indicated by the increasing

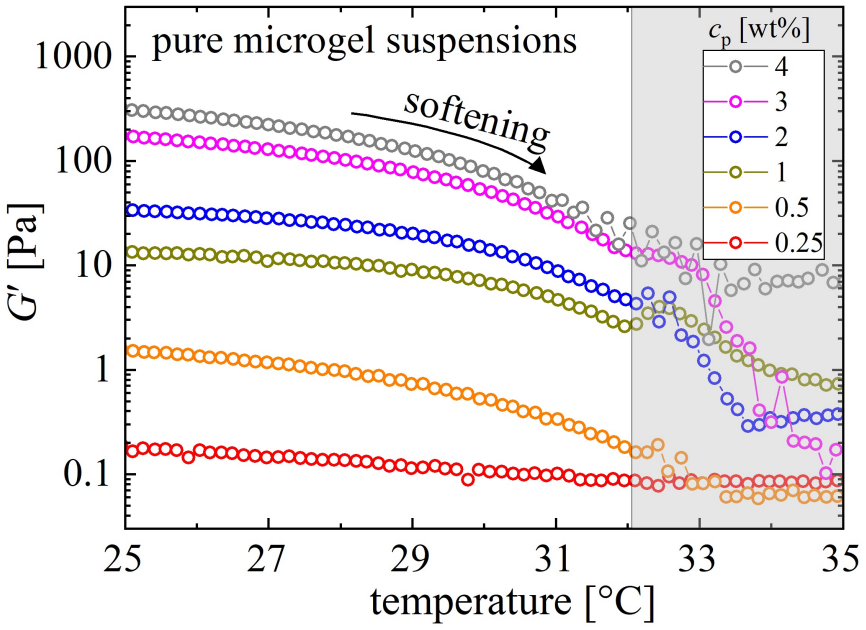

Figure 7.2: At all concentrations of pure pNIPAM suspensions, G' decreases with temperature. G' values above the LCST (shaded region) show a non-monotonic trend with concentration. This is attributed to the sample inhomogeneity above the LCST (repeat measurements in Appendix Fig. E.4).

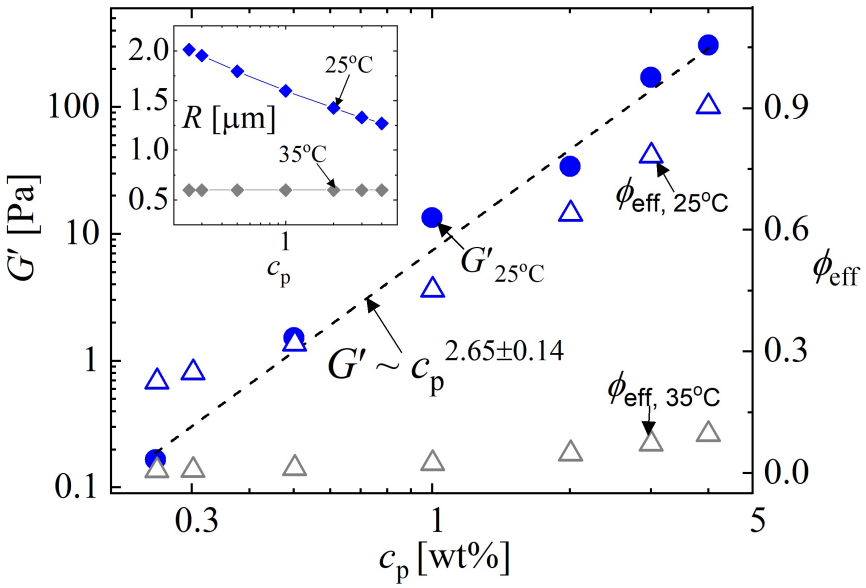

Figure 7.3: Concentration dependence of G' of pure pNIPAM suspensions at low temperature, 25°C, shows a strong apparent power-law (best fit shown by the dashed black line) which is indicative of concentrations in the glassy fluid regime before the soft jamming crossover. For context, the estimated effective volume fraction ϕ and particle radius R is shown for both low and high temperature (see right vertical axis).

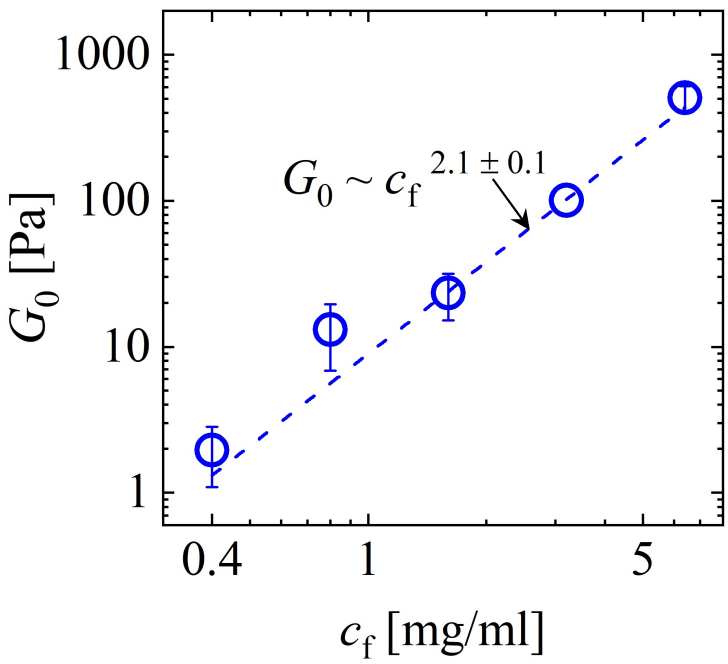

Figure 7.4: The concentration dependence of the linear elastic modulus G_0 agrees closely with the theoretical predictions for semiflexible polymer networks.

first-harmonic (average) elastic modulus, is most apparent when the imposed shear strain is greater than 10-20 %. This is attributable to the nonlinear force displacement relationship of the individual strands as their thermal slack is reduced with external deformation [74, 237, 238]. Alternative explanations for such strain stiffening also exist in the literature based on the non affine network rearrangements in the network [239]. The average shear elastic modulus at the maximum strain before the network breaks irreversibly is roughly 10 times higher than the linear elastic modulus As a function of increasing temperature, the pure fibrin networks. The average shear elastic modulus at the maximum strain before the network breaks irreversibly is roughly 10 times higher than the linear elastic modulus. As a function of increasing temperature, the pure fibrin networks show a very weak softening at all concentrations used here (Fig. E.5).

7.3.4 Fibrin-Microgel Composite Rheology

Figure 4 demonstrates that fibrin networks readily form in the presence of these microgel colloidal particles at the concentrations studied (Appendix Fig. E.6 for all other compositions). Polymerizing fibrinogen in the presence of colloidal particles is a complex process since colloids can disrupt network formation [224]. We observe similar formation

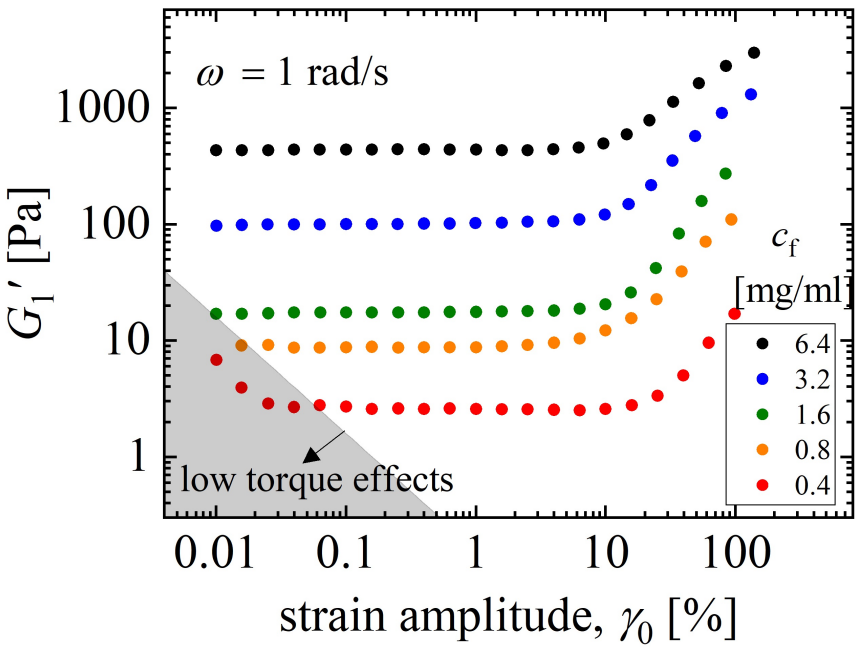

Figure 7.5: Strain stiffening response of the oscillatory first-harmonic elastic modulus (G_1') (filled symbols) is prominent when shear strains exceed 10-20 %. The normal force measurements for these experiments is provided in Appendix Fig. E.5.

timescales even in the presence of microgel particles and the linear moduli approach a constant plateau at long times, indicating that all the available fibrinogen has been converted into fibrin. Composites are predominantly elastic ($G' > G''$) with an elastic modulus similar to that of pure fibrin (c.f. Fig. 7.4).

The particles do tend to slightly increase the elastic modulus of the composite, though the trend is non-monotonic and seemingly unsystematic. It is striking that the effects are so small, considering the high effective volume fraction ϕ of the microgel particles (from Fig. 7.3, for $c_p > 1$ wt%,$\phi > 45$ %,). In traditional polymer-colloid composites involving 'hard' colloidal inclusions in a flexible polymer network, the mechanical stiffness is more dramatically increased by the reinforcement effects from inclusions [240]. We attribute the weaker inclusion effects here to several distinct features of the fibrin composites. Foremost is the fact that fibrin networks have large pore sizes compared to the inclusion, i.e. pore size is on order of microns, similar to the diameter of the microgel particles, unlike in flexible polymer composites where the mesh size is typically much smaller than the inclusion. Additionally, the preparation protocol involves gelling a premixed solution of fibrinogen and microgels. We expect some fraction of fibrinogen may get adsorbed on the particles and becomes unavailable to form the fibrin network as indicated in one previous work [224]. Furthermore, the salt concentration in the hydrogel composite will vary as a function of

the microgel concentration since the microgel stock solution was prepared with deionized water. The architecture and mechanics of fibrin networks are known to depend on salt concentration [236]. For example, with microgel concentration varying from $0 - 3$ wt%, the Ca^{2+} concentration in the composite will decrease from 20-6.4 mM. For pure fibrin networks, it has been shown [236] that decreasing salt concentration in this range will tend to decrease the mesh size, decrease the fiber diameter, increase the fiber and branch density, and increase the elastic modulus by about a factor of two. For our composites, the smaller mesh size would serve to improve trapping of the microgel particles and a higher fibrin network modulus may partly contribute to the composite elastic modulus increasing by a factor of 2-3 with increased microgel particle loading (Fig. 7.6). Finally, the microgels are soft and very lightly crosslinked, hence there can be a possible modification of microgel coronas due to the fibrin network [229] and fibrin polymer chains may penetrate the microgel corona. We note that some of the aforementioned features, can be eliminated in experiments by a better chemical control of the species, which will a subject of the future work. Any further investigation into such very complex effects is beyond the scope of this work, but it is clear from Fig. 7.6 and Appendix Fig. E.6 that composites successfully form and at fixed temperature, the microgel inclusions have only a slight effect on the elastic modulus.

Increasing the temperature shrinks the microgel particles, decreasing their effective volume fraction. But in qualitative contrast to standard composites, this results in a striking increase of the overall elastic stiffness of the composite. Figure 7.7 shows the linear viscoelastic moduli and how they respond to temperature cycling. Two extreme compositions are shown in Fig. 7.7, a high concentration of both fibrin and microgel ($c_f = 6.4$ mg/ml, $c_p = 3$ wt% microgels) and a low concentration of both fibrin and microgel ($c_f = 0.4$ mg/ml, $c_p = 0.5$ wt% microgels). Thrombin concentration is held fixed at 0.5 U/ml for both the composites. Although the fibrin concentration (and hence the elasticity) is different in both the cases, the temperature-dependent response is very similar. As the temperature is increased at a rate of 1°C/min, initially at $25 - 28^{\circ}$C a weak decrease in the linear shear moduli (G', G'') is observed, followed by a sharp increase in the linear moduli within a narrow temperature range of $28 - 32^{\circ}$C around the microgel LCST. Further increase in temperature $32 - 35^{\circ}$C leads to a weak increase in the moduli. The response is reversible in the cooling cycle accompanied by a hysteresis (Appendix Fig. E.9). The latter can be attributed to hysteresis in the deswelling/swelling of pure microgels during heating/cooling cycles (Fig. 7.1).

The temperature-dependent response of the composite is contrary to that observed for pure microgel suspensions (Fig. 7.2) and pure fibrin network, where monotonically de-

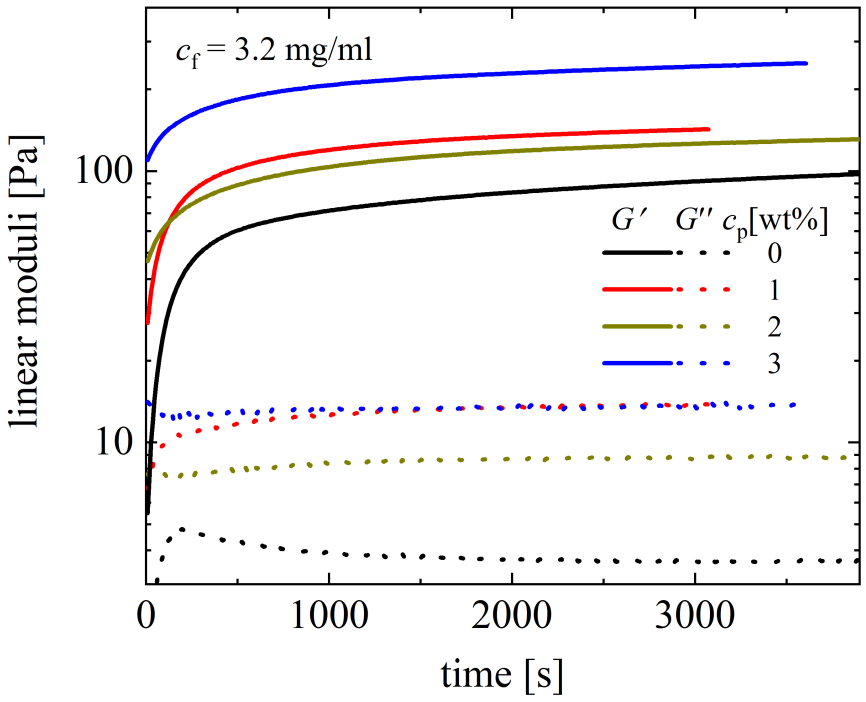

Figure 7.6: Composite formation by polymerizing fibrinogen into a fibrin network in the presence of pNIPAM microgel suspensions at different particle loading c_p [wt%]. Evolution of viscoelastic moduli show weak effects from the pNIPAM that are non-monotonic but tend to increase the overall linear moduli. (see Appendix Fig. E.6 for all other compositions)

creases with increasing temperature. The normal force variation during the heating/cooling cycles is also shown in Fig. 7.7. No clear trend for a composite with 0.4 mg/ml fibrin is seen, with roughly constant, i.e. changes are less than the instrument resolution of 0.05 N (i.e. a resolution of 300 Pa average normal stress on the bounding surface, $\sigma_N \approx F_N/\pi r^2$, r being the radius of the sample/plate). However, for the higher-concentration composite ($c_f = 6.4$ mg/ml) we observe a measurable during the heating and cooling cycles. The normal force acts to pull down the upper rheometer plate (gap is kept fixed) during the heating cycle as temperature crosses the LCST, up to $F_N = -0.11$ N (700 Pa), while during the cooling cycle this normal force vanishes. This is likely a consequence of decreasing volume of microgels as they shrink, resulting in a tensile force within the network and a downward force on the upper plate.

Beyond the LCST, temperature-induced stiffening is observed for all compositions studied. Fig. 7.8 shows the effect of increasing microgel concentration for the two extremes of high and low fibrin concentration (data for all compositions is given in Appendix Figs. E.7 and E.8, only the second heating cycle is shown for comparison. Increasing the concentration of microgel particles increases the relative stiffening of the linear moduli. We also observe a similar response in G'' but for all cases the response is predominantly elastic at all temperatures, i.e. $G' > G''$. Similar observations were made for other fibrin concentrations ($c_f = 0.8, 1.6, 3.2$ mg/ml) (Appendix Figs. E.7 and E.8). The mild softening of the modulus in the range $25 - 28°$C appears to follow the same trend as the softening of the shear modulus of pure microgel suspensions. However, this effect is not noticeable when the modulus of pure fibrin is significantly higher than that of pure microgel suspensions. The weak stiffening of the modulus in the range of $32 - 35°$C is directly correlated to the weak decrease in the microgel size.

To compare the thermoresponsive stiffening across the concentrations, we plot in Fig. 7.9 the stiffening observed in all cases as the dimensionless ratio, $G'_{35°C}/G'_{min}$. Here, G'_{min} is the minimum value of the composite elastic modulus before it begins to stiffen (indicated in Fig. 7.8 B), and $G'_{35°C}$ is the modulus at $35°C$. Some general trends are evident from Fig. 7.9. A higher concentration of microgel particles leads to a higher stiffening ratio. The stiffening in terms of absolute difference is even more dramatic, as shown in the inset of Fig. 7.9. The fibrin concentration also plays a significant role. The absolute changes are larger at higher c_f, i.e. for stiffer networks. But, interestingly, the relative changes (main Fig. 7.9) are larger at lower c_f , i.e. softer networks have more dramatic relative changes in stiffness. A wide range of baseline modulus is covered by these compositions since the linear modulus of the fibrin network scales sensitively with concentration ($G_0 \sim c_f^{2.1}$, Fig. 7.4).

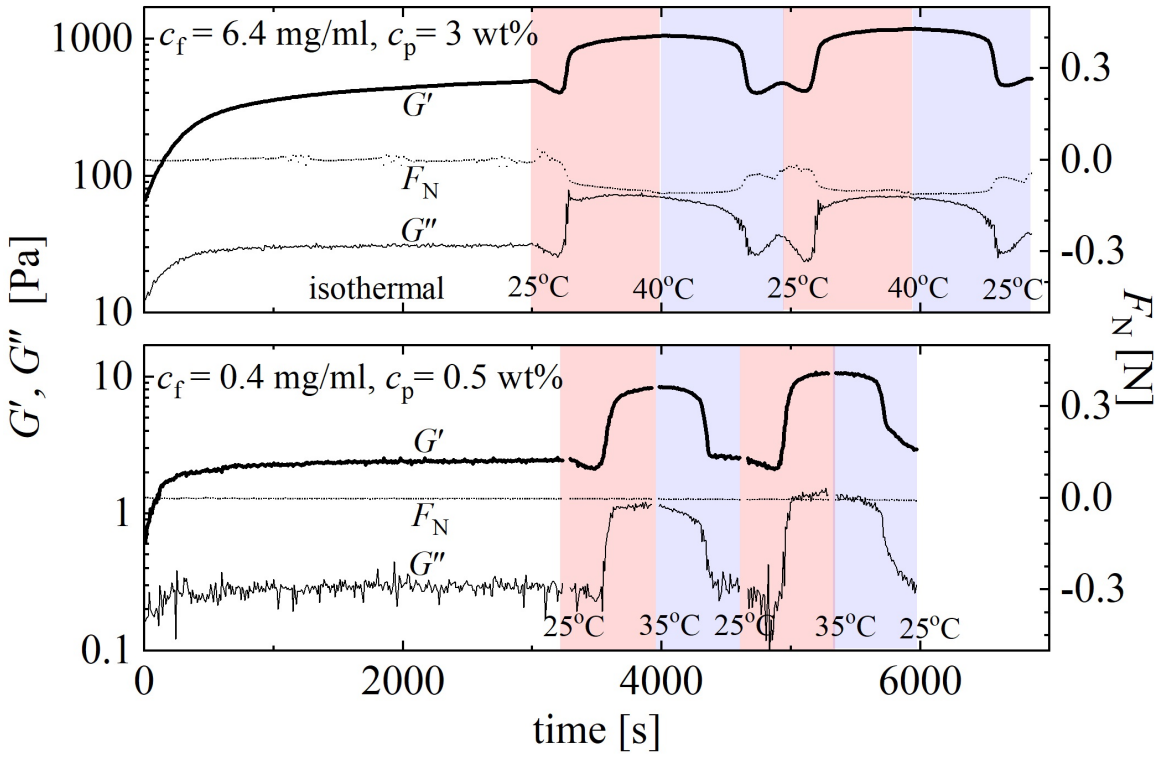

Figure 7.7: Dependence of composite rheology on temperature. The linear moduli and normal force for two different compositions of composites: 6.4 mg/ml fibrin with 3 wt% microgels (top) and 0.4 mg/ml fibrin with 0.5 wt% microgels (bottom) are shown. The composite is prepared by polymerizing fibrin in the microgel suspension at a fixed temperature 25°C followed by the application of repeated temperature increase (shaded red) and decrease (shaded blue) at 1°C/min to probe the temperature dependence. The linear moduli show reversible stiffening as the temperature is raised above the LCST (strain amplitude 1 %, angular frequency 1 rad/s).

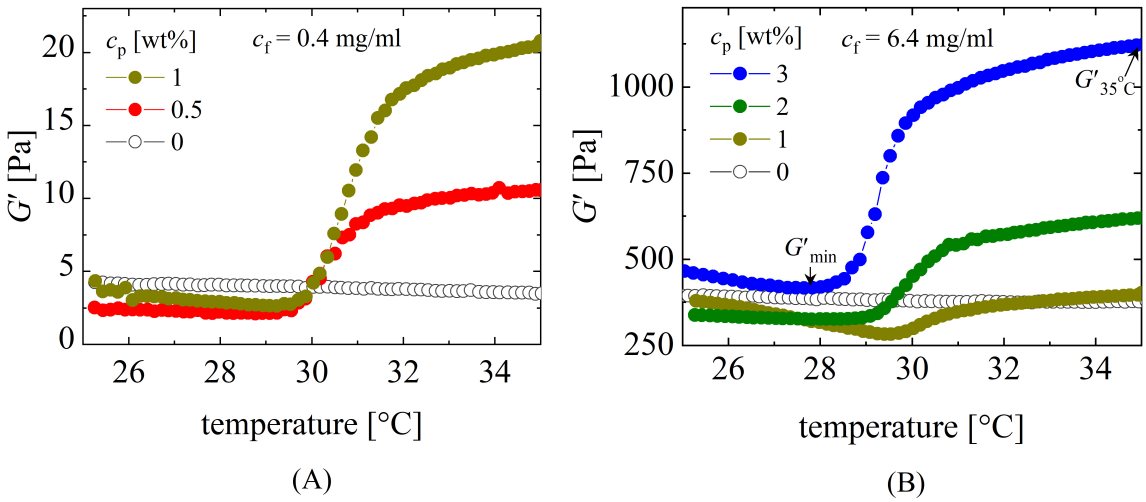

Figure 7.8: Temperature dependence of the storage modulus of pNIPAM-fibrin composites. (A) The concentration of fibrinogen and thrombin is held constant at 0.4 mg/ml and 0.5 U/ml, respectively, while the concentration of pNIPAM microgels is varied. Varying the concentration of pNIPAM microgels stiffens the network as the temperature is increased above LCST. (B) Similar data for 6.4 mg/ml fibrin and 0.5 U/ml thrombin. Note that only the second temperature ramp-up cycle is shown in the figures. Data for all other compositions is given in Appendix Figs. E.7, and repeat measurements at selected compositions are shown in Appendix Figs. E.8.

We used confocal imaging to investigate the structure of the fibrin matrix in the composites and test our assumption that microgel particles are shrinking within the network at elevated temperature. Fig. 7.10 shows the confocal images of the composite at 25 and 35°C. Qualitatively, it appears that the presence of microgels does not interfere with the formation of the fibrous network, which appears similar to that of pure fibrin hydrogels. The volume fraction of microgels decreases as the sample is heated from 25 to 35°C as is apparent by the decreasing intensity of emission from tagged microgel particles, consistent with microgel particle shrinking at elevated temperatures. However, no apparent change can be observed in the fibrous network visually between 25 to 35°C. In contrast to the pure microgel suspensions, where we observed the aggregation of particles above the LCST, such behavior is not apparent when the particles are in the fibrin matrix. This is expected since the de-swollen size of particles is similar to that of fibrin mesh which perhaps hinders the particle aggregation. We do not make quantitative comparisons of the network topology features with and without the microgels.

Fig. 7.11 verifies that strain-stiffening is retained in the composites, a property native to pure fibrin (Fig. 7.5) which we hypothesize may play a central role in the temperature-induced stiffening caused by de-swelling microgel particles. Large-amplitude oscillatory

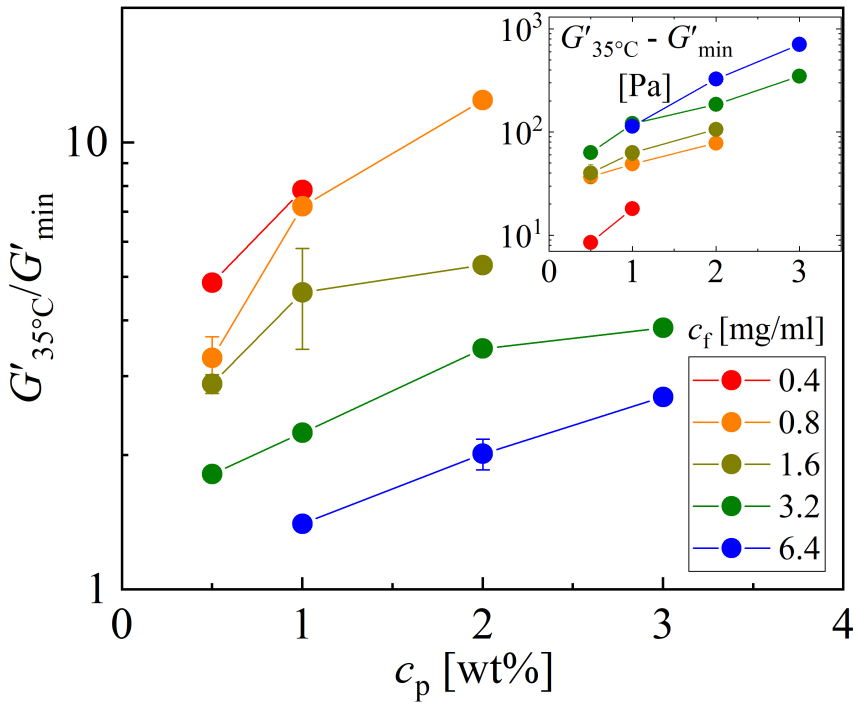

Figure 7.9: Stiffening ratio (relative modulus change) for all fibrin concentrations c_f plotted as a function of microgel content c_p in the composites. Inset shows absolute change in modulus for the same compositions. (Raw data for $c_f = 0.4, 6.4$ mg/ml in Fig. 7.8; all other raw data in Appendix Figs. E.7 and E.8.)

shear (LAOS) results in Fig. 7.11 are shown in terms of the first-harmonic elastic modulus (representing the average energy storage during the deformation [241]), as the shear strain amplitude is varied at 25 and 35°C for three different compositions of the composite. At 25°C, all three composites show strain-stiffening behavior similar to pure fibrin (Fig. 7.5). At 35°C, the composites still show strain stiffening, but it is less dramatic. The reason is associated with a higher initial plateau modulus in the linear regime, but a similar final elastic modulus at the largest imposed strain. The retention of strain-stiffening features in the fibrin matrix below and above the LCST suggest that the large deformation rheological response in the composite is being dominated by fibrin, i.e. the presence of microgels during the fibrin polymerization may not affect the underlying mechanism of strain-stiffening of the network. However, as mentioned earlier, the salt concentration in the composites is different than the pure fibrin network, which may lead to architectural/topological differences between the composite fibrin networks and pure fibrin networks [236]. Regardless, the thermoresponsive stiffening is still observed at all compositions, and may be linked to the underlying strain-stiffening of fibers, an idea that will be explored in the discussions.

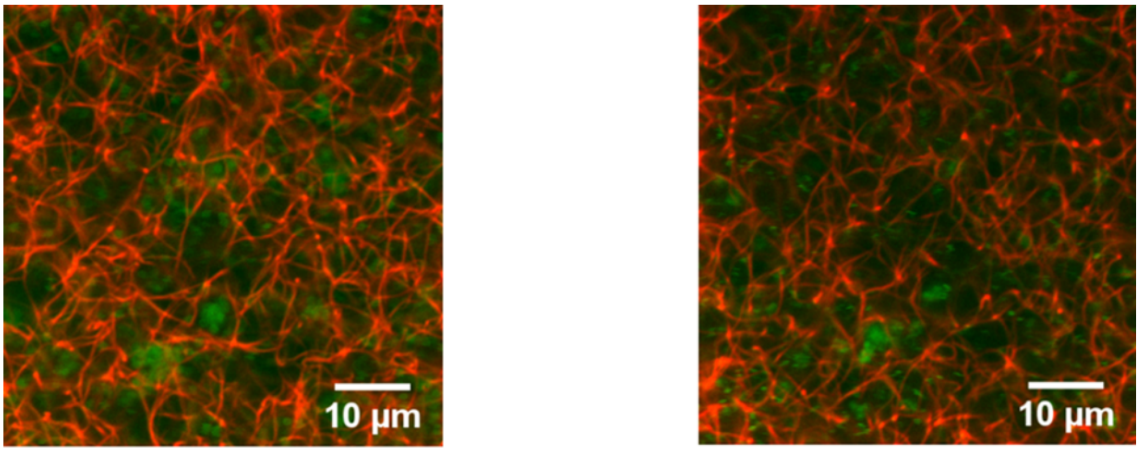

(A) T = 25°C (B) T = 35°C

Figure 7.10: Confocal images of fibrin-microgel composite at (A) T = 25°C and (B) T = 35°C . The fibrin fibers (tagged red) and the microgels (tagged green) have a concentration of $c_f = 3.5$ mg/ml and $c_P = 3$ wt%, respectively. Above the LCST(~ 32°C), de-swelling of microgels can be observed.

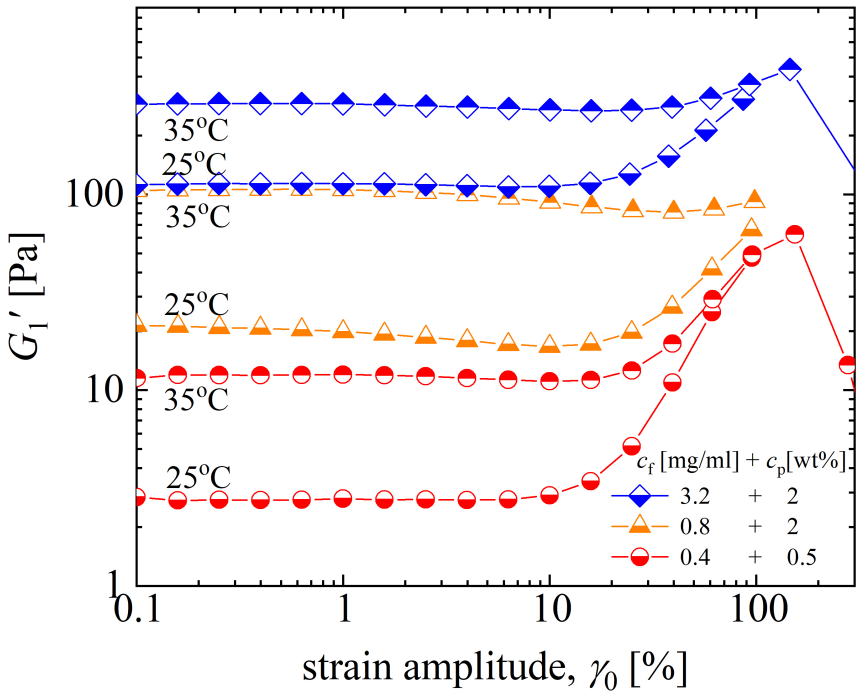

Figure 7.11: Nonlinear response of fibrin-microgel composites at selected compositions, each at low and high temperature (compared to LCST). Both below and above the LCST, the composites retain a strain-stiffening response similar to pure fibrin hydrogel in Fig. 7.5.

7.4 Discussion and Theoretical Modeling

Although soft microgels have been previously incorporated into fibrous matrices to modulate properties (e.g. transport [229] and mechanical [242, 243, 244]), the thermoresponsive sensitivity we report here is unique. While the individual components mechanically soften when the temperature is raised from $25 - 35°$C, the composites show significant stiffening. The fundamental question then arises as to the physical mechanism. There are various speculative hypotheses in the literature that might be relevant to our observations, although the problem is very complicated for many reasons including the crucial aspect that the precise nature of the coupling between the components is not well understood. Prior work on pNIPAM microgel-flexible polymer composites attributed the thermosensitive response to the transition of microgels from soft to hard fillers, [244] and the ability to microgels to act as additional crosslinking. Such continuum ideas are unemployable to our system since the microgels are relatively soft and even in their de-swollen state are not large compared to the mechanical length scale (polymer mesh) of the matrix. Nevertheless, if we adopt this perspective, then based on our volume fraction estimates for the range of microgel concentration studied (above the LCST, only $\phi_P = 0.012 - 0.07$) one predicts G_c/G_m is only $\sim (1.03 - 1.17)$, far smaller than we observe. We therefore conclude that the stiffening mechanism observed in our experiments is qualitatively different from that proposed for previously studied systems [243, 244].

Our limited goal in this section is to formulate speculative, but we think plausible, microscopic physical models for the stiffening mechanism. Two mechanisms are considered, both based on the idea of microgel-induced modification of the network beyond the LCST. We hypothesize that microgels de-swell at high temperatures in the composite as they do in dilute solution, and a strong fibrin-microgel attraction (of hydrophobic or other physicochemical origin which does not break on the relevant experimental time scale) allows the microgel shrinking to pull on the surrounding network. This induces a structural change in the fibrous mesh surrounding the de-swollen microgels and results in an overall stiffening of the composite. Fibrin adsorption on various hydrophobic surfaces has been demonstrated in the past [245, 246], and we hypothesize for the current system that the exposed hydrophobic domains in pNIPAM chains (beyond the LCST) provide sites for the assumed attractions [246]. We note that the effective interactions between the fibrin and pNIPAM microgels in this work are unknown, and a precise knowledge and control over such interactions may enable several other interesting paradigms.

The problem, in principle, could be approached from an equilibrium thermodynamics perspective where the total composite free energy is minimized. The latter involves the

competing effects of distortion of the fibrous mesh, polymer-microgel interactions, and microgel deswelling. But quantification of these factors requires knowledge of the details of connectivity and interactions between the fibrous mesh and microgel, the nature of junctions in the fibrous mesh (chemical crosslinks or physical entanglements), and free energy functionals for the fibrin network and microgels. Such an analysis is beyond the scope of current work.

We construct two simple physical models which differ with regard to how the network is hypothesized to change when microgels shrink: (i) an effectively stretched polymer network model (fixed junctions), and (ii) an adjusted mesh model (mobile junctions). In both cases, the de-swelling of microgel particles will generate contractile forces in the fibrous network to which they are attached. However, the effects of such contractile force is realized differently in the two models, and thus the underlying physical origins of stiffening are different. Based on fibrin networks that we have used in the experiments, we expect the first model with fixed junctions (crosslinked network) to describe our fibrin-based system, since our preparation protocol is known to create fixed junctions [236, 233, 218]. The second model (adjusted mesh model) is included as a plausible scenario for semiflexible networks where physical entanglements are important, such as uncrosslinked fibrin, actin, or carbon nanotubes, showing the possible extension of our work to these broader scenarios.

7.4.1 Stretched Network Model (Fixed Junctions)

The observation of a negative pull (normal force) on the upper rheometer plate above the LCST indicates that a net tensile stress exists in this state. We hypothesize that microgel deswelling results in a microscopic stress in the fibers which manifests itself as a bulk contractile pull in the network. Such microscopic deformations may be responsible for the stiffened composite response above the LCST. For example, the average value of the tensile (normal) stress $\tau_N \approx 700$ Pa for the sample with $c_f = 6.4$ mg/ml and $c_P = 3$ wt% (from Fig. 7.7) is significantly higher than the average shear stress at the onset of nonlinear strain stiffening of the network ($\tau_c \approx 50$ Pa, obtained by $\tau_c \approx G_0\gamma_c$, where γ_c is the characteristic strain at which the shear response begins to show measurable nonlinearity, in this case $\gamma_c \approx 0.1$ from Fig. 7.5). However, a direct comparison cannot be made since these measured normal stresses arise from different modes of deformation. Further, the normal stresses at other composite compositions were below the instrument measuring limit, and hence cannot be reliably resolved.

We note that the hypothesis of microscopic internal strain induced stiffening was invoked

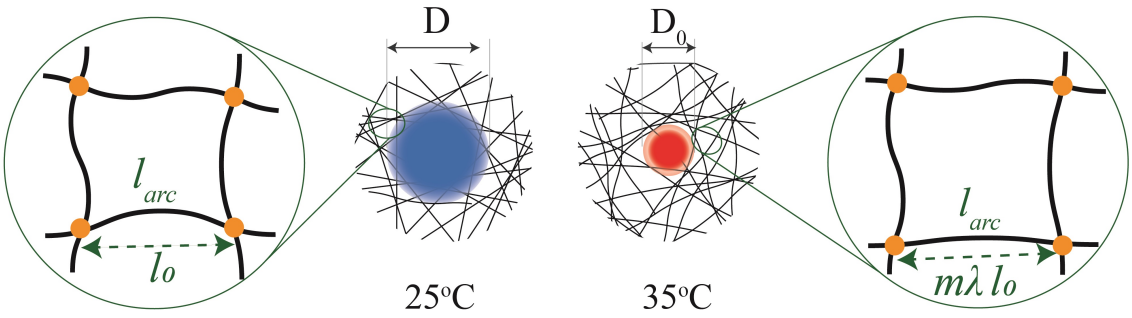

Figure 7.12: Effectively stretched polymer network model. At low temperature (T < LCST), the fibrin network is polymerized around the swollen microgel. The sketch of a single two dimensional lattice shows the key length scales in the network: the contour length l_{arc} of the polymer in between the nodes/crosslinks, and the end-to-end distance between the crosslinks. When the temperature is raised above the LCST of the microgel, its size abruptly shrinks to and this imposes a strain on the attached fibrin network. The consequence of this strain is in a mean-field-like sense is schematically shown in the two dimensional lattice sketch, where the end-to-end distance changes to $\lambda_f l_0$ but l_{arc} remains constant as a result of the inextensibility assumption.

in recent work involving multiaxial deformation of fibrin networks [247]. These workers hypothesized that external uniaxial extension applied to the network removes undulations in some of the fibers (along with changing the orientation of fibers from the undeformed state) and results in a higher shear modulus, whereas uniaxial compression induces a higher level of undulations and buckling, resulting in a softening response of the network. Deformation fields in that work are qualitatively different from our experiments. In the case of our fibrin-microgel composite, the deformation fields are spatially inhomogeneous on the scale of the mesh surrounding the microgel particles. In the simplistic scenario of a fibrous mesh bound to a deswelling microgel, we expect the fibers aligned in the radial direction experience a stretch and fibers aligned orthogonal experience a compression. The bulk network response will thus have two contrasting contributions: a stiffening response from the stretched fibers and a softening response from the compressed fibers. From our experimental observations, the mechanical response from stiffened fibers dominates the bulk response. The nonlinear shear response of our fibrin-microgel composites (Fig. 7.11) shows similarities to fibrin networks with imposed uniaxial extension [247]. In the pre-stressed state (here above LCST, in the prior work for extensional pre-strain), the onset of stiffening shifts to a higher value of applied shear strain in all the cases probed. Thus, we suspect similar underlying origins of the induced stiffening, i.e. the nonlinear deformation (strain-stiffening) response of individual fibers.

To test if such a hypothesis is physically consistent with our experimental observations,

we adopt a constitutive model for semiflexible polymer networks from the literature. The polymer network is assumed to have fixed junctions (e.g., effective chemically crosslinked at the branch points or nodes) consistent with the observations from the literature where the fibrin networks were formed using similar preparation protocols to the one followed in the current work [236, 233, 218]. The Euclidean distance between the nodes, l, is different than the fiber arc length, l_{arc}, such that the normalized end-to-end distance, $x = l/l_{arc} < 1$ in the reference state. Adopting a mean-field-like approach to model the fiber inextensibility, an analytical form for the free energy of a semiflexible polymer chain as a function x has been previously derived [220]

$$u_{fiber} = k_B T \pi^2 \nu (1 - x^2) + \frac{k_B T}{\pi \nu (1 - x^2)} \tag{7.1}$$

where k_B is Boltzmann's constant, $\nu = \kappa / 2 K_B T L_c$ is a dimensionless stiffness parameter with bending rigidity κ defined as and $l_p = 32\,\mu$m is the fiber persistence length assuming that the fibers in the network are composed of many protofibrils that are held together by molecular bonds [236, 218] (a precise value of l_p depends on the fibrinogen, thrombin, and salt concentration but for the purpose of simplicity of analysis, we assume a fixed value at all concentrations). The two terms on the right hand side of the Eq. 7.1 represent the contributions from fiber bending energy and entropy, respectively. The force-displacement $(f - x)$ relationship for such a fiber derived from Eq. 7.1 diverges as $f \sim (1 - x)^{-2}$ as $x \to 1$, a result of finite extensibility of a fiber pulled taut when $l = l_{arc}$. Eq. 7.1 has been previously employed [220, 221, 238] to constitutively model the nonlinear shear elastic response of semiflexible polymer networks assuming a 3-chain and an 8-chain network model. The advantage of using cubic lattice models is the ability to obtain analytic expressions for the shear stress. We use a 3-chain model since it captures some salient features of semiflexible polymer networks such as negative normal stresses in shear in addition to generic strain-stiffening effects. We refer the readers to previously published work for details of the models [221, 238]. Here, we directly employ the constitutive relation for the nominal linear shear modulus G in the limit of zero shear strain for a 3-chain network model given by

$$G(x, \nu) = \frac{2}{3} n_f k_B T x^2 \left[\frac{1 - x^4}{\nu \pi [1 - 2x^2 + x^4]^2} - \nu \pi^2 \right] \tag{7.2}$$

where n_f is the density of crosslinked chains. Eq. 7.2 was derived for a pure semiflexible polymer network in which each mesh/lattice cell is deformed affinely with an external shear strain. The deformation field in the network resulting from a de-swelling microgel is more

complex and highly dependent on the geometry and nature of fiber-microgel contacts. A quantification of such inhomogeneous deformation of the mesh is possible in principle but is beyond the scope of the current work.

To simplify the analysis, we therefore adopt a mean field like approach. Based on our experimental observations of a net stiffening response, we assume that microgel particle deswelling results in the entire fibrous network changing to an "effectively stretched" state. In the stretched state some of the thermal undulations in the fibers are removed compared to their conformations below the LCST, i.e. $x > x_0$, where x_0 is the fiber normalized end-to-end distance for the reference state ($25°$C). As a result we expect the individual fiber response to stiffen, which then results in bulk network stiffening. Our approach assumes that the effective stretch in the entire network is uniform regardless of the spatial orientation and location of fibers relative to the microgel. The effective stretch λ is defined from the change in the volume of the fibrous network compared to a reference state

$$\lambda^3 = \frac{V}{V_0}. \tag{7.3}$$

We will consider the fibrin network at $25°$C (initial state) and $35°$C (final state). The volume of the fibrous network is the fraction of the total volume of the composite V_t based on the theoretical effective volume fraction ϕ_P of microgels, $V = (1 - \phi_P)V_t$.

The theoretical microgel de-swelling may not exactly transfer to a volume increase of the fibrin phase due to, for example, imperfect adhesive contact between microgels and fibrin, or a good adhesive contact for which the stiffness of the fibers resists microgel de-swelling. We therefore introduce a prefactor m to map the theoretical to the actual volume increase of the fibrin phase. For the case of perfect binding and complete de-swelling, $m = 1$, whereas the other extreme applies if the fibrin network volume is unchanged. For realistic scenarios we expect $0 < m < 1$. Hence, we can write

$$\lambda_f = m\lambda = m\left(\frac{1 - \phi_{P,35°C}}{1 - \phi_{P,25°C}}\right) \tag{7.4}$$

where $\phi_{P,25°C}$ and $\phi_{P,35°C}$ are the theoretical effective microgel volume fractions at 25 and $35°$C respectively. Since the free energy contribution from fibrin is highly nonlinear Eq. 7.1 and strongly depends on λ, it is reasonable to expect beyond a certain value of λ that the free energy cost of deforming the fibrin network becomes larger than the lowering of free energy associated with full deswelling of the microgels. Hence, in equilibrium the microgel deswelling may be limited by the deformation of attached fibrin matrix and the particles would not achieve exactly the same size reduction as in dilute suspension, and thus $\lambda_f < \lambda$.

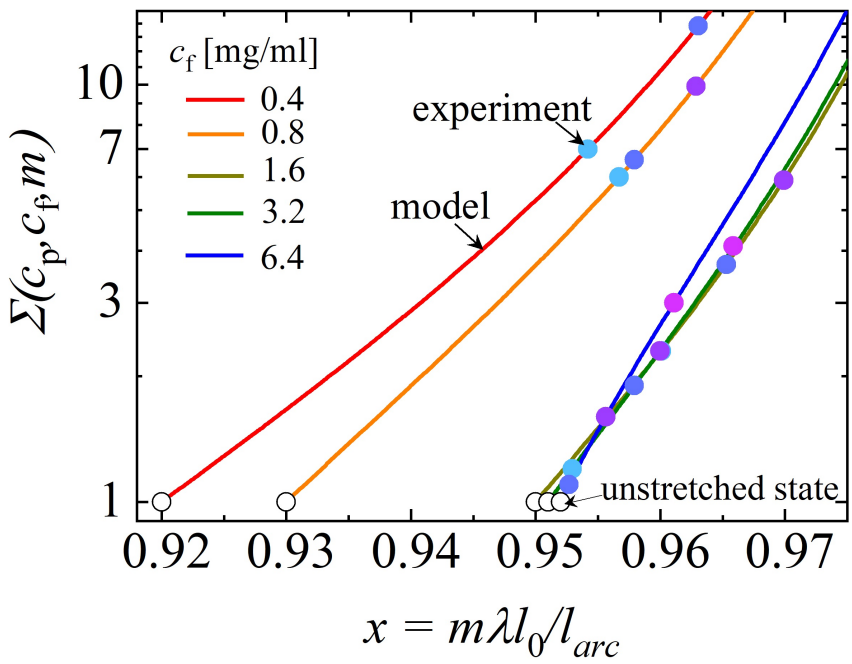

Figure 7.13: Model predictions (curves) of the linear shear modulus normalized by its values at $x = x_0$. The finite extensibility of the fibers between fixed junctions leads to a drastic increase in the stiffness of the network as apparent from the plots. The symbols are experimentally measured values of Σ and by forcing σ to match the model we infer m for various compositions.

Within the mean field approach, the fibers are in a pre-stretched state when the microgels shrink with end-to-end distance $x = \lambda_f x_0$. The shear modulus is predicted to change, based on Eq. 7.2, from $G(x_0)$ to $G(x)$. The relative stiffening as the temperature is varied across the LCST can now can be expressed as the ratio $\Sigma = G(x)/G(x_0)$. Being more explicit about functional dependence, $\Sigma = (x, x_0, \nu)$ where x_0 and ν are set by the fibrin concentration, c_f. The stretched state $x = \lambda_f x_0$ depends on the factor m and the microgel effective volume ϕ_P through Eq. 7.4, and ϕ_P in turn depends on the microgel concentration c_P. Thus the stiffening ratio can be expressed in terms of known material composition (c_f, c_P) and the unknown factor m as

$$\Sigma(c_P, c_f, m) = \frac{G(m; c_P, c_f)}{G_0(c_p, c_f)}. \tag{7.5}$$

In Eq. 5, m is the only unknown fit parameter. Other parameters are *a priori* known from the fibrin and microgel concentrations, and we use literature data to determine values of l_0 and l_c (see Appendix table E.3). Fig. 7.13 shows the computed value of Σ as a function of the end-to-end distance $x = m\lambda_0/l_{arc}$. The front factor m (Fig. 7.14) was determined by requiring the predictions of Eq. 7.5 agree with the experimentally observed stiffness

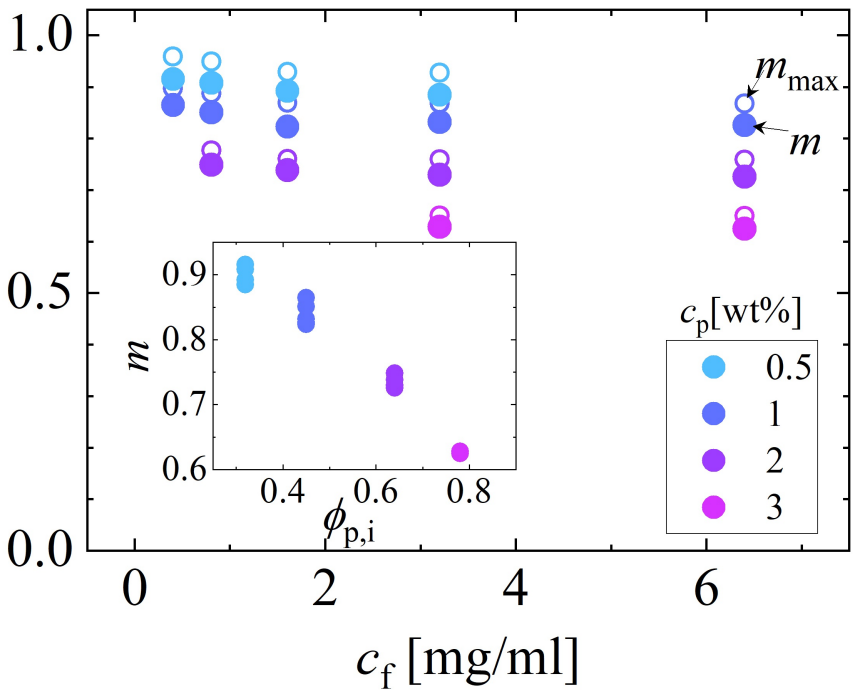

Figure 7.14: The values of m (closed symbols) for which the experimental stiffening ratio and model predictions match. The maximum value of m given by Eq. 7.6 are plotted as open circles. Inset shows the monotonically decreasing trend of m as a function of effective volume fraction of microgels.

ratios at various compositions (c_f, c_P). We find that a marginal change (0.5-5 %) in x is sufficient to observe the range of stiffness in the modulus that we experimentally observed. The reason for such strong sensitivity is the result of the intrinsic nonlinear response of such fibers, where a small deformation is enough to pull out some thermal slack from the polymer chains and is enough to produce a highly nonlinear force-displacement relation. This is also supported by the evidence of a minimal apparent change in the fibrin network topology as seen from the confocal images in Fig. 7.10. It is also consistent with the mild level of stiffening that we observe in contrast to pure fibrin networks which can in principle stiffen to a much larger extent under large external deformation (by reorientation, straightening, bending, and buckling) [239, 248, 127]. However, it should be noted that the values of x represent the stretching in an average sense. In reality, the orientation-dependent stretch can be much different than the average x.

The computed values of m, the efficiencies of transferred volumetric strain to the fibrin network, are plotted in Fig. 7.14 as a function of the fibrin concentration. They vary within a narrow range, $m = 0.62 - 0.91$, for the full range of compositions probed in the experiments (inset shows the values of at various volume fraction of microgels and the numerical values of are provided in the Appendix table E.2). It is significant that the efficiency factor m is always rather large, that is, most of the strain of the shrinking particle is transferred to the surrounding fibrin network. More interesting is that m is nearly constant for each particle concentration (i.e. negligible dependence on fibrin concentration c_f) and shows a monotonic decrease with particle concentration c_P. Taken together, along with the experimental observation of tension in the network at high temperature, these trends support the hypothesis of shrinking microgel particles causing tensile stress in the fibrin which creates overall stiffening due to the inherent strong nonlinearity of the fibrous network. Note that the values of m will also depend on the initial value $x = x_0$, in the current work we have used the values available in literature [248].Hence, the values of m (and x) in the deformed state will be different from the ones shown in Fig. 7.13 if a different x_0 values were used.

A remaining uncertainty of this model is to *a priori* predict m, rather than infer it from our measurements. This would require much more detailed knowledge about the interaction of microgel particles with the fibrin network. Nevertheless, we can still rationalize the trend of decreasing m with particle concentration by considering that finite fiber extensibility implies an upper bound on m (shown in Fig. 7.14). That is, the full strain of the shrinking microgel particles cannot be transferred to the surrounding network if this strain goes beyond the finite extensibility limit at $x = 1$. Finite extensibility therefore imposes $x < 1$ which creates an upper bound on λ_f, which can be translated to an upper bound on

m as

$$m < m_{max} = \frac{1}{x_0}\left(\frac{1-\phi_t}{1-\phi_f}\right)^{1/3}. \tag{7.6}$$

We find m_{max} varies from $0.65 - 0.96$, generally decreasing as a function of microgel particle loading as shown in Fig. 7.14 (open symbols). Our experimentally inferred values of m are fairly close to this upper bound limit. It is possible for $m_{max} = 1$, but we never see this in our composition space due to the high volume fraction of microgel particles. In this limit, even a small volume change of particles requires a large relative volume change of the fibrin, and it is the relative volume change that creates the stretch λ in Eq. 7.3. Designing composites such that $m_{max} < 1$ is a strategy for dramatic stiffening, since the full theoretical de-swelling of microgel particles is beyond the finite extensibility limit. In practice, $m = m_{max}$ cannot be achieved exactly, but the fixed junction model helps elucidate how close the limit is approached in our experiments.

7.4.2 Mesh Adjustment Model (Mobile Junctions)

In addition to the crosslinked semiflexible network that we considered in the experiments and stretched network model, a similar design concept can be extended to physically entangled semiflexible networks such as actin and collagen or stiff networks such as microtubules and carbon nanotubes. For such cases we present a physical hypothesis on how such a network might change when it experiences attractive interactions with deswelling microgels. We model the junctions between the fibers as physical entanglements (mobile junctions). In such cases, a microgel-induced change of the network mesh size ($\sim$entanglement length) could be a potential mechanism for composite stiffening which does not necessarily involve significant deformation of fibers. In this minimalist model, we assume that the fibers can slide relative to each other at the entanglement points and adjust their network mesh size ξ and entanglement density locally without (to leading order) bending, compressing, or stretching of filaments which is energetically expensive. A schematic of this idea, which we call the "mesh adjustment model", is given in Fig. 7.15

To quantify this idea we adopt the well-known analysis for the linear shear elasticity of semiflexible entangled polymer networks [74, 127]. In the limit of infinitesimal strain, the linear elastic modulus can be written as $G \sim \frac{\rho k_B T l_p^2}{l_e^3}$. Here, the leading factor of $\sim \xi^{-2}$ is a (stoichiometric) contribution to the modulus. In addition, the entanglement length is given by $l_e \sim \xi^{4/5} l_P^{1/5}$ [74, 127]. Hence the linear elastic modulus can be expressed as $G \sim \rho k_B T l_P^{7/5} \xi^{-12/5}$. Note that there are two different types of filament density dependences: (a) dependence of number density of polymers that does not correlate with struc-

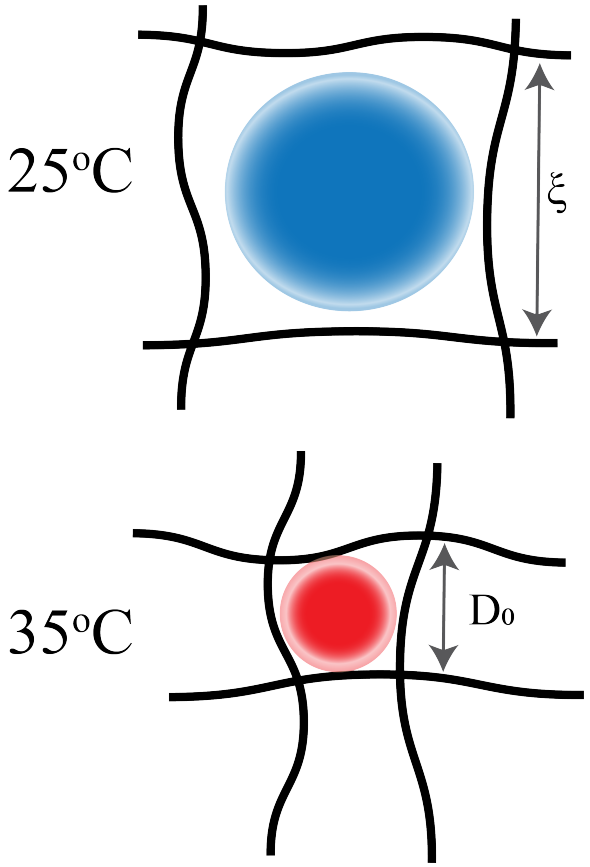

Figure 7.15: Schematic describes the adjustment of a entangled polymer mesh cell that encapsulates a microgel particle as the particle de-swells beyond its LCST.

tural changes, and (b) one that directly impacts the force-extension behavior of individual fibers via the entanglement length l_e. For the simple "adjusted mesh" model described below we assume contribution (b) is the source of reinforcement.

We consider the pure polymer matrix to have an average mesh size ξ, and hence total network volume of $V_t = N\xi^3$, where N is the total number of 3-d meshes or pores. If the composites are synthesized at low temperature by polymerizing the monomers around the microgel, we hypothesize that the initial volume fraction of microgels determines the covered fraction of polymer meshes, where "covered fraction" means meshes that encapsulate a single microgel particle. Our central hypothesis for the reinforcement mechanism then is that at the temperatures beyond the LCST there are strong polymer-microgel adhesive contacts which induce the covered meshes to attain a size equal to that of a completely de-swollen microgel D_0. Note that this hypothesis assumes the microgels collapse in the composite to the same degree as they do in dilute solution. Such a strong collapse seems physically plausible, or at least consistent with, the idea that the fibers do not deform per the core assumption of the "adjusted mesh" model. Conservation of total volume then implies that the meshes not encapsulating a microgel must expand to compensate for the shrunken meshes. This allows us to write

$$N\xi^3 = N\phi D_0^3 + N(1-\phi)\xi_1^3 \tag{7.7}$$

where ξ_1 is the average size of the expanded or "renormalized" mesh which is given in terms of the known average mesh size for pure fibrin (ξ) and the de-swollen microgel diameter D_0. In an effective medium spirit where a mesh is the elementary unit, we now invoke the scaling relation for shear elastic modulus described earlier to write the composite modulus as a weighted sum of contributions from shrunken meshes (which locally stiffen) and loosened ones (which locally soften):

$$= \frac{G_{composite}}{G_{network}} = \phi\left(\frac{\xi}{D_0}\right)^{12/5} + (1-\phi)\left(\frac{\xi}{\xi_1}\right)^{12/5}. \tag{7.8}$$

The above equation for the composite modulus above LCST is normalized to its pure network value. A caveat is that we find the above simple model gives a renormalized mesh size when the pure network mesh size is smaller than the core diameter of microgel, or, more precisely, $\xi < \phi^{1/3}D_0$. We make quantitative predictions for stiffening adopting such a simple approach (Eq. 8) in Appendix table **??** and Fig. 7.16. The stiffening ratio predictions generally under predict the stiffness ratios that we observed from our experiments with crosslinked fibrin networks. This is expected since unlike the case of crosslinked poly-

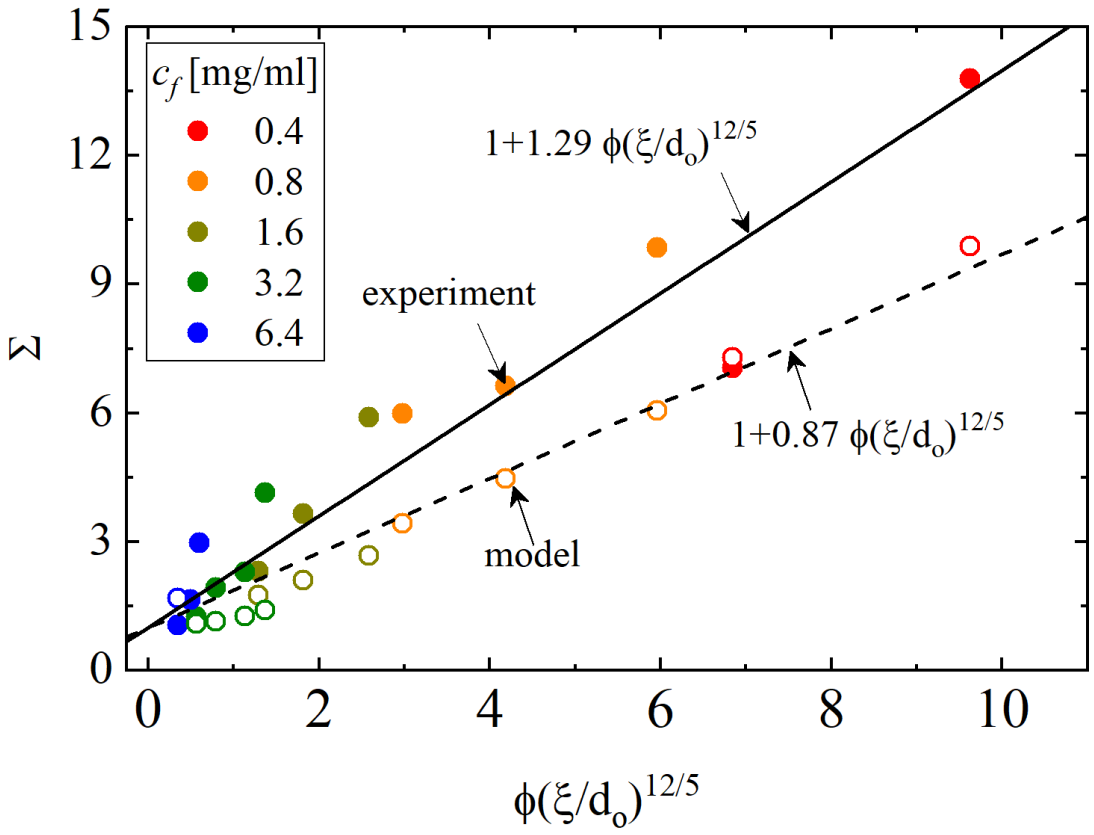

Figure 7.16: Model predictions (open symbols) of relative stiffening from Eq. 7.8. The dashed line is the best-fit line to the model predictions.

mer network, the polymer chains in the entangled polymer matrix are not deformed (to the leading order), and the stiffening is a consequence of the appearance of two different mesh sizes (shrunk and loosened mesh) and their relative contribution to the network elasticity. Yet, this mobile junction models shows that similar thermo-responsive stiffening may be possible with semiflexible networks even in the absence of fixed crosslinks.

7.5 Conclusions

We experimentally demonstrated and theoretically modeled a new stimuli-responsive particle-polymer composite system which is able to achieve a multifold change in its shear elastic modulus under thermal excitation. The constituents, a semiflexible biopolymer network of fibrin and thermoresponsive ultra-soft microgels, provide a novel mechanism for achieving triggerable *in situ* stiffening. The fundamental principle governing the responsiveness of the composite is the coupling between the strain-stiffening polymeric network of fibrin

and the thermoresponsive microgels. The degree of achievable stiffness depends on the composition of both polymer and microgels. Our modeling approaches provide physical insights into the microscale mechanics of the composites and rationalizes the composition-dependent experimental trends.

Biopolymers in general perform varying functions in living organisms. Their ability to achieve a large range of mechanical properties makes them vital for many biological functions and important candidates for the development of bioinspired functional materials. Our approach highlights an effective way of harnessing the intrinsically nonlinear properties of a semiflexible polymer network into functional material design that can find applications in several potential areas such as soft robotics and biomedicine where modulating and tuning stiffness can provide novel functionality.

The nominal stiffness increase (factor of three) at the highest concentration of biopolymer and microgels also highlights the limitations in the approach that we have adopted. Biopolymer fibrin in principle can stiffen to a significantly large extent (approximately ten times the linear shear modulus) under an applied deformation, which we achieve only for the softest networks. One possible way to improve the performance of the fabricated composites and extend similar design principles to stiffer biopolymer matrices will be to either strengthen the coupling (attractions) between the microgel and the fibrous network or to fabricate microgels capable of a higher degree of volume change.

The thermoresponsive stiffening concept is not limited to biomaterial systems. Synthetic semi-flexible networks are being developed and becoming better understood [230, 231, 232]. The concept described here should in principle work with any network with strong nonlinearities where stiffness is sensitive to structural changes of the network, so long as the embedded particle free energy changes are sufficiently strong to modify the surrounding network. Our modeling approach provides a general understanding to design and engineer such composites and potentially optimize performance by a rational design of the components.

Acknowledgement

This work was performed at the University of Illinois and supported by DOE-BES under Grant No. DE-FG02-07ER46471 administered through the Materials Research Laboratory. RHE thanks Anton Paar for providing the rheometer MCR702 which was used for some of the rheology experiments.

CHAPTER 8

SEMIFLEXIBLE MAGNETORESPONSIVE COMPOSITE

8.1 Introduction

In Chapter 7, we presented a new paradigm for designing soft materials with large changes of reversibly triggerable stiffness based on volume changing particles embedded in the semiflexible polymer mesh. In this chapter, we build on similar ideas, but instead of thermal excitation, we use a magnetic field as an external stimulus. Building on the preliminary idea presented in a previous work [249], we embed iron particles at very low volume fractions ($\phi < 4$ % v/v) in the fibrin matrices, and utilize the interactions between the particles (with induced magnetic dipoles) using an externally controlled magnetic field to control the overall stiffness of the composite. We then describe a simple model which quantifies the contribution of inter-particle interactions and the mesh stiffening.

8.2 Materials and Methods

8.2.1 Sample Preparation

The carbonyl iron (CI) particles used in the study were obtained from Sigma Aldrich. The particles were functionalized with aminopropyl trimethoxysilane. The particles were incubated in a solution of silane with 90% ethanol for 12 h while on a shake table, and then washed 3-4 times with deionized water before use. Bovine fibrinogen (free of plasminogen and fibronectin) and thrombin were acquired commercially (Enzyme Research Laboratories, South Bend, IN, USA) and stocked at 70°C. The aqueous buffer used in all the samples was produced by mixing 25 mM HEPES, 150 mM NaCl, and 20 mM $CaCl_2$ in type 1 water and adjusting the pH to 7.4. Prior to composite preparation, fibrinogen was thawed at 37°C and diluted to the required concentration with the aqueous buffer. To prepare pure fibrin hydrogels, predetermined volumes of solutions of fibrinogen and thrombin were mixed in a centrifuge tube and immediately loaded between the plates on the rheometer. Fibrin-CI

composites of varying concentrations were prepared by mixing predetermined quantities of CI particles and fibrinogen followed by polymerizing fibrinogen with thrombin at 20°C for an hour. Aqueous solutions of Carbopol 940 (obtained from Acros Organics) were prepared by mixing with deionised water overnight. The solutions were then neutralized to pH=7 using sodium hydroxide solution. Xanthan gum (Sigma Aldrich) solution was prepared by mixing Xanthan powder with deionised water for 3 hours.

8.2.2 Rheological Characterization

Viscoelastic properties of all materials were probed using a torque-controlled rotational rheometer (Discovery Hybrid 3, TA instruments) using a plate-plate geometry. A 20 mm diameter aluminum plate was used in all experiments with a fixed gap setting (1 mm). A uniform magnetic field of controlled strength was produced using the magnetorheological accessory (TA instruments) to study the field-dependent rheological properties (Fig. 8.1). Strain amplitude sweeps were also performed on the pure fibrin hydrogels and fibrin–particle composites to probe the strain-dependent viscoelasticity at a fixed angular frequency of 1 rad/s.

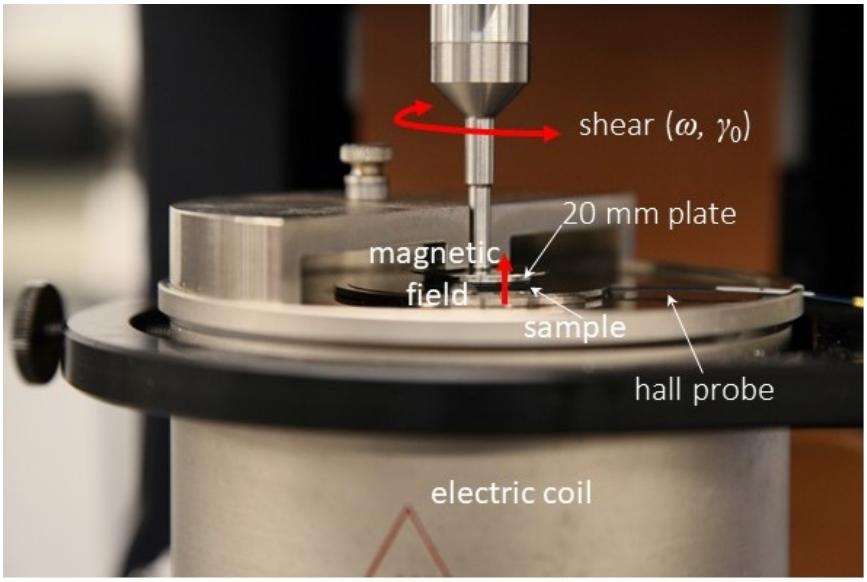

Figure 8.1: The rheological setup consists of a coil (under the bottom plate) producing a nearly uniform magnetic field in the region between the top non magnetic aluminum plate with field lines perpendicular to the direction of shear.

8.2.3 Microscopy

Samples for scanning electron microscopy were prepared using the methods from literature [250]. The fixed samples were critical point dried which lead to a significant reduction in the sample volume, and then coated with gold-palladium ($\approx$ 5 nm). Low vacuum mode of SEM (FEI Quanta FEG 450 ESEM) was used to image the sample. For x-ray micro-computed tomography, MicroXCT-200 (Xradia) was used, and the samples were prepared and held in a microcentrifudge tube. A commercially purchased permanent magnet was used to provide magnetic field while imaging the sample.

8.3 Results

Figure 8.2 a shows the SEM image of the dry CI powder used in this work. Particle size distribution obtained from such images is shown in Fig. 8.2 b. Particles are roughly spherical in shape, though small deviations can be visually observed. The mean particle diameter is $2a = 2$ μm with a standard deviation of 0.75 μm.

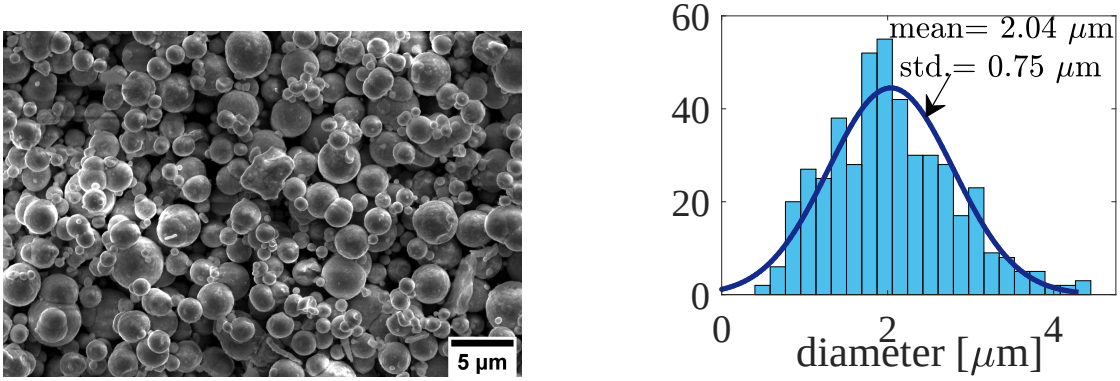

(a) **(b)**

Figure 8.2: (a) Scanning electron micrograph of the Carbonyl Iron particles used in the composite. (b) The CI particles are polydisperesed with a mean size of 2 μm and a standard deviation of 0.75 μm (obtained using a normal distribution fit to the data).

In the following subsections, the results describing the effects of incorporating the magnetic particles within various base matrices are described. We will first look at the effect of such particles in yield stress fluids of various yield strengths. In such cases, the particle are expected to undergo large displacements and align into chains in the direction of magnetic field lines when the sample is subjected to strong enough magnetic field. The resistance of such chains to an applied shear deformation leads to the observed stiffening in the composite. The rheological results for the effect of magnetic particles embedded in crosslinked

fibrin matrices of various mesh sizes are then presented. Figures 8.9 and 8.10 show the key experimental observations. As will be described in a later section, the magnetoresponsive stiffening that is observed for fibrin-particle composite is dependent on the relative size of particle compared to the fibrous mesh. Although stiffening is observed in both the cases, the qualitatively and quantitative trends in stiffening is different, and depends on the particle displacement inside the fibrous matrix: large displacements (chaining) and small displacements (nonlinear mesh stiffening).

8.3.1 CI Particles in Yield Stress Matrix

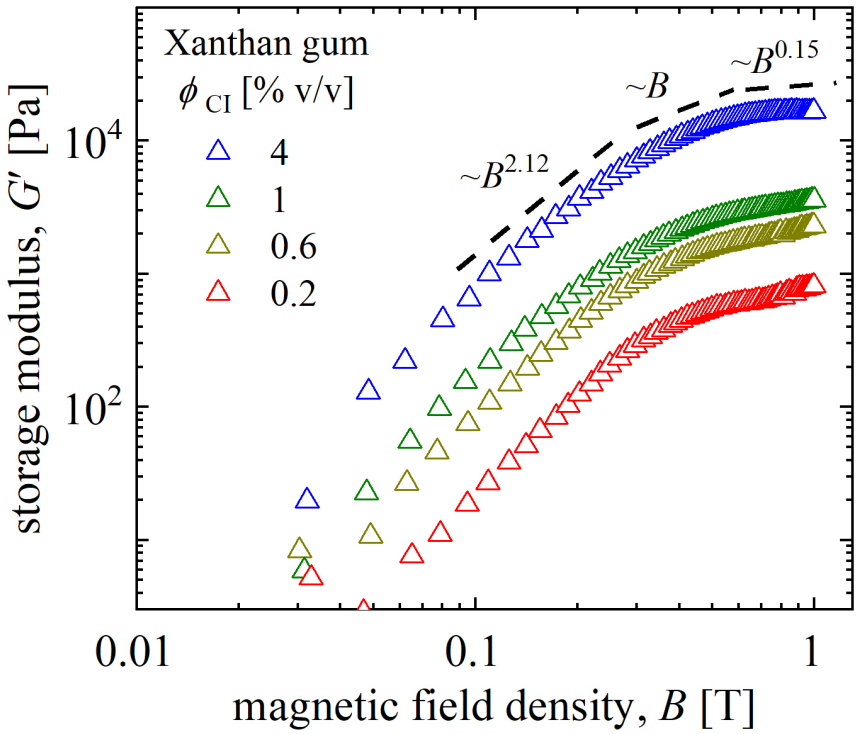

Figure 8.3: The magnetorheological response of suspensions of CI particles in a yield stress fluid of Xanthan gum (yield stress$\approx$ 0.3 Pa) at various particle concentrations. The shear modulus at all compositions increases with a nearly quadratic dependence on the field strength, and then saturates at higher field strength.

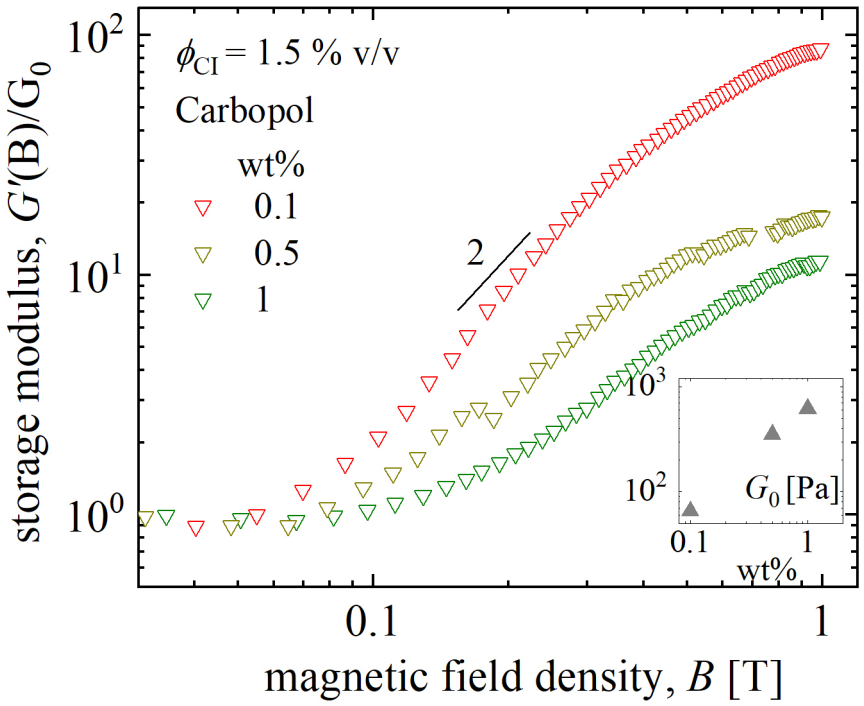

Figure 8.4: The magnetorheological response of various Carbopol yield stress fluids with the same CI particle volume fraction. The relative change in the shear modulus is higher for a weaker concentration of carbopol (or lower yield stress sample). (inset) linear shear modulus of the Carbopol composites at $B = 0$.

The magnetorheological (MR) response from a suspension of CI particles at various volume fractions (ϕ_{CI}) in a yield stress fluid (Xanthan gum, yield stress $\sigma_y \approx 0.3$ Pa) is shown in Fig. 8.3. The linear elastic shear moduli G' of the samples, probed via oscillatory shear with a strain amplitude $\gamma_0 = 1$ % and and angular frequency $\omega = 1$ rad/s, is shown as the magnetic field strength (B) is varied. The distinct regimes in the power-law response of G' with (B) is observed. Below $0 < B < 0.3$ T, the samples roughly follows a quadratic ($\sim B^2$) dependence of the field strength followed by a roughly linear dependence in the range $0.3 < B < 0.6$ T, and the MR effect essentially saturates at higher field strength $0.6 < B < 1$ T. This is consistent with the prior observation of the saturation magnetization of similar particles beyond $B < 0.6$ T. The scaling of ($\sim B^2$) at low field strength has been observed previously [13, 251], and is well understood theoretically.

Fig. 8.4 shows the magnetorheological response of a suspension of CI particles ($\phi_{CI} = 1.5$ % v/v) in the yield stress fluid of carbopol of varying yield strengths (σ_y = 5, 70 and 100 Pa. The linear shear modulus $G'(B)$ is normalized by the modulus at $B = 0$. The relative stiffening, i.e. $G'(B)/G_0$, is higher for a softer matrix (lower yield strength). Unlike Fig. 8.3, in this case the modulus has a weak increase at low field strengths, followed by a stronger stiffening which eventually saturates. The microCT images in Fig. 8.5 show the

distribution of CI particles in a carbopol matrix with yield strength of 70 Pa. In the absence of a magnetic field the particles are well-dispersed inside the carbopol matrix. When exposed to a magnetic field by holding a permanent magnet underneath the sample, the CI particles undergo large displacements, and align into chains along the direction of the field. The concentration of particles is higher at the bottom of the image (sample is held on the top of a permanent magnet).

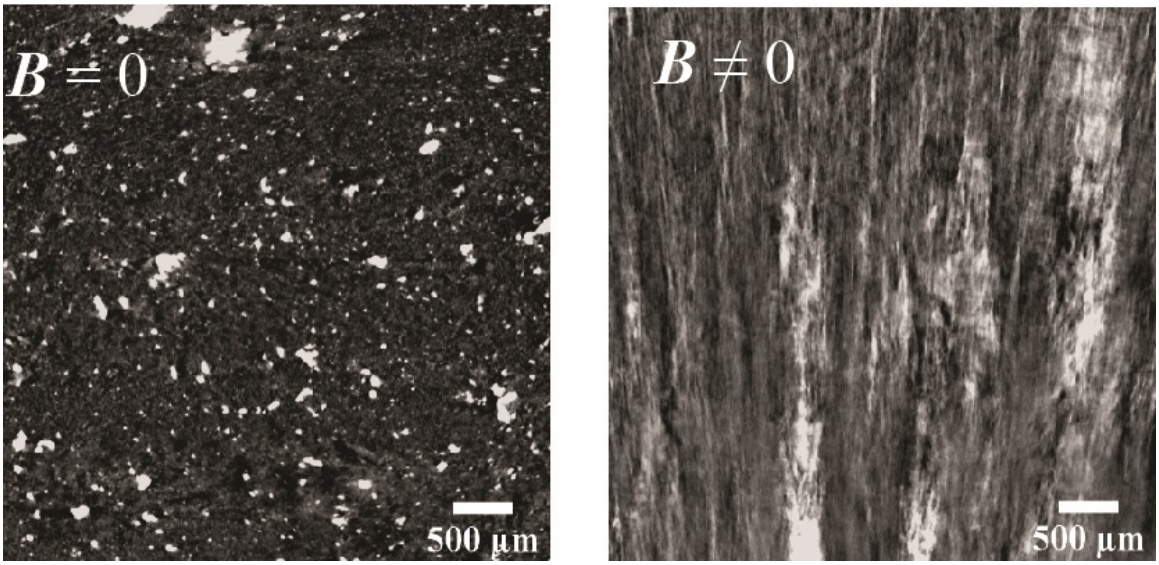

Figure 8.5: CI particles dispersed inside a Carbopol (yield stress fluid) matrix in the absence of a magnetic field (left) undergo large displacements to form chains in the direction of magnetic field lines (right). Nonuniform magnetic field is produced by a permanent magnet held under the sample.

8.3.2 Pure Fibrin Shear Rheology

Fibrinogen polymerizes into a polymer network of fibrin filaments in the presence of thrombin following a cascade of events [236]. Pure fibrin networks have a viscoelastic solid-like response in the linear response regime. Fig. 8.7 shows the nonlinear shear strain-stiffening response of pure fibrin networks at $c_f = 1.6$ and 6.4 mg/ml when probed with an oscillatory strain of increasing strain amplitude. The stiffening, indicated by the increasing first-harmonic (average) elastic modulus, is most apparent when the imposed shear strain is greater than 10-20 %. This is attributable to the nonlinear force displacement relationship of the individual strands as their thermal slack is reduced with external deformation [74, 237, 238]. Alternative explanations for such strain stiffening also exist in the literature based on the non-affine network rearrangements in the network [239]. The average shear

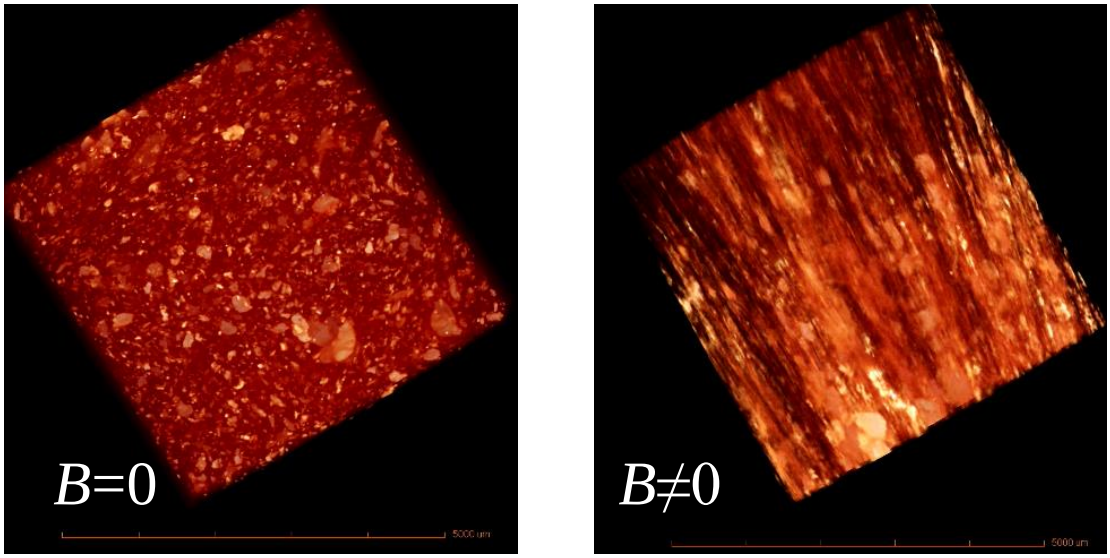

Figure 8.6: 3D reconstruction of X-ray CT images for Carbopol-CI particle composite.

elastic modulus at the maximum strain before the network breaks irreversibly is roughly 10 times higher than the linear elastic modulus. In this work, the idea that small deformation (on global or local level) can nonlinearly stiffen the semiflexible networks will be utilized to design magnetically responsive soft materials that can stiffen under the application of an external field.

8.3.3 Fibrin-CI Composites

The polymerization of fibrinogen occurs in the presence of CI particles to produce an interconnected network, similar to the pure fibrin, as shown in the electron micrograph in Fig. 8.8 b. Thus, the presence of CI particles seem to negligibly affect the formation of the fibrin network. Since the volume fraction of CI particles is relatively small, $\phi_{\text{CI}} < 5$ % v/v, the presence of particles does not offer any significant chemical or physical deterrence to the network formation [224]. The bulk sample, as shown in Fig. 8.8 a, is stable for long durations (observed for ~ 2 week period) when its solvent loss from evaporation is prevented.

Figures 8.9 and 8.10 show the effect of magnetic field on the linear shear modulus of the CI-fibrin composite prepared with different concentration for fibrin, 1.6 mg/ml and 6.4 mg/ml, respectively. To make quantitative comparison of the MR effect at various compositions, we plot the shear modulus normalized by its value in the absence of a magnetic field, i.e. $G(B)/G_0$. The value of G_0 at various low ϕ_{CI}, is very weakly dependent on ϕ_{CI}

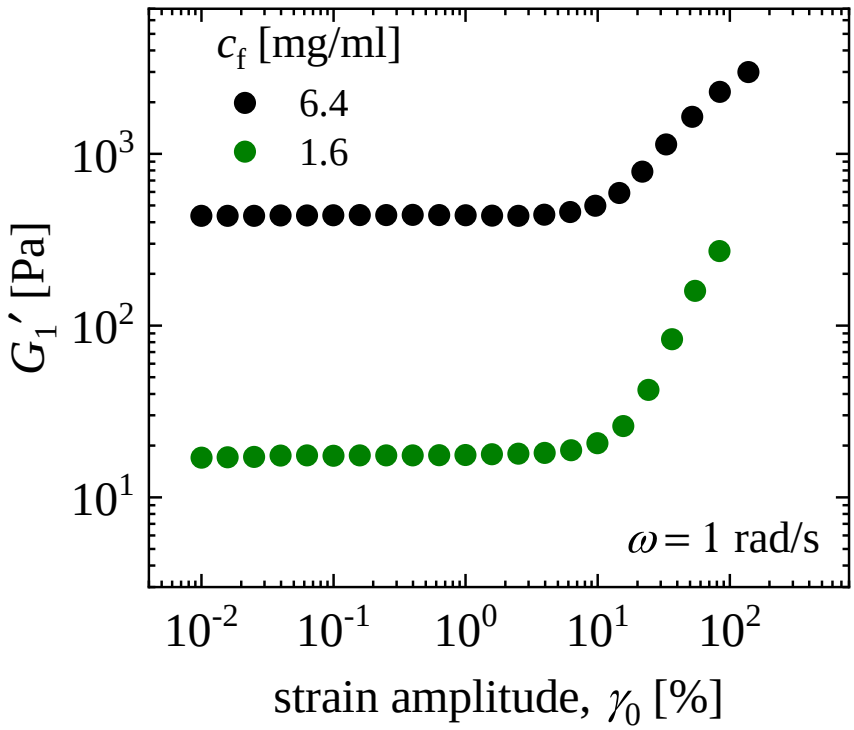

Figure 8.7: The crosslinked networks of fibrin used in the this work exhibit a strong strain-stiffening response at nominal deformations.

and is close to the linear elastic shear modulus of pure fibrin network as shown in the figure insets. In both the composites, several common signatures in the rheological response can be observed. For very low ϕ_{CI}, less that 0.4% v/v for $c_{\text{f}} = 1.6$ mg/ml and 0.6% v/v for $c_{\text{f}} = 6.4$ mg/ml, increasing magnetic field strength leads to a very modest increase in the shear modulus of the sample. Above certain value of ϕ_{CI}, a drastic change in the shear modulus is observed above a specific value of magnetic field strength (B_{crit}). B_{crit} decreases with increasing ϕ_{CI}. The normalized shear modulus, above B_{crit}, shows a strong apparent power-law dependence on the magnetic field density, $G/G_0 \sim B^n$, where $n \approx 3 - 4.5$. At the highest applied field ($B = 1$ T), for most cases, a monotonic trend between G/G_0 and ϕ_{CI} is observed. However, while at $c_{\text{f}} = 1.6$ mg/ml, the normalized shear modulus roughly approaches a plateau value, such a trend is not observed at $c_{\text{f}} = 6.4$ mg/ml. Note that because of the non-monotonicity in the values of G_0 with ϕ_{CI}, the shear modulus $G(B)$ versus B will shift non-monotonicity, but the qualitatively trends do not change.

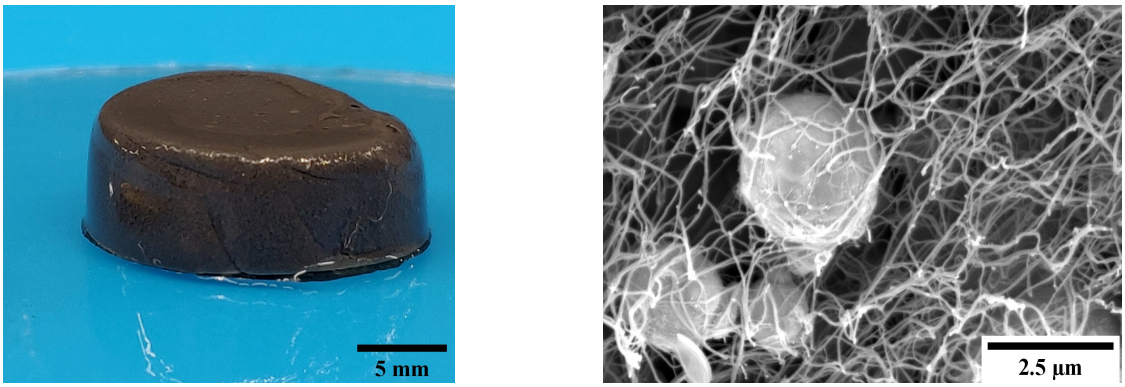

Figure 8.8: (a) A fibrin-CI composite fabricated using the method described in this work. (b) SEM image shows that fibrinogen successfully polymerizes around the CI particles and causes no apparent changes in the network architecture compared to a pure fibrin network.

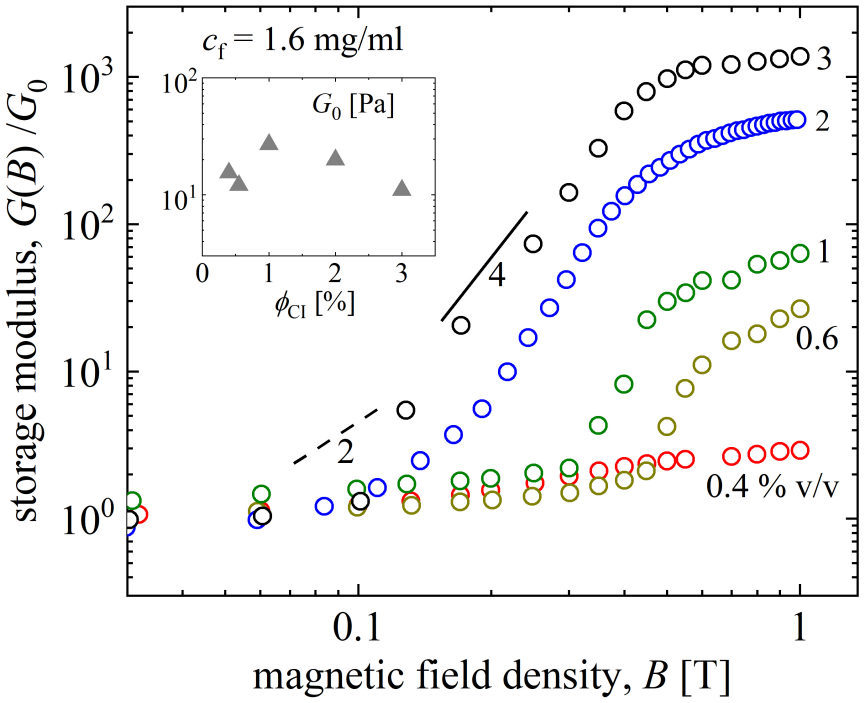

Figure 8.9: The relative stiffening, $G(B)/G_0$, of the fibrin-CI composite with (c_f = 1.6 mg/ml) compared to its value in the absence of the field as the strength of the field is varied. A strong stiffening of the composite, higher than the expected $\sim B^2$ scaling, can be observed above a certain concentration.

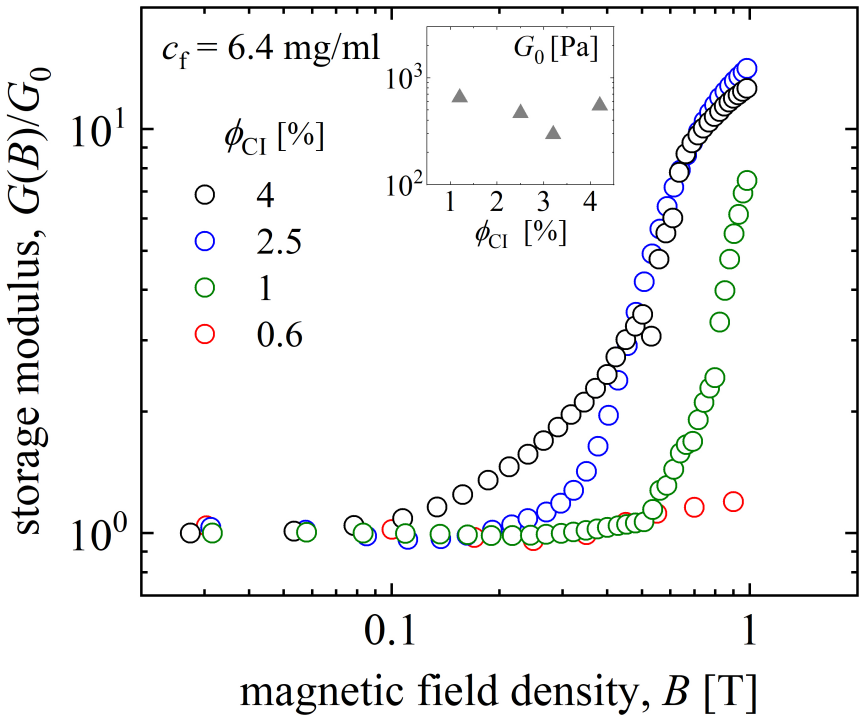

Figure 8.10: The relative stiffening, $G(B)/G_0$, of the fibrin-CI composite with (c_f = 6.4 mg/ml) also shows strong sensitivity to the magnetic field.

Figures 8.12 and 8.13 show the X-ray micro CT images of various samples in the presence and absence of the magnetic field. Three-dimensional views of the all the samples are provided in the SI. Note that the field in these images is being produced by a permanent magnet positioned just under the sample. Hence, the magnetic field strength is not uniform inside the sample, but rather have a gradient in its strength with field strength decreasing away from the magnet. Hence, we cannot make a one-to-one comparisons between the the microstructure of the composites under uniform field and xμCT images. However, certain vital observations can be made. The CI particles are homogeneously distributed in the fibrin meshes in the absence of magnetic field. Under the field, we observe slight rearrangement of particles. It is unclear from the images whether the particles get displaced to align into small chains, but large displacements and formation of particle chains as seen in the case with yield stress fluid composites (Fig. 8.5) are clearly not seen in both the cases.

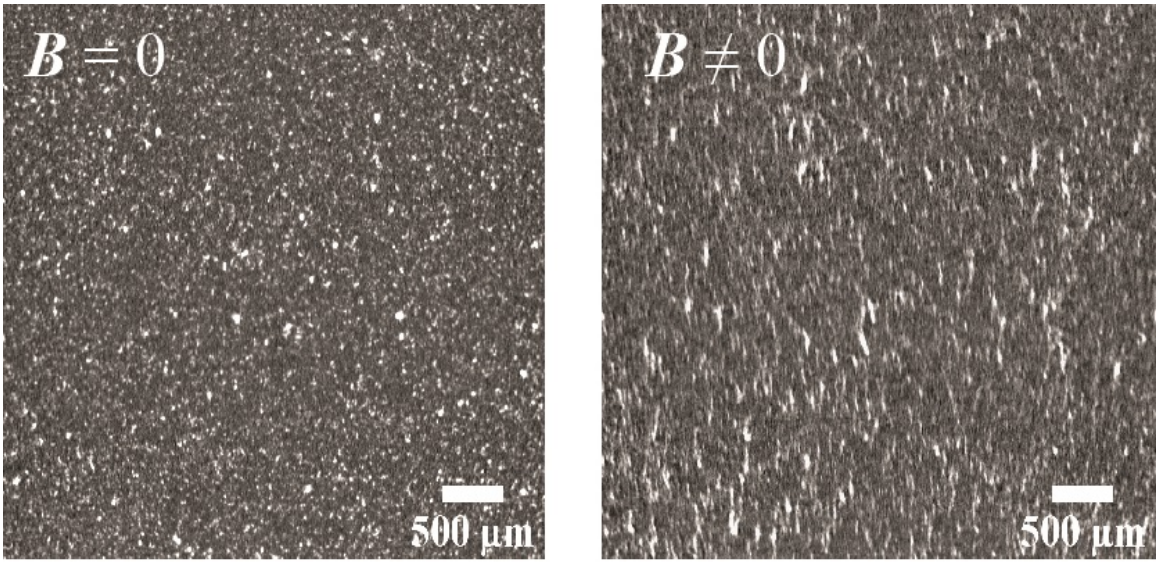

Figure 8.11: Fibrin-CI composite ($\phi_{CI} = 2\ \%$ and $c_f = 1.6$ mg/ml) with uniform distribution of CI particles in the absence of field (left). CI particles undergo small displacements (compared to large displacements in Fig. 8.5) in the presence of magnetic field (right).

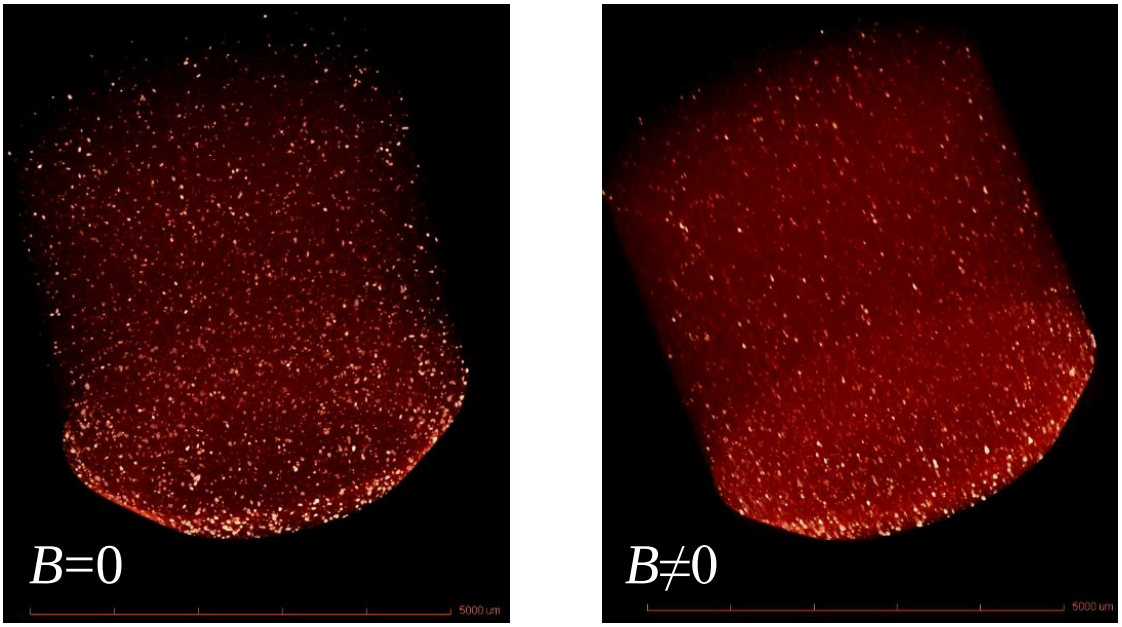

Figure 8.12: 3D reconstruction of X-ray CT images for Fibrin-CI composite ($\phi_{CI} = 2\ \%$ and $c_f = 1.6$ mg/ml).

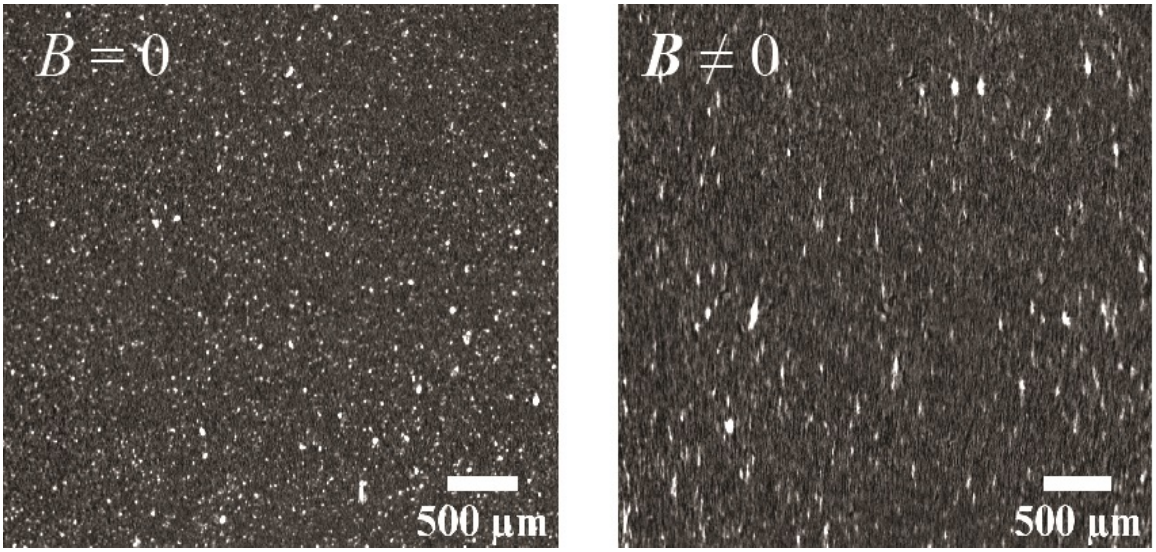

Figure 8.13: Fibrin-CI composite ($\phi_{CI} = 2\ \%$ and $c_f = 6.4$ mg/ml) with uniform distribution of CI particles in the absence of field (left). CI particles undergo small displacements (compared to large displacements in Fig. 8.5) in the presence of magnetic field (right).

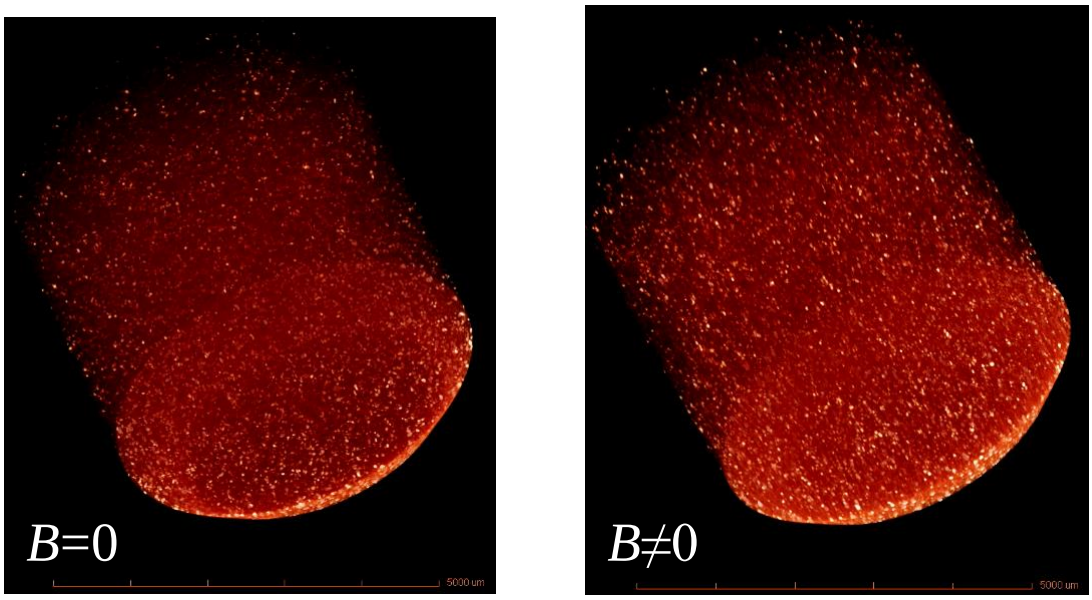

Figure 8.14: 3D reconstruction of X-ray CT images for Fibrin-CI composite ($\phi_{CI} = 2\ \%$ and $c_f = 6.4$ mg/ml).

8.3.4 Fibrin-Submicron Fe Composites

Extending the idea presented in the previous subsection, the effect of relative particle to mesh size on the magnetorheological effect is explored further. In this case, submicron

sized (30-100 nm) Fe particles, much smaller than the mean fibrin mesh size, are utilized. Figures 8.15 and 8.16 show the effect of magnetic field strength for the composites prepared with submicron Fe particles using the same fibrin concentrations as used in last subsection. The shear modulus of the composite in the absence of a magnetic field is affected by the presence of particles. Generally, we find the shear elastic modulus of the composite is lower than the pure network modulus. Such an effect has been observed in the past with systems of particle inside fibrin matrices. The effect of varying magnetic field strength is different from CI-fibrin system discussed earlier. The normalized shear modulus $G(B)/G_0$, shows a monotonic increase with the increasing B. Compared to the composites prepared with submicron particles, the power-law sensitivity of the shear modulus to the magnetic field also decreases and stays close a quadratic dependence i.e. $\frac{G}{G_0} \sim B^2$. However, in some cases we do observe a stronger dependence as shown in Fig. 8.16. The observations that we make for submicron Fe-fibrin system are similar to a magneto-yield stress fluid (CI particles suspended in a yield stress matrix of carbopol). The concentrations of carbopol were selected to get a linear shear modulus close to the fibrin matrices that we have employed. The field-dependence at various concentrations show similar trends to that of Fe-fibrin composites, where we found a monotonic increase in shear modulus with the strength of applied field.

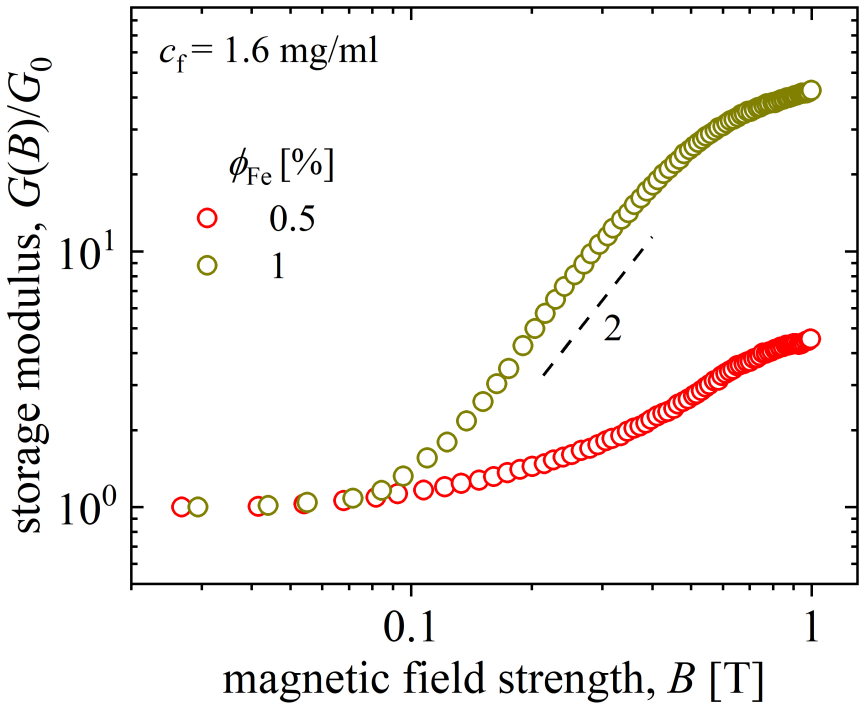

Figure 8.15: The relative stiffening, $G(B)/G_0$, of the fibrin-submicron Fe composite with $c_f = 1.6$ mg/ml. The composites do not show the strong stiffening effect as with the micron sized particles of ϕ_{CI} below a critical concentration.

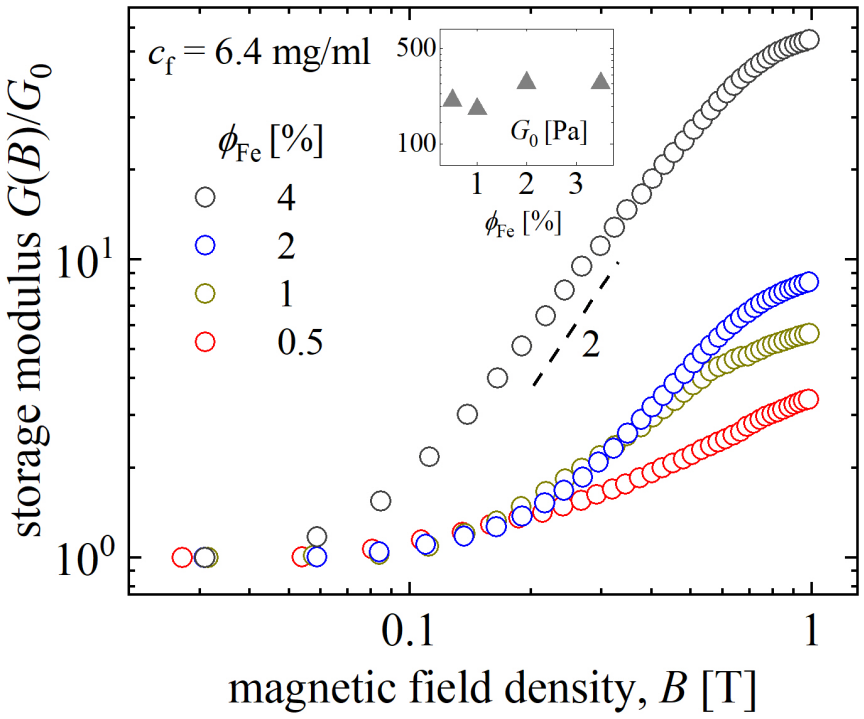

Figure 8.16: The relative stiffening, $G(B)/G_0$, of the fibrin-submicron Fe composite with $c_f = 1.6$ mg/ml.

The submicron Fe particles inside organize into aggregates inside the fibrin network in the absence of magnetic field as shown in Fig. 8.17. It is unclear from the current experimental evidence whether this is simply a consequence of effective attractive interactions between the particles that drive formation of such blobs against the thermal fluctuation forces or if the polymerization of fibrinogen influences the arrangements of particles or perhaps a combination of both. Under an external field particles chain-up and accumulate towards the direction of higher field strength under the magnetic field. Such an observation points towards the idea that the stiffening observed in such cases is a consequence of submicron Fe particles forming chains in the direction of the magnetic field which resist the external deformations leading to net stiffening.

8.3.5 Nonlinear Rheology Fibrin-CI Composites

In order to understand the origin of stiffness in the particle-fibrin composites, the nonlinear response of the composite is studied. Figure 8.19 shows the rheological response of the composites formed with fixed concentration of fibrin ($c_f = 6.4$ mg/ml) and varying content of CI particles (ϕ_{CI}) under oscillatory shear deformation of increasing amplitudes. The strength of uniform magnetic field is also varied as shown. At low $\phi_{CI} = 0.8\%$ (Fig-

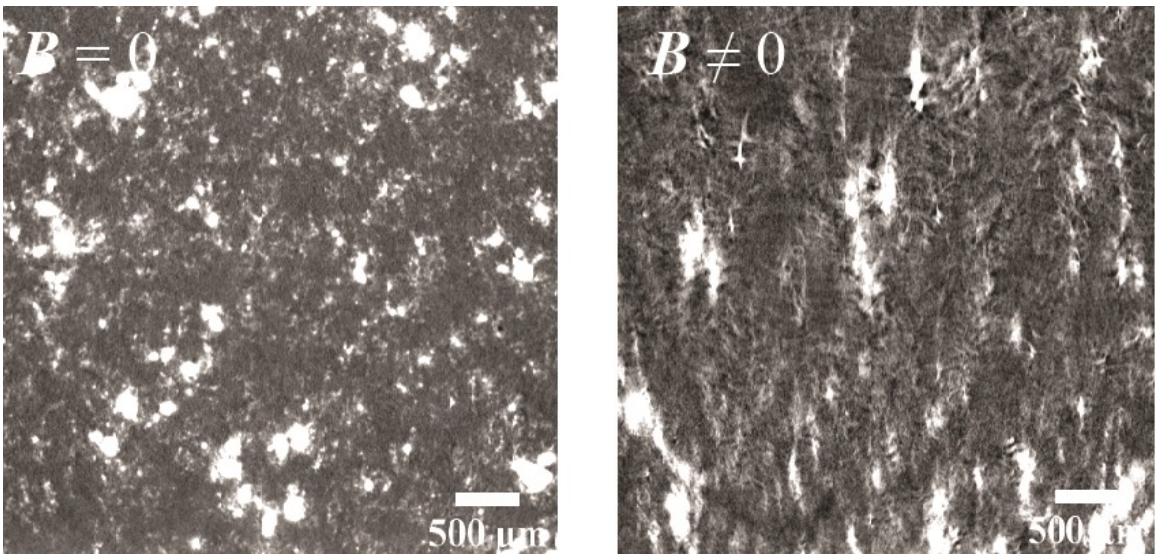

Figure 8.17: Submicron Fe particles arrange into aggregates inside the fibrin mesh (6.4 mg/ml) in the absence of magnetic field (left). The Fe aggregates undergo large displacements, and align to form chains along the magnetic field lines (right).

ure 8.19 a), the linear shear modulus stiffens by a factor of $2-3$ while the nonlinear stiffening nature G_1' of the composite appears to be the same as the pure fibrin network (Fig. 8.19) even in the presence of magnetic field. This suggests that the presence of particles in the fibrin network negligibly interferes with the strain-stiffening nature of the fibrin. At $\phi_{\text{CI}} = 2.5\%$, while the nonlinear response at $B = 0$ T is similar to the pure fibrin network, the shear modulus has an increases by a factor $4-8$ with the increasing magnetic field strength. The nonlinear response under a magnetic field at this concentration is distinct from the composite with $\phi_{\text{CI}} = 0.8\%$ or the pure fibrin network. Instead of a leading order stiffening in G_1' that was observed for the composite with $\phi_{\text{CI}} = 0.8\%$ (Fig.8.19 a) and pure fibrin network (Fig.8.19 b), G_1' softens at leading order followed by stiffening at higher strains. At even higher particle volume fraction $\phi_{\text{CI}} = 4\%$ (Fig. 8.19 c), the linear shear modulus shows an increase by a factor of 6-20 in the presence of magnetic field. However, in this case while a leading order softening is observed, the network only stiffens very weakly with further increase in strain amplitude. It is important to note that the softening response is observed in the low strain amplitude range, $\gamma_0 = 0.01 - 0.1$, which is typically below the critical strain at which the stiffening becomes significant in pure fibrin or in composite, $\gamma_{0,crit} \approx 0.1$.

The experimental observations in Fig. 8.19 can be explained from the understanding of nonlinear stiffening mechanisms in semiflexible polymers. The leading order reason for nonlinear stiffening is the presence of floppy modes such as small thermal undulations in

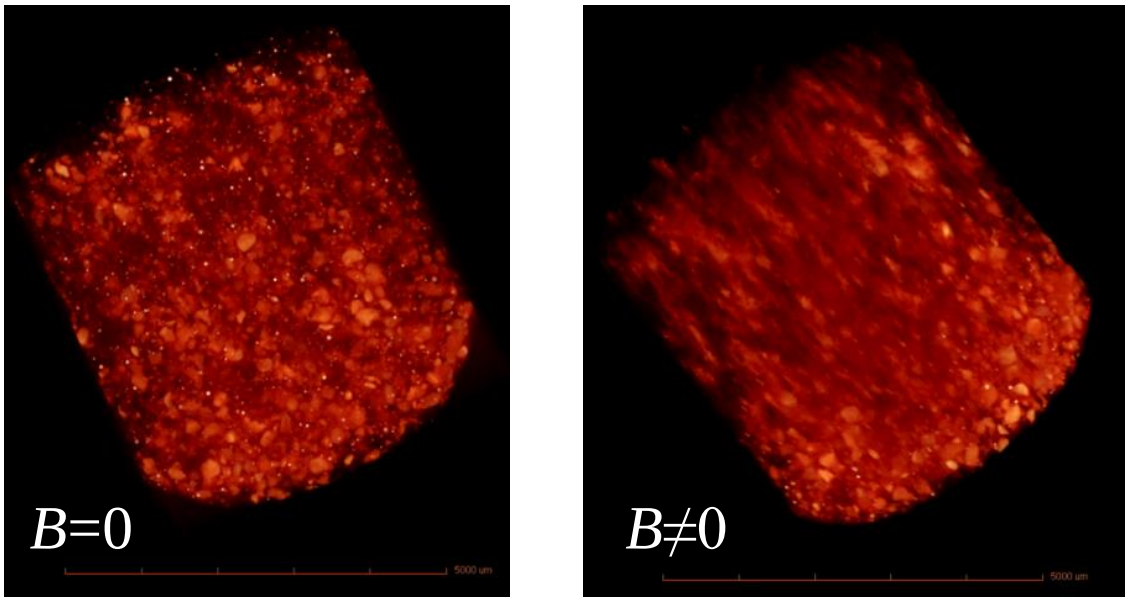

Figure 8.18: 3D reconstruction of X-ray CT images for Fibrin-submicron Fe composite ($\phi_{Fe} = 2\ \%$ and $c_f = 6.4$ mg/ml).

the filaments which are pulled-out under an applied deformation. Our hypothesis is that the presence of magnetic dipoles within the network contribute to composite stiffening in a similar way. The interaction forces between the particles (which depend on both ϕ_{CI} and B) deforms the fibrin matrix. This deformation pulls out the floppy modes in the principle direction of extension, thus leading to the field-dependent stiffening of the linear modulus.

A key observation is that in all the cases, the onset of nonlinear stiffening is nearly at the same applied strain amplitude. This suggests that most likely the underlying cause of eventual stiffening is the pulling out of floppy modes from the fibers (even in cases, Fig. 8.19 b and c, where we observed a softening response at intermediate strains). The key question that remains is regarding the leading order cause of softening at intermediate strains in at $\phi_{\text{CI}} = 2.5\%$ and $4\ \%$. One possibility of irreversible breaking of crosslinked junctions in the fibers which are nonlinearly deformed due magnetic forces and are further deformed by the external shear field. Obviously in the presence of two simultaneous deformation fields, analysis is more involved and is beyond our current scope.

8.4 Discussion and Modeling

As observed in the last section, the fibrin-magentic particle composites magnetorheological features which have not been reported for the previously studied magnetorheological

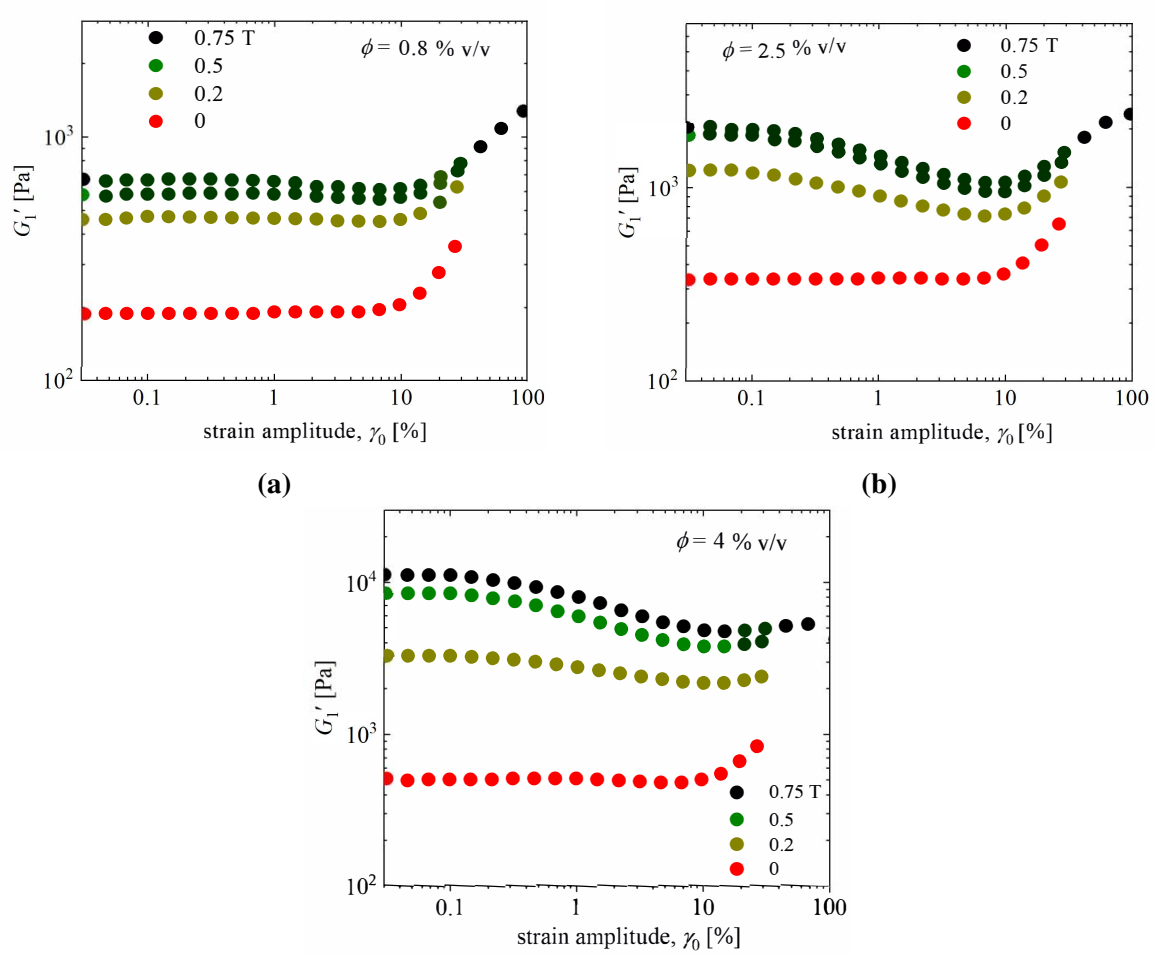

Figure 8.19: (a) At $\phi_{CI} = 0.8\%$ v/v, the a modest stiffening of linear shear modulus is observed, while the stiffening under nonlinear deformation (large strains) is apparently similar to that of pure fibrin network (Fig. 8.7). (b) While the linear modulus is enhanced by increasing ϕ_{CI} to 2.5%, the nonlinear properties show a leading order softening followed by stiffening. (c) At an even high particle concentration, ϕ_{CI} to 4%, the leading order softening in response to nonlinear external deformation is still observed followed by a fairly weak stiffening.

systems, e.g. higher power-law sensitivity og stiffenss ratio to the magnetic field strength. First, comparisons of the magnetorheological performance of the systems studied here are made with the literature though material performance charts that highlight such differences. Next, a modeling approach is presented to describe such features of magnetorheological response in the composites. To this effect, some of the established ideas in the magnetorheological modeling and semiflexible polymer networks are utilized.

8.4.1 Material Performance Charts

Figure 8.20, plots the stiffness-change properties of various magnetorheological elastic systems that have been presented in the literature [252, 253, 254, 255, 256, 257, 14, 258]. Fig. 8.20 a plots the power-law exponent of the shear modulus dependence of magnetic field strength ($G \sim B^n$) against the linear shear modulus of the systems in the absence of field. Two key features are evident: (1) the sensitivity (quantified by the value of n) is significantly higher for our systems than the systems presented in the literature both via experiments and theory, and (2) the fibrin-magnetic particle composites are relatively much softer than the traditionally studied systems. Fig. 8.20 b shows the range relative stiffening, $G(B)/G_0$, achievable under the application of an external magnetic field ($G \sim B^n$) against the linear shear modulus of the systems in the absence of field. Again, we see that the relative stiffening that we can achieve via fibrin-particle composites is significantly higher. Note that this however does not mean the absolute change in the stiffness follows the same trend. In the following sections, we model the systems studied in this work and provide insights into the microstructural features that may dominant the mechanics of the composites we presented.

8.4.2 Modeling Magnetorheologcal Response

The MR effect in magnetorheological fluids, hydrogels, and elastomers is attributed to interactions between magnetic particles that act as magnetic dipoles under an externally applied magnetic field [259, 260]. In magnetoelastomers, depending on whether a field is applied before or after crosslinking, particles can either form chains or have other types of distribution. Most experimental and theoretical studies on magnetoelastomers have employed flexible polymeric scaffolds, and in general such systems have micron sized particles embedded in a polymer matrix whose mesh size is significantly smaller than the particle size, essentially a continuum elastic matrix [261, 13, 262, 263, 251, 259, 260, 14]. In continuum sense, the flexible polymeric matrices exhibit a linear stress-strain relation up

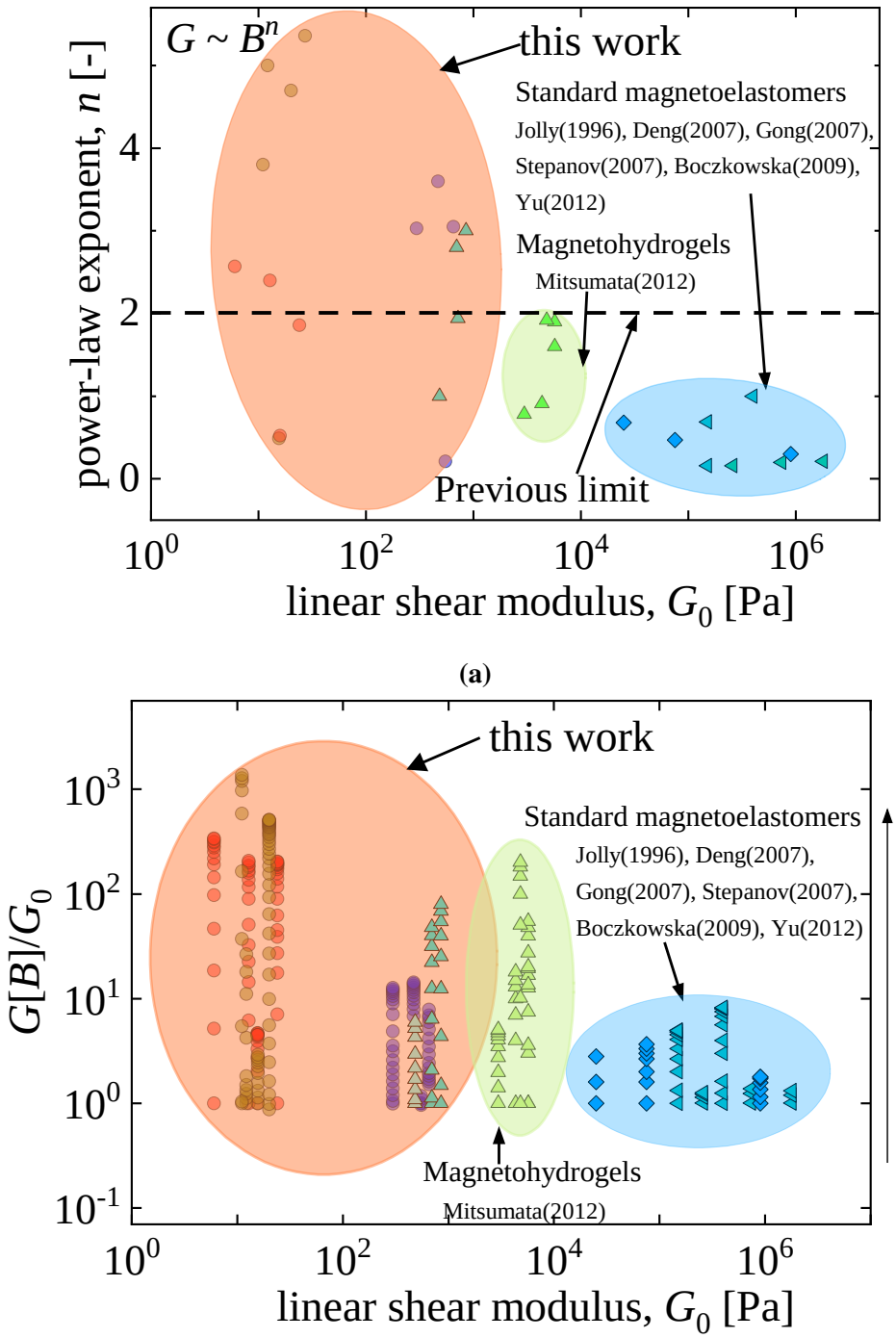

Figure 8.20: Material performance charts. (a) Ashby style chart comparing the maximum sensitivity (power-law exponent, n for various systems studied in the literature in comparison to the systems considered in this study against the linear shear modulus G_0 in the absence of magnetic field. (b) Ashby chart comparing the maximum stiffening ratio $(G(B)/G_0)$ in various systems. In all the cases the intensity of magnetic field strength varies between $(0-1)$T.

to large strains when compared to their semiflexible counterparts, and hence their mechanical properties can be described by a constant elastic modulus for the particle displacements involved.

A simple explanation of the magnetic field-dependent stiffening of material response is the field-dependent magnetic interaction energy that exists between the magnetic particles (dipoles) in addition to the elastic deformation energy of the polymer matrix [262, 263, 251]. Hence, the shear modulus can be expressed as a superposition of the elastic modulus from the polymer chains deformation and the changing magnetic dipole interactions as a result of the applied external deformation,

$$G(B) = G_0 + G_m(B) \tag{8.1}$$

An inherent assumption in such an analysis is that the deformation energy of the polymer matrix and the magnetic dipole interaction energy are independent of each other. Next, an approach described in the literature is used to evaluate the term $G_m(B)$ on the right hand side of Eq. 8.1.

Evaluating Magnetic Dipole Interactions

The potential energy between magnetic dipoles F_m can be expressed as a sum over all the possible pair-potentials between the dipoles with the dipole moments $\mathbf{m}_i$ and $\mathbf{m}_j$, connected by a radial vector $\mathbf{R}_{ij}$, as follows [262, 264]

$$F_m = -\frac{1}{V}\frac{\mu_r \mu_0}{4\pi} \sum_{\substack{i,j \\ i \neq j}} \left[\frac{3(\mathbf{m}_i \cdot \mathbf{R}_{ij})(\mathbf{m}_j \cdot \mathbf{R}_{ij})}{|\mathbf{R}_{ij}|^5} - \frac{(\mathbf{m}_i \cdot \mathbf{m}_j)}{|\mathbf{R}_{ij}|^3} \right] \tag{8.2}$$

where μ_0 is the permeability of vacuum, V is the volume of the sample, and μ_r is the relative permeability of the medium (assumed to be 1 from here on). Assuming two particles (with magnetic dipoles $\mathbf{m}_i$ and $\mathbf{m}_i$) and having identical geometry and magnetic properties, the dipole strength $|\mathbf{m}_i| = |\mathbf{m}_i| = m$ can be expressed in terms of the particle magnetization M as $m = v_0 M$, where $v_0 = \frac{4\pi}{3}a^3$ is the particle volume, a being the radius of the particle. The particle magnetization can then be related to the external magnetic field strength $B = |\mathbf{B}|$ by the Fröhlich-Kennely equation [265]

$$M[B] = \frac{M_s(\mu_{ini} - 1)(B/\mu_0)}{M_s + (\mu_{ini} - 1)(B/\mu_0)} \tag{8.3}$$

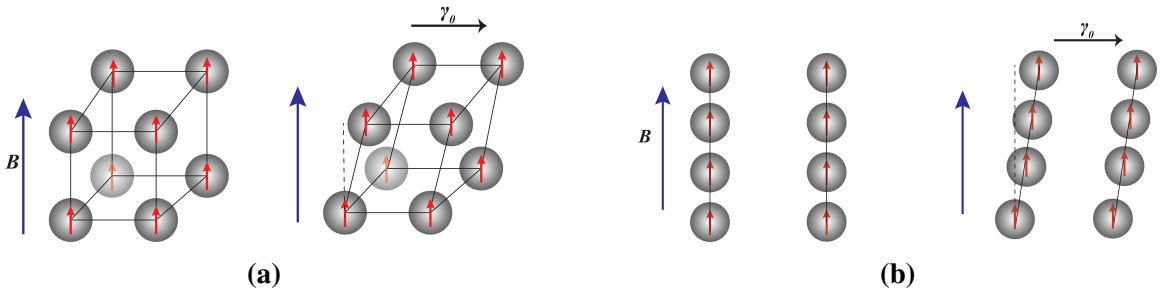

Figure 8.21: Spatial distribution of particles. (a) A uniform distribution assumed to be represented by a cubic lattice structure. (b) A chained distribution.

where M_s is the saturation magnetization and μ_{ini} is the magnetic permeability of the particle. Without losing any generality, we assume the external magnetic field **B** is aligned with the y-axis, and a simple shear deformation (in the $x-y$ plane) modifies the x-component of $\mathbf{R}_{ij}$. The total magnetic interaction energy of the sample (Eq. 8.2) hence can written as

$$F_m(\gamma, B) = -\frac{\mu_0 M[B]^2}{4\pi}\frac{N}{V}\sum_i \left[\frac{3(R_{i,y})^2 - |\mathbf{R}_i(\gamma)|^2}{|R_i(\gamma)|^5}\right] \tag{8.4}$$

where N is the total number of dipoles and $\mathbf{R}_i$ is the radius vector $\mathbf{R}_{i,j}$ with $j-th$ particle centered at the origin. Hence, the contribution to the shear modulus from the magnetic interactions can be evaluated as

$$G_m(B) = \frac{\partial^2}{\partial\gamma^2} F_m(\gamma, B)\bigg|_{\gamma\to 0}. \tag{8.5}$$

At low field strength Eq.8.3 gives $M \sim B$, hence $m \sim B$. Thus Eq. 8.5 implies $G_m \sim B^2$. Under an external shear deformation, the contribution from magnetic interactions is additive to that of elastic contribution from polymer chains. This leads the commonly observed enhancement in the shear modulus of magnetoelastomers of the form, $G = G_0 + cB^2$, where G_0 is the elastic shear modulus of the polymer matrix (with rigid inclusions and absence of magnetic field). To simplify the evaluation of magnetic interaction energy, we assume two simplified particle distributions as shown in Fig. 8.21. A simple cubic arrangement is used to approximate the uniform particle distribution and a chained distribution mimics the scenario when the particles undergo large displacements and align to form chains in the direction of field lines.

Next, the comparison of the simple procedure described above to account for the MR effect in linear elastic materials is made against the results that were obtained for the MR yield stress fluids. The idea here to verify that the simple model is able to capture the quantitative trends in the well studied systems of MR yield stress fluids.

Our experiments with CI particles suspended in yield stress fluids of Xanthan gum (Fig. 8.3) and carbopol (Fig. 8.4.) closely agree with the model describe above. Dipoles in both the cases align into chains along the direction of magnetic field lines (Fig. 8.5). In general for the system involving magnetic particles suspended in matrices (polymeric network or yield stress fluid), its is energetically favorable (lower magnetic potential energy) for the magnetic dipoles to align into chains parallel to the direction of external magnetic field. However, particles need to overcome several other barriers to reach such a configuration, e.g. in the case of submicron or nanoscale particles, the thermal fluctuations may tend to perturb the particles from the chained structures, or in a yield stress fluid, the dispersed particle must overcome the static yield strength, σ_y, of the matrix to plastically deform the surrounding matrix and align into chains. An estimate of such magnetic stresses on the surrounding fluid matrix is given by

$$\tau_{mag} = \frac{f_{mag}}{4\pi a^2}. \tag{8.6}$$

The magnetic force between two attracting dipoles of strength $m(B)$ with their centers separated by a distance R is given by [13]

$$f_m = \frac{3\mu_0 m(B)^2}{R^4} \tag{8.7}$$

Since, the magnetic stress depends on magnetic field strength, we expect that beyond a critical value of magnetic field, the magnetic dipoles will be uniformly distributed within the matrix, and once the magnetic stress exceeds the yield strength, they will begin to align into chains. Hence, at low field strengths we expect that the predictions based on cubic lattice (uniform) distribution to agree with the experiments, and at high field strengths, the chained distribution predictions should match the experimental observations. For the cases of CI particles in Xanthan gum, since the yield strength of fluid is very small, we expect the chained predictions to match the experiments in almost the entire range of field strengths. Fig. 8.22 shows the close agreement between the experiments with Xanthan-CI systems and the model predictions.

For the case of varying yield strength fluids in Carbopol-CI system we expect the de-

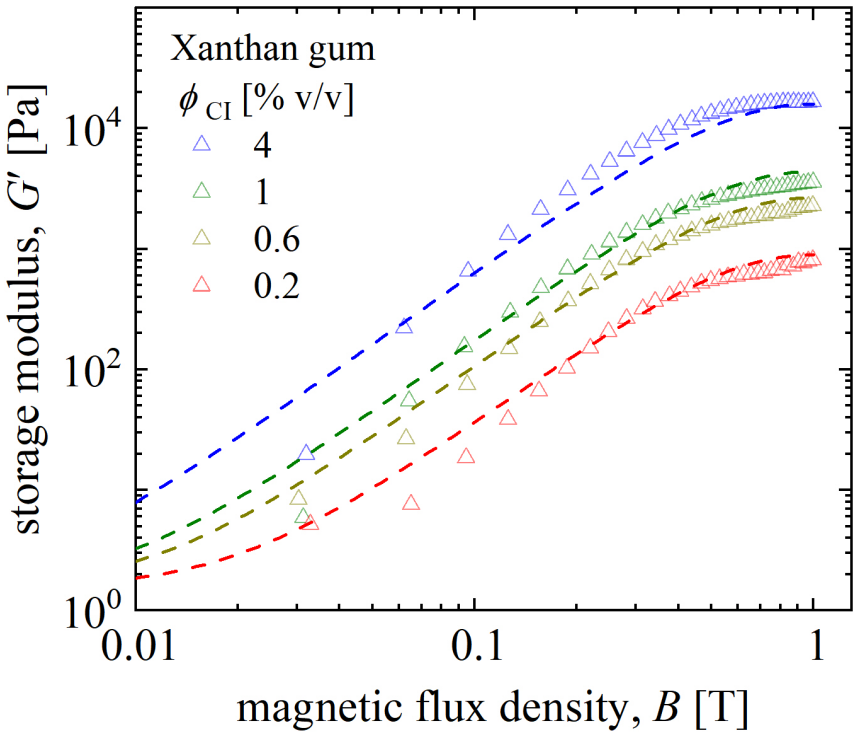

Figure 8.22: Comparison of model predictions with the experiments. The predictions assuming chained distribution (dashed lines) agree well with the response of magnetorheological system of Xanthan gum and CI powder.

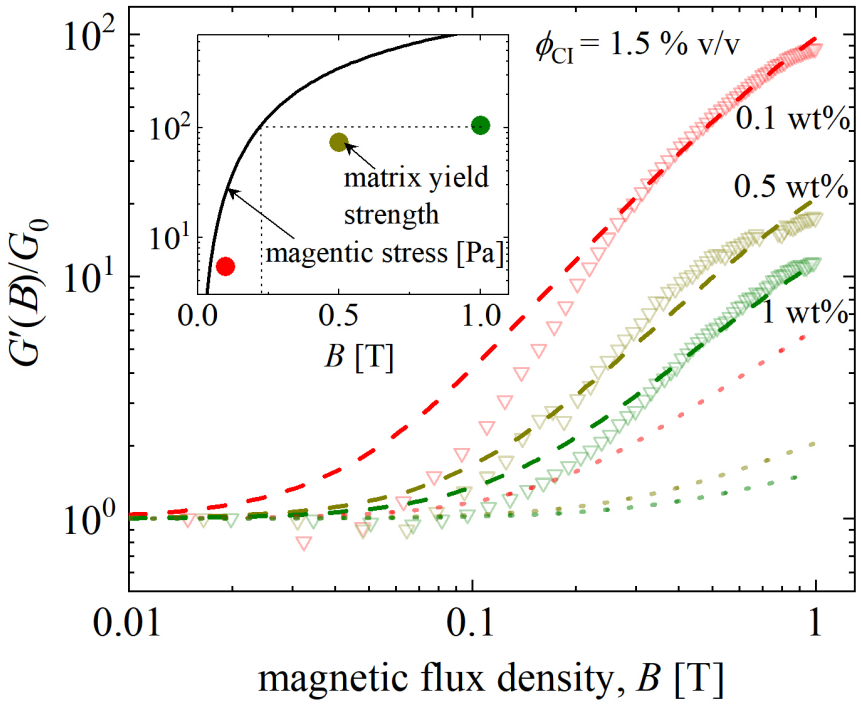

Figure 8.23: Comparison of model predictions with the experiments for the Carbopol-CI system. The cubic lattice predictions (dotted lines) match well the the experiments at low strengths of magnetic field, while at high field strengths the chained distribution predictions (dashed lines) agree well. (inset) The estimate of the stress imposed by a magnetic particle (dipole) on the surrounding matrix is shows by the solid line and the experimentally measured yield strength of the composite in the absence of field is shown by solid circles.

viation from cubic lattice arrangement beyond a threshold magnetic field. The inset of Fig. 8.23 shows the comparison of estimated magnetic stress and the yield strength of various experimental systems. The trends from predictions show that the deviation from the cubic lattice predictions beyond a critical field strength. At high field strengths, the chained predictions closely follow experiments in all cases. As noted before, since the model in an equilibrium state model, it is unable to predict trends when the distribution changes from cubic to chain-like.

Modeling Fibrin-Magnetic Particle Composites

The fibrin-particle composite systems that we discussed in this work have several contrasting features to the analysis described in previous sections: (1) the mesh size (ξ) of semiflexible fibrin network is comparable to the CI particle $(2a)$ or much larger than the submicron Fe particle, (2) the fibrin network exhibits a highly nonlinear stiffening response (Fig. 8.7) compared to the flexible polymers used in prior studies [251, 263, 14]. Hence,

the linear continuum approach that we summarized before is not directly applicable to the fibrin-particle composite presented in this work. Based on our rheological and microstructural observations, we expect new physics in the underlying system. In the fibrin-particle composite system that we used in experiment, the fibrin mesh is chemically cross-linked with fixed junctions. The volume fraction of fibers is typically very low and the composite has significant pores filled with solvent (water). Hence, particle rearrangement in the crosslinked fibrin matrix will depend on the size of particles relative to ξ of the crosslinked network.

We envision three different scenarios purely based on the geometric constraints as shown in Fig. 8.24. The distinct scenarios that we envision are (a) $2a > \xi$, particles are physically arrested inside the fibrous mesh, e.g. for the case of CI particles in the fibrin mesh with $c_f = 6.4$ mg/ml, (b) $2a < \xi$, particles can move through the mesh when they experience magnetic forces, and can align into chains, e.g. for the case of submicron Fe particles in the fibrin mesh with $c_f = 1.6,\ 6.4$ mg/ml, and (c) $2a \approx \xi$, particles can show both the arrested and chained behaviour, e.g. for the case of CI particles in the fibrin mesh with $c_f = 1.6$ mg/ml. Such scenarios are qualitatively consistent with the X-ray CT images.

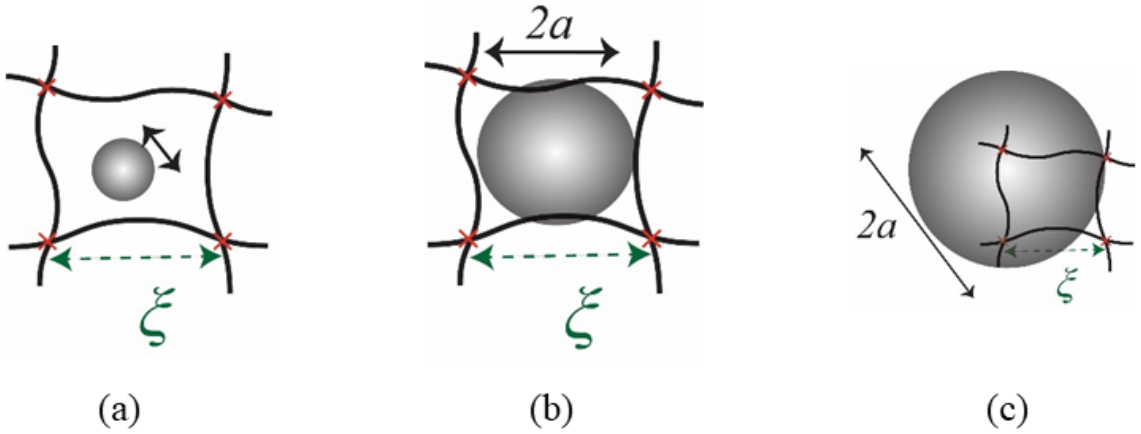

Figure 8.24: Schematic of different cases considered in this work. The ratio of particle size to mesh size is varied either by changing the particle size (micron size CI particles and submicron sized Fe particles) or by varying the fiber concentration.

Interaction forces between the embedded magnetic dipoles can likely deform the surrounding matrix, and the magnitude of such forces will be determined by the particle distribution function, particle volume fraction, and strength of the applied field. Owing to the strain-stiffening nature of the crosslinked fibrin matrix, even nominal deformations can induce a nonlinear response from the matrix (Fig. 8.7). Hence, unlike the typical approach adopted in magentoelastomers, where the flexible polymer matrix would typically not undergo noticeable nonlinear deformation, we propose that in our system, the elastic energy

of the fibrin matrix is indirectly dependent on the magnetic field strength.

Fig. 8.25 shows the estimated values of stress that dipoles, distributed uniformly inside the fibrin network, apply on the mesh. In both the cases, $c_f = 1.6$ and 6.4 mg/ml, it is evident that the magnetic stress exceeds the critical stress value, beyond which significant nonlinear response of fibrin network is observed, beyond a critical magnetic field strength at various particle concentrations. In the case of $c_f = 1.6$ mg/ml, we also expect that the dipoles can irreversibly deform the mesh. Thus, the overall stiffening that we observe for fibrin-magnetic particle composites has a contribution for stiffening polymer mesh (that depends on the strength of magnetic interactions between the particles).

We now derive a scaling prediction for the fibrin mesh stiffening as a function of magnetic field strength. We assume individual filaments between the chemically crosslinked junctions are inextensible. As the network is stressed, the thermal undulations in the fibers are pulled out. The force-extension relationship for such an inextensible fiber scales as $f \sim (1-x)^2$ as $x \to 1$, where x is the the end-to-end distance between the junctions normalized by the contour length of the fiber between the junctions [237, 220, 127]. Thus, the spring constant k for such a fiber scales as $k \sim \frac{\partial}{\partial x} f \sim f^{3/2} \sim \sigma^{3/2}$. Thus, the shear modulus, $G \sim \sigma^{3/2}$ [237, 220]. By force balance, the stress σ experienced by a fiber at a radial distance r from the center of a magnetic dipole scales as $\sigma \sim f_m/r^2$. Thus, we get the scaling relationship between shear modulus and the magnetic dipole moment as,

$$G \sim m(B)^3/(r^3 R^6). \tag{8.8}$$

Figure 8.27 shows the comparison of model predictions with the experiments for the case with $c_f = 1.6$ mg/ml fibrin network. We envision this case is represented by Fig. 8.24 b. It is evident that the predictions from uniform distribution (cubic lattice) agree well with the experiments at low field strength. Beyond a critical field strength, the uniform modulus predictions underpredict the observed modulus. We also find that the predictions from assuming a chained structure typically over predicts the observed modulus. The trends from the scaling predictions described by the scaling law discussed above tends to describe the stiffening, but there are systematic deviations from the experiments. Since the mean mesh size in this case is comparable to the particle diameter, we expect a combination of all the above effects. Note that the scaling law is shifted by an empirical front factor to visually match the modulus at the onset of sharp stiffening.

Figure 8.28 shows the comparison of model predictions with the experiments for the case with $c_f = 6.4$ mg/ml fibrin network. We envision this case is represented by Fig. 8.24 b. Similar to the case with $c_f = 1.6$ mg/ml fibrin, it is evident that the predictions from uniform distribution (cubic lattice) agree well with the experiments at low field strength.

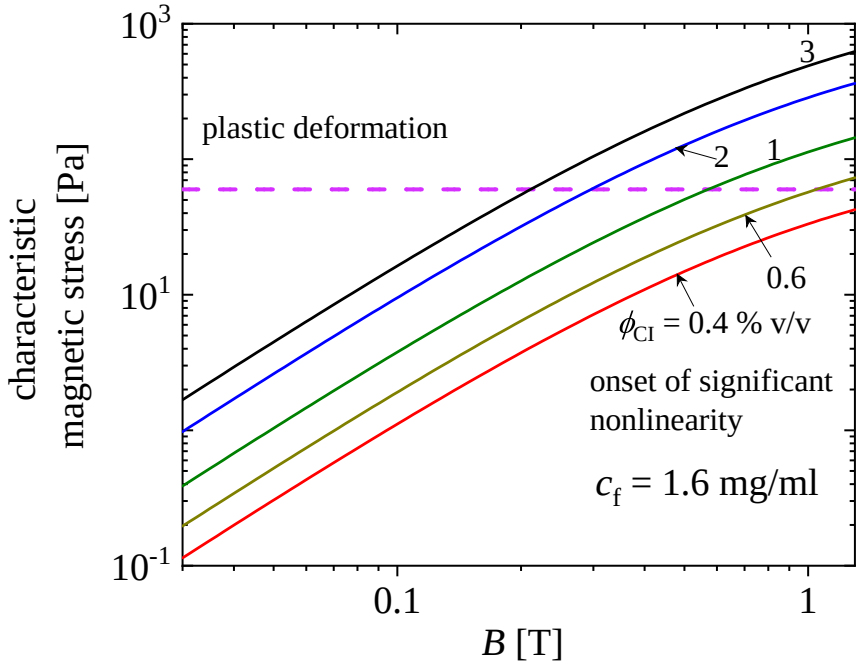

(a)

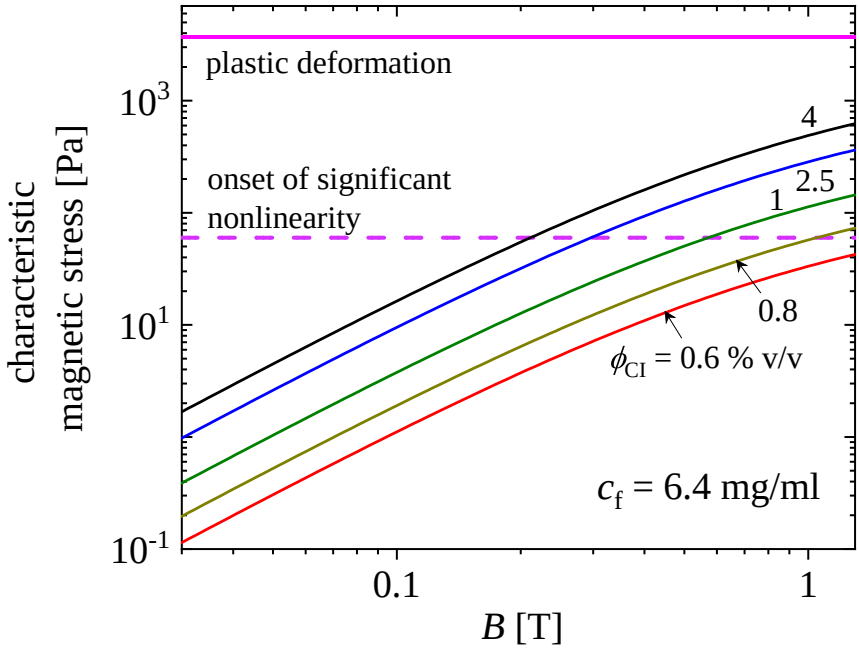

(b)

Figure 8.25: Characteristic magnetic stress on the fibrin mesh due to dipole interaction as the CI particle volume fraction and the field strength (B) is varied for (a) $c_f = 1.6$ mg/ml and (b) $c_f = 6.4$ mg/ml. The dashed purple lines show the characteristic stress at the onset of nonlinear stiffening in fibrin mesh. The solid purple lines indicate the stress to irreversibly deform the crosslinked fibrin networks.

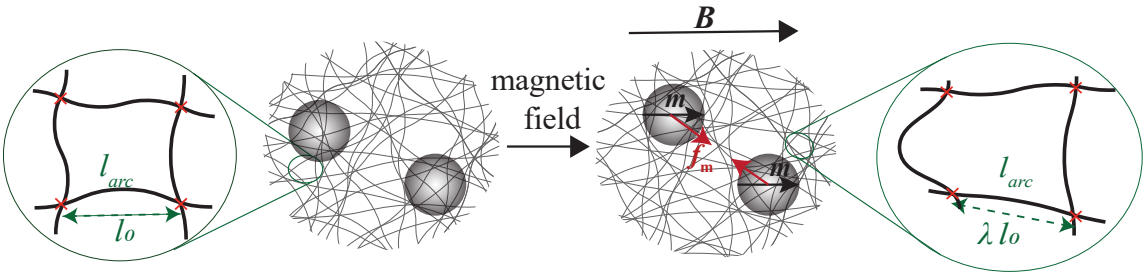

Figure 8.26: Schematic of the fibrin-CI composite model. An isotropic inextensible fibrous network with mean end-to-end distance l_0 between the crosslinked junctions and contour length l_{arc} is assumed to be deformed by an embedded magnetic dipole which experiences a force due to other dipoles. In mean-field sense we assume that this in-homogeneous deformation results in a deformed state where the end-to-end distance between the crosslinked junctions changes by a factor λ. λ depends on the stiffness of the polymer matrix, volume fraction ϕ_{CI} of the particles and the magnetic field density B.

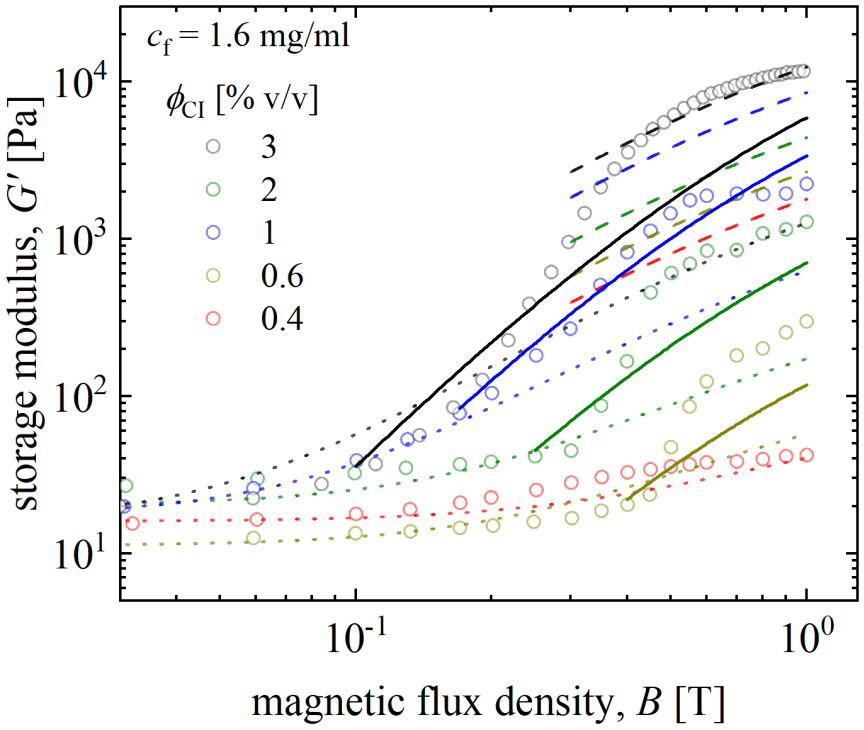

Figure 8.27: Model predictions for CI-fibrin composite (c_f = 1.6 mg/ml) (case Fig. 8.24 b). At low field strength the cubic lattice predictions (dotted lines) agree closely with the experiments. At high field strengths, the chained-distribution predictions (dashed lines) overestimate the stiffening. The solid-lines show the predictions from Eq. 8.8.

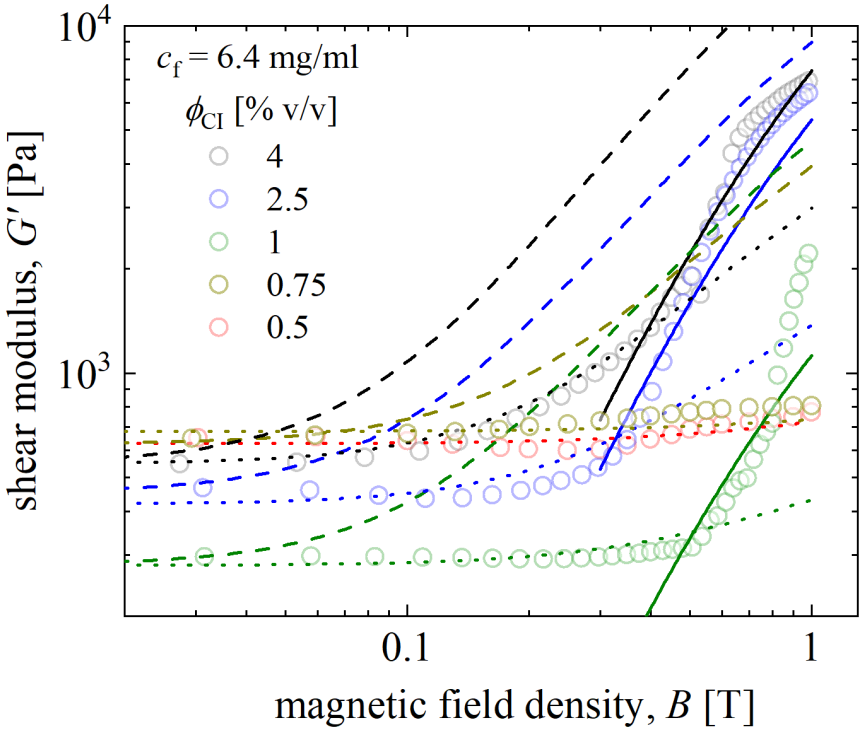

Figure 8.28: Model predictions for CI-fibrin composite ($c_f = 6.4$ mg/ml) (case Fig. 8.24 c). At low field strength the cubic lattice predictions (dotted lines) agree closely with the experiments. At high field strengths, the chained-distribution predictions (dashed lines) overestimate the stiffening. The solid-lines show the predictions from Eq. 8.8.

Beyond a critical field strength, the uniform distribution model predictions do not capture the sharp change in the modulus. The chained structure typically over predicts the observed modulus. In this case,we find that the trends from the the scaling predictions described by the scaling law discussed above, tend to closely follow the stiffening trend, but there are systematic deviations from the experiments. The deviations can be attributed to the polydispersity in the particle size distribution. The particles which are much smaller than the mean mesh size, may form chains. But we conclude that the leading order effect comes from a superposition of components from uniformly distributed dipole interactions and fibrin mesh stiffening.

Figure 8.29 shows the comparison of model predictions with the experiments for the fibrin-Fe composite at $c_f = 1.6$ mg/ml. In this case, we expect the formation of chains at large enough magnetic fields. Since, the particles form aggregates at low field strengths, magnetic interactions need to overcome the interactions holding the particles in aggregates. At large fields, we see the chained-model predictions closely in agreement with the experiments. At high concentration of particles ($\phi_{Fe} = 0.5$ %), the scaling predictions from the mesh stiffening model also comes in close agreement with the experiments. Figure 8.30

shows the comparison of model predictions with the experiments for the fibrin-Fe composite at $c_f = 6.4$ mg/ml. Here also we find that the chained predictions match the experiments fairly well at low concentrations ($\phi_{Fe} < 2$ %). But at highest concentration ($\phi_{Fe} = 4$ %), we find that even the chained prediction cannot account for the observed stiffening. The previously described scaling law matches the stiffening in this case very well.

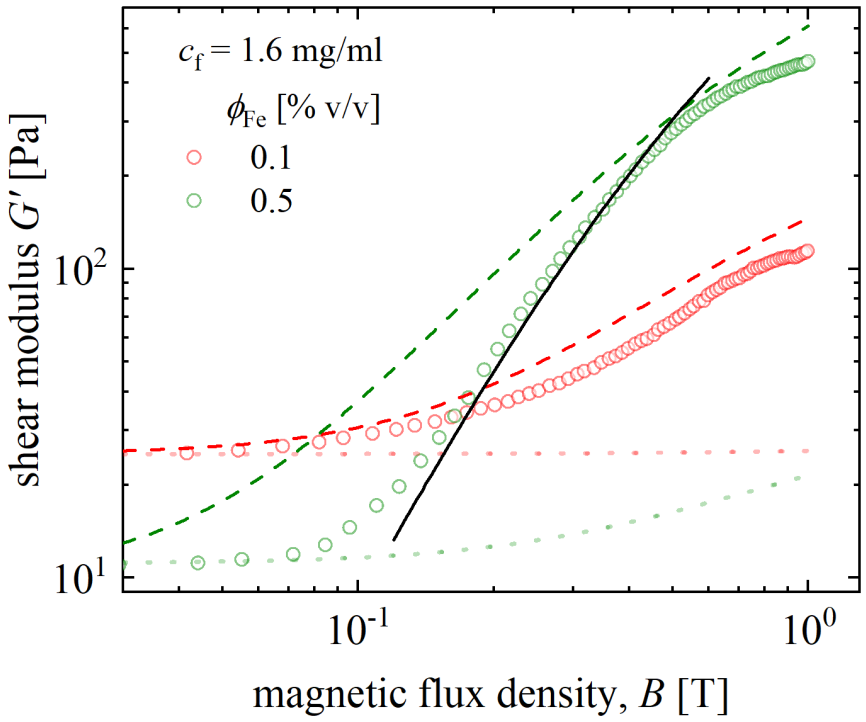

Figure 8.29: Model predictions for fibrin-Fe composite ($c_f = 1.6$ mg/ml) (case Fig. 8.24 a) Dotted and dashed lines represent the predictions assuming uniform (cubic lattice) and chained distribution, respectively. The solid-lines show the predictions from Eq. 8.8.

The different systems that we utilized in this work are capable of achieving magnetic field responsive stiffening. We found that mechanisms of achieving stiffness are different, and hence so is the sensitivity of modulus to the field-strength. For the case of magnetic particles suspended in a yield-stress fluid, we observe that the dipoles undergo large displacements to align into chains in the direction of applied field, which is the primary reason for drastic stiffening. In the scenarios presented in Figs. 8.24 a and b (fibrin-Fe and fibrin-CI systems ($c_f = 1.6$ mg/ml)), we find that a combination of particles partially chaining and deforming the polymeric mesh lead to the drastic stiffening. While in the case presented in Fig. 8.24 c fibrin-CI systems ($c_f = 6.4$ mg/ml)) the leading case of stiffening is dipole induced network deformation.

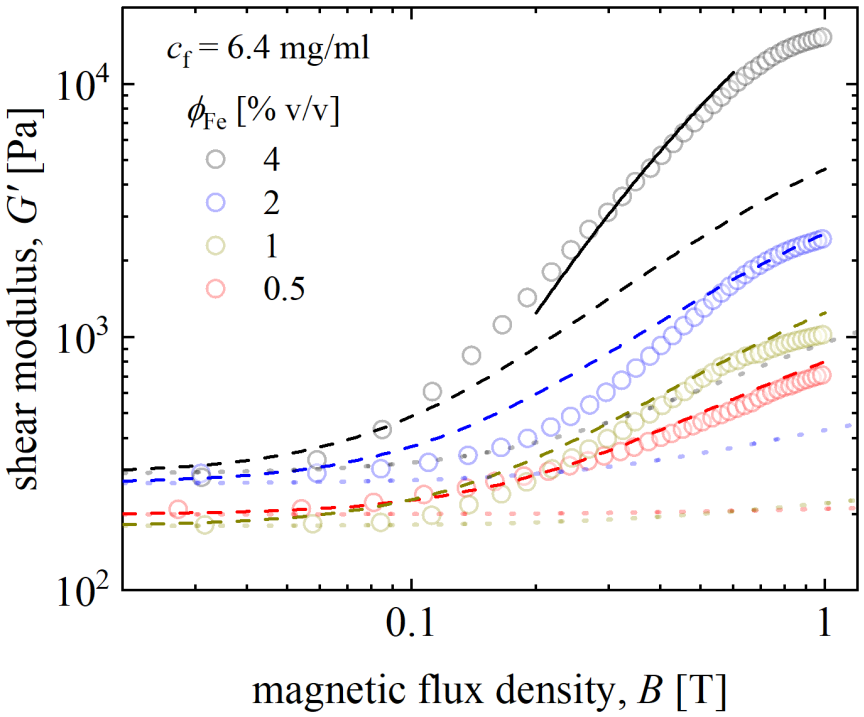

Figure 8.30: Model predictions for fibrin-Fe composite ($c_f = 6.4$ mg/ml) (case Fig. 8.24 a) Dotted and dashed lines represent the predictions assuming uniform (cubic lattice) and chained distribution, respectively. The solid-lines show the predictions from Eq. 8.8.

8.5 Summary

We presented a new approach of fabricating magnetically responsive soft composites using semiflexible polymer matrix (chemically crosslinked fibrin). Our results highlight that unlike traditional magnetorheological elastomers formed using flexible polymer scaffolds, the senstivity to the applied fields can be drastically enhanced due to the strain-induced stiffening of the semiflexible polymer matrix. Additionally, we show that the geometric length-scales that originate in the composites (particle size and mesh size) dictate the physics behind the stiffening response. The simple scaling arguments that we present elucidate the microstructural understanding of the system. With the continuing progress in the fields of soft robotics, drug delivery and artificial muscles, and the recent progress made in synthesis of synthetic semiflexible network, the ideas described here should pave the way for design of materials for new applications.

Acknowledgement

This work was performed at the University of Illinois and supported by DOE-BES under Grant No. DE-FG02-07ER46471 administered through the Materials Research Laboratory. We thank Leilei Yin, Beckman Institute for the help with X ray micro CT imaging.

CHAPTER 9

CONCLUSIONS AND OUTLOOK

From the results discussed in the previous chapters of this thesis, it is clear that the combination of polymer-colloids or polymers of very different length scales can produce materials with properties that are very different from their constituents in pure state. This is attributable to the competing physical phenomenon that occurs in the individual constituents, and the coupling of such phenomenon across the constituents that leads to unprecedented material response. Three major themes were studied as a part of this thesis.

First, a naturally occurring hydrogel, hagfish slime, that has an ultra-soft material response was studied. Through a combination of experiments and mathematical modeling, some of the key features of slime and the process of its formation were discovered. Through a non-standard method of relating rheology to material structure, and a comparative study across various soft systems, it was shown that unlike any other soft material, the relaxation exponent (and the fractal dimension) of hagfish slime remarkably constant across a very wide range of concentration. Such a remarkable feature may be desirable in the scenarios where the applications require the use of material in an uncontrolled setting. For example, hagfish slime inspired nonlethal weapons that can capsize or clog the target, and slime inspired adhesives which can work underwater. The results also indicate the double-network structure of hagfish slime where the large pore size network of threads dominate the linear/nonlinear properties of slime while the mucus network is likely formed with a much smaller pore size and gives slime its low permeability. Such an idea can be utilized to develop new materials where the strength and permeability can be independently controlled.

Hydrodynamic unraveling of hagfish skein was another key idea that was established in this thesis. Not only does it provide an alternative and rigorous view about the fast unraveling process, it has the potential to provide new ways of designing biomaterials which can undergo on demand expansion. For example, in drug delivery, where the drugs that can be injected/consumed in a compact way expand dramatically at the target site. Of course more insights into the packing and hierarchical looping of hagfish skein should accompany such efforts.

New understanding for the dynamics of pure pNIPAM suspensions focused on eluci-

dating the dynamics of such suspensions in different regimes. To the best of our knowledge, this is the first attempt to quantitatively understand structure, quiescent relaxation and shear elasticity, and nonlinear yielding of dense microgel suspensions using microscopic force based theoretical methods that include activated hopping processes. Further, the rich temperature-dependent behavior was studied, and we showed that the temperature leads to a concentration-dependent particle size change but also changes the interactions potential between the particles. With the growing interest in self-assembly of soft functional colloids that can form structures on various length scales, the fundamental work performed in this thesis can offer new ways to assemble structures. A key application that can benefit from this understanding is direct-wire writing (3D printing). The controllable stiffness (and yield strength) of such suspensions make them a strong candidate for such an application.

The stiffness changing soft composites that were demonstrated as a part of this work offer new methods of designing responsive soft materials. The proof-of-concept idea of utilizing the intrinsically nonlinear stiffening of semiflexible biopolymers with responsive particle suspensions can now be extended to new directions. In order to further control the interactions between the polymer-colloid and control the base stiffness of the composite, the possibility of using synthetic semiflexible polymers will be an exciting direction for future work. Recent development in the synthetic semiflexible networks from polyisocyanopeptides [230, 231, 232] with known and controllable chemistry for programming composites to exhibit dramatic stimuli-responsiveness such as strain-stiffening. An alternative route to achieve stimuli responsiveness using the core-shell structured colloidal particles that go beyond the present microgel design. Such particles hold the potential to be tuned over a wider range of reversible sticking/unsticking from the polymer mesh and thus expand the change of composite bulk properties induced by the particles.

Another fascinating direction that will enhance the potential of the magnetoelastomers (with mesh size bigger then the particle size) is to chemically tune the particles (e.g. repulsion) that can drive the particles back to uniform distributions within the polymer matrix after they have formed chains. This may offer the use of such composites where insulator-conductor transitions are required.

The flexibility in tuning the mechanical properties of the composites make them a potential material to develop adaptable manipulators for various biomedical applications e.g artificial muscles, grippers and tissue scaffolds. The degree of compliance which the composites offer both in their field sensitivity and dynamic moduli can be advantageous in wearable medical devices e.g. soft orthodics for human ankle-foot rehabilitation, cardiac actuators, soft wearable motion sensing suits etc [266, 267, 268, 269]. Such an approach may have drastic impact in healthcare as it offers improved tools for patient rehabilitation

and well-being. A potential challenge in using stimuli responsive composites is the requirement of large amounts of magnetic power to induce property changes. The superior sensitivity of the developed composites which may require low strength of magnetic field to modulate mechanics may overcome that challenge. One approach is to distribute the particles inhomogeneously inside the polymer mesh. This will locally vary the stiffness and can produce movements like bending/folding. The success of such robotic structures will rely on the ability to fabricate them. The advancement in 3D printing methods for soft materials has aided the construction of complex structures capable of functionality. Although printing a biomaterial such as fibrin is challenging using traditional fabrication methods, recently developed methods such as reversibly embedding soft gels into a secondary hydrogel [270] offers way to 3D print.

Recently, development of small scale soft robots capable of multimodal locomotion [271, 272, 273] using composite materials have gained significant attention (based on the principle that magnetic composites change their shape under the influence of magnetic field (magnetostriction)). Using the stimuli-responsive composites, strategies for movements like crawling can be developed by combining the ideas of inhomogeneous distribution of particles inside the mesh and a spatial-time varying external field. This experience should feed into achieving complex motion like flapping of wings which may enable swimming-like motion [274, 275]. Based on the success in initial efforts, careful consideration can be given to efficiently design the robot body plan and architecture. Consideration of biomimetic approaches that can be helpful in understanding the optimal design features from real organisms. A key difference in the proposed work compared to the literature will be the high degree of inhomogenity in the stress, and deformation field in the robots designed with the novel stimuli responsive material. This will help enhance the performance of the robot.

Appendices

APPENDIX A

HYDRODYNAMIC UNRAVELING OF HAGFISH SKEIN

A.1 Materials and Microscopy

Pacific (*Eptatretus stoutii*) and Atlantic (*Myxine glutinosa*) hagfish were maintained at the University of Guelph as previously described [42]. All housing, feeding, and experimental conditions were approved by the University of Guelph Animal Care Committee (Animal Utilization Protocol 2519). Hagfish were anesthetized before the extraction of exudate. Electrical stimulation near the slime glands resulted in the secretion of the exudate locally near the site of stimulation [42]. The exudate was collected directly from fish using a spatula, stored in a microcentrifuge tube at $10^{\circ}\mathrm{C}$. No buffer or oil was used to stabilize the exudate from Pacific hagfish and it was used within 2–5 hours from the time of extraction to ensure sample viability. The exudate extracted from Atlantic hagfish was stabilized under mineral oil and stored on ice for transport to the testing location [38].

For microscopy studies, an inverted optical microscope with brightfield imaging was used. To visualize a single skein unraveling, a very small volume of Atlantic hagfish exudate was added to a pool of artificial sea water and an isolated skein was located and observed under a flow created by manually disturbing the sample. For the network images, a precise volume of exudate from Pacific hagfish was introduced into a centrifuge tube containing artificial sea water ($1\,\mathrm{ml}$) and the contents were sloshed back and forth in the closed tube six times, similar to prior work [33]. Following this the sample looked like a cohesive mass. Gel samples of various exudate concentrations were transferred to glass slides with small wells. A Nikon 90i Eclipse microscope was used to visualize the network with differential interference contrast (DIC) to image the slime network.

A.2 Minimum Peeling Force

Assuming only van der Waals interactions exist at the peeling site, we estimate of the minimum peeling force required for peeling. For an inextensible fiber, with negligible

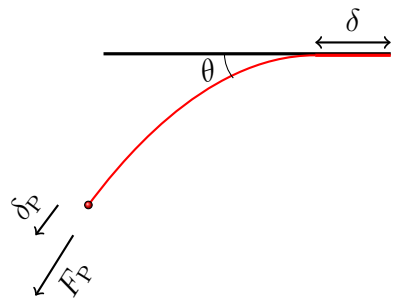

Figure A.1: Schematic of a fiber (red) peeling from a substrate (black).

bending energy storage during peeling, the work done by the peeling force F_{P} in moving a point on the fiber by a distance δ_{P} is $F_{\mathrm{P}}\,\delta_{\mathrm{P}}$ (schematic in Fig. A.1). The energy involved in creating new surface at the peeling site is equal to the van der Waals interaction energy released at the peeling site, given by $E_A A_{\mathrm{P}}$, where E_A is adhesion energy per unit area for van der Waals surfaces. The area created at the peeling site is $A_{\mathrm{P}} \approx (2r)\,\delta$, where r is the thread radius and δ is the displacement length of the peeling front created by the fiber displacement δ_{P}. The energy balance, rearranged, gives $F_{\mathrm{P}} = 2E_A\,r\,(\delta/\delta_{\mathrm{P}})$. For a wide range of peeling angles θ, $\delta_{\mathrm{P}} \sim \delta$ (note that $\delta_{\mathrm{P}} = \delta$ for $\theta = \pi/2$), and we get $F_{\mathrm{P}} \sim 2E_A r$. A typical adhesion energy for van der Waals surfaces is 50–$60\,\mathrm{mJ/m^2}$ [276, 277] and $r \approx 1\,\mu\mathrm{m}$, which gives $F_{\mathrm{P}} \approx 0.1\,\mu\mathrm{N}$.

A.3 Hagfish Defense in Suction Flow

Evidence of hagfish defense with slime secretion is available for both biting and suction feeding predators [23, 35]. Here, we treat the case where the predator creates a suction flow to engulf the prey. A good approximation of suction flow is provided by numerous experimental and computational studies [278, 279, 280, 281, 282]. A one dimensionless parametrization of an observed suction flow with bluegill fish is

$$u(x_g^*, t) = u(x_g^* = 0, t)(1 - 2.19x_g^* + 1.86x_g^{*2} - 0.70x_g^{*3} + 0.09x_g^{*4}) \qquad \text{(A.1)}$$

where $u(x_g^* = 0, t)$ is the flow speed at the mouth of the predator and x_g^* is the non-dimensional distance from the predator mouth normalized by the gape size (the diameter of the open mouth). In (A.1), both the velocity *and* the extensional strain rate decay for $x^* > 0$ (away from the mouth of the predator). The form (A.1) represents a time-varying velocity profile at the mouth of predator. Note that (A.1) applies outside the mouth. We do not have data for the flow profile inside the mouth, but for our purpose here we assume a constant

centerline velocity equal to the peak velocity (velocity at the gape), as if the flow was sucked into a constant diameter tube with a negligibly small boundary layer (Fig.A.2B). The velocity field is continuous, though the spatial derivative is not. This discontinuous strain rate is not a problem since we eventually integrate the velocity to get an average over the unraveled length. To simplify the analysis, we use a time-invariant version of this velocity profile. We note that (A.1) is obtained by polynomial fit to PIV data, and hence should only be used in the range of x_g^* in which it makes physical sense, i.e. monotonically decreasing $\partial u(x_g^*, t)/\partial x_g^*$, which is true only for $x_g^* < 1.36$. We use a gape length of $10\,\mathrm{cm}$, an approximate scale obtained from Fig.A.2A.

We solve for the case of a skein pinned at different locations x^* where the unraveling force is due to the drag on the unraveled fiber under the suction flow given by Eq. (A.1) (Fig. A.2C). The governing equations are the same as derived in the paper:

$$(\dot{L})^m = -4\pi\mu\,\alpha^{-1} L\,\delta(L)\left(\dot{L} + \bar{u}(L, X, t)\right). \tag{A.2}$$

Figure A.3 shows the numerical solution for this case. Compared to the case of uniform velocity field of $1\,\mathrm{m/s}$ solved in the paper, the unraveling time is longer with a spatially-varying velocity that decays away from the predator's mouth. The location of the pinning point of the skein has a huge impact on the unraveling timescales as shown in Fig. A.3, since being farther from the predator means a lower flow velocity and extensional strain rate. The strain rate for the chosen velocity profile outside the predator's mouth lies between $2.19\,\mathrm{s}^{-1}$ at $x_g^* = 0$ and $0.27\,\mathrm{s}^{-1}$ at $x_g^* = 0.9$. From the video evidence of hagfish-predator attack, we note that exudate is released at a distance less than one-third of the gape size. This proximity to the mouth, in this flow field, results in an unraveling timescale close to the physiological one. Note that we used a velocity profile that was experimentally obtained for suction feeding fish with a gape size of only $1.5\,\mathrm{cm}$ (bluegill). We therefore expect the magnitude of velocity in the real scenarios to be higher, and hence the unraveling times will be smaller for hagfish predators. It does pose the interesting possibility that smaller fish, with weaker suction flow, may not create a flow field that unravels the hagfish threads within hundreds of milliseconds.

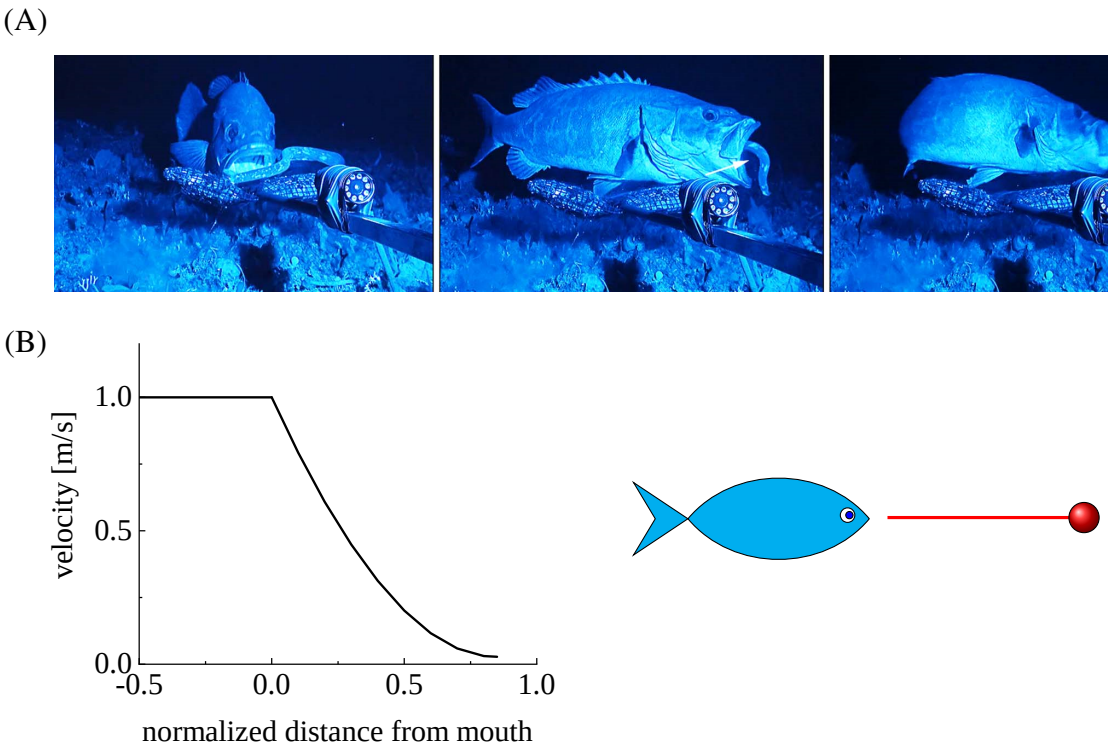

Figure A.2: (A) Evidence of hagfish (*Eptatretus sp.* 2) defense against suction feeding predator (*Polyprion americanus*, Atlantic wreckfish) (adapted from Zintzen et al. [23], by permission from SpringerNature). A suction feeding fish induces flow into its mouth by expanding its buccal cavity and drawnig its prey along with the flow. We hypothesize the suction flow to aid in unraveling of thread cells and set up the slime network. (B) The one-dimensional suction flow profile (A.1) with an assumption of constant velocity inside the predator's mouth. (C) A schematic of the fish-thread-skein system (not to scale).

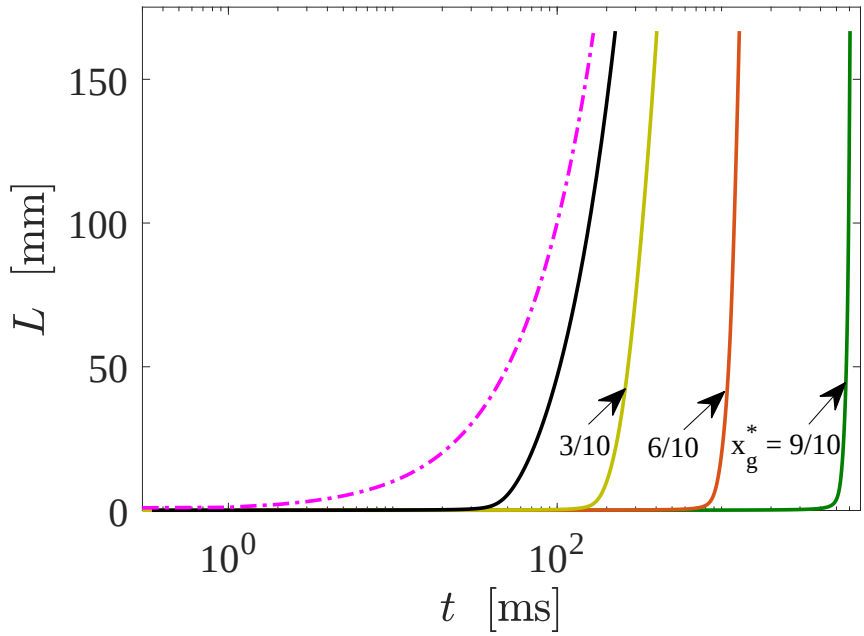

Figure A.3: Numerical solution (dashed black line) of (A.2) for the parameter values $R_0 = 50\,\mu\mathrm{m}$, $L_0 = 2R_0$, $\wp = 0.5$, $m = 1/2$, and velocity profile given by (A.1) with $u(x_g = 0, t) = 1\,\mathrm{m/s}$ with varying the location of the pinned point. Yellow, orange and green are the solution to the cases where the skin in pinned at locations $3/10$, $6/10$ and $9/10$ of the gape size ($= 10\,\mathrm{cm}$). Solid black line is the numerical solution for the case of constant velocity of $1\,\mathrm{m/s}$. The dotted line is the upper bound $L = L_0 + Ut$, with $U = 1\,\mathrm{m/s}$.

APPENDIX B

RHEOLOGY OF HAGFISH SLIME

B.1 Box-counting Fractal Dimension Evaluation

The universality in the time-dependence of strain evolution in creep experiments suggests an underlying self-similar structure. Such self-similarity very often arises from the fractal nature of the structure. A structure is deemed fractal if it is self-similar or length-scale independent (at least in a good approximation for some limited range of length scales). As a result, the structure appears the same under different magnifications. Most structures found in nature do not display exact self-similarity but rather statistical or average self similarity (i.e. the correlation function describing the structure has a scale invariant). Moreover, their scaling is not valid for all length scales, e.g. for a biopolymer fiber network, at length-scales larger than the mean distance between crosslinks, the scaling does not longer hold. A popular method to determine the fractal dimension, d_f, of a structure is using the box counting algorithm [283]. In simplest terms, box-counting involves super-imposing smaller and smaller square grids of normalized length, r (where r is box length divided by the characteristic length of the mapped area) over a thresholded image. The number of boxes occupied by the entity of fractal structure, N, is given by

$$N \sim r^{-d_f} \tag{B.1}$$

where N is the number of boxes of a linear size r that covers the structural features present in a two-dimensional plane. d_f is the box-counting fractal dimension. At a given value of r, the number of boxes needed to cover an array of features should be minimized; hence, the grid is progressively rotated at 90° at set angular increments. The number of occupied boxes is counted and only the minimum value of N is used to calculate d_f. If the set is fractal, the log-log plot of N versus l obeys a straight line with slope $-d_f$, which takes absolute values in the interval $[1 - 2]$. To obtain evenly spaced points in the log-log plot, the box sizes employed follow a geometric progression (TruSoftInt'l Inc., 1999). The maximum size of the box was selected as to not greatly exceed the distance between the crosslinks.

Prior to analysis, images were inverted using Fiji Software [284], to represent fibers as white features in a black background. Additionally, undesirable features like intact thread cells or air bubbles were also removed. $N(r)$ was calculated using the box counting method included in Benoit 1.3 software package (TruSoft International Inc., St. Petersburg, FL). To estimate the fractal dimension, we fit the power-law form described by Eq.B.1, minimizing the residual sum of squares. The fits to the complete data sets obtained from the Benoit software are shown by the red lines in the figures S1-S3. In using this method, it is important to note some of the major limitations of the box fractal dimension including: (1) the range of the power law: is limited in one end by the finite resolution of the fractal object and on the other end by the fractal's own finite size and (2) lack of general means of calibration (i.e. there are not standard profiles or correction factors applicable to the data) and (3) lack of provision for weighting according to the number of data points inside the box (i.e. a box is counted as occupied and it is considered in the calculation of N(d) irrespective of whether it contains one point or a relatively large number of points). The main uncertainties associated with the implementation of the box-counting algorithm and sample preparation include: (1) Lack of standard method for estimation of the slope from the log-log plot. In our study, we have chosen to calculate the slope from the entire plot, while some other researchers opt to fit only a section of the plot, which would change the power law exponent. (2) Non-uniformly populated samples especially at higher concentrations of slime. In this case, a lack of effective weighting to the boxes as earlier mentioned, can affect the estimation of the fractal dimension. Additionally, we also evaluate the box-counting fractal dimension using an improved box-counting technique [285]. This method defines a lower limit on fractal behaviour (r_{cutoff}) using the condition $\frac{ds}{dr} \rightarrow 0$, where s is the standard deviation from a linear regression equation fitted to $log(N)$ versus $log(r)$ with data for $r < r_{cutoff}$ sequentially excluded. We observe an increased value of d_f using the improved box-counting technique, consistent with the literature. Nevertheless, our analysis shows that the network of fibers in hagfish slime is able to assemble into a fractal structure under mixing, Fig. S1-S3. To estimate the true fractal dimension of hagfish slime, we further need to take into account the structures formed by the mucus in the slime. Such effort is beyond the scope of the work described here.

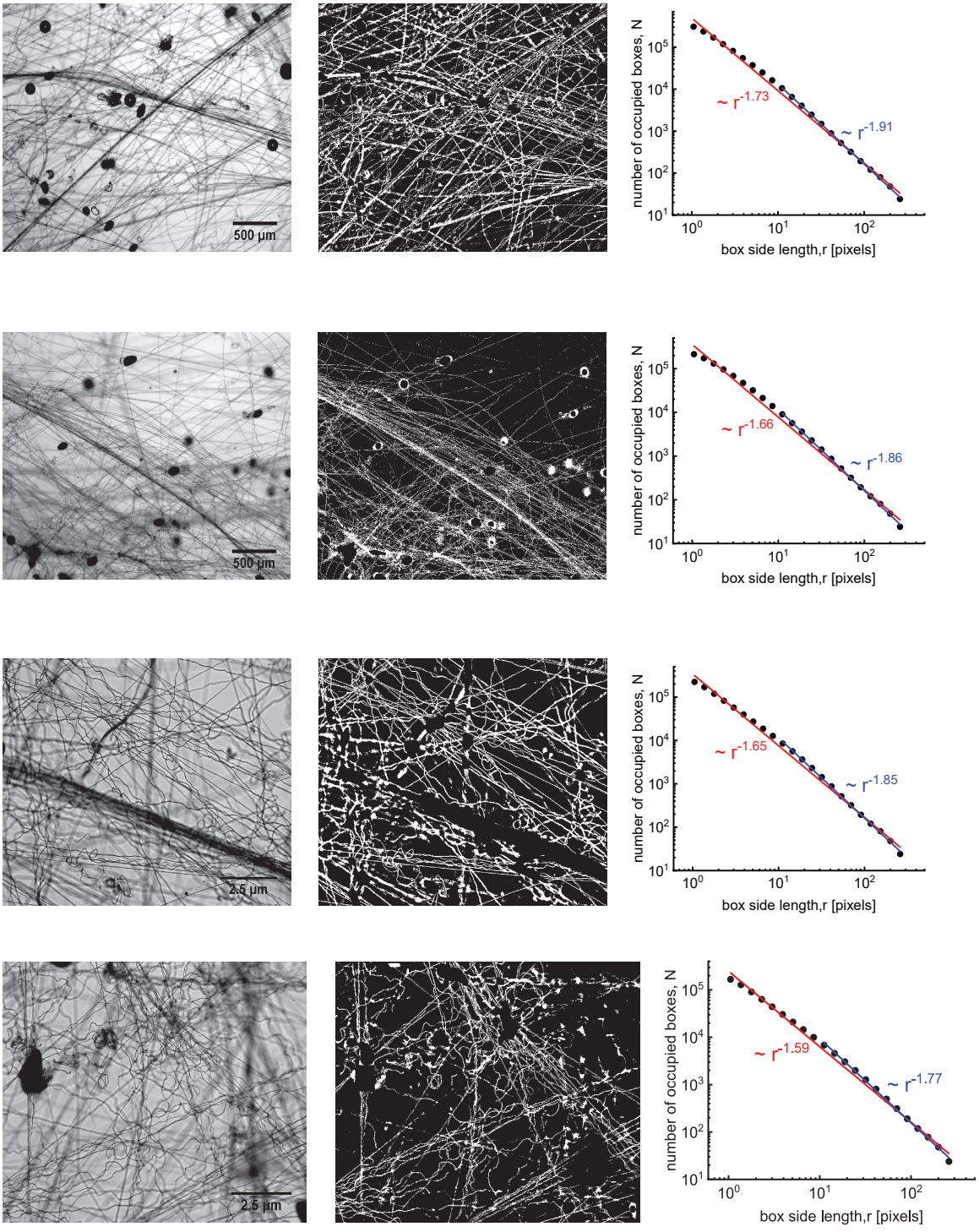

Figure B.1 (cont.)

Figure B.1 (cont.)

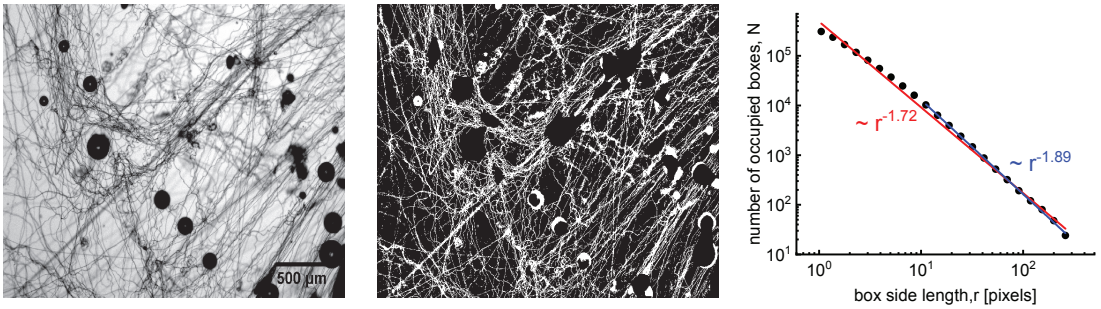

Figure B.1: Fractal analysis of microstructure of hagfish slime (0.8 mg/ml). The first column gives the raw DIC image followed by the thresholded images in the second column. The fractal dimension of obtained using the power-law fit to the data, as shown in third column.

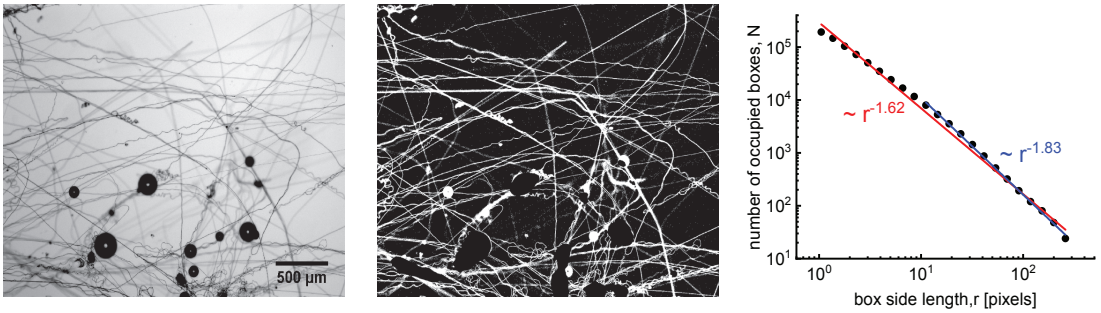

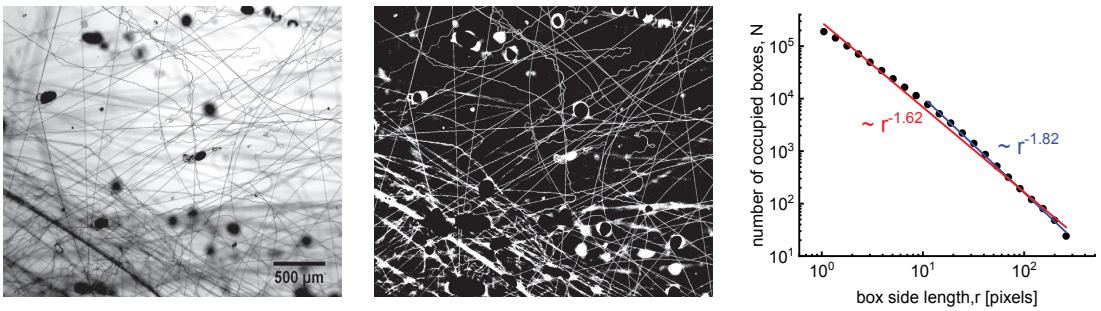

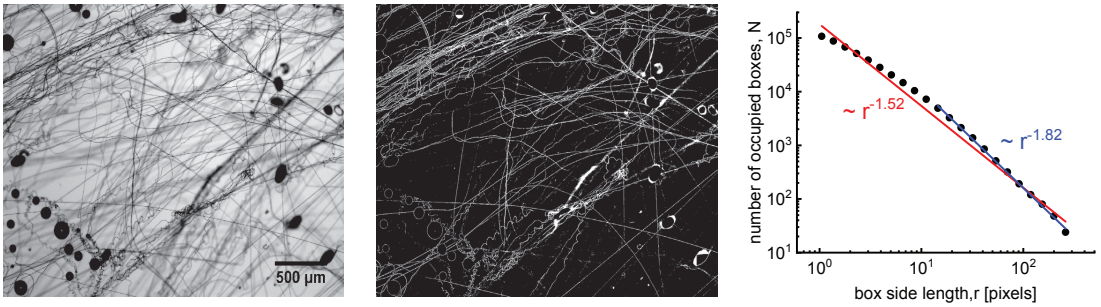

Figure B.2 (cont.)

Figure B.2 (cont.)

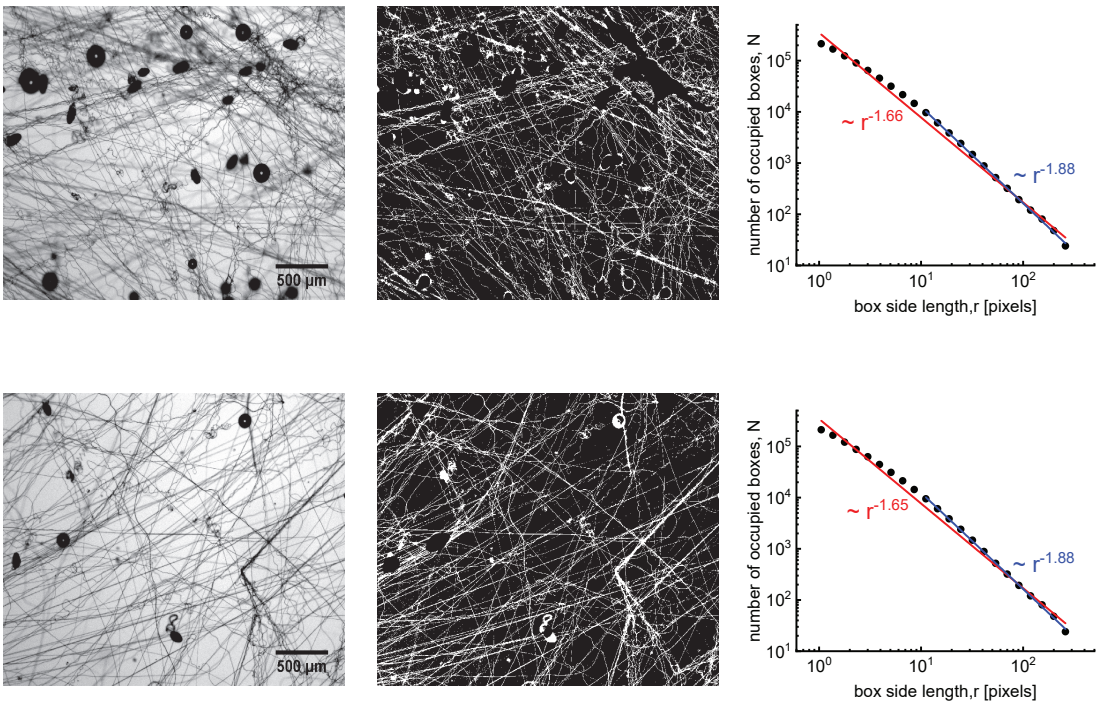

Figure B.2: Fractal analysis of microstructure of hagfish slime (0.4 mg/ml).

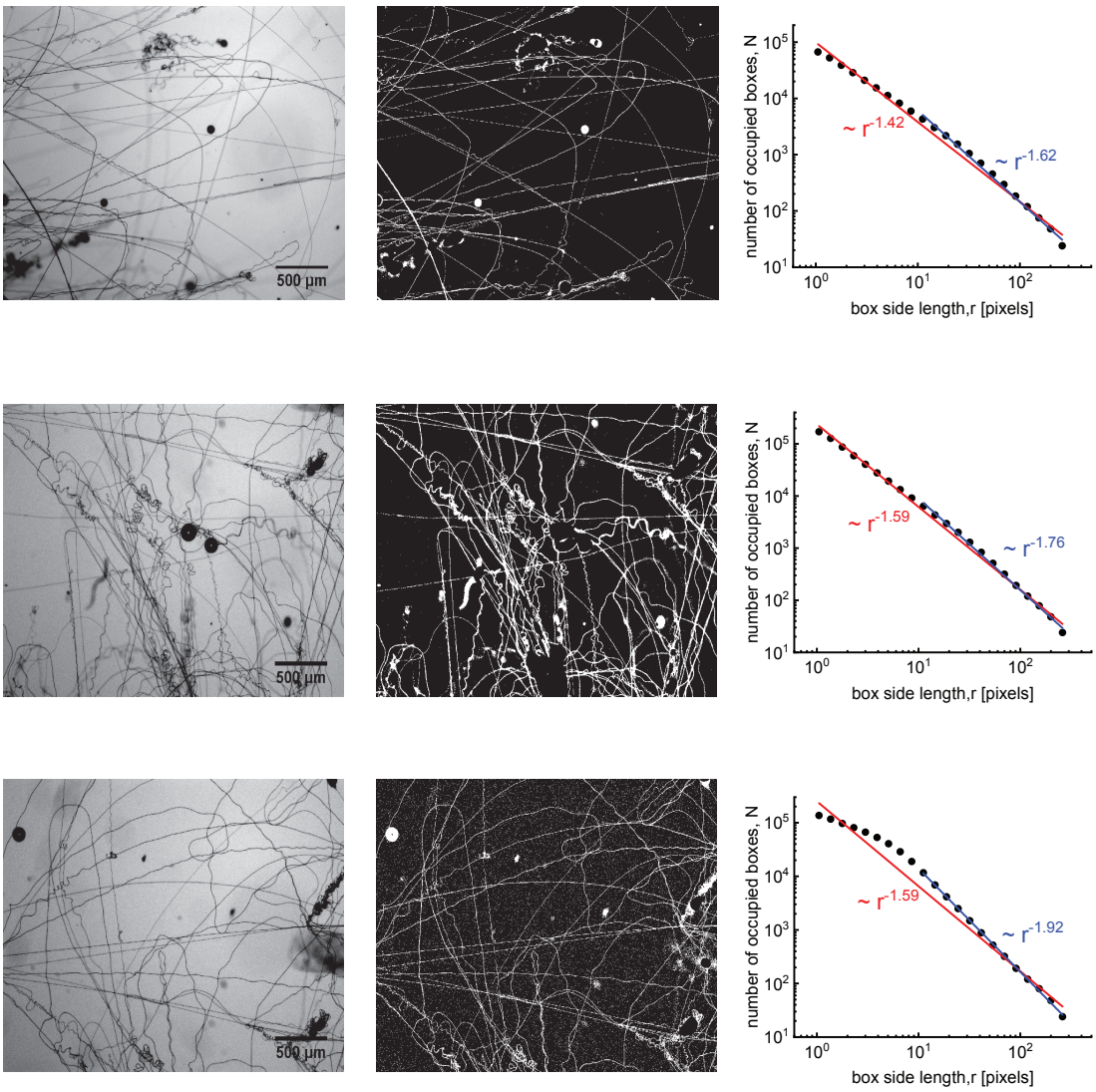

Figure B.3: Fractal analysis of microstructure of hagfish slime (0.08 mg/ml).

B.2 Strain-dependent Viscoelasticity

Samples were subjected to oscillatory shear deformation with increasing strain amplitude ($0.01-4000\%$) and a fixed angular frequency ($\omega = 0.2$) rad/s to study their strain dependent properties. A low frequency was intentionally chosen so as to have negligible instrument inertia and sample inertia effects in the measurements. Amplitude sweeps for five different concentrations are plotted in Figure B.4. Only the first harmonic response is shown which represents the average storage, G_1', (Figure B.4 A) and loss modulus, G_1'', (Figure B.4 B). As expected the elastic modulus increases with the concentration. G_1' has an extremely low value ~ 0.02 Pa, at the lowest concentration of 0.083 wt $\%$. It is interesting to note that the basic nature of the average response over the range of concentrations probed is similar in nature (data appears to be vertically shifted).

The material being very soft, presents several challenges in its rheological characterization [68, 69] on commercial rheometers. The measurements can be significantly affected by various experimental artifacts. Here, we demarcate the region, in Figure B.4 A and Figure B.4 B, where the experimental data should have negligible effect from such artifacts and should be believable. We identify three main experimental limits, namely: (i) the instrument torque limit, (ii) instrument inertia limit and (iii) the sample inertia limit, which are relevant to the measurement we made. We refer the reader to literature [68] for the details on plotting these limits.

We also show the data for the control experiment on distilled water obtained on the same experimental setup. We use this as a control experiment to understand the effects of surface tension in our experiments. It has been shown that surface tension artifacts can affect the rheological measurement in very soft samples or low torque rheometry. Such effects can even show up as apparent elastic modulus in case of a low-viscosity liquid such as water [69] and can be misleading. Our oscillatory shear measurements for water confirm that surface tension artifacts are negligible in our measurements. The elastic modulus, G'_{water} was measured to be $O(10^{-8})$ Pa. The measured loss modulus of water, G''_{water} of $O(10^{-4})$, is at least an order of magnitude lower that measured response at the lowest concentration of hagfish slime. Moreover, G''_{water} shows an excellent agreement with the theoretical prediction i.e. $G''_{water} = \eta_w \omega$, where η_w is the viscosity of water ($\eta_w = 10^{-3}$ Pa.s) and ω is the angular frequency of sinusoidal deformation ($\omega = 0.15$ rad/s). The theoretical G''_{water} is co-plotted with the experimental data in Figure B.4 B and we find that the match is reasonably good once the torque signal is out of torque noise floor. Hence, we believe that our measurements are reporting the true material response and are free from the above mentioned experimental artifacts and limitations.

The plot in Figure B.4 A-B, show the first harmonic response which softens above strain amplitude 20% for all the concentrations. We also analyze the raw stress response signal to understand the local material response. Figure B.5 A-E shows Lissajous curves for various concentrations obtained using MITLAOS software. Lissajous curves at all concentrations have similar features. At low strains (20%), a linear viscoelastic response is observed, evident by an elliptical curve where as at higher strains, non-linear effects (deviation from elliptical shape) become evident. A clear intra-cycle strain stiffening can be seen in Figure B.5 D. At very high strains, viscous effects start dominating. Normalized Lissajous curves are also shown, Figure B.6 A-E for each concentration tested, where stress and strain are normalized by their respective maximum values in the oscillatory cycle.

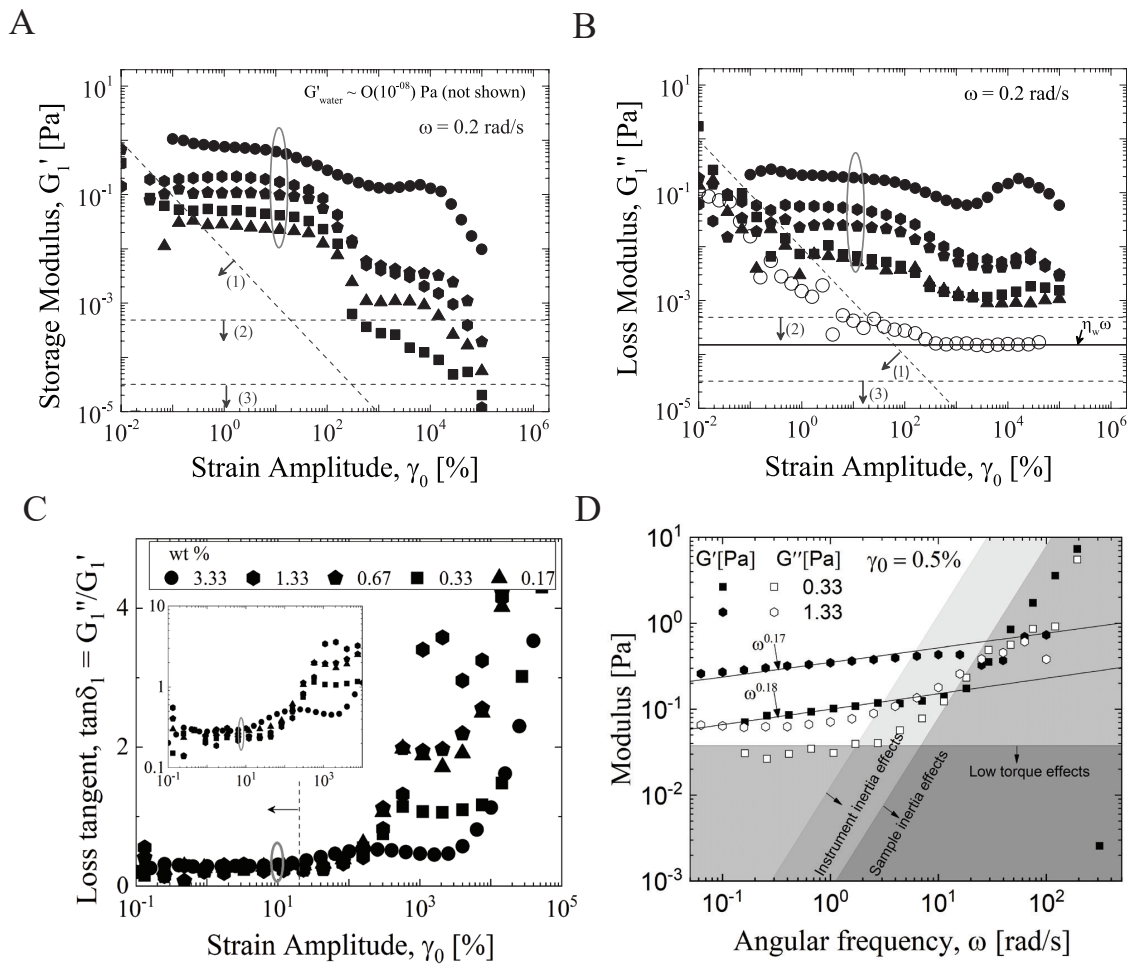

Figure B.4: Amplitude and Frequency sweep data. (A) Average elastic modulus, G_1', response for different exudate concentrations. G_1' shows strain softening above $\gamma_0 = 20\%$. Dashed lines indicate: (1) Instrument low torque limit, (2) Instrument inertia limit and (3) Sample inertia limit. (B) Average loss modulus, G_1'' is plotted for different exudate concentrations. The experimental data for distilled water using the same experimental set-up (black open circles), matches the theoretical prediction for G_1'' (solid black line) outside the low torque limit. This exemplifies that the data collected on this experimental set-up is free from any undesirable surface effects and instrument inertia. (C) The ratio of G_1'' and G_1', has values within narrow band $(0.2-0.3)$ in the linear viscoelastic regime ($\gamma_0 < 20\%$). The encircled data in the plots was used to determine the modulus-concentration dependence in Figure 3. (D) Frequency sweeps for hagfish slime at two different concentrations. The effects due to the instrument inertia limits the reliability of data beyond a certain frequency.

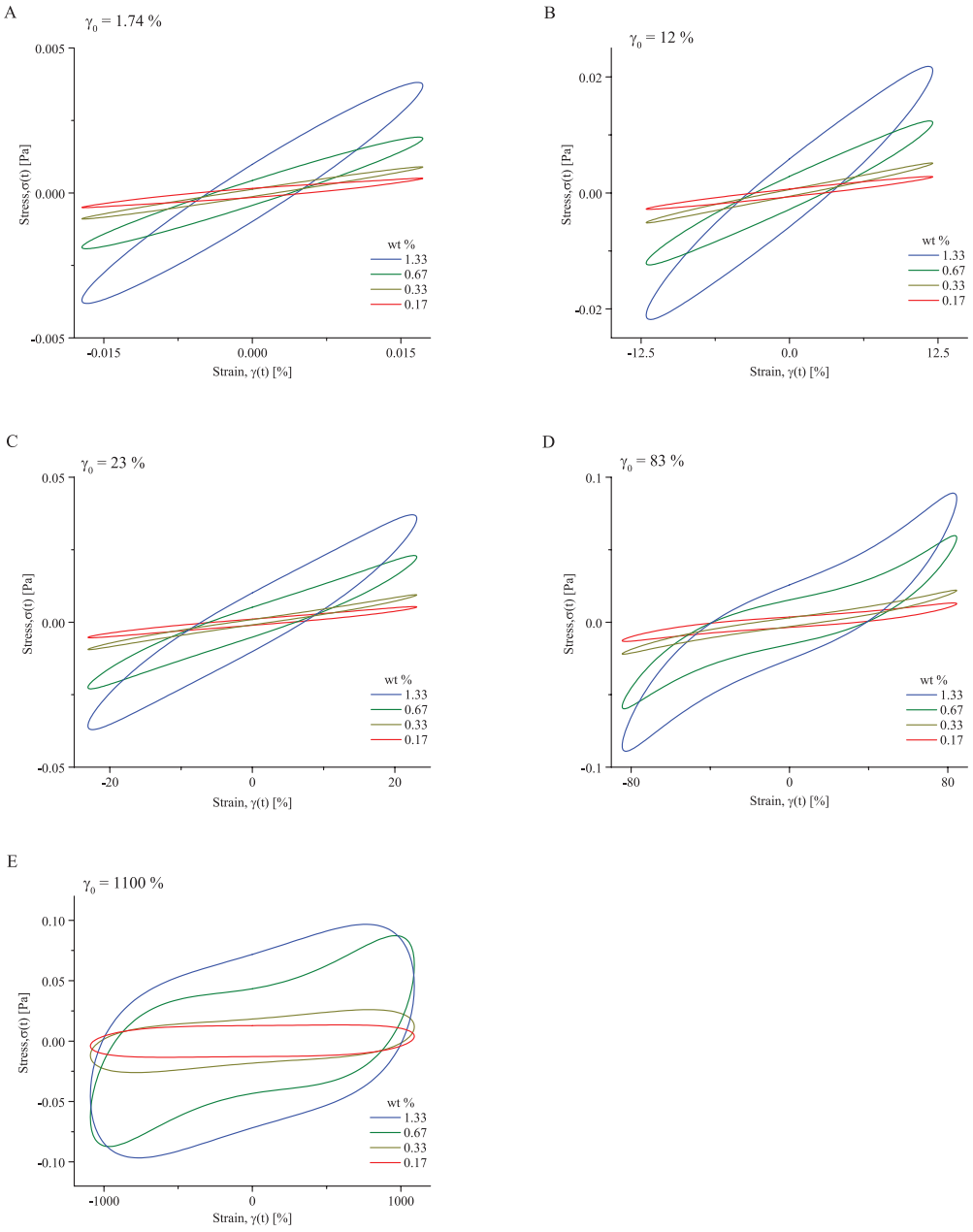

Figure B.5: Lissajous curves. The raw data in form of Lissajous curves is shown for different concentrations at five different strain amplitudes (A) 1.74% (B) 12% (C) 23% (D) 83% (E) 1100%. (A) and (B) correspond to the strains corresponding to the linear viscoelastic regime, hence the shape of the stress-strain curve for a sinusoidal deformation is an ellipse. Nonlinear behavior is apparent from the Lissajous curves in (C) and (D), where the shape deviated from an ellipse. The sample has an intracycle strain-stiffening response. At very high strain,(E), the network junctions are broken and the viscous nature dominates the response.

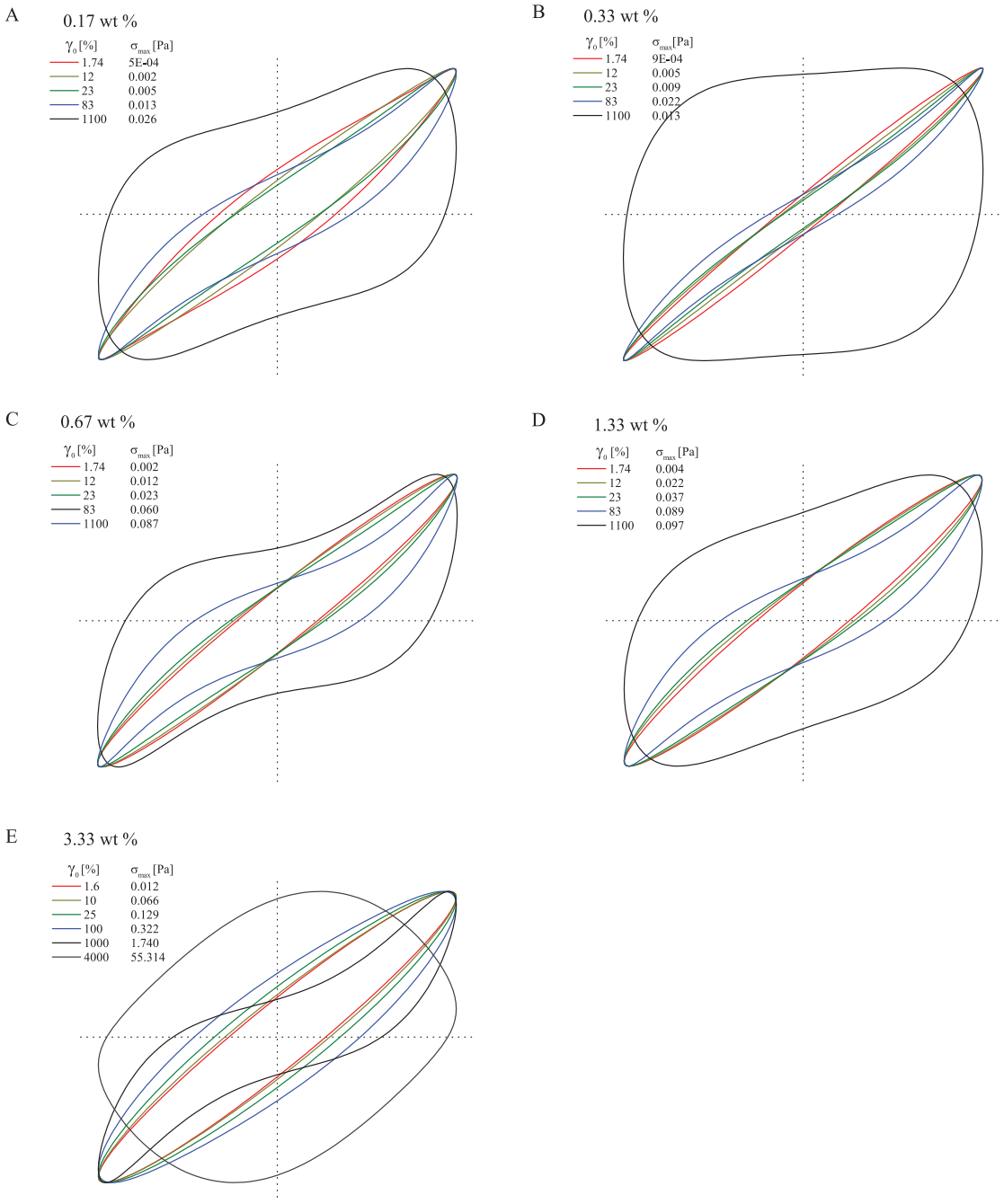

Figure B.6: Normalized Lissajous curves. Same data as Figure B.5, normalized by the maximum strain and stress for each case for the ease of comparison.

B.3 Time-dependent Viscoelasticity

The repeat measurements in the linear viscoelastic creep are shown for different concentrations in Figure B.7 at a stress of 0.01 Pa corresponding to the linear viscoelastic regime. Repeat measurements are for different sample loading.

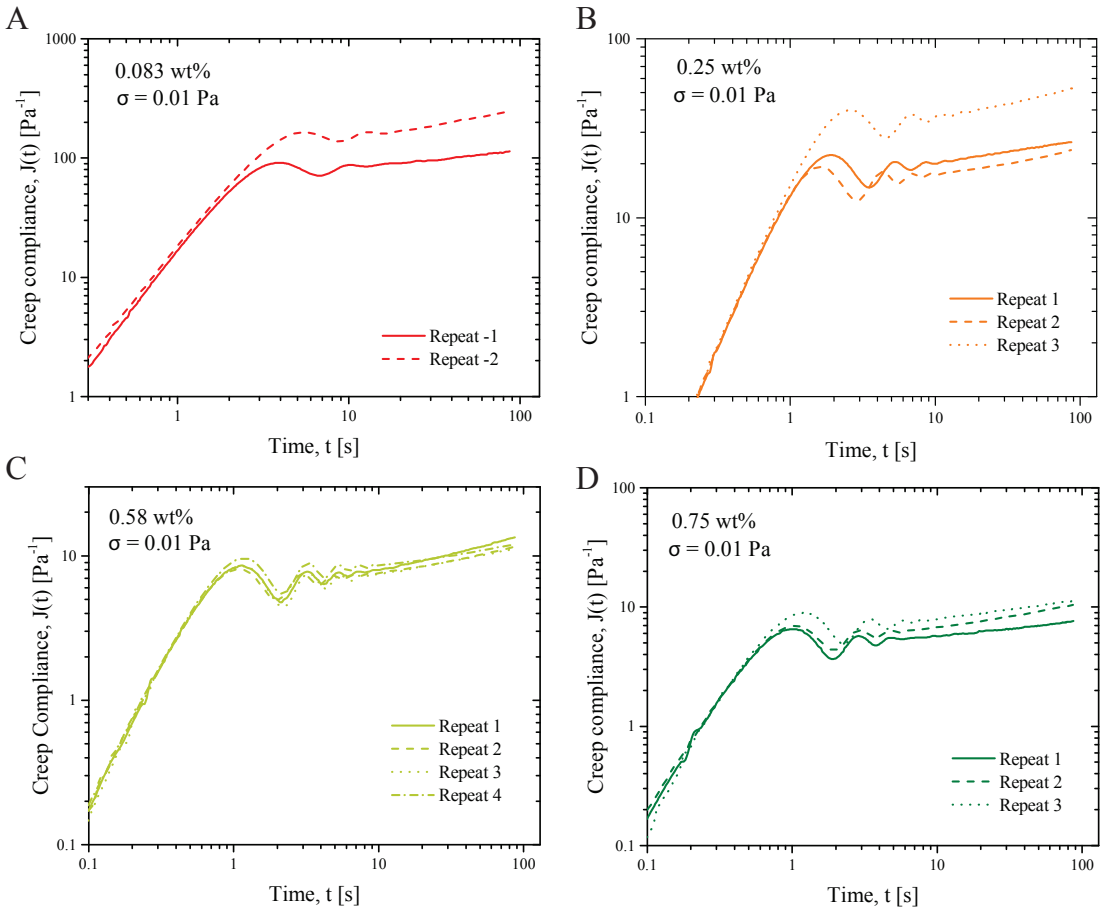

Figure B.7: Repeat data for creep tests at different concentrations. (A) 0.083 wt %, (B) 0.25 wt %, (C) 0.58 wt %, (D) 0.75 wt % for an applied stress of 0.01 Pa which corresponds to the linear viscoelastic regime.

B.4 Creep-ringing Analysis

It has been shown that viscoelastic properties of a soft material can be extracted from inertio-elastic oscillations if the ringing frequency, ω^* and logarithmic decrement of ringing amplitude,Δ are known [92, 33, 93]. Following the methods described in literature [91, 33], we extracted local, tangent material response (Figure B.8 A) of this material. We use a Maxwell model (Figure B.8 B) superimposed with decaying oscillations to approximate ω^* and Δ

$$J(t) = Xexp(-\Delta\frac{\omega^* t}{2\pi})sin(\omega^* t + \psi) + Y + Zt \tag{B.2}$$

where X is the ringing amplitude, Y is the initial compliance and Z is the fluidity. ψ is an arbitrary phase angle. Using the methods described in literature[33], we find the exact values of ω^* and Δ by fitting Eq.B.2 to the creep data. Hence, we estimated tangent moduli K' and K'' using the following expressions

$$K' \approx \frac{I\omega^{*2}}{b}\Big(1 + (\frac{\Delta}{2\pi})^2\Big),\ K'' \approx \frac{I\omega^{*2}}{b}(\frac{\Delta}{2\pi}) \tag{B.3}$$

A secant modulus, G_0 can also be defined, $G_0 = \frac{1}{Y}$. Using this procedure for the creep data across all the concentrations, we obtained the viscoelastic information at shorter timescales. We found that tangent moduli, K' and K'', show a power-law dependence on exudate concentration. The power-law exponents are 0.91 ± 0.08 and 0.92 ± 0.08 for K' and K'' respectively, corresponding to an applied shear stress of 0.01 Pa (Figure B.8 D). For an input stress of 0.0316 Pa, power-law exponents are 0.90 ± 0.08 and 0.83 ± 0.06 for K' and K'', respectively (Figure B.8 F). Thus, tangent moduli, similar to the scaling of the average elastic modulus from amplitude sweep, also vary linearly with concentration. The ratio of K'' and K' was nearly constant for all the tested concentrations (Figure B.8 H). Secant modulus, G_0, also shows a linear variation with concentration (power-law exponents 1.1 ± 0.1 and 0.95 ± 0.1 for input stress of 0.01 Pa and 0.0316 Pa, respectively) (Figure B.8 D & F). The ratio of K'' and K', tan δ_k, has a very narrow range (0.25-0.4), similar to what was observed in the linear oscillatory experiments (Figure B.8 H).

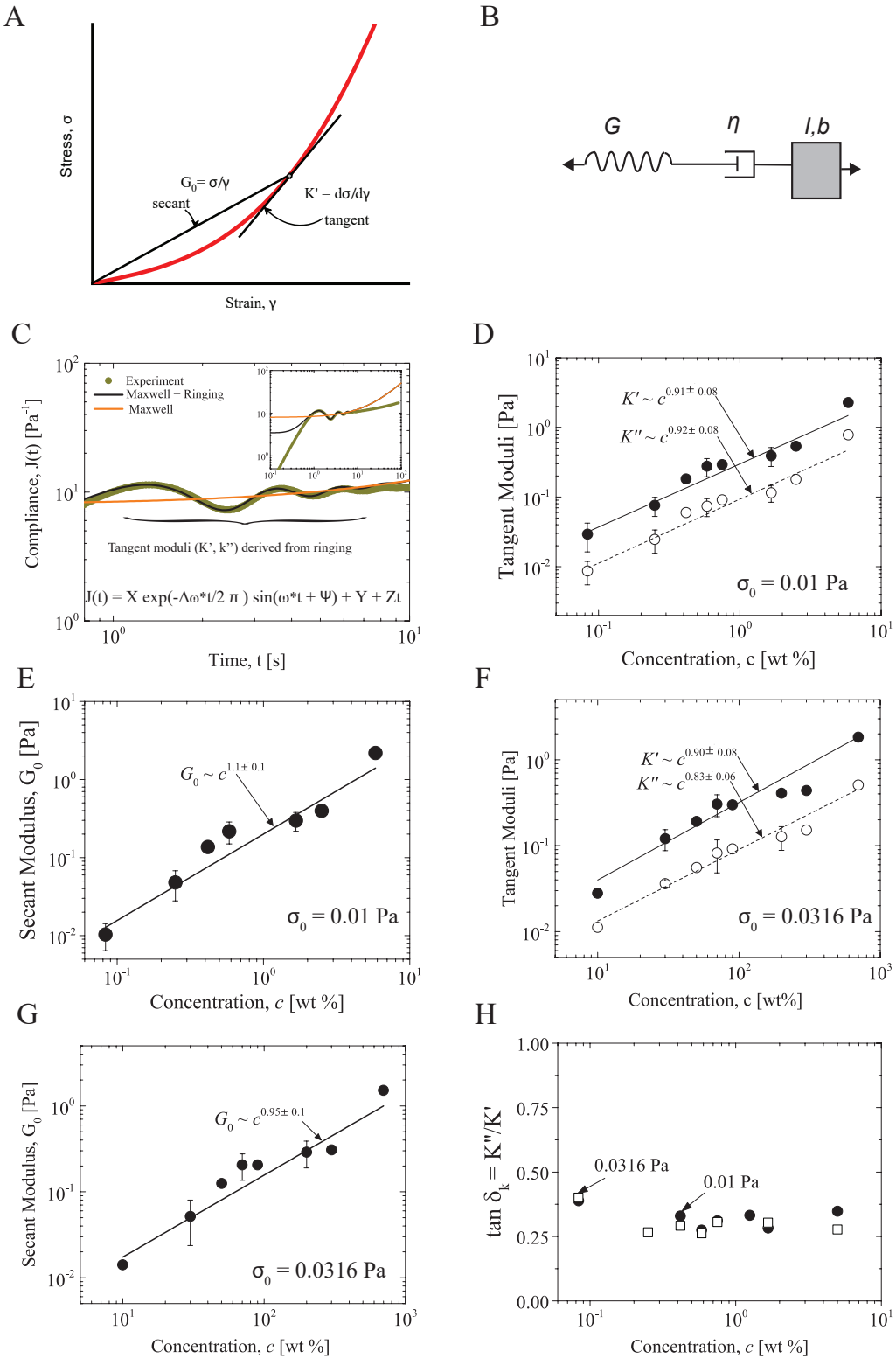

Figure B.8 (cont.)

Figure B.8 (cont.)

Figure B.8: Figure on from previous page. (A) A schematic depicting the difference between the secant and tangent modulus. In the linear elastic regime of a material, the relationship between stress, (σ), and strain (γ), is a simple, linear relationship: $\sigma = G_0\gamma$, where G_0 is the elastic modulus and has a constant value. A linear response is typically observed in materials at small enough range of stresses and strains. At larger stresses or strains, the nonlinear effects can start to dominate the response. In nonlinear regime, the linear relationship is no longer followed. We can see that from the schematic data in the red curve. The secant modulus ($G_0 = \frac{\sigma}{\gamma}$) will have a different magnitude than the tangent modulus ($K' = \frac{d\sigma}{d\gamma}$). Hence, in the nonlinear response, there are different measures of elastic modulus, which are generally not equal. (B) A Maxwell model in series with an inertial mass is used to extract viscoelastic information from the inertia-elastic ringing observed at short times. (C) Maxwell model response superimposed with decaying oscillations is used fit the creep compliance response at short times. A fit is shown for a 0.41 wt $\%$ sample. Four successive peaks from the damping oscillations are used to evaluate all the parameters (X, Y,Z,ω^* and Δ). A comparison of experimental data and constitutive model fit is shown. The agreement between experiment and fit is excellent. The model deviates significantly at longer times as shown in inset. (D) The fit parameters are used to extract a viscoelastic storage (K') and loss moduli (K''). A short time secant modulus (G_0) can be evaluated from the underlying Maxwell evaluation ($G_0 = \frac{1}{Y}$). (E) Tangent moduli plotted as a function of exudate concentration for an input stress of 0.01 Pa. Both storage and loss moduli depend linearly on the exudate concentration. (E) The secant modulus, G_0, has a linear concentration dependence as well. Similar observations are made for the stress input of 0.0316 Pa, shown in (F) and (G). (H). tan $\delta_k = K''/K'$ varies within a narrow band ($0.25 - 0.4$) for all concentrations, suggesting that the viscoelastic nature of the slime remains similar at short timescales.

B.5 Nonlinear Creep

The non-linear creep for various concentrations are shown in Fig.SB.9. The data at all the concentrations have similar nature of response. A solid-like power-law creep response is observed in the viscoelastic regime. The network becomes stiff with a small increase in stress input. As stress is increased further, the material yields to a liquid-like response. Above this stress, purely viscous response (slope=1) was observed. We use the same analysis to derive tangent moduli from the creep experiments at all the stresses. It can be seen in the Figure B.10 that the tangent storage modulus, K'', and tangent loss modulus, K', both show stiffening as the input stress is increased. It should be noted that tangent storage modulus, K' is higher than the secant modulus, G_0, at both the input stresses and at all concentrations indicating that we are probing non-linear properties of the material [33] (Figure B.10 C).

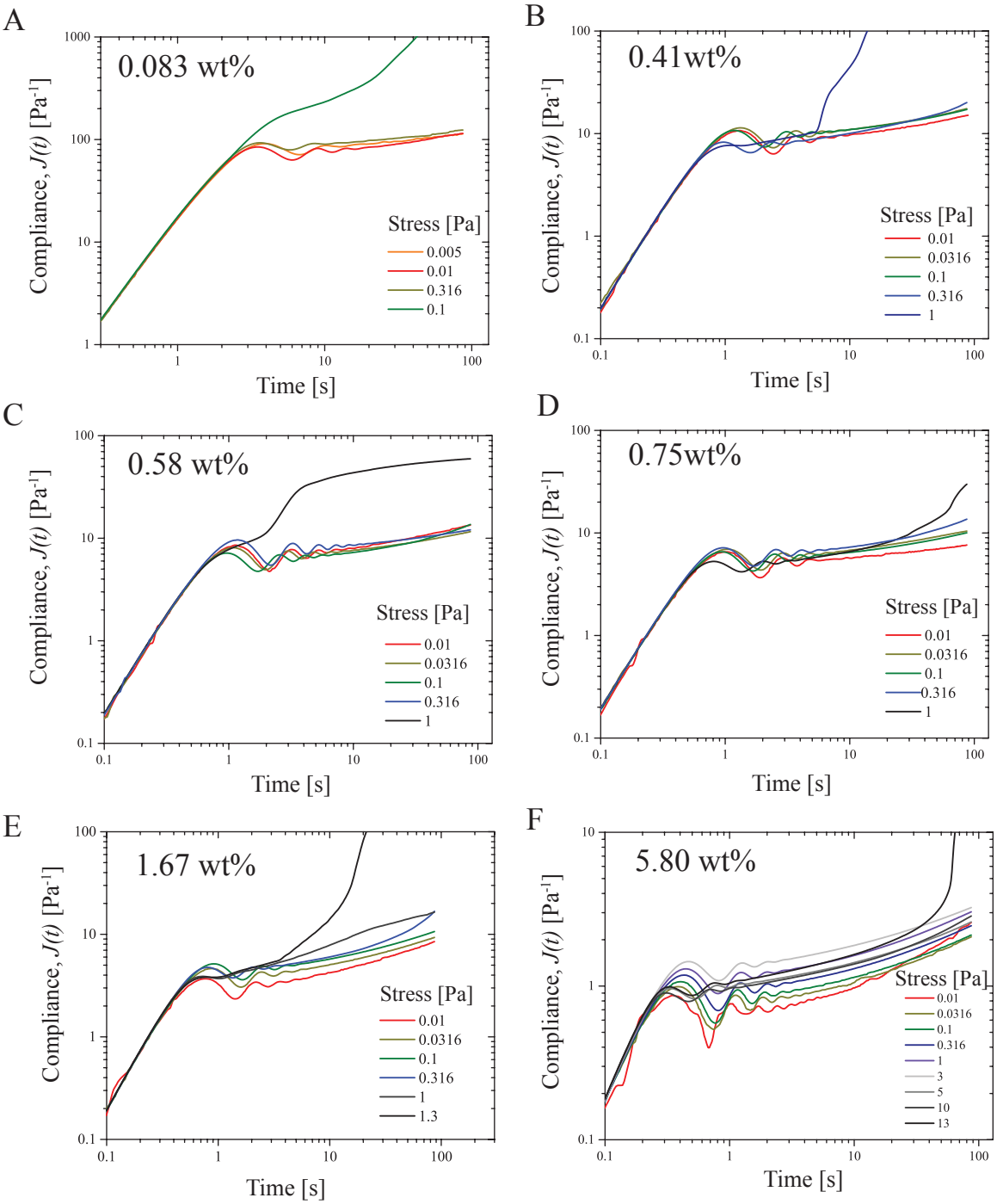

Figure B.9: Nonlinear creep of hagfish slime. Creep response at various applied stresses. The response changes from linear viscoelastic power-law solid at low stresses to viscous high stress, with a yield/failure stress in between. The data shown if for different concentrations of hagfish defense gel (A) 0.083 wt %, (B) 0.41 wt %, (C) 0.58 wt %, (D) 0.75 wt %, (E) 1.67 wt %, (F) 5.80 wt %.

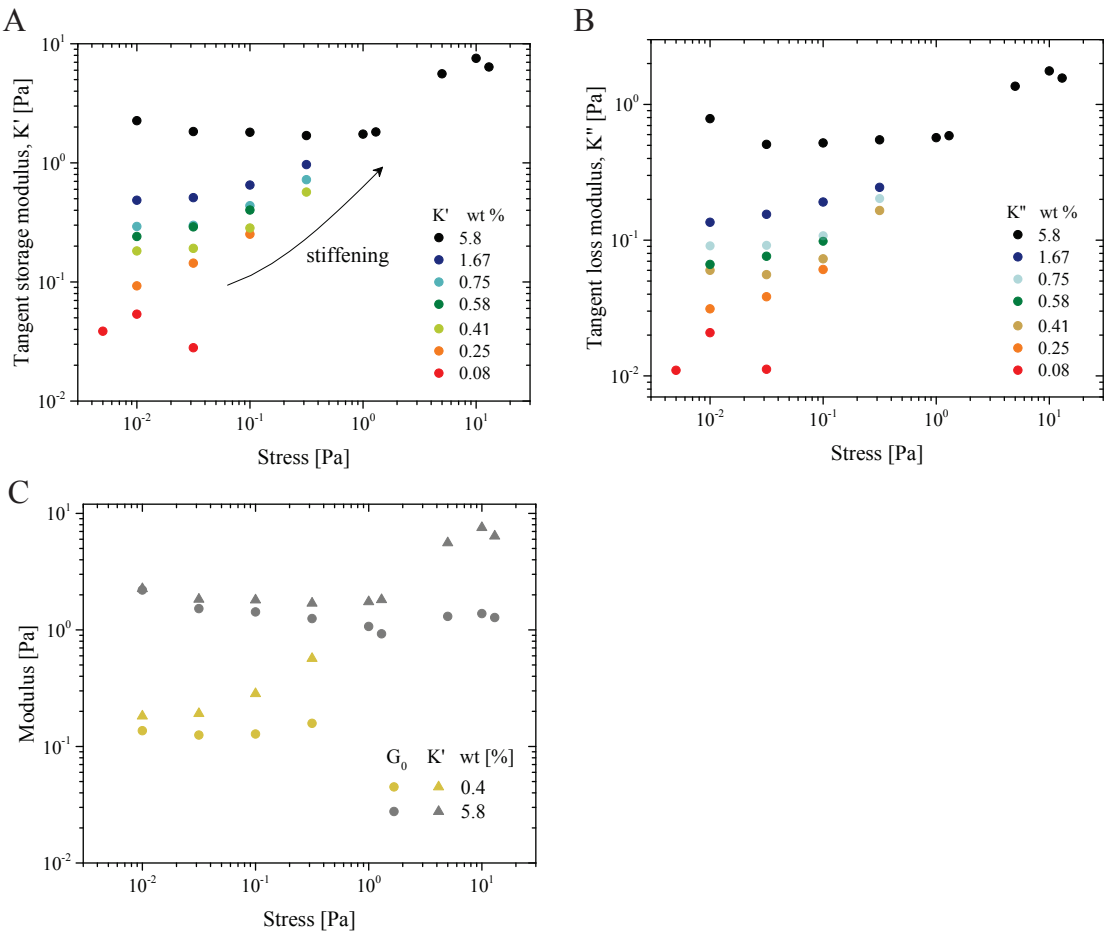

Figure B.10: Stiffening tangent moduli with stress. With increase in the input stress, the samples at all concentrations, show a stiffening of tangent moduli, before yielding.

B.6 Fractional Constitutive Model

We utilize constitutive models to compare the data over all the tested time scales and concentrations. Classically, a combination of mechanical elements, springs and dashpots, is used to model viscoelastic materials. Such models involve only integer derivative operators to describe the material response of complex materials. However, they tend to become complex and hence impractical in describing the material response in certain cases. For example, it would require a very large number of springs and dashpots arranged in a complex fashion to describe a power-law behavior which is very common in many materials. Increasing the number of elements results in higher number of parameters to describe the material response and it is difficult to ascribe a physical meaning to them. Recently, constitutive models involving fractional-order operators have become very popular for describing material response of several different material system. We utilize such a fractional constitutive model to describe slime behavior.

The concept and applicability of fractional models has been discussed in detail in literature [95, 97, 98, 104]. The basic element in a fractional model is a spring-pot that combines the features of classical elements: spring and dashpot. It has been demonstrated that a spring-pot has a physical behavior similar to a hierarchical arrangement of infinite number of springs and dashpots [95]. The mathematical description of a spring-pot is given by the fractional differential equation

$$\sigma(t) = G\frac{d^{\alpha}}{dt^{\alpha}}\gamma(t) = G\int_{0}^{t}(t-t')^{-\alpha}\dot{\gamma}(t')dt' \tag{B.4}$$

where α is the order of derivative and its values lies in $[0, 1]$, $\sigma(t)$ is the stress in the material and $\gamma(t)$ is the strain. G is a quasi-property and has units of [Pa s^{α}]. Eq.B.4 appears as an interpolation between a linear elastic behavior, $\sigma(t) \propto \gamma(t)$, for $\alpha = 0$ and liquid-like behaviour, $\sigma(t) \propto \frac{d}{dt}\gamma(t)$, for $\alpha = 1$. For $0 < \alpha < 1$, it describes viscoelastic behavior. An inherent advantage in using fractional order operator is clear from its definition. Unlike the integer order derivatives which involve local information of the function of $\gamma(t)$, a fractional order derivation requires its whole history, which makes it ideal for describing materials with memory [97]. The second equality in the governing equation for spring-pot comes from the Caputo definition of fractional derivative [95].

We use a special case of a generalized fractional Kelvin-Voigt model to describe the observations from creep experiments. A dashpot(η) in parallel with a spring-pot(α, G) is used (Figure B.11 B). The governing equation for such a model can be written as

$$\sigma(t) = \Big(\eta\frac{d}{dt} + G\frac{d^{\alpha}}{dt^{\alpha}}\Big)\gamma(t) \tag{B.5}$$

Such a model can be analytically solved and provides a closed form expression for creep compliance, $J(t)$

$$J(t) = \frac{t}{\eta}E_{1-\alpha,2}[-\big(\frac{t}{\tau}\big)^{1-\alpha}] \tag{B.6}$$

where $\tau = \Big[\frac{\eta}{G}\Big]^{\frac{1}{1-\alpha}}$. $E_{1-\alpha,2}$ is the Mittag-Leffler function given by $E_{1-\alpha,2}(t) = \sum_{j=0}^{\infty}\frac{t^j}{\Gamma((1-\alpha)j+2)}$. $\Gamma(x)$ is the gamma function. To account for the instrument inertia which is very prevalent in the creep experiments at short times, we solve the equation of motion for the spindle of a stress controlled rheometer, in addition to Eq.B.5, given by

$$\frac{I}{b}\frac{d^2}{dt^2}\gamma(t) = H(t)\sigma_0 - \sigma(t) \tag{B.7}$$

where I is the moment of inertia of the rheometer spindle with measuring system attached and b is the geometric factor dependent on the instrument and geometry used. A coupled fractional order equation can be easily obtained that will describe the instrument and material response to a step stress input

$$\Big[\frac{I}{b}\frac{d^2}{dt^2} + \eta\frac{d}{dt} + G\frac{d^{\alpha}}{dt^{\alpha}}\Big]\gamma(t) = H(t)\sigma_0 \tag{B.8}$$

Since the material has no deformation at the start,$t = 0$, $\gamma(0) = \dot{\gamma}(0) = 0$. This equation can be solved analytically using Laplace transform. However, here we obtain the solution numerically using the methods described in literature[101]. The numerical solutions to the fractional Kelvin-Voigt model, with and without inertial mass, are plotted in Figure B.12 for various values. The numerical solution converges to the analytical solution that was obtained without considering inertial effects as in Eq.B.6 at long times after the inertial effects subside and material deformation alone produces stress. Similar approach was used in literature[98] with a fractional Maxwell model.

The constitutive model predictions are compared to the experimental data over the entire concentration range with η, G and α as fit parameters. The best fits were obtained by minimizing the residual sum of squares in MATLAB. The fitting results are given in Table B.1.

Concentration [wt %]	G	η	α
0.083	0.0224 (0.02213-0.02275)	0.003403 (0.002908-0.003898)	0.1908 (0.187-0.1947)
0.25	0.07119 (0.0792-0.07147)	0.009979 (0.009669-0.01029)	0.1306 (0.1295-0.1318)
0.41	0.1529 (0.152-0.1539)	0.006262 (0.005483-0.007041)	0.1556 (0.1527-0.1575)
0.58	0.1957 (0.1945-0.197)	0.001	0.1827 (0.1807-0.1846)
0.75	0.2524 (0.2508-0.254)	0.003979 (0.002765- 0.0051931)	0.1816 (0.1797-0.1835)
1.67	0.391 (0.386-0.396)	0.001	0.2367 (0.2328-0.2405)
5.80	1.462 (1.441-1.483)	0.001	0.1996 (0.1952-0.2041)

Table B.1: Fractional constitutive parameters (with 95 $\%$ confidence interval).

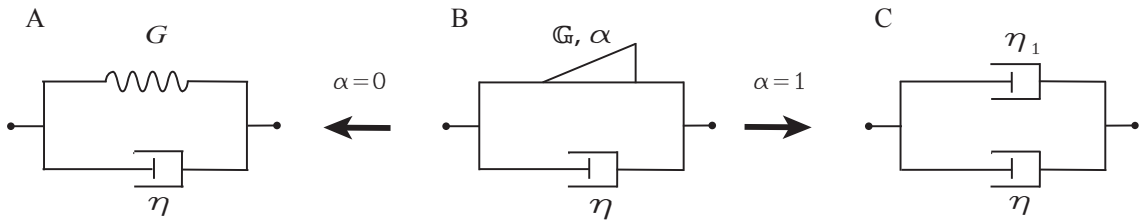

Figure B.11: The fractional Kelvin-Voigt model reduces to a typical Kelvin-Voigt model with a spring and dashpot in parallel for $\alpha = 0$. An effective dashpot is obtained for $\alpha = 1$.

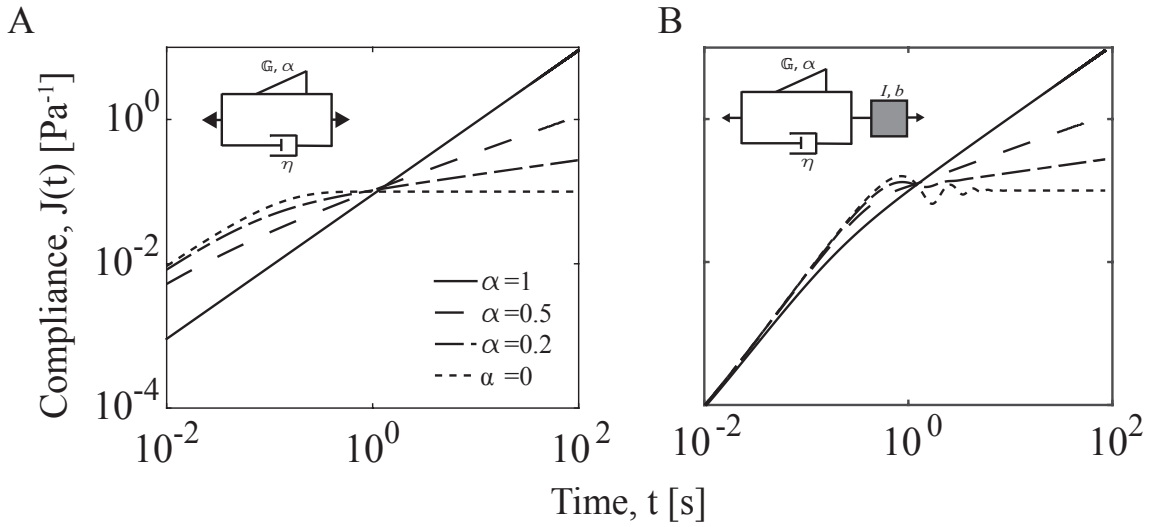

Figure B.12: Constitutive model for comparing experiments. (A) A fractional Kelvin-Voigt model, with parameter $\eta, \mathbb{G}, \alpha$ gives a power-law creep response. The response for four different values of α and other parameters fixed ($\eta = 1, G = 10$ and $\sigma_0 = 1$). A Viscoelastic-solid like response is obtained for $\alpha = 0$ and viscous-liquid like response is obtained for $\alpha = 1$. (B) A fractional Kelvin-Voigt model with an inertial element in series captures inertial response and creep ringing at shorter time scales while predicting a power-law creep response at long times. The plotted data is four different values of α, keeping other parameters fixed $\eta = 1, G = 10, \sigma_0 = 1, I = 1, b = 1$.

B.7 Relaxation exponent (n or α) for various systems

The data used to plot Figure 8 in the paper is given in table. Table B.2.

Materials	Conc. [wt %]	Exponent
Collagen (type I rat tail collagen (RTC)) [108]	0.4	0.84
	0.6	0.72
	0.8	0.65
Agarose [109]	0.1	0.08
	0.15	0.07
	0.2	0.1
	0.25	0.09
	0.3	0.2
	0.35	0.1
Human Fibrinogen (Diluted human blood) [110]	0.27	0.69
	0.23	0.71
	0.21	0.73
	0.12	0.77
	0.07	0.83
Methylcellulose (Different MW methocellulose) [75]		
MC 530	0.35	0.85
	0.5	0.75
	1.5	0.54
	2.5	0.54
MC 300	0.75	0.8
	1.1	0.72
	1.7	0.74
	2.5	0.69
	4	0.54
MC 150	1.36	0.9
	3.12	0.81
	5.18	0.72
	7.63	0.6
	9.1	0.54

Table B.2 (cont.)

Table B.2 (cont.)

Cellulose solutions [111]	2.5	0.890
	2.67	0.891
	2.85	0.892
	3	0.889
Lentinan (extracted from *L. edodes*) [112]	0.2	0.85
	0.3	0.58
	0.4	0.36
	0.5	0.29
	0.6	0.2
	0.7	0.22
	0.8	0.19
Pectin (low-methoxyl pectin sample) [113]	1.5	0.6
	2	0.69
	2.5	0.69
	3	0.55
Chitosan (unmodified chitosan and hydrophobically-modified chitosan) [114]	3.9	0.36
	3	0.46
	1.75	0.46
Guar (Borate crosslinked Hydroxypropyguar) [115]	0.21	0.5
	0.35	0.42
	0.5	0.31
	0.6	0.25
	0.7	0.21
	1	0.18
	1.5	0.145
Ethyl(hydroxyethyl)cellulose [116]	1	0.3
	2	0.56
	4	0.64
Alginate (with different mannuronate/guluronate ratios) [117]		
AG-M1H	3	0.83
	5	0.76
	7	0.74
AG-G1H	3	0.53

Table B.2 (cont.)

Table B.2 (cont.)

	5	0.49
	7	0.31
κ-carrageenan (Ca^{2+} induced gelation)[118]	2	0.52
	2.5	0.52
	3	0.523
	3.5	0.52
	4	0.523
Gellan gum (Deacetylated potassium-type gellan gum aqueous solutions) [119]	1	0.75
	1.5	0.52
	2	0.49
	2.5	0.39
Alginate [120]	2	0.76
	3	0.73
	4	0.7
	5	0.67
Alginate (Different molecular weights and M/G ratio) [121]		
Ca-ML GL	2	0.68
	3	0.69
	4	0.64
	5	0.64
	6	0.64
Ca-ML GH	2	0.72
	3	0.71
	4	0.71
	5	0.7
	6	0.68
Ca-MH GL	2	0.77
	3	0.55
	4	0.43
	5	0.42
	6	0.41
Ca-MH GH	2	0.72
	3	0.5
	4	0.37

Table B.2 (cont.)

	5	0.37
	6	0.37

Table B.2: Relaxation exponents for different systems as the concentration of primary component is varied.

B.8 Structure-Property Relationship

In this section we lay out the details of the expressions used in the section on structure-property relationship. We first describe the mechanics of a single fiber with natural bends in it. The individual fibers can be treated as cylindrical elastic rods of radius $a \approx 1.25$ μm. The Young's modulus has been reported to be $E_f = 6.8$ MPa for hagfish defense gel fibers. We treat the fibers as athermal elastic rods and neglect any thermal energy changes during deformation. Under an applied deformation, the bends in a fiber tend to straighten out. The fiber may not experience a physical stretch unless all the bends in it are straightened out depending on its geometry, hence acts inextensible.

B.8.1 Energy Balance in a Bending Filament

The energy involved in deforming an inextensible fiber of total length l from its a natural curvature κ_0 to a new curvature $\kappa(\gamma, s)$ can be expressed as

$$E_{fiber} = \int_0^l ds \frac{EI}{2}(\kappa(\gamma, s) - \kappa_0)^2 \tag{B.9}$$

Under a small applied strain, γ, we express $\kappa(\gamma, s)$ as Taylor expansion around the natural configuration,

$$\kappa(\gamma, s) = \kappa(0, s) + \left.\frac{d\kappa}{d\gamma}\right|_{\gamma=0} \gamma + O(\gamma^2)$$

Hence, Eq.B.9 becomes

$$E_{fiber} = \int_0^l ds \frac{EI}{2}(\left.\frac{d\kappa}{d\gamma}\right|_{\gamma=0})^2\gamma^2$$

Thus, the bending energy per unit volume can be written as

$$e_{network} = \rho\frac{EI}{2}\langle(\left.\frac{d\kappa}{d\gamma}\right|_{\gamma=0})^2\rangle\gamma^2$$

where EI is the flexural rigidity of the fiber and ρ is the total fiber length per unit volume. $\langle(\left.\frac{d\kappa}{d\gamma}\right|_{\gamma=0})^2\rangle$ is the average of square of differential change in the curvature of fibers under an applied differential strain.

Assuming a small deformation, the deformation energy per unit volume due to a differential applied strain ($d\gamma$) is given by

$$w = \frac{1}{2} G \gamma^2 \tag{B.10}$$

Assuming, negligible dissipation and a purely elastic response, energy balance in the differential volume gives,

$$e_{network} = w \tag{B.11}$$

or

$$G = \rho E I \langle (\frac{d\kappa}{d\gamma}\Big|_{\gamma=0})^2 \rangle \tag{B.12}$$

In the following section, we derive the closed form expression for $\langle (\frac{d\kappa}{d\gamma}\Big|_{\gamma=0})^2 \rangle$ from geometry of the problem.

B.8.2 Bending of Curved Filament

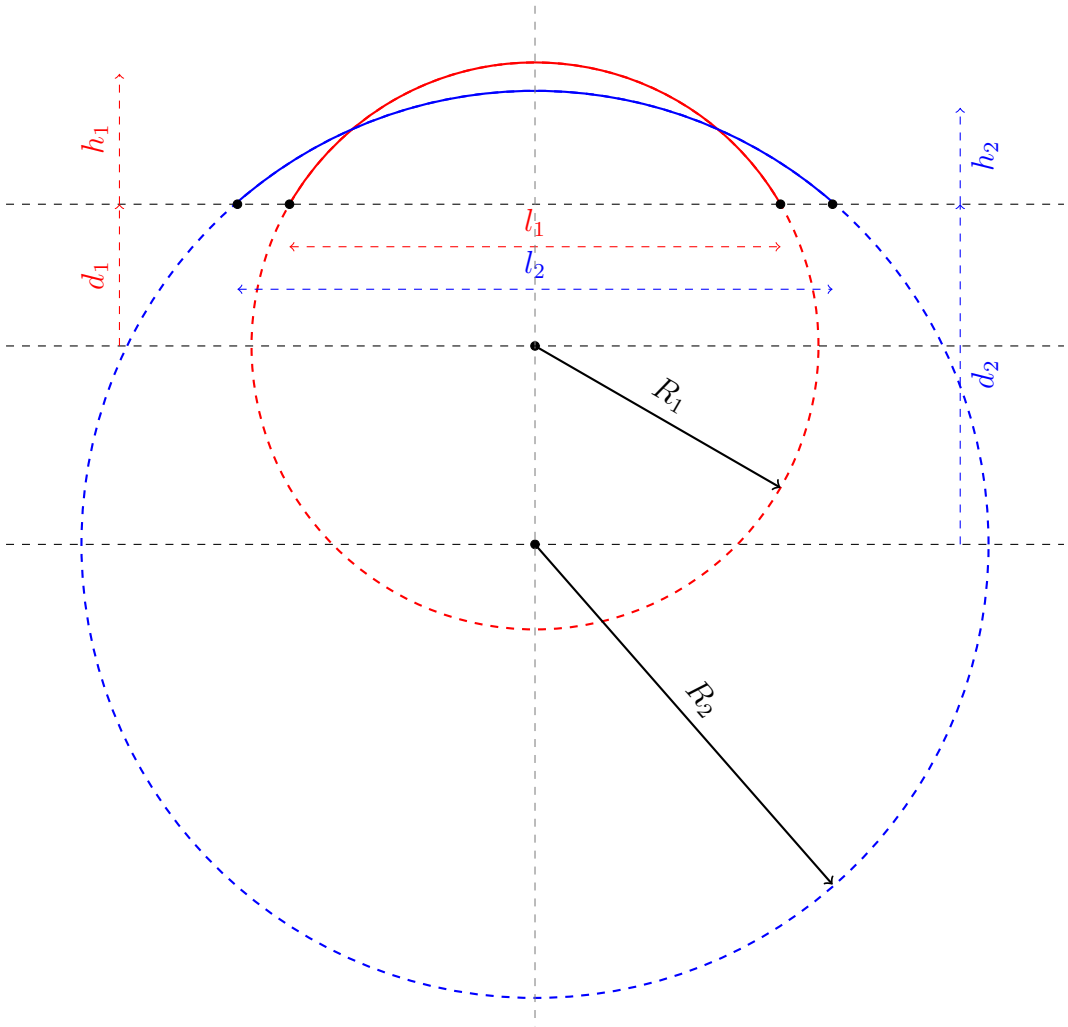

Figure B.13: Relevant parameters for an arc (in red) deforming to a new configuration under deformation (in blue).

Let the initial configuration of a curved fiber is shown by the red arc (Figure B.13). The blue arc is the final (strained) configuration. Subscripts 1 and 2 are for initial and final configurations, respectively. We are assuming that the initial and final configurations are axisymmetric.

The chord length l_1 is strained by an extensional strain, ϵ, hence

$$l_2 = l_1(1 + \epsilon) \tag{B.13}$$

The approximate formula for the arc length is given by [286]

$$s \approx \left(l^2 + \frac{16}{3} h^2 \right)^{\frac{1}{2}} \tag{B.14}$$

This approximation is accurate to within 0.3% for $0^\circ \leq \theta \leq 90^\circ$, where θ is the angle the arc subtends at the center. Even for $90^\circ < \theta < 180^\circ$, this is a reasonable approximation, e.g. for $\theta = 115^\circ$ the error is 0.5%, for $\theta = 180^\circ$ the error is 2.8%. For higher accuracy we can write an infinite series for the arc length, but it leads to unnecessary complexity for our purposes here.

Let s_1 and s_2 be the arc lengths of initial and final configuration.

Assuming pure bending deformation, $s_1 = s_2$.

$$s_1 = s_2$$

$$l_1^2 + \frac{16}{3} h_1^2 = l_2^2 + \frac{16}{3} h_2^2$$

Using Eq.B.13 to write l_2 in terms of l_1,

$$h_2 = \left(h_1^2 - \frac{3}{16} l_1^2 ((1+\epsilon)^2 - 1) \right)^{\frac{1}{2}}$$

or,

$$h_2 = \left(h_1^2 - \frac{3}{16} l_1^2 (2\epsilon + \epsilon^2) \right)^{\frac{1}{2}} \tag{B.15}$$

The chord length, l, is given by

$$l = 2 \left(h(2R - h) \right)^{\frac{1}{2}} \tag{B.16}$$

Therefore, using Eq.B.15 and Eq.B.16 we get

$$l_1(1+\epsilon) l_2 = 2 \left(\left(h_1^2 - \frac{3}{16} l_1^2 (2\epsilon + \epsilon^2) \right)^{\frac{1}{2}} \left(2R_2 - \left(h_1^2 - \frac{3}{16} l_1^2 (2\epsilon + \epsilon^2 \right)^{\frac{1}{2}} \right) \right)^{\frac{1}{2}} \tag{B.17}$$

using Eq.B.13,

$$\frac{l_1^2 (1+\epsilon)^2}{4} \left(h_1^2 - \frac{3}{8} l_1^2 \epsilon - \frac{3}{16} l_1^2 \, \epsilon^2 \right)^{-\frac{1}{2}} = \left(2R_2 - \left(h_1^2 - \frac{3}{8} l_1^2 \epsilon - \frac{3}{16} l_1^2 \, \epsilon^2 \right)^{\frac{1}{2}} \right)$$

Writing the equation for a general R under a strain ϵ

$$R = \frac{1}{2}\left(\frac{l^2(1+\epsilon)^2}{4}\left(h^2 - \frac{3}{8}l^2\epsilon - \frac{3}{16}l^2\,\epsilon^2\right)^{-\frac{1}{2}} + \left(h^2 - \frac{3}{8}l^2\epsilon - \frac{3}{16}l^2\,\epsilon^2\right)^{\frac{1}{2}}\right) \quad \text{(B.18)}$$

Taking derivative with respect to ϵ,

$$\begin{aligned}\frac{dR}{d\epsilon} &= \frac{1}{4}l^2(1+\epsilon)\left(h^2 - \frac{3}{8}l^2\epsilon - \frac{3}{16}l^2\,\epsilon^2\right)^{-\frac{1}{2}} \\ &+\frac{1}{4}\frac{l^2(1+\epsilon)^2}{4}\left(h^2 - \frac{3}{8}l^2\epsilon - \frac{3}{16}l^2\,\epsilon^2\right)^{-\frac{3}{2}}\left(\frac{3}{8}l^2 + \frac{3}{8}l^2\,\epsilon\right) \\ &-\frac{1}{4}\left(h^2 - \frac{3}{8}l^2\epsilon - \frac{3}{16}l^2\,\epsilon^2\right)^{-\frac{1}{2}}\left(\frac{3}{8}l^2 + \frac{3}{8}l^2\,\epsilon\right)\end{aligned}$$

Curvature (κ) of an arc is defined as the inverse of the radius of curvature, R

$$\kappa = \frac{1}{R}$$
$$\frac{d\kappa}{d\epsilon} = -\frac{1}{R^2}\frac{dR}{d\epsilon}$$

Substituting the value of $\frac{dR}{d\epsilon}$, we get

$$\begin{aligned}\frac{d\kappa}{d\epsilon} &= -\frac{1}{R^2}[\frac{1}{4}l^2(1+\epsilon)\left(h^2 - \frac{3}{8}l^2\epsilon - \frac{3}{16}l^2\,\epsilon^2\right)^{-\frac{1}{2}} \\ &+\frac{1}{4}\frac{l^2(1+\epsilon)^2}{4}\left(h^2 - \frac{3}{8}l^2\epsilon - \frac{3}{16}l^2\,\epsilon^2\right)^{-\frac{3}{2}}\left(\frac{3}{8}l^2 + \frac{3}{8}l^2\,\epsilon\right) \\ &-\frac{1}{4}\left(h^2 - \frac{3}{8}l^2\epsilon - \frac{3}{16}l^2\,\epsilon^2\right)^{-\frac{1}{2}}\left(\frac{3}{8}l^2 + \frac{3}{8}l^2\,\epsilon\right)]\end{aligned}$$

This analysis is valid for a fiber extension under an extensional strain aligned with the end-to-end vector of fiber (or chord). However, in a more general case of the fiber oriented randomly in two-dimensional space, the equation for $\frac{d\kappa}{d\epsilon}$ can be used with slight modification as discussed next.

Consider the schematic shown in Figure B.15, under a small shear strain a fiber (dashed red) with its end-to-end vector inclined at an angle, α, with respect to the direction of shear. Under shear, the deformed orientation of fiber is shown by dashed blue curve. Imposing

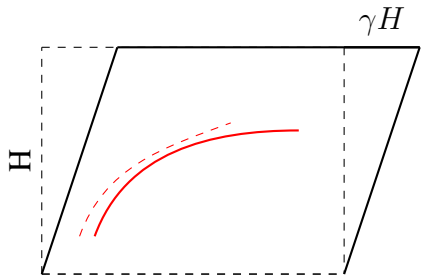

Figure B.14: Schematic of a body under shear. The fibrous microstructure also elongates and rotates depending on its orientation with respect to the direction of shear.

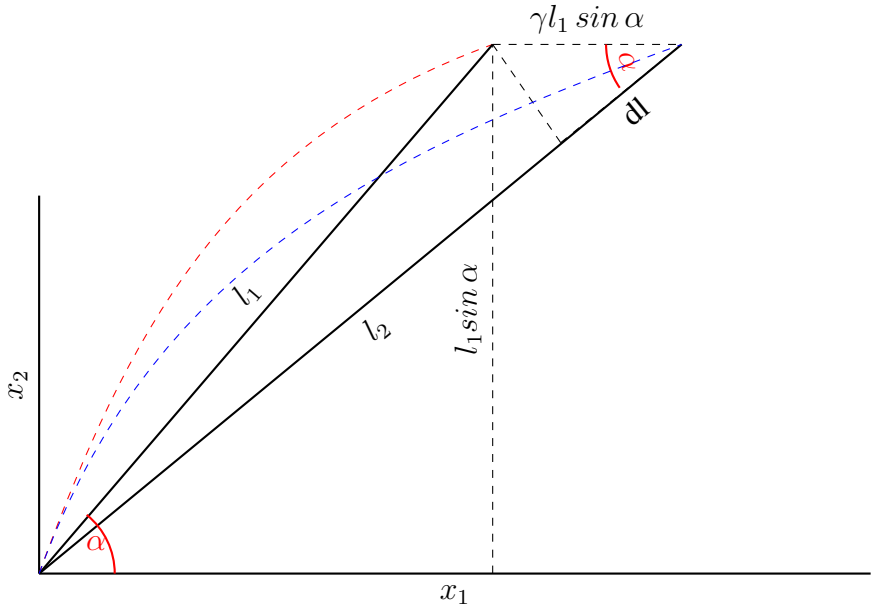

Figure B.15: A schematic of a fiber with an orientation α with respect to the direction of shear

the geometric constraints under the assumption of small strain we get,

$$l_2 = l_1(1 + \gamma \ sin\alpha \cos\alpha) \tag{B.19}$$

Comparing Eq.B.13 and B.19, it is clear that for an inclined curved fiber, ϵ gets replaced by $\gamma \ sin\alpha cos\,\alpha$. Hence, we can just replace ϵ in the previously derived results with $\gamma \ sin\alpha \cos\alpha$ to obtain

$$\begin{aligned}
\frac{d\kappa}{d\gamma} \quad = \quad & -\frac{1}{R^2}[\frac{1}{4}l^2(1+\gamma\, sin\alpha\cos\alpha)\left(h^2 - \frac{3}{8}l^2\gamma\, sin\alpha\cos\alpha - \frac{3}{16}l^2\left(\gamma\, sin\alpha\cos\alpha\right)^2\right)^{-\frac{1}{2}}(sin\alpha\cos\alpha) \\
& + \frac{1}{4}\frac{l^2(1+\gamma\, sin\alpha\cos\alpha)^2}{4}\left(h^2 - \frac{3}{8}l^2\gamma\, sin\alpha\cos\alpha - \frac{3}{16}l^2\left(\gamma\, sin\alpha\cos\alpha\right)^2\right)^{-\frac{3}{2}} \\
& \cdot\left(\frac{3}{8}l^2 sin\alpha\cos\alpha + \frac{3}{8}l^2\,\gamma\, sin^2\alpha\, cos^2\alpha\right) \\
& - \frac{1}{4}\left(h^2 - \frac{3}{8}l^2\gamma\, sin\alpha\cos\alpha - \frac{3}{16}l^2\left(\gamma\, sin\alpha\cos\alpha\right)^2\right)^{-\frac{1}{2}}\left(\frac{3}{8}l^2 sin\alpha\cos\alpha + \frac{3}{8}l^2\,\gamma\, sin^2\alpha\, cos^2\alpha\right)]
\end{aligned}$$

As $\gamma \to 0$, we get

$$\left.\frac{d\kappa}{d\gamma}\right|_{\gamma=0} = -\frac{l}{32R^2}\left(\frac{3}{4}\left(\frac{l}{h}\right)^3 + 5\frac{l}{h}\right) sin\,\alpha\, cos\,\alpha \tag{B.20}$$

Substituting the value of R in the above equation we get

$$\left.\frac{d\kappa}{d\gamma}\right|_{\gamma=0} = -\frac{l^2\left(3l^2+20h^2\right)\sin(2\alpha)}{4h\left(l^2+4h^2\right)^2} \tag{B.21}$$

To find $\langle(\left.\frac{d\kappa}{d\gamma}\right|_{\gamma=0})^2\rangle$, we average the square of Eq.B.21 over all the fiber orientations contributing to the elastic response in a 2D plane, i.e. $0 < \theta < \frac{\pi}{2}$

$$\langle(\left.\frac{d\kappa}{d\gamma}\right|_{\gamma=0})^2\rangle = \frac{1}{\pi}\int_0^{\frac{\pi}{2}}(\left.\frac{d\kappa}{d\gamma}\right|_{\gamma=0})^2 d\alpha \tag{B.22}$$

Hence,

$$\langle(\left.\frac{d\kappa}{d\gamma}\right|_{\gamma=0})^2\rangle = \frac{l^4\left(3l^2+20h^2\right)^2}{64h^2\left(l^2+4h^2\right)^4}$$

or

$$\langle(\left.\frac{d\kappa}{d\gamma}\right|_{\gamma=0})^2\rangle = \frac{\left(3+20(\frac{h}{l})^2\right)^2}{64h^2\left(1+4(\frac{h}{l})^2\right)^4} \tag{B.23}$$

Substituting Eq.B.23 into Eq.B.12 we get

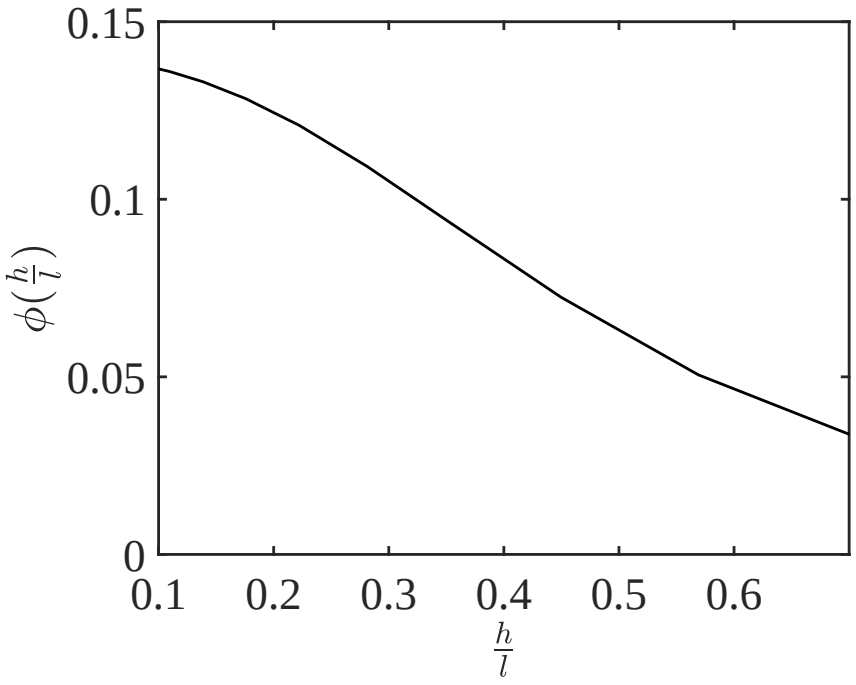

Figure B.16: For $\frac{h}{l} < 1$, the shear modulus is a very weak function of $\frac{h}{l}$

$$G = \rho E I \frac{\left(3 + 20(\frac{h}{l})^2\right)^2}{64h^2\left(1 + 4(\frac{h}{l})^2\right)^4} \tag{B.24}$$

$$G = \rho E I \frac{1}{h^2}\phi(\frac{h}{l}) \tag{B.25}$$

Eq.B.24 intuitively makes sense. First, shear modulus increases with decreasing h. Higher h means more curvy fiber, hence easier to straighten it. We also find that the factor $\phi(\frac{h}{l}) = \frac{\left(3+20(\frac{h}{l})^2\right)^2}{64\left(1+4(\frac{h}{l})^2\right)^4}$ appearing in the expression of shear modulus is nearly constant for $\frac{h}{l} < 1$ (Fig. B.16), hence weakly changes the shear modulus.

B.8.3 Pure Stretching Response

In this section, we evaluate the fibrous network modulus, assuming the fibers to be straight elastic rods without any bends. Hence, applied deformation will lead to stretching of fibers depending on their orientation with respect to the applied strain

In is clear from the above Figure B.15 that under an applied shear strain, γ, elastic rod, length l_1 will stretch, new length l_2, and rotate. The deformation of a rod aligned at an angle α to the direction of shear

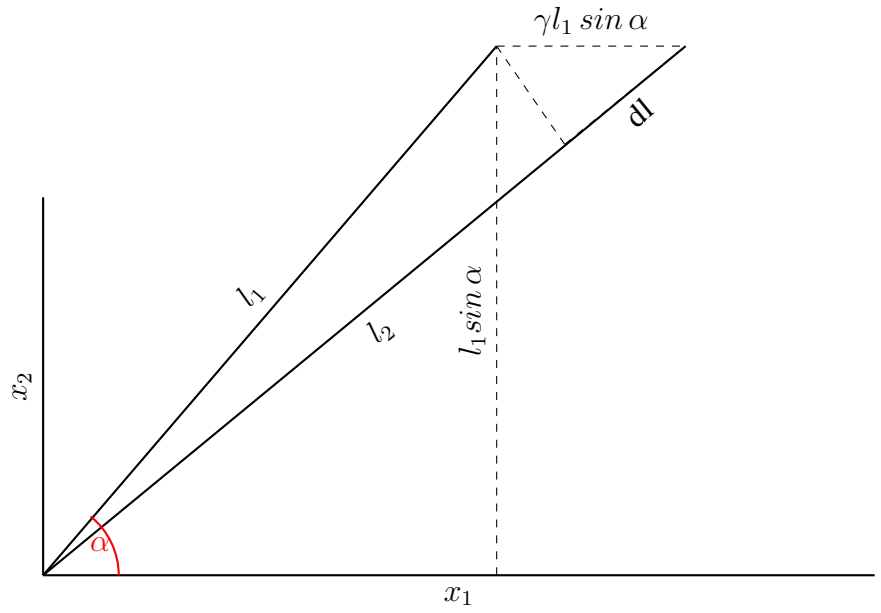

Figure B.17: A schematic of a straight elastic rod with an orientation α with respect to the direction of shear

$$\frac{\Delta l}{l} = \gamma \; sin\alpha \, cos\, \alpha \tag{B.26}$$

Hence, the energy stored per unit length in the elastic rod is given by

$$dE_{stretch} = \frac{1}{2} E_f a^2 (\gamma \; sin\alpha \, cos\, \alpha)^2 \tag{B.27}$$

where a is the fiber radius.

To get an average response from the network of randomly oriented chains, we average over all orientations. Hence,

$$\langle dE_{stretch} \rangle = \frac{\frac{1}{2} E_f a^2 \int_0^{\frac{\pi}{2}} (\gamma \; sin\alpha \, cos\, \alpha)^2 d\alpha}{\pi} \tag{B.28}$$

Hence,

$$\langle dE_{stretch} \rangle = \frac{1}{32} E_f a^2 \gamma^2 \tag{B.29}$$

We can now evaluate the a shear modulus, $G_{stretch}$, based on the response from stretched fibers by an energy balance with the applied deformation. We obtain

$$G_{stretch} = \frac{\rho}{16} E_f a^2 \tag{B.30}$$

where ρ is the total fiber length per unit volume.

B.8.4 Estimates

From the microscopic images, we find the average values of the parameters involved in the expressions (Table S B.3). We evaluate the modulus from the estimates in Eq.B.24 and B.30.

Table B.3: Relevant parameters for hagfish defense gel

parameter	value
geometric dimension, h	23 ± 3.7 μm
geometric dimension, l	121 ± 32 μm
fiber radius, a	1 μm
fiber length, L_{fiber}	10 cm
thread cell radius, $R_{thread\,cell}$	50 μm
Young's modulus, E_f	6.8 MPa

ρ is proportional to the total number of fibers, n, in the sample which in turn is proportional to the volume of exudate ($V_{exudate}$) that is introduced into the artificial sea water to produce the hagfish defense gel sample. Hence, we can find the total number of thread cells given by the ratio of exudate volume to that of the volume of a single thread cell (Assuming sphere of radius, R). Hence we obtain, $n = \frac{0.5*0.33*\mathbf{V}_{exudate}}{\mathbf{V}_{thread\,cell}}$. The factor 0.5 appears because exudate has mucins and thread cells in approximately equal proportion. Since 66% of exudate is water by volume, the factor 0.33 appears as a front factor.

Alternatively, we can express n in terms of the sample concentration of final sample. Here we assume that the density of exudate is similar to that of water, since 66% of exudate is water [33]. The $V_{thread\,cell}$ is assumed to be equal to a sphere of radius, $R_{thread\,cell}$. Having obtained, n, we find the effective length per unit volume, $\rho = \frac{L_{fiber}n}{\mathbf{V}}$, where L_{fiber} is the total fiber length and $\mathbf{V}$ is the total sample volume.

Using the parameters given in the table B.3 and hence find the modulus estimate. For a concentration of 0.17 wt $\%$, we find a bending dominated response with a shear modulus, $G = 0.03$ Pa whereas we find that a stretching dominated response gives a shear modulus $G_{stretch} = 60$ Pa. The experimental measurement using oscillatory shear gives a value of 0.02 Pa. The slight mismatch may arise because of several factors such as, viscous dissipation,fraction of intact thread cells in the sample etc. Similarly, we can evaluate the shear modulus arising from a pure bending and stretching response from the fibers for all concentrations. Hence, we believe the linear response from the hagfish defense gel is purely a bending dominated response.

Error Propagation

Neglecting correlations between the variables (a, l, h), we can propagate error in Eq. B.24 as follows

$$G_{sd} = \sqrt{\left(\frac{\partial G}{\partial a}\right)^2 a_{sd}^2 + \left(\frac{\partial G}{\partial h}\right)^2 h_{sd}^2 + \left(\frac{\partial G}{\partial l}\right)^2 l_{sd}^2} \tag{B.31}$$

We estimate the values of parameters h and l from multiple microscopic images. The values are listed Table B.1. For the parameter,r, our microscopic images could not provide sufficient resolution to determine the values and standard deviation. So, we make a rough estimate of the standard deviation in r as, 5% of r.
This gives a standard deviation, G_{sd}, using Eq.B.31 in the elastic modulus, G, which is around 43% of G.

B.8.5 Response from Mucus Networks

We now evaluate the contribution from the mucus network in the mechanics of hagfish defense gel. It has been well reported in the literature [21, 35] that the concentration of mucus in hagfish slime is much lower than various other mucus secretions. Figure B.18 shows the dependence of mucus steady shear viscosity as the concentration of mucus is varied (adapted with permission [21]). The data is well described by a power series expansion

$$\frac{\eta}{\eta_s} = 1 + [\eta]c_m \tag{B.32}$$

where η is the dynamic viscosity of mucus solution, η_s is the solvent viscosity and c_m is the concentration of mucus in mg/L. $[\eta]$ is the intrinsic viscosity. A linear fit to the experimental data provides the value of $[\eta] = 0.0005\, L/mg$. The efficiency of the linear fit in describing the data also indicates that the tested concentrations are in the dilute regime i.e. the individual polymer chains are not interacting on the bulk scales. A system where the chains are starting to interact or overlap show much stronger concentration dependence that linearity. A critical overlap concentration is often defined as $c^* = \frac{1}{[\eta]}$. For hagfish mucus, $c^* = \frac{1.4}{0.0005}\frac{mg}{L}$ or 0.3 wt $\%$. As, mentioned earlier hagfish exudate is 66% water, hence mucus corresponds to 0.17% of the total exudate mass (assuming equal proportion of mucus and threads). Hence, we expect that for exudate concentration below ≈ 1.7 wt $\%$, mucus concentration is below the critical overlap concentration required to form a volume spanning network. Therefore, we argue that in the concentration range that we have probed, mucus does not form a volume spanning network of their own, they can rather form local

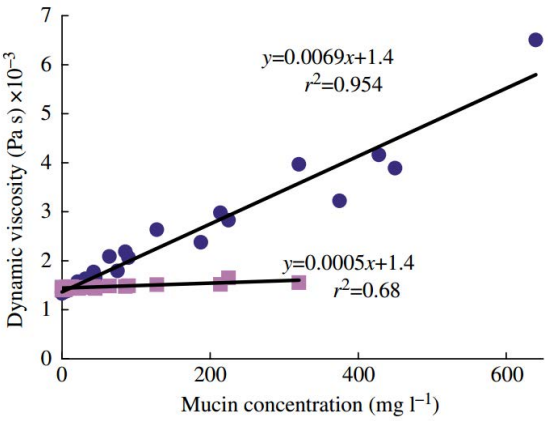

Figure B.18: Concentration dependence of steady shear viscosity of pure mucus solutions (adapted with permission [21]). Viscosity follows a linear relationship with the concentration. The purple squares shows the data for solutions prepared in sea water and the blue circles are for the solutions prepared in distilled water.

networks within the fibrous mesh. Such effects are beyond the scope of our zeroth order model, since it would require appropriate assumptions about the fiber-mucus interactions and the geometric details of it.

APPENDIX C

RHEOLOGY OF REPULSIVE PNIPAM MICROGEL SUSPENSIONS

parameter	value	method
$2R$	550 nm	Measured by DLS at low concentration (0.4 wt%)
c_1	0.4 wt%	Lowest concentration studied in experiments
c_2	1.5 wt%	Observed concentration where $G'(c)$ plot turns to linear dependence
$(\phi_{0.5\ wt\%}, E)$	(0.5067, 30000)	Volume fraction $\phi_{0.5\ wt\%}$ and softness parameter E are determined simultaneously from the inset of Fig. 4.9 the theoretical prediction of modulus to match the modulus at 0.5 wt% and additionally requiring that theory produces a similar order of magnitude growth in G' as that of experiments before soft jamming occurs.
		$\phi \sim c^{1/2}$ for $0.5 < c < 1.5$ wt% and $\phi \sim c^0$ for $1.5 < c < 9$ wt%

Table C.1: Parameters used in theory.

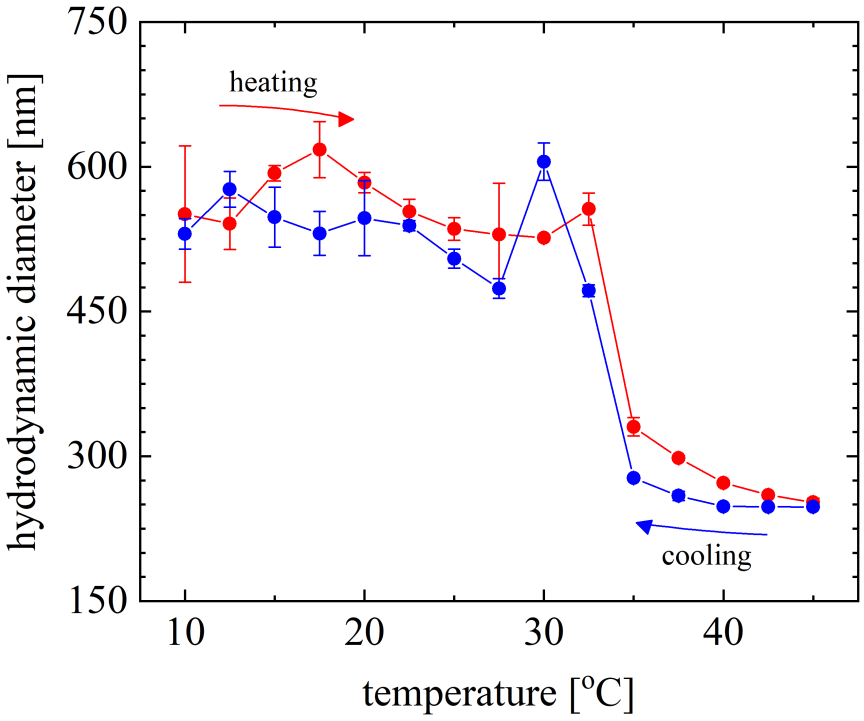

Figure C.1: Temperature dependence of the hydrodynamic diameter in the low concentration limit (0.04 wt%) of slightly charged microgels measured via DLS. As temperature increases in the region $T = 10 - 32°$C, there is a weak roughly linear decrease of the average hydrodynamic diameter. As the lower critical solution temperature (LCST) of pNIPAM microgels is crossed, microgels become hydrophobic and undergo massive deswelling.

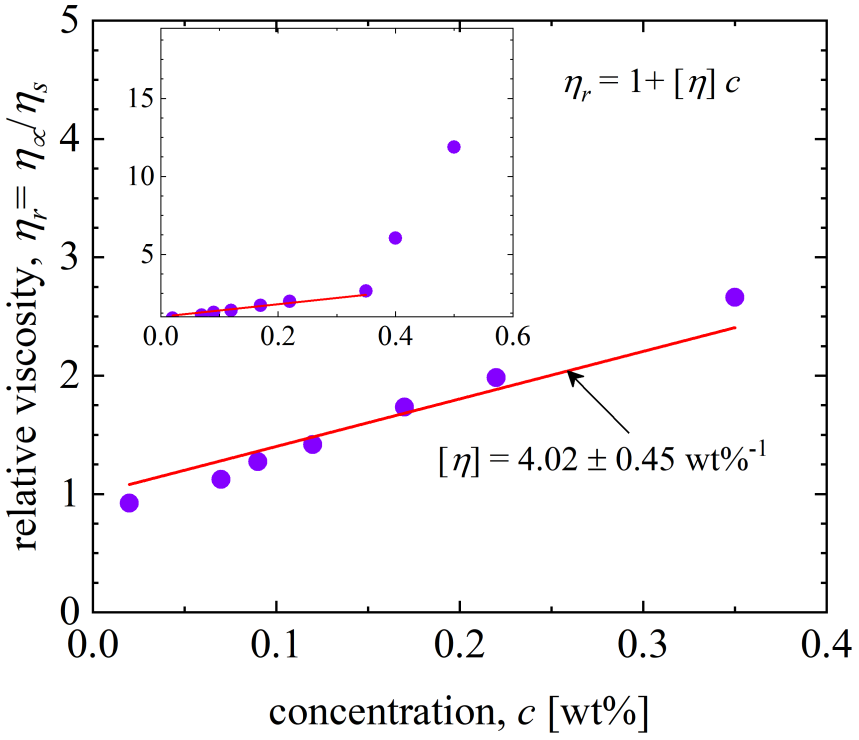

Figure C.2: At low concentrations, the relative viscosity $\eta_r = \eta_\infty/\eta_s$ at infinite shear rate (obtained using a Carreau-Yasuda model fits, $\eta(\dot{\gamma}) = \eta_\infty + (\eta_0 - \eta_\infty)[1 + (k\dot{\gamma})^1]^{\frac{n-1}{a}}$ agrees well with the Einstein equation ($\frac{\eta}{\eta_s} = 1 + 2.5\phi$). For dilute suspensions ($c \to 0$), the effective volume fraction can be related to the mass fraction using, $2.5\phi = [\eta]c$, where $[\eta]$ is the intrinsic viscosity ($[\eta] = 4.02 \pm 0.45$ wt%$^{-1}$). The solvent viscosity, η_s, is taken as that of deionized water (=0.001 Pa.s). At higher concentrations ($c > 0.35$ wt%) the viscosity strongly deviates in an upward direction due to inter-particle repulsions, consistent with our observation of a measurable linear elastic moduli at $c = 0.4$ wt%.

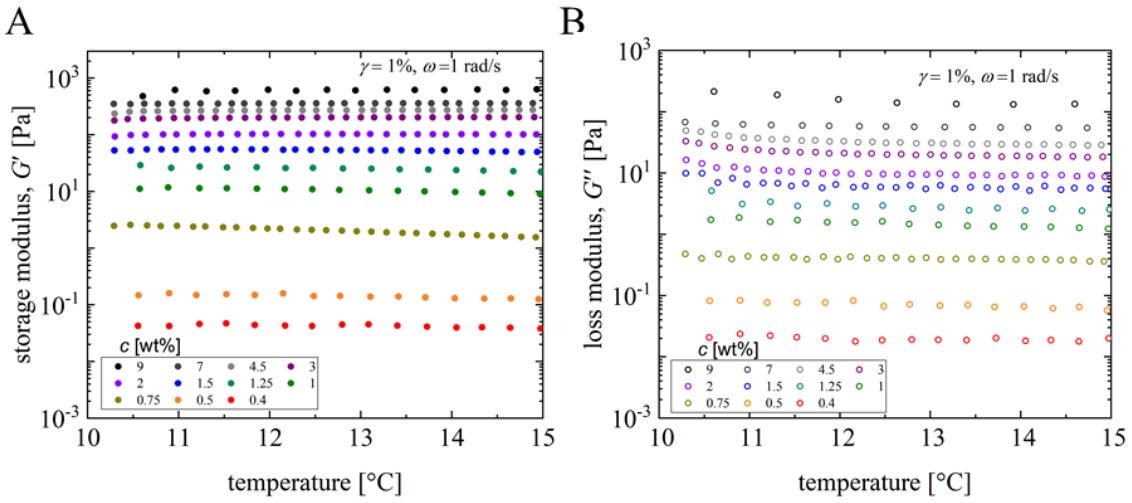

Figure C.3: (A) Storage modulus, G' and (B) Loss modulus, G'' , for various microgel concentrations in the temperature range $(10-15)°$C probed at a fixed strain amplitude of $\gamma_0 = 1\%$ in the linear response regime at an angular frequency of $\omega = 1$ rad/s The temperature is increased at a rate of $1°$C/min. The rheological properties are temperature independent in the range of probed temperature.

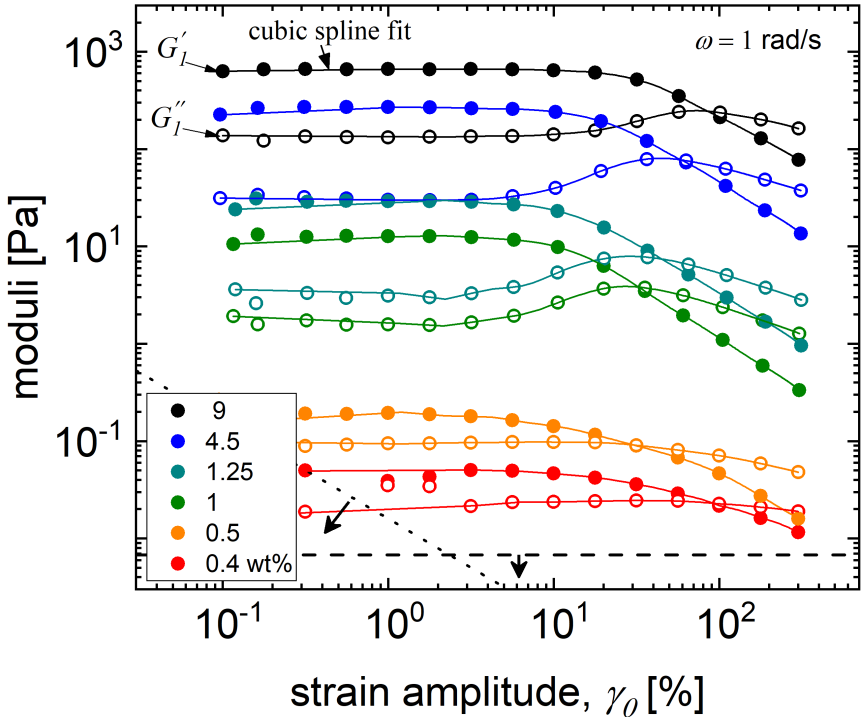

Figure C.4: Cubic spline fits to the amplitude sweep data to extract the yield properties. The strain amplitude at which a cubic spline fit to G_1'' achieves a maximum is taken as the dynamic yield strain and the point of intersection of cubic spline fits to G_1' and G_1'' is taken as the absolute yield strain.

APPENDIX D

RHEOLOGY OF DENSE ATTRACTIVE MICROGEL SUSPENSIONS

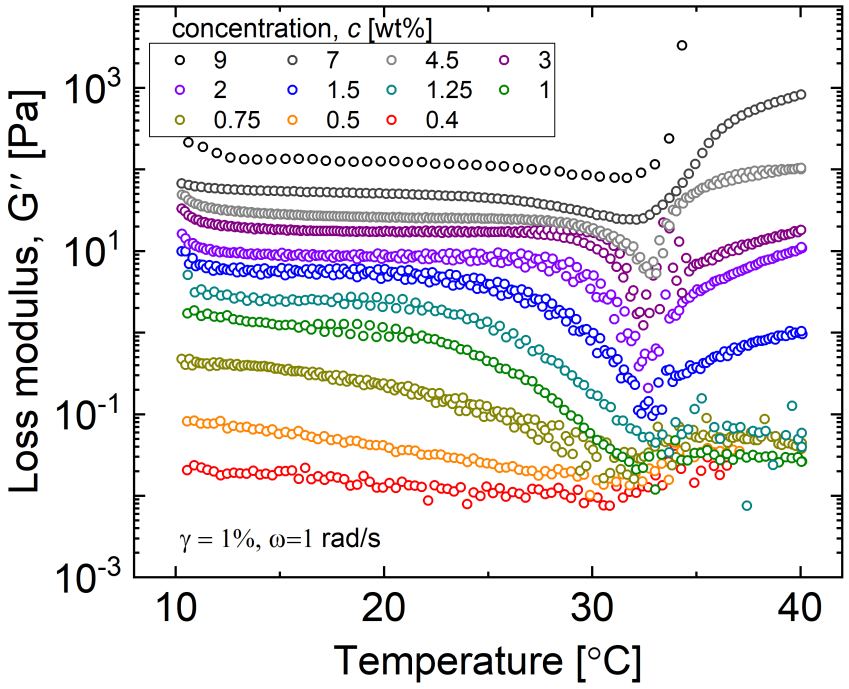

Figure D.1: Loss modulus for various suspension concentrations as a function of temperature.

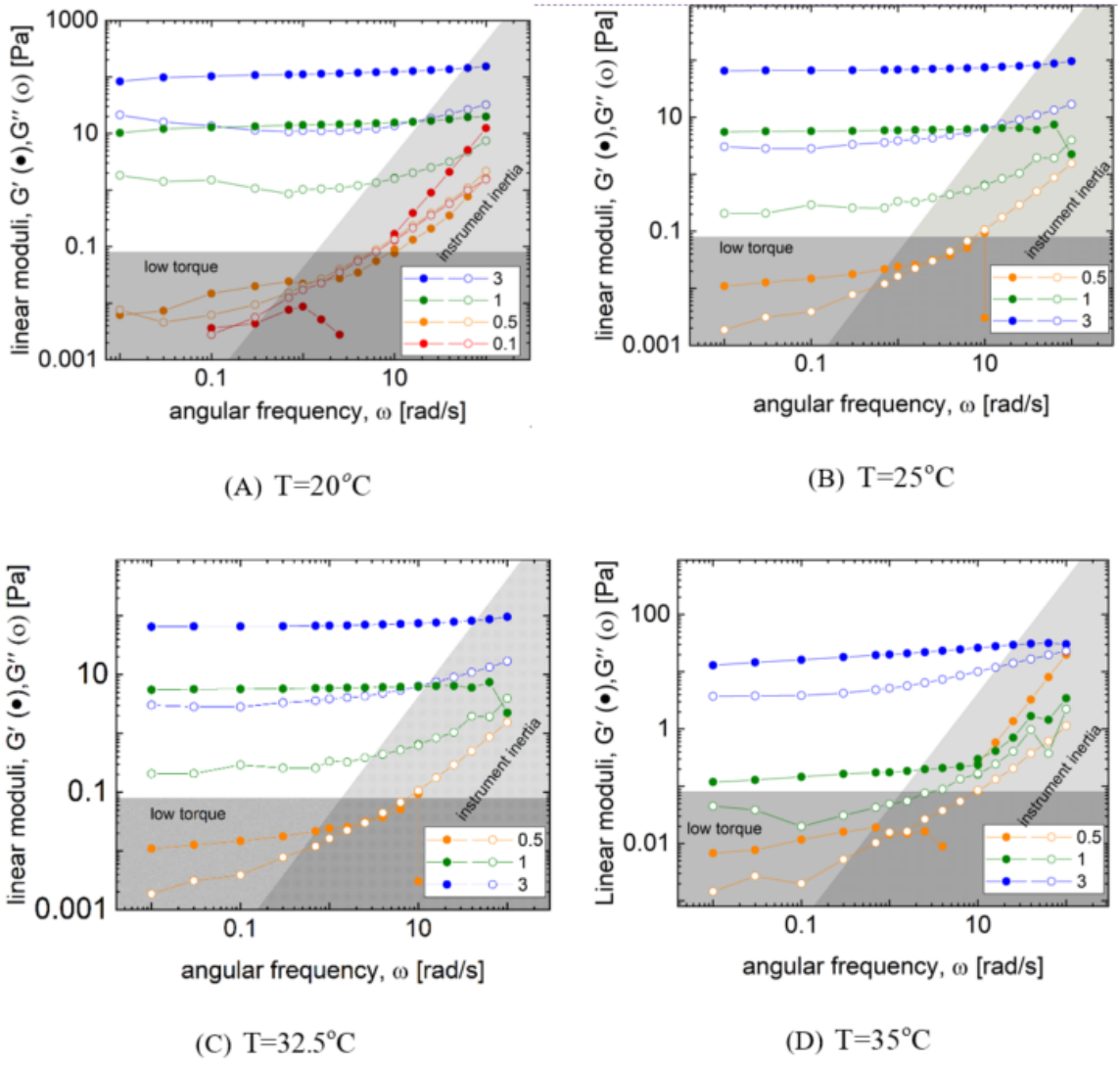

Figure D.2: Frequency sweep data for pure pNIPAM suspensions at various concentrations and temperatures.

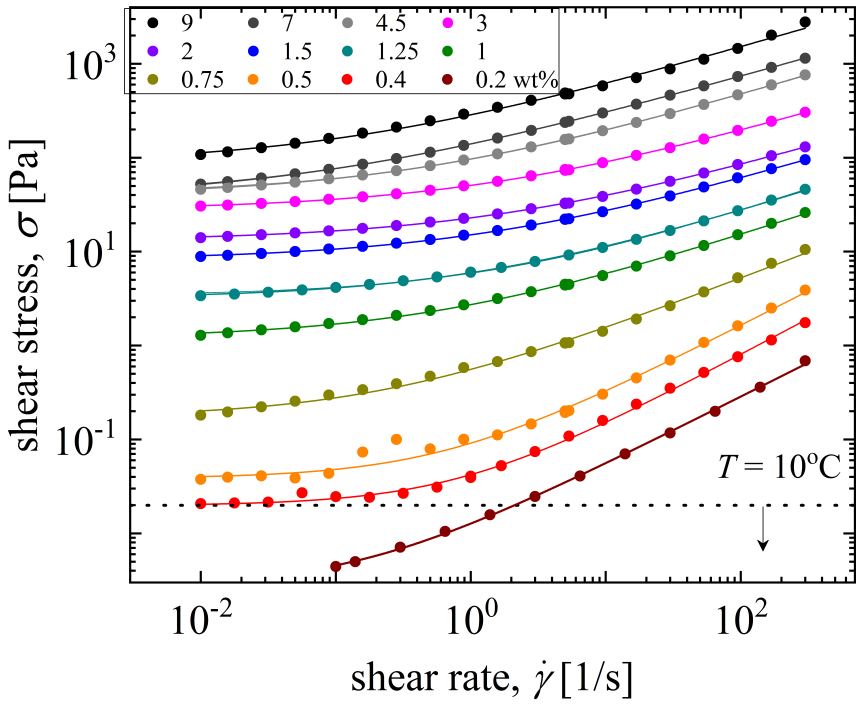

(a)

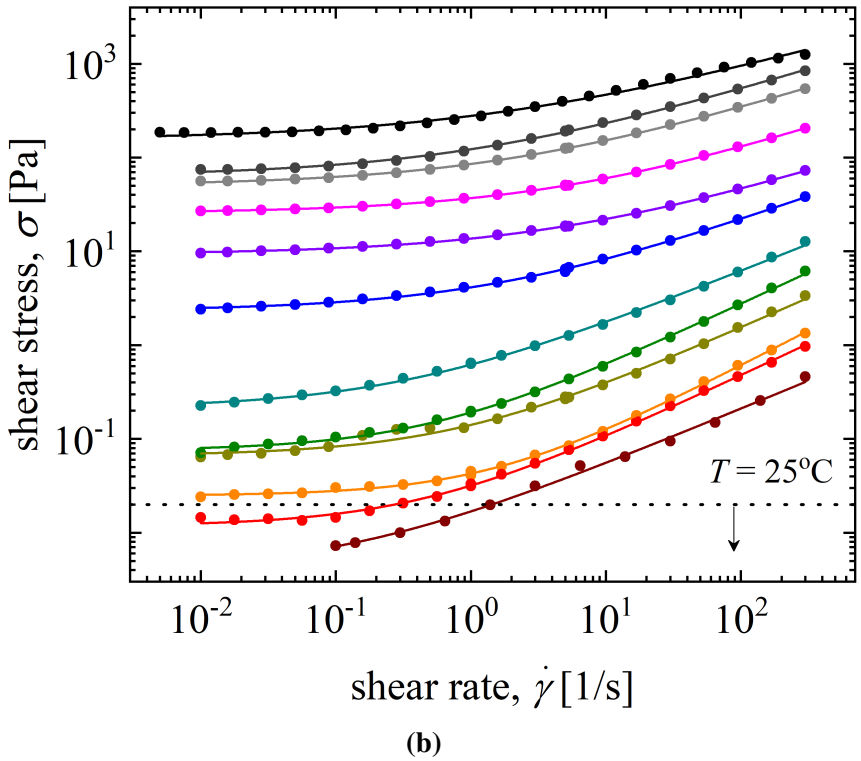

(b)

Figure D.3: Steady state shear flow curves for various suspension concentrations at (A)$10°C$ and (B)$25°C$. The solid lines shows the Herschel-Bulkley variance weighted fits to the experimental data.

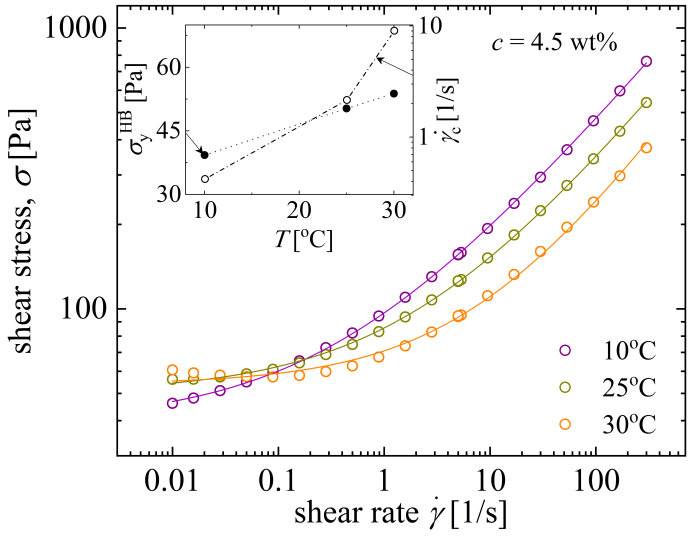

(a)

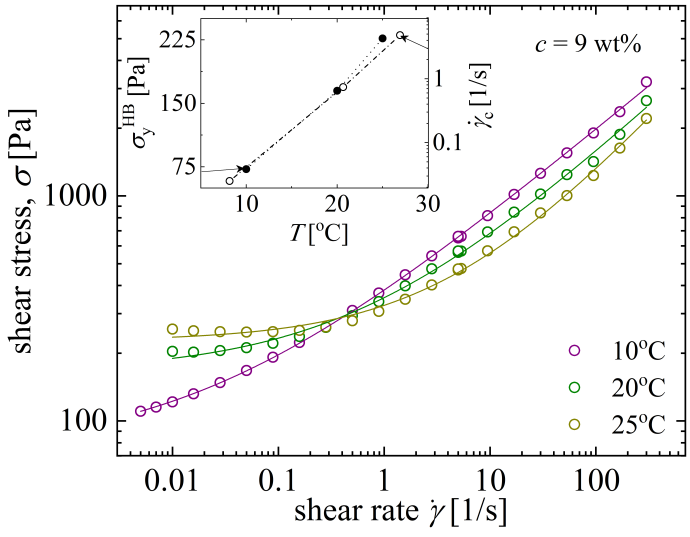

(b)

Figure D.4: Steady state shear flow curves at (a) 4.5 wt% and (b) 9 wt%.

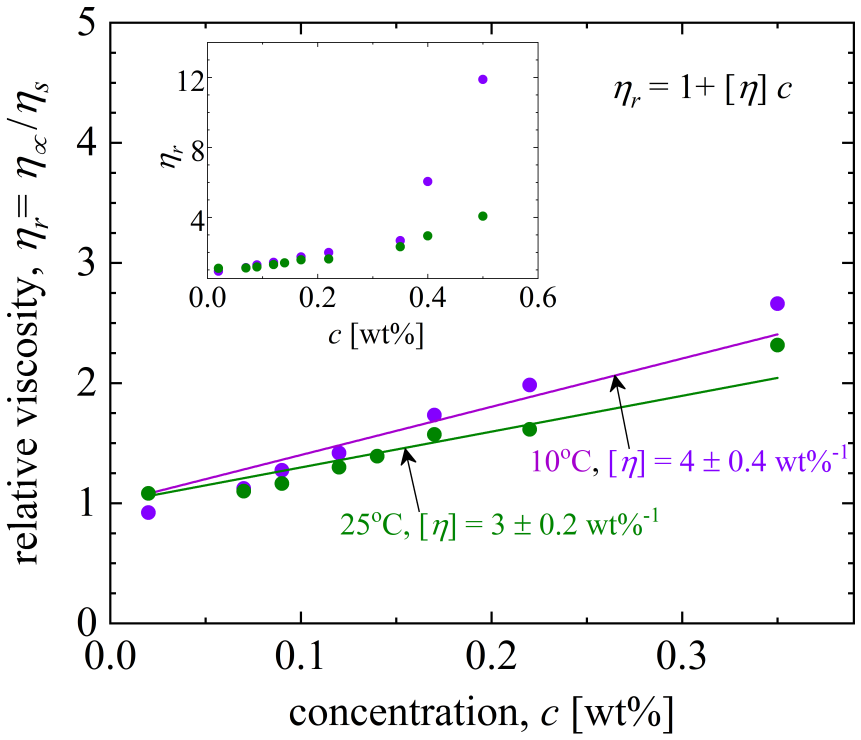

Figure D.5: At low concentration, the relative viscosity $\eta_r = \eta_\infty/\eta_0$ at infinite shear rate agrees well with Einstein equation ($\frac{\eta}{\eta_s} = 1 + 2.5\phi$). For dilute suspensions ($c \to 0$), the effective volume fraction can be related to the mass fraction using, $2.5\phi = [\eta]c$, where $[\eta]$ is the intrinsic viscosity and η_s is the pure solvent viscosity. We obtain variance weighted best fit values of $[\eta] = 4 \pm 0.4\,\text{wt}^{-1}$ and $[\eta] = 3 \pm 0.2\,\text{wt}^{-1}$ at $10°C$ and $25°C$, respectively.

APPENDIX E

THERMORESPONSIVE COMPOSITE

E.1 Microgel Synthesis

The lightly cross-linked monodisperse PNIPAM microgels were prepared by the surfactant-free emulsion polymerization (SFEP) method. 100 ml of Type I water (18.2 MÎl' cm) was filtered through a 0.2 μm Acrodisc syringe filter. Then, 146 mM (1.65 g) of N-isopropylacrylamide (NIPAM, 99%, Acros) monomer was dissolved in filtered water. The monomer solution was again filtered through a 0.2 μm Acrodisc syringe filter into a 3-neck round bottom flask. The solution was stirred at 500 rpm, purged with nitrogen, and heated to 45°C in a temperature-controlled oil bath until the temperature of the solution became stable (1 hour typically). We then injected a solution of 2.8 mM (80 mg) potassium peroxodisulfate (KPS, 99 %+, Sigma-Aldrich) dissolved in 1 ml of the pre-filtered Type 1 water through a 0.2 μm Acrodisc syringe filter to initiate the polymerization. The temperature was increased to 68oC roughly at a rate of 30°C/hr. The mixture was left to react under continuous stirring at 500 rpm in nitrogen atmosphere overnight. After the polymerization, the solution was cooled down to room temperature and filtered with a glass wool pad five times to remove large particulates. The microgel particles were then thoroughly purified via five cycles of a centrifuge/dispersion process. The centrifugation was done at 15000 x g of relative centrifugal force (RCF), and dispersion was enabled by a mixing process of ultrasonication followed by magnetic stirring. The cleaned particles were then lyophilized for further characterization.

E.2 Average Fiber Length

The values of and used in the effectively stretched polymer network model are obtained from literature [248] and extrapolated to estimate the values at missing concentrations (highlighted). The extrapolation was performed by assuming $l_0 = Ac_f^{-2/5} l_p^{1/5}$. Table E.1 gives the values of parameters used in the manuscript.

c_f [mg/ml]	l_0 [μm]	l_{arc} [μm]	x_0
0.4	7.17	8.2	0.92
0.8	5.15	5.7	0.93
1.6	3.8	4	0.95
3.2	3.1	3.26	0.951
6.4	2.37	2.49	0.952

Table E.1: Length scales of fibrin network used in the effective stretching polymer network model

c_f [mg/ml], c_P [wt%]	m
0.4, 0.5	0.915
0.4, 1	0.864
0.8, 0.5	0.908
0.8, 1	0.851
0.8, 2	0.749
1.6, 0.5	0.892
1.6, 1	0.823
1.6, 2	0.738
3.2, 0.5	0.885
3.2, 1	0.832
3.2, 2	0.730
3.2, 3	0.629
6.4, 1	0.827
6.4, 2	0.726
6.4, 3	0.625

Table E.2: Parameter m extracted from the effectively stretched polymer network model

The values of m for various composite compositions are given in the following table E.2:

E.3 Mesh Size of Fibrin

The mean mesh size and concentration of pure fibrin networks are related as $\xi \sim \rho^{-1/2}$, where ρ is the fiber length density [218]. Piechocka et al. [218] have determined ρ to be 6.1×10^{11} m^{-2} for $c = 1$ mg/ml. We employ the known ÏĄ to estimate average mesh size of pure fibrin as,

$$\xi = \left(\frac{1}{6.1 \times 10^{11} c_f} \right)^{1/2} \tag{E.1}$$

The quantitative estimates we employ are given in the table E.3

c_f [mg/ml]	ξ [μm]
0.4	2.02
0.8	1.43
1.6	1.01
3.2	0.72
6.4	0.51

Table E.3: Fibrin mesh size as a function of fibrin concentration

c_f [mg/ml], c_P [wt%]	ξ_1[μm]	stiffening ratio
0.4, 0.5	2.35	7.29
0.4, 1	2.57	9.9
0.8, 0.5	1.65	3.42
0.8, 1	1.80	4.46
0.8, 2	2.20	6.05
1.6, 0.5	1.15	1.75
1.6, 1	1.24	2.10
1.6, 2	1.5	2.68
3.2, 0.5	0.76	1.1
3.2, 1	0.81	1.15
3.2, 2	0.93	1.27
3.2, 3	1.2	1.40
6.4, 1	0.33	1.68
6.4, 2		
6.4, 3		

Table E.4: Model parameters for the adjustable mesh model

The various parameters involved in the adjusted mesh model are given in the following table E.4.

E.4 Elastic Modulus of a Single Microgel Particle and its Deswelling in the Fibrin Mesh

We first model the thermoresponsive phase transition behavior of a single pNIPAM microgel in a dilute aqueous suspension. Such systems have been widely modeled using Flory-Rehner theory [169, 234] The key idea is the balance of elastic ($\pi_{elastic}$) and mixing (π_{mix}) components of osmotic pressure (π) within the particle to calculate an equilibrium degree of swelling [234]

$$\pi = \pi_{elastic} + \pi_{mix} = 0 \tag{E.2}$$

ϕ_0	0.81
χ_2	0.3
χ_3	0.27
χ_4	0.72
A	-7.13
Θ	305.65

Table E.5: Fit parameters for the Flory-Rehner model employed

$$\pi = \frac{k_B T}{\alpha^3}\left(\frac{\phi_0}{N_{gel}}\left[\frac{\phi}{2\phi_0} - (\frac{\phi}{\phi_0})^{1/3}\right] + [-\phi - ln(1-\phi) - \chi\phi^2]\right) = 0 \qquad \text{(E.3)}$$

where N_{gel} is the average number of monomers between crosslinks, k_B is Boltzmann's constant, ϕ is the polymer volume fraction in a microgel, ϕ_0 is the polymer volume fraction in the collapsed state, α is the monomer size, and χ is the Flory-Huggins parameter. To describe microgel collapse, a temperature and concentration dependence of χ is necessary [287]. The following form has been widely used in the literature

$$\chi = \chi_1 + \chi_2\phi + \chi_3\phi^2 + \chi_4\phi^3 \qquad \text{(E.4)}$$

where $\chi_1 = 0.5 - A(1 - \Theta/T)$, Θ is the theta temperature, A depends of the mixing thermodynamics, and $\chi_2, \chi 3, \chi 4$ are the temperature independent coefficients that account for higher order interactions between polymer and solvent molecules [60].For the case of isotropic swelling, $\phi/\phi_0 = (d_0/d)^3$ where d_0 and d are particle sizes in reference and current state, respectively. We use the mean hydrodynamic diameter obtained from our light scattering experiments,d. Hence, by using the equilibrium condition of Eq.(S2), we extract the fit parameters: $N, \phi_0, A, \Theta, \chi_2, \chi_3, \chi_4$. Fig. S1 shows the best fit curve to the DLS data. The values of fit parameter are given in table E.5.
The shear modulus for polymer networks in solvent is given by [37,40]

$$\mu = \left(\frac{\phi_0 k_B T}{2N_{gel}\alpha^3}\right)\left(\frac{\phi}{\phi_0}\right)^{1/3} \qquad \text{(E.5)}$$

The parameter α cannot be obtained from fitting, hence we used its literature value $\alpha = 6.7 \times 10^{-10}$ m [37]. This gives a shear modulus of 1.5 kPa for the fully swollen microgel particle in dilute suspension at $25°$C using the DLS data and the fit parameters described above. For evaluating the shear modulus of particle in its shrunk state above the LCST temperature we employ the classic rubber elasticity theory for cross-linked polymer

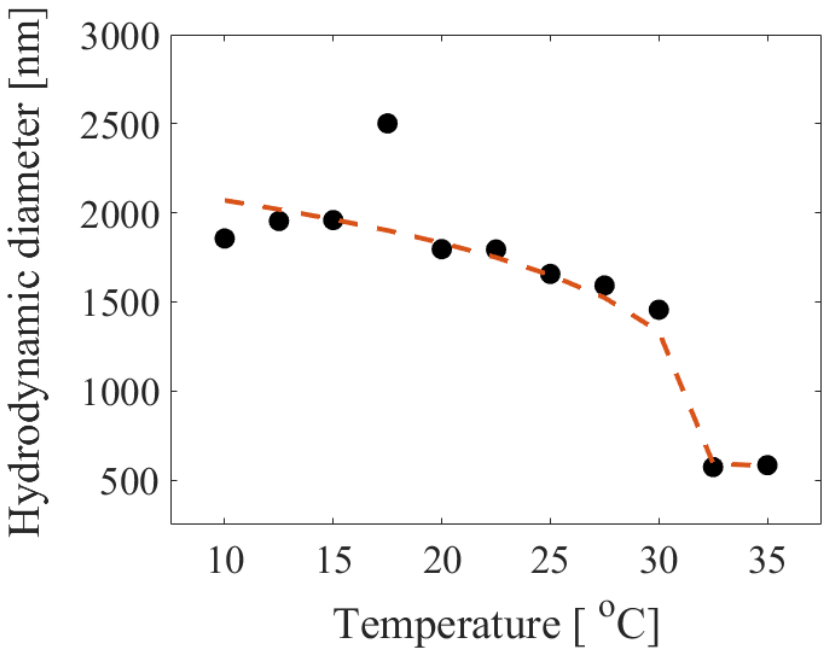

Figure E.1: The Flory-Rehner theory fit to the DLS data appears to capture the trends in the microgel hydrodynamic size.

c_P [mg/ml]	$\phi_{eff,i}$ [25°C]	$\phi_{eff,i}$ [35°C]
0.25	0.23	0.005
0.5	0.32	0.012
1	0.45	0.024
2	0.64	0.048
3	0.78	0.072

Table E.6: The effective volume fraction of the microgel suspensions used in the experiments.

networks in absence of solvent to estimate the shear elastic modulus as [37],

$$\mu = \left(\frac{k_B T}{2N_{gel}\alpha^3}\right)\phi \tag{E.6}$$

We obtain a microgel shear modulus of 4.6 kPa at 35°C.

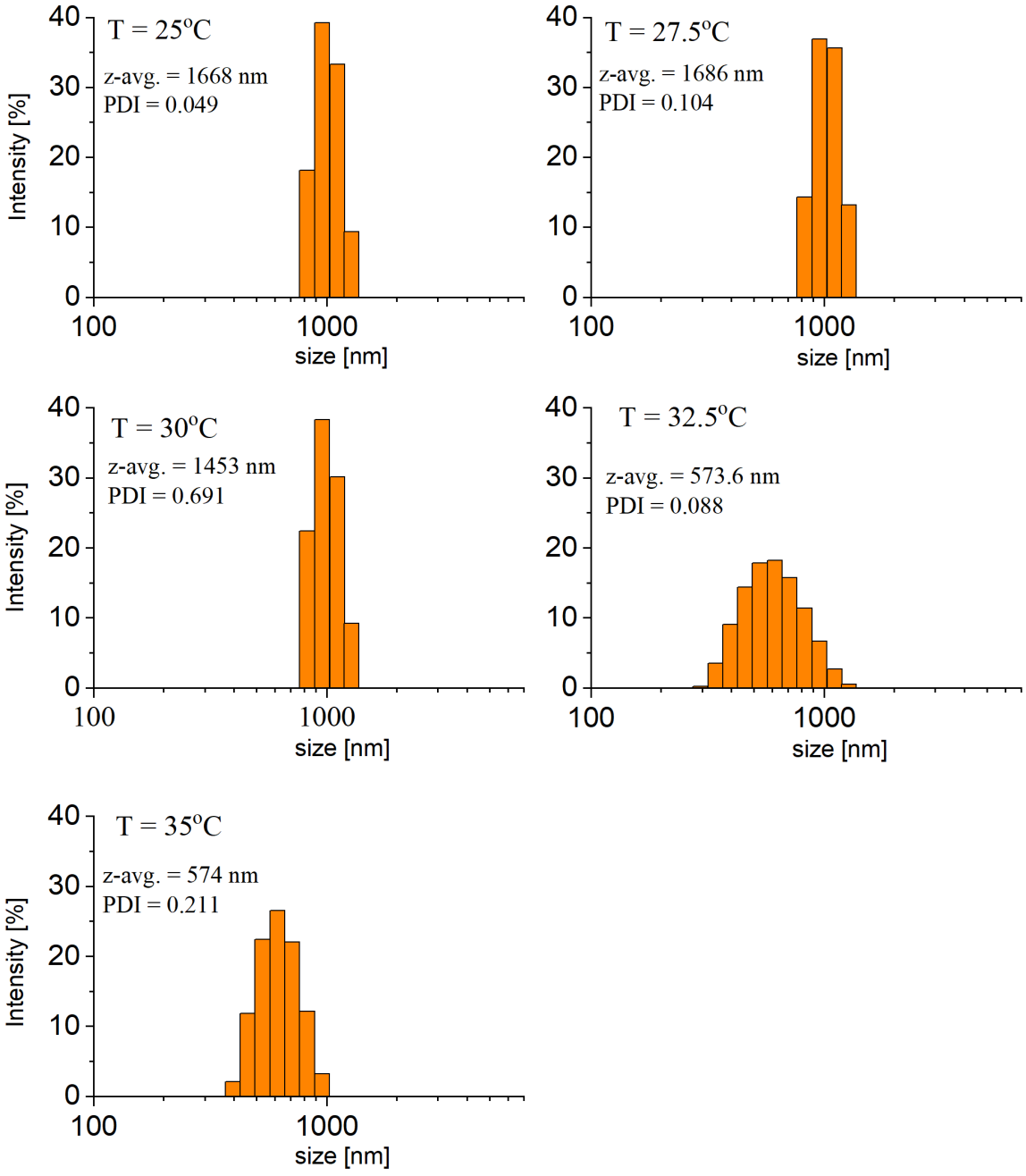

Figure E.2: Intensity versus microgel size data from the dynamic light scattering measurements (DLS) showing the distribution of particle sizes.

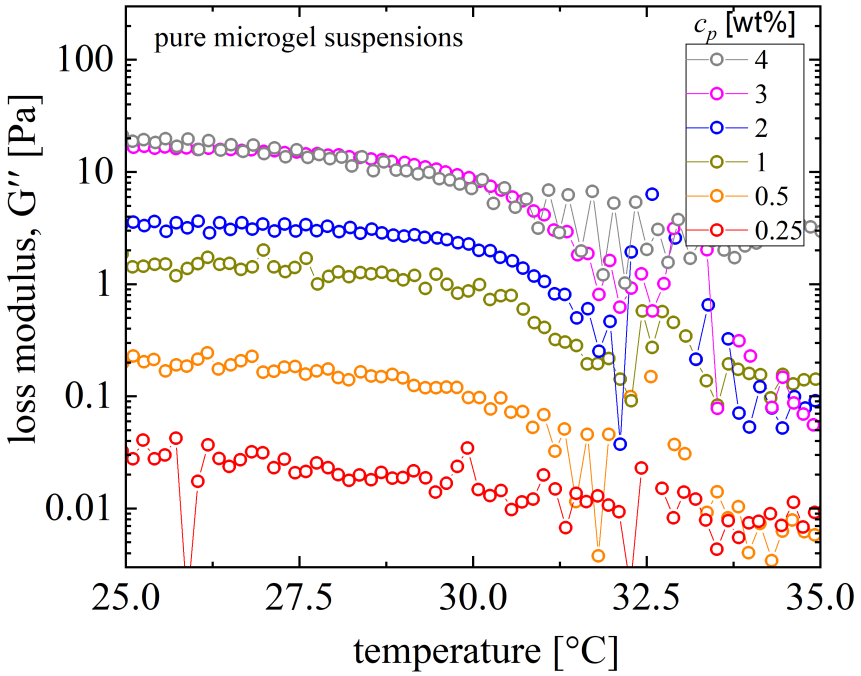

Figure E.3: The loss modulus G'' for pure pNIPAM suspensions.

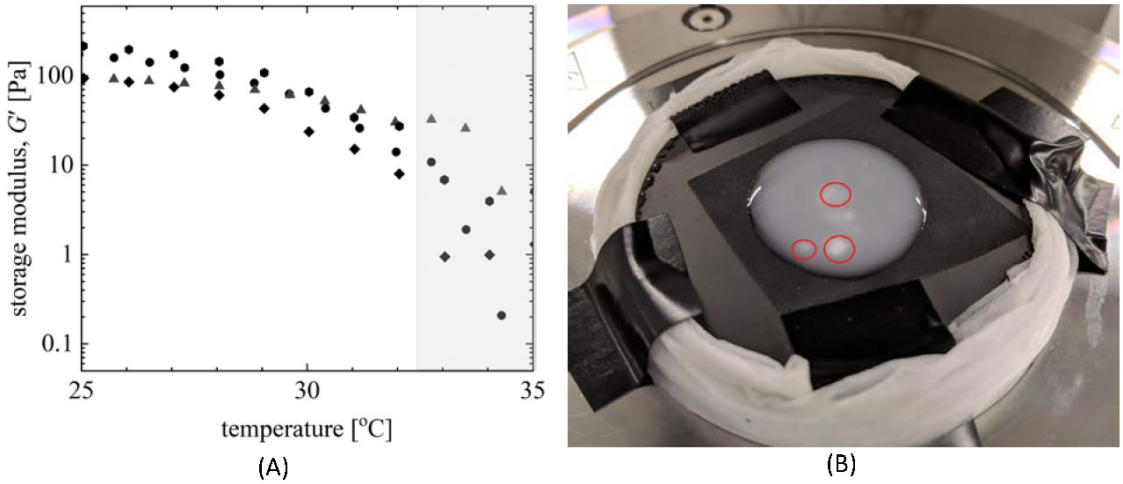

Figure E.4: (A) Repeatability of measurements for pure pNIPAM microgel suspensions. The data sets shown are for cp = 3 wt%. Above the LCST (shaded region), distinct trends can be observed in the values of G' because of the aggregation of microgels due to attractive interactions. Since the samples are unable to form a volume spanning network above the LCST, the inhomogeneity in the sample possibly are the origin of the variable behavior observed. (B) A photograph of the sample above the LCST showing the aggregation of microgels and there inhomogeneous distribution in the solvent.

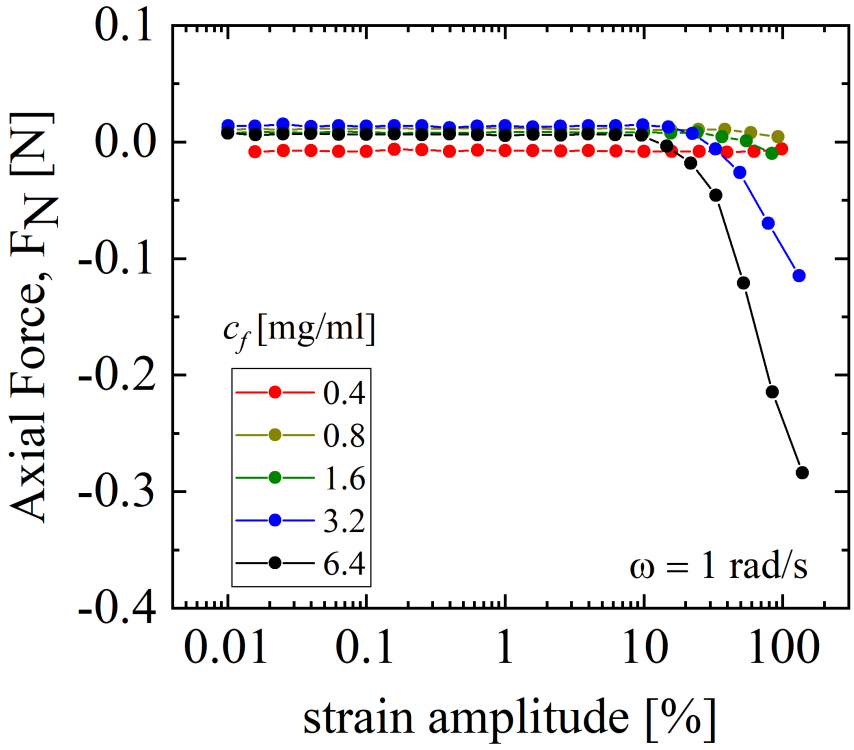

Figure E.5: Axial force for pure fibrin networks at various concentration studied as a function of applied shear strain amplitude.

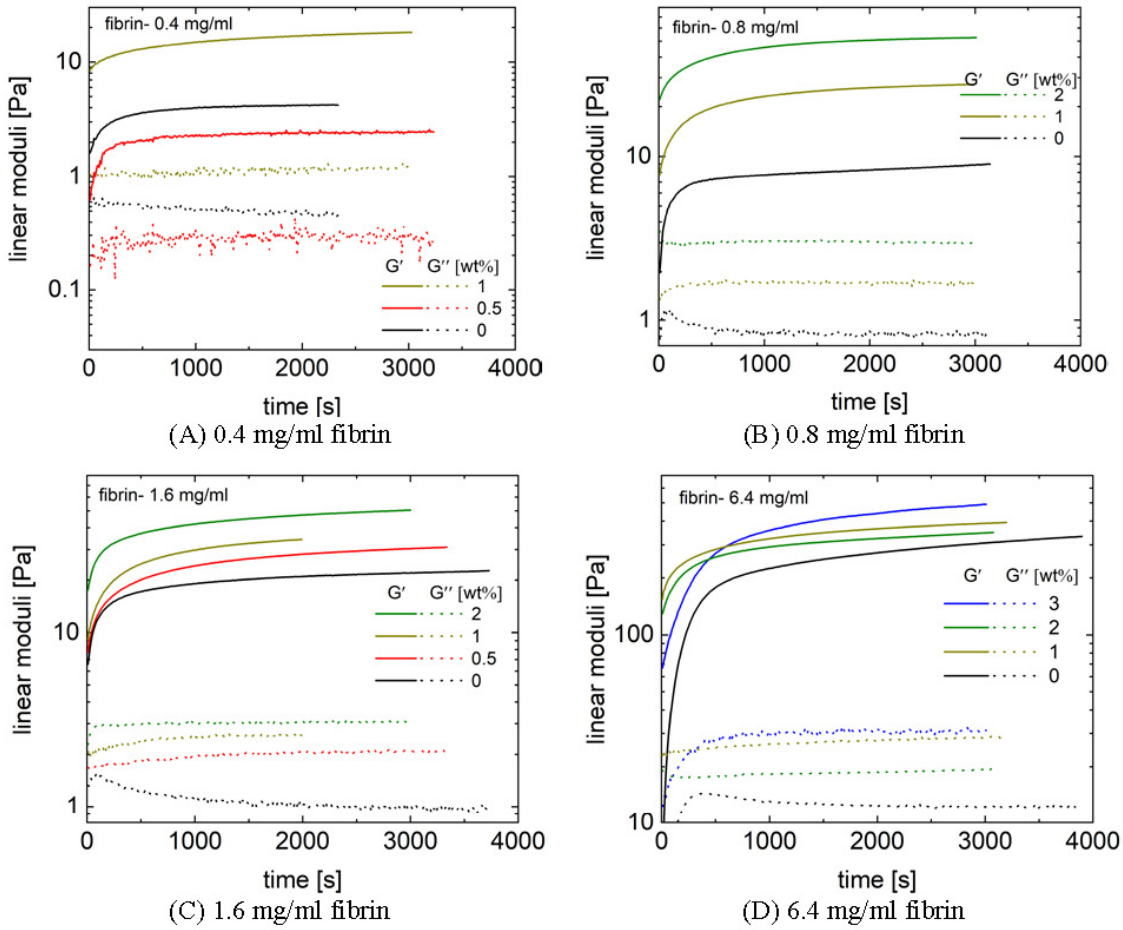

Figure E.6: Gelation of fibrin-pNIPAM composites. The concentration of pNIPAM microgels [wt%] used in the composites is given in the legend.

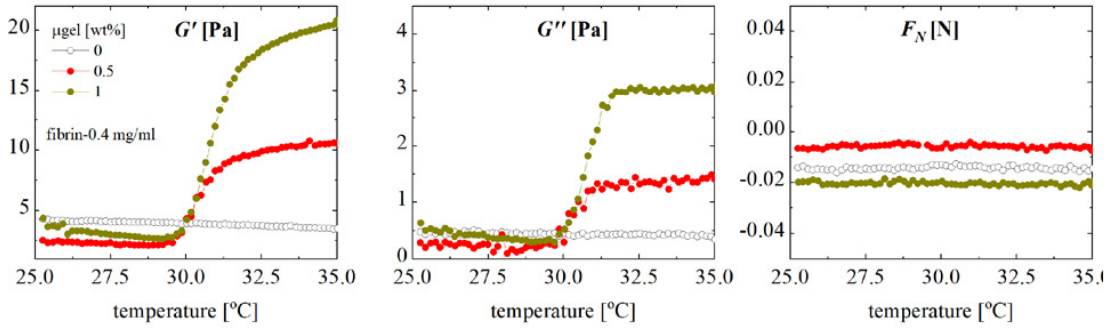

(A) 0.4 mg/ml

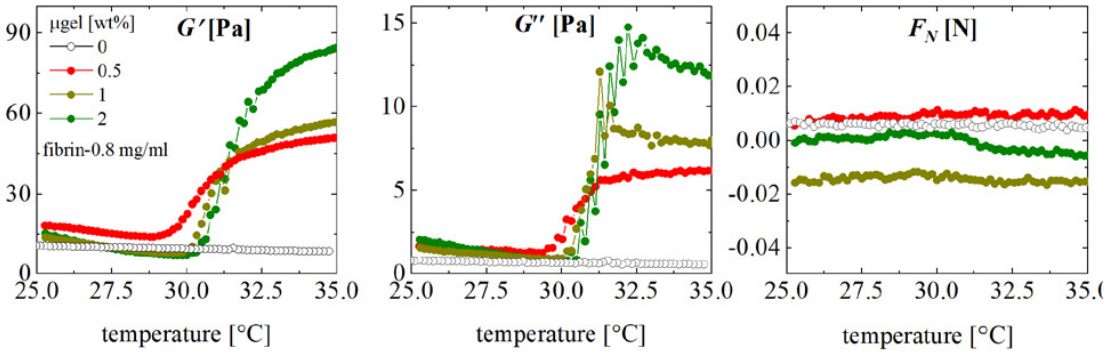

(B) 0.8 mg/ml

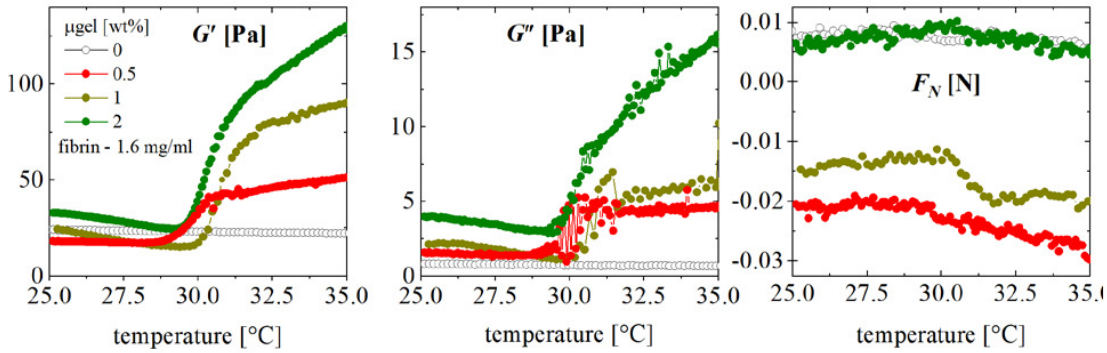

(C) 1.6 mg/ml

Figure E.7 (cont.)

Figure E.7 (cont.)

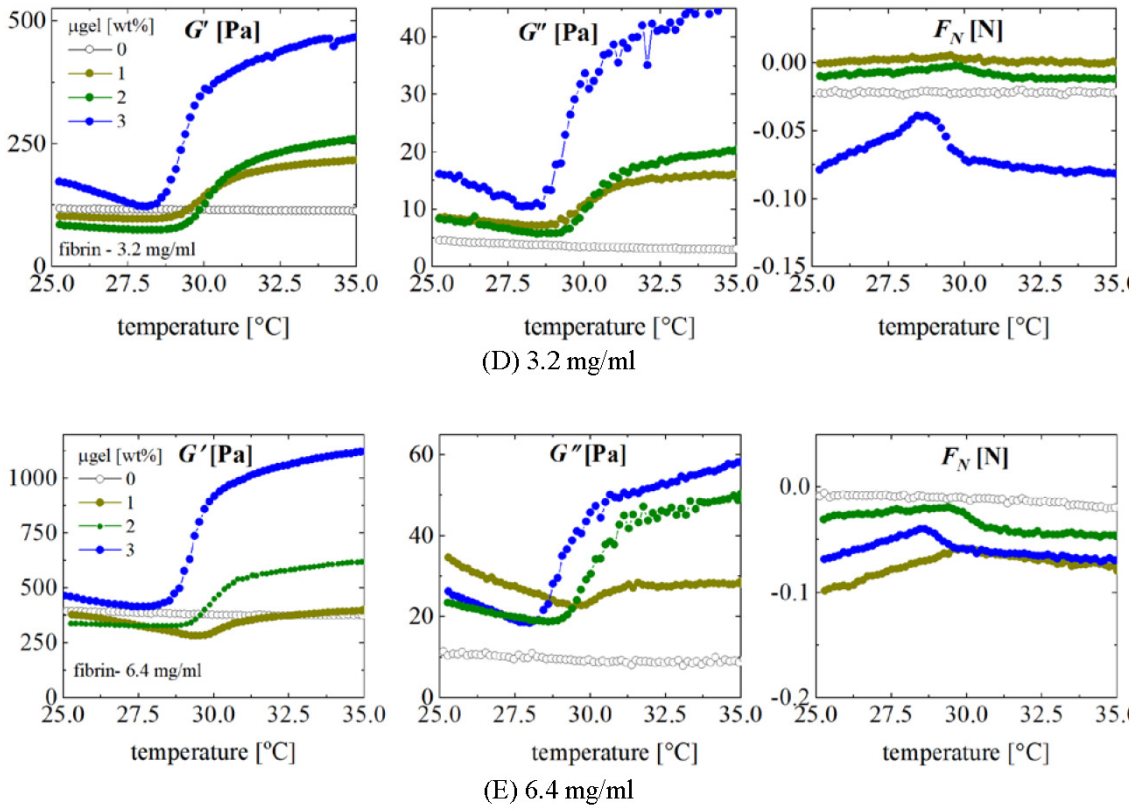

Figure E.7: Temperature-dependent viscoelasticity of composites with varying fibrin concentrations. The linear storage modulus G', the linear loss modulus G'', and the axial (normal) force F_N is shown for all the samples. The negative normal force indicates a downward pull on the upper plate of the rheometer.

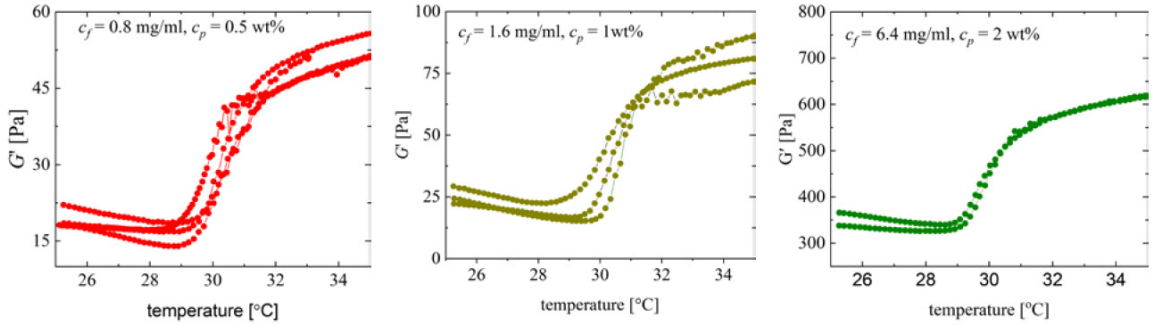

Figure E.8: Repeat measurements at selected compositions of composites.

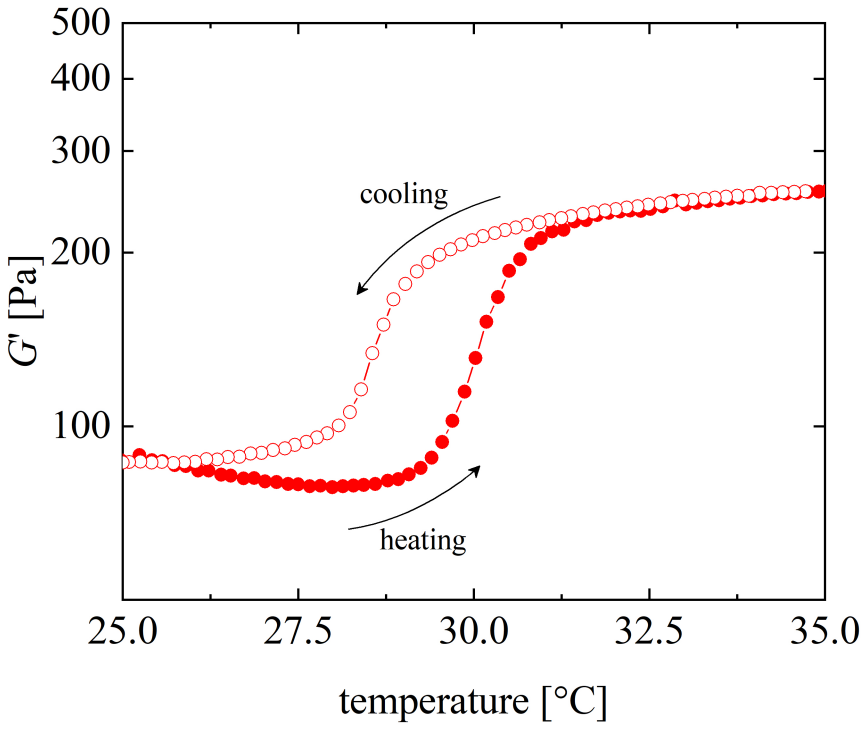

Figure E.9: Hysteresis in the stiffening and softening response in heating and cooling cycle (fibrin-3.2 mg/ml and microgels-2 wt%).

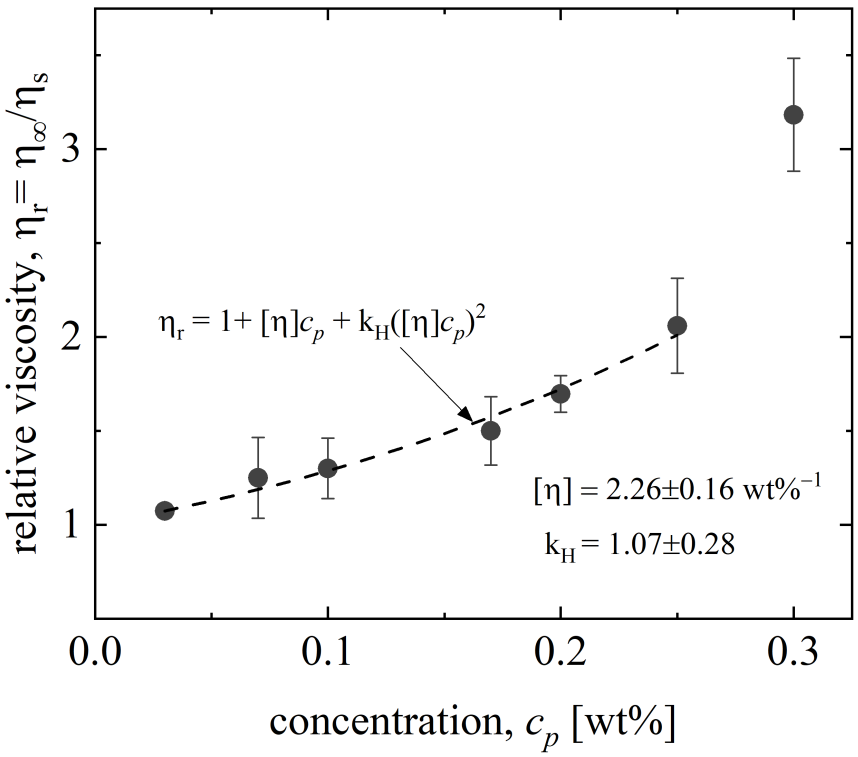

Figure E.10: Relative viscosity as a function of pNIPAM microgel wt% along with an empirical fit to the experimental data. The parameters $[\eta]$ and k_H are the intrinsic viscosity and Huggins coefficient, respectively. For a dilute suspension ($c_P \rightarrow 0$), the effective volume fraction can be related to the mass fraction as $2.5\phi = [\eta]c_P$.

REFERENCES

1. Capadona, J. R., Shanmuganathan, K., Tyler, D. J., Rowan, S. J. & Weder, C. Stimuli-Responsive Polymer Nanocomposites Inspired by the Sea Cucumber Dermis. *Science* **319,** 1370–1374 (2008).
2. Espinosa, L. M. D., Meesorn, W., Moatsou, D. & Weder, C. Bioinspired Polymer Systems with Stimuli-Responsive Mechanical Properties. *Chemical Reviews* **117,** 12851–12892 (2017).
3. Dawson, C., Vincent, J. F. & Rocca, A.-M. How pine cones open. *Nature* **390,** 668 (1997).
4. Fratzl, P. & Barth, F. G. Biomaterial systems for mechanosensing and actuation. *Nature* **462,** 442 (2009).
5. Reyssat, E. & Mahadevan, L. Hygromorphs: from pine cones to biomimetic bilayers. *Journal of the Royal Society Interface* **6,** 951–957 (2009).
6. Forterre, Y., Skotheim, J. M., Dumais, J. & Mahadevan, L. How the Venus flytrap snaps. *Nature* **433,** 421–425 (2005).
7. Zhao, Q. *et al.* A bioinspired reversible snapping hydrogel assembly. *Materials Horizons* **3,** 422–428 (2016).
8. Wang, M., Tian, X., Ras, R. H. A. & Ikkala, O. Sensitive Humidity-Driven Reversible and Bidirectional Bending of Nanocellulose Thin Films as Bio-Inspired Actuation. *Advanced Materials Interfaces* **2,** 1500080 (2015).
9. Peng, K., Tomatsu, I. & Kros, A. Light controlled protein release from a supramolecular hydrogel. *Chem. Commun.* **46,** 4094–4096 (23 2010).
10. Lee, K. M. *et al.* Photodriven, Flexural-Torsional Oscillation of Glassy Azobenzene Liquid Crystal Polymer Networks. *Advanced Functional Materials* **21,** 2913–2918 (2011).

11. Fukushima, T., Asaka, K., Kosaka, A. & Aida, T. Fully Plastic Actuator through Layer-by-Layer Casting with Ionic-Liquid-Based Bucky Gel. *Angewandte Chemie International Edition* **44,** 2410–2413 (2005).

12. Okuzaki, H. & Kunugi, T. Electrically induced contraction of polypyrrole film in ambient air. *Journal of Polymer Science Part B: Polymer Physics* **36,** 1591–1594 (1998).

13. Rich, J. P., Doyle, P. S. & Mckinley, G. H. Magnetorheology in an aging, yield stress matrix fluid. *Rheologica Acta* **51,** 579–593 (2012).

14. Jolly, M. R., Carlson, J. D., Munoz, B. C. & Bullions, T. A. The Magnetoviscoelastic Response of Elastomer Composites Consisting of Ferrous Particles Embedded in a Polymer Matrix. *Journal of Intelligent Material Systems and Structures* **7,** 613–622 (1996).

15. Liu, Z.-X. *et al.* Multistimuli Responsive Dendritic Organogels Based on Azobenzene-Containing Poly(aryl ether) Dendron. *Chemistry of Materials* **24,** 3751–3757 (2012).

16. Yildirim, T. *et al.* Dual pH and ultrasound responsive nanoparticles with pH triggered surface charge-conversional properties. *Polym. Chem.* **8,** 1328–1340 (8 2017).

17. Hoogenboom, R. in *Smart Polymers and their Applications* (eds Aguilar, M. R. & Roman, J. S.) 15 –44 (Woodhead Publishing, 2014). ISBN: 978-0-85709-695-1.

18. Liu, Z. *et al.* Transient adhesion in a non-fully detached contact. *Scientific Reports* **8,** 6147 (2018).

19. Jackson, J. A. *et al.* Field responsive mechanical metamaterials. *Science Advances* **4** (2019).

20. Ferry, J. D. A fibrous protein from the slime of the hagfish. *Journal of Biological Chemistry* **138,** 263–268 (1941).

21. Fudge, D. S., Levy, N., Chiu, S. & Gosline, J. M. Composition, morphology and mechanics of hagfish slime. *Journal of Experimental Biology* **208,** 4613–4625 (2005).

22. Lim, J., Fudge, D. S., Levy, N. & Gosline, J. M. Hagfish slime ecomechanics: testing the gill-clogging hypothesis. *Journal of Experimental Biology* **209,** 702–10 (2006).

23. Zintzen, V. *et al.* Hagfish slime as a defence mechanism against gill-breathing predators. *Scientific Reports* **1,** 131 (2011).

24. Bishop, K. L., Wainwright, P. C. & Holzman, R. Anterior-to-posterior wave of buccal expansion in suction feeding fishes is critical for optimizing fluid flow velocity profile. *Journal of The Royal Society Interface* **5,** 1309–1316 (2008).

25. Yaniv, S., Elad, D. & Holzman, R. Suction feeding across fish life stages: flow dynamics from larvae to adults and implications for prey capture. *Journal of Experimental Biology* **217,** 3748–3757 (2014).

26. Chapman, J. W. *et al.* Animal Orientation Strategies for Movement in Flows. *Current Biology* **21,** R861–R870 (2011).

27. Oteiza, P., Odstrcil, I., Lauder, G., Portugues, R. & Engert, F. A novel mechanism for mechanosensory-based rheotaxis in larval zebrafish. *Nature* **547,** 445–448 (2017).

28. Waggett, R. J. & Buskey, E. J. Calanoid copepod escape behavior in response to a visual predator. *Marine Biology* **150,** 599–607 (2006).

29. Downing, S. W., Salo, W. L., Spitzer, R. H. & Koch, E. A. The hagfish slime gland: a model system for studying the biology of mucus. *Science* **214,** 1143–1145 (1981).

30. Jørgensen, J. M., Lomholt, J. P., Weber, R. E. & Malte, H. *The biology of hagfishes* (Springer Science & Business Media, 2012).

31. Fernholm, B. Thread cells from the slime glands of hagfish (Myxinidae). *Acta Zoologica* **62,** 137–145 (1981).

32. Bernards, M. A., Oke, I., Heyland, A. & Fudge, D. S. Spontaneous unraveling of hagfish slime thread skeins is mediated by a seawater-soluble protein adhesive. *Journal of Experimental Biology* **217,** 1263–1268 (2014).

33. Ewoldt, R. H., Winegard, T. M. & Fudge, D. S. Non-linear viscoelasticity of hagfish slime. *International Journal of Non-Linear Mechanics* **46,** 627–636 (2011).

34. Winegard, T. *et al.* Coiling and maturation of a high-performance fibre in hagfish slime gland thread cells. *Nature Communications* **5,** 3534 (2014).

35. Böni, L., Fischer, P., Böcker, L., Kuster, S. & Rühs, P. A. Hagfish slime and mucin flow properties and their implications for defense. *Scientific Reports* **6** (2016).

36. Böni, L. J. *et al.* Effect of ionic strength and seawater cations on hagfish slime formation. *Scientific Reports* **8,** 9867 (2018).

37. Chaudhary, G., Fudge, D. S., Macias-Rodriguez, B. & Ewoldt, R. H. Concentration-independent mechanics and structure of hagfish slime. *Acta Biomaterialia* **79,** 123–134 (2018).

38. Herr, J. E., Winegard, T. M., Odonnell, M. J., Yancey, P. H. & Fudge, D. S. Stabilization and swelling of hagfish slime mucin vesicles. *Journal of Experimental Biology* **213,** 1092–1099 (2010).

39. Herr, J. E., Clifford, A., Goss, G. G. & Fudge, D. S. Defensive slime formation in Pacific hagfish requires Ca^{2+} and aquaporin mediated swelling of released mucin vesicles. *Journal of Experimental Biology* **217,** 2288–229 (2014).

40. Newby, W. W. The slime glands and thread cells of the hagfish, Polistrotrema stouti. *Journal of Morphology* **78,** 397–409 (1946).

41. Koch, E. A., Spitzer, R. H., Pithawalla, R. B. & Downing, S. W. Keratin-like components of gland thread cells modulate the properties of mucus from hagfish (Eptatretus stouti). *Cell and Tissue Research* **264,** 79–86 (1991).

42. Winegard, T. M. & Fudge, D. S. Deployment of hagfish slime thread skeins requires the transmission of mixing forces via mucin strands. *Journal of Experimental Biology* **213,** 1235–1240 (2010).

43. Tornberg, A.-K. & Shelley, M. J. Simulating the dynamics and interactions of flexible fibers in Stokes flows. *Journal of Computational Physics* **196,** 8–40 (2004).

44. Hong, D. C. & Yue, S. Deterministic Chaos in Failure Dynamics: Dynamics of Peeling of Adhesive Tape. *Physical Review Letters* **74,** 254–257 (1995).

45. Cortet, P.-P., Ciccotti, M. & Vanel, L. Imaging the stick-slip peeling of an adhesive tape under a constant load. *Journal of Statistical Mechanics* **2007,** P03005 (2007).

46. Mohammed, I. K., Charalambides, M. N. & Kinloch, A. J. Modeling the effect of rate and geometry on peeling and tack of pressure-sensitive adhesives. *Journal of Non-Newtonian Fluid Mechanics* **233,** 85–94 (2016).

47. Dalbe, M.-J., Santucci, S., Cortet, P.-P. & Vanel, L. Strong dynamical effects during stick-slip adhesive peeling. *Soft Matter* **10,** 132–138 (2014).

48. Wang, Z., Wang, Z., Dai, Z. & Gorb, S. N. Bio-Inspired Adhesive Footpad for Legged Robot Climbing under Reduced Gravity: Multiple Toes Facilitate Stable Attachment. *Applied Sciences* **8,** 114 (2018).

49. De, R., Maybhate, A. & Ananthakrishna, G. Dynamics of stick-slip in peeling of an adhesive tape. *Physical Review E* **70,** 046223 (2004).

50. Griffin, M. A. *et al.* Patterning, Prestress, and Peeling Dynamics of Myocytes. *Biophysical Journal* **86,** 1209–1222 (2004).

51. Eisner, T & Meinwald, J. Defensive secretions of arthropods. *Science* **153,** 1341–1350 (1966).

52. Johnson, S. R., Copello, J. A., Evans, M. S. & Suarez, A. V. A biochemical characterization of the major peptides from the venom of the giant neotropical hunting ant Dinoponera australis. *Toxicon* **55,** 702–710 (2010).

53. Kicklighter, C. E., Shabani, S, Johnson, P. M. & Derby, C. D. Sea hares use novel antipredatory chemical defenses. *Current Biology* **15,** 549–554 (2005).

54. Derby, C. D., Tottempudi, M, Love-Chezem, T & Wolfe, L. Ink from longfin inshore squid, Doryteuthis pealeii, as a chemical and visual defense against two predatory fishes, summer flounder, Paralichthys dentatus, and sea catfish, Ariopsis felis. *The Biological Bulletin* **225,** 152–160 (2013).

55. Nolen, T. G., Johnson, P. M., Kicklighter, C. E. & Capo, T. Ink secretion by the marine snail Aplysia californica enhances its ability to escape from a natural predator. *Journal of Comparative Physiology A* **176,** 239–254 (1995).

56. Mair, J & Port, G. R. The influence of mucus production by the slug, Deroceras reticulatum, on predation by Pterostichus madidus and Nebria brevicollis (Coleoptera: Carabidae). *Biocontrol Science and Technology* **12,** 325–335 (2002).

57. Wiedorn, W. S. A New Experimental Animal for Psychiatric Research: The Opossum, Didelphis virginiana. *Science* **119,** 360–361 (1954).

58. Wood, W. F., Sollers, B. G., Dragoo, G. A. & Dragoo, J. W. Volatile Components in Defensive Spray of the Hooded Skunk, Mephitis macroura. *Journal of Chemical Ecology* **28,** 1865–1870 (2002).

59. Newar, J & Ghatak, A. Studies on the Adhesive Property of Snail Adhesive Mucus. *Langmuir* **31,** 12155–12160 (2015).

60. Noel, A. C., Guo, H, Mandica, M & Hu, D. L. Frogs use a viscoelastic tongue and non-Newtonian saliva to catch prey. *Journal of The Royal Society Interface* **14,** 20160764 (2017).

61. Jatkar, A. A. *et al.* Coral mucus: the properties of its constituent mucins. *Biomacromolecules* **11,** 883–888 (2010).

62. Spitzer, R. H., Koch, E. A. & Downing, S. W. Maturation of hagfish gland thread cells: composition and characterization of intermediate filament polypeptides. *Cytoskeleton* **11,** 31–45 (1988).

63. Koch, E. A., Spitzer, R. H., Pithawalla, R. B. & Parry, D. A. An unusual intermediate filament subunit from the cytoskeletal biopolymer released extracellularly into seawater by the primitive hagfish (Eptatretus stouti). *Journal of Cell Science* **107,** 3133–3144 (1994).

64. Fudge, D. S., Gardner, K. H., Forsyth, V. T., Riekel, C & Gosline, J. M. The Mechanical Properties of Hydrated Intermediate Filaments: Insights from Hagfish Slime Threads. *Biophysical Journal* **85,** 2015–2027 (2003).

65. Salo, W. L. *et al.* Fractionation of hagfish slime gland secretions: partial characterization of the mucous vesicle fraction. *Preparative Biochemistry* **13,** 103–135 (1983).

66. Böcker, L, Rühs, P., Böni, L, Fischer, P & Kuster, S. Fiber-Enforced Hydrogels: Hagfish Slime Stabilized with Biopolymers including κ-Carrageenan. *ACS Biomaterials Science & Engineering* **2,** 90–95 (2016).

67. Böni, L. J. *et al.* Hagfish slime exudate stabilization and its effect on slime formation and functionality. *Biology Open* **6,** 1115–1122 (2017).

68. Ewoldt, R. H., Johnston, M. T. & Caretta, L. M. in *Complex Fluids in Biological Systems: Experiment, Theory, and Computation* 207–241 (Springer New York, New York, NY, 2015). ISBN: 978-1-4939-2065-5.

69. Johnston, M. T. & Ewoldt, R. H. Precision rheometry: Surface tension effects on low-torque measurements in rotational rheometers. *Journal of Rheology* **57,** 1515–1532 (2013).

70. Ganeriwala, S. N. & Rotz, C. A. Fourier transform mechanical analysis for determining the nonlinear viscoelastic properties of polymers. *Polymer Engineering & Science* **27,** 165–178 (1987).

71. Ewoldt, R. H., Hosoi, A. E. & McKinley, G. H. New measures for characterizing nonlinear viscoelasticity in large amplitude oscillatory shear. *Journal of Rheology* **52,** 1427–1458 (2008).

72. Ewoldt, R. H., Hosoi, A. E. & McKinley, G. H. Nonlinear viscoelastic biomaterials: meaningful characterization and engineering inspiration. *Integrative and Comparative Biology* **49,** 40–50 (2009).

73. Gardel, M. L., Valentine, M. T., Crocker, J. C., Bausch, A. R. & Weitz, D. A. Microrheology of Entangled F-Actin Solutions. *Physical Review Letters* **91,** 158302 (15 2003).

74. MacKintosh, F. C., Käs, J & Janmey, P. A. Elasticity of Semiflexible Biopolymer Networks. *Physical Review Letters* **75,** 4425–4428 (24 1995).

75. Arvidson, S. A. *et al.* Interplay of Phase Separation and Thermoreversible Gelation in Aqueous Methylcellulose Solutions. *Macromolecules* **46,** 300–309 (2013).

76. Schopferer, M *et al.* Desmin and vimentin intermediate filament networks: their viscoelastic properties investigated by mechanical rheometry. *Journal of Molecular Biology* **388,** 133–143 (2009).

77. Pavlovsky, L, Younger, J. G. & Solomon, M. J. In situ rheology of Staphylococcus epidermidis bacterial biofilms. *Soft Matter* **9,** 122–131 (2013).

78. Khan, S. A., Schnepper, C. A. & Armstrong, R. C. Foam rheology: III. Measurement of shear flow properties. *Journal of Rheology* **32,** 69–92 (1988).

79. English, R. J., Raghavan, S. R., Jenkins, R. D. & Khan, S. A. Associative polymers bearing n-alkyl hydrophobes: Rheological evidence for microgel-like behavior. *Journal of Rheology* **43,** 1175–1194 (1999).

80. Lidon, P, Villa, L & Manneville, S. Power-law creep and residual stresses in a carbopol gel. *Rheologica Acta* **56,** 307–323 (2016).

81. Rodd, A. B., Cooper-White, J. J., Dunstan, D. E. & Boger, D. V. Polymer concentration dependence of the gel point for chemically modified biopolymer networks using small amplitude oscillatory rheometry. *Polymer* **42,** 3923–3928 (2001).

82. Tempel, M, Isenberg, G & Sackmann, E. Temperature-induced sol-gel transition and microgel formation in α-actinin cross-linked actin networks: A rheological study. *Physical Review E* **54,** 1802–1810 (1996).

83. Celli, J. P. *et al.* Rheology of Gastric Mucin Exhibits a pH-Dependent Sol-Gel Transition. *Biomacromolecules* **8,** 1580–1586 (2007).

84. Cocard, S, Tassin, J. F. & Nicolai, T. Dynamical mechanical properties of gelling colloidal disks. *Journal of Rheology* **44,** 585–594 (2000).

85. Winter, H. H. & Mours, M. in *Neutron Spin Echo Spectroscopy Viscoelasticity Rheology* 165–234 (Springer Berlin Heidelberg, Berlin, Heidelberg, 1997). ISBN: 978-3-540-68449-7.

86. Brenner, T, Nicolai, T & Johannsson, R. Rheology of thermo-reversible fish protein isolate gels. *Food Research International* **42,** 915–924 (2009).

87. Leocmach, M, Perge, C, Divoux, T & Manneville, S. Creep and fracture of a protein gel under stress. *Physical Review Letters* **113,** 038303 (2014).

88. Muthukumar, M. Screening effect on viscoelasticity near the gel point. *Macromolecules* **22,** 4656–4658 (1989).

89. Hung, K, Jeng, U & Hsu, S. Fractal Structure of Hydrogels Modulates Stem Cell Behavior. *ACS Macro Letters* **4,** 1056–1061 (2015).

90. Patricio, P, Leal, C. R., Duarte, J & Januário, C. Rheology of the cytoskeleton as a fractal network. *Physical Review E* **92,** 040702 (2015).

91. Ewoldt, R. H. & McKinley, G. H. Creep ringing in rheometry or how to deal with oft-discarded data in step stress tests! *Rheology Bulletin* **76,** 4–6 (2007).

92. Struik, L. C. E. Free damped vibrations of linear viscoelastic materials. *Rheologica Acta* **6,** 119–129 (1967).

93. Yao, N. Y., Larsen, R. J. & Weitz, D. A. Probing nonlinear rheology with inertio-elastic oscillations. *Journal of Rheology* **52,** 1013–1025 (2008).

94. Møller, P. C. F., Fall, A & Bonn, D. Origin of apparent viscosity in yield stress fluids below yielding. *Europhysics Letters* **87,** 38004 (2009).

95. Heymans, N & Bauwens, J. C. Fractal rheological models and fractional differential equations for viscoelastic behavior. *Rheologica Acta* **33,** 210–219 (1994).

96. Schiessel, H, Metzler, R, Blumen, A & Nonnenmacher, T. F. Generalized viscoelastic models: their fractional equations with solutions. *Journal of Physics A: Mathematical and General* **28,** 6567–6584 (1995).

97. Heymans, N. Fractional calculus description of non-linear viscoelastic behaviour of polymers. *Nonlinear Dynamics* **38,** 221–231 (2004).

98. Jaishankar, A & McKinley, G. H. Power-law rheology in the bulk and at the interface: quasi-properties and fractional constitutive equations. *Proceedings of the Royal Society A: Mathematical, Physical & Engineering Sciences,* 1–21 (2012).

99. Jaishankar, A. *The linear and nonlinear rheology of multiscale complex fluids* PhD thesis (Massachusetts Institute of Technology, 2014).

100. Faber, T. J., Jaishankar, A & Mckinley, G. H. Describing the firmness, springiness and rubberiness of food gels using fractional calculus. Part I: Theoretical framework. *Food Hydrocolloids* **62,** 311–324 (2017).

101. Monje, C. A., Chen, Y, Vinagre, B. M., Xue, D & Feliu, V. in *Fractional-order Systems and Controls: Fundamentals and Applications* 213–256 (Springer London, London, 2010). ISBN: 978-1-84996-335-0.

102. Blair, G., Veinoglou, B. & Caffyn, J. Limitations of the Newtonian time scale in relation to non-equilibrium rheological states and a theory of quasi-properties. *Proceedings of the Royal Society of London A: Mathematical, Physical and Engineering Sciences* **189,** 69–87 (1947).

103. Schiessel, H & Blumen, A. Mesoscopic Pictures of the Sol-Gel Transition: Ladder Models and Fractal Networks. *Macromolecules* **28,** 4013–4019 (1995).

104. Warlus, S & Ponton, A. A new interpretation for the dynamic behaviour of complex fluids at the sol-gel transition using the fractional calculus. *Rheologica Acta* **48,** 51–58 (2009).

105. Izuka, A, Winter, H. H. & Hashimoto, T. Molecular weight dependence of viscoelasticity of polycaprolactone critical gels. *Macromolecules* **25,** 2422–2428 (1992).

106. Hsu, S & Yu, T. Dynamic viscoelasticity study of the phase transition of poly(N-isopropylacrylamide). *Macromolecular Rapid Communications* **21,** 476–480 (2000).

107. Izuka, A, Winter, H. H. & Hashimoto, T. Self-Similar Relaxation Behavior at the Gel Point of a Blend of a Cross-Linking Poly(ϵ-caprolactone) Diol with a Poly(styrene-co-acrylonitrile). *Macromolecules* **30,** 6158–6165 (1997).

108. Curtis, D. J. *et al.* Validation of optimal Fourier rheometry for rapidly gelling materials and its application in the study of collagen gelation. *Journal of Non-Newtonian Fluid Mechanics* **222,** 253–259 (2015).

109. Goff, K. J. L., Gaillard, C, Helbert, W, Garnier, C & Aubry, T. Rheological study of reinforcement of agarose hydrogels by cellulose nanowhiskers. *Carbohydrate Polymers* **116,** 117–123 (2015).

110. Lawrence, M. J. *et al.* A new structural biomarker that quantifies and predicts changes in clot strength and quality in a model of progressive haemodilution. *Thrombosis Research* **134,** 488–494 (2014).

111. Lue, A & Zhang, L. Effects of carbon nanotubes on rheological behavior in cellulose solution dissolved at low temperature. *Polymer* **51,** 2748–2754 (2010).

112. Zhang, Y, Xu, X & Zhang, L. Dynamic viscoelastic behavior of triple helical Lentinan in water: Effect of temperature. *Carbohydrate Polymers* **73,** 26–34 (2008).

113. Werner, B, Bu, H., Kjøniksen, A, Sande, S. A. & Nyström, B. Characterization of gelation of aqueous pectin via the Ugi multicomponent condensation reaction. *Polymer Bulletin* **56,** 579–589 (2006).

114. Nyström, B, Kjøniksen, A & Iversen, C. Characterization of association phenomena in aqueous systems of chitosan of different hydrophobicity. *Advances in Colloid and Interface Science* **79,** 81–103 (1999).

115. Power, D. J., Rodd, A. B., Paterson, L & Boger, D. V. Gel transition studies on nonideal polymer networks using small amplitude oscillatory rheometry. *Journal of Rheology* **42,** 1021–1037 (1998).

116. Kjøniksen, A, Nyström, B & Lindman, B. Dynamic viscoelasticity of gelling and nongelling aqueous mixtures of ethyl (hydroxyethyl) cellulose and an ionic surfactant. *Macromolecules* **31,** 1852–1858 (1998).

117. Matsumoto, T, Kawai, M & Masuda, T. Viscoelastic and SAXS investigation of fractal structure near the gel point in alginate aqueous systems. *Macromolecules* **25,** 5430–5433 (1992).

118. Liu, S, Bao, H & Li, L. Thermoreversible gelation and scaling laws for graphene oxide-filled κ-carrageenan hydrogels. *European Polymer Journal* **79,** 150–162 (2016).

119. Dai, L, Liu, X, Liu, Y & Tong, Z. Concentration dependence of critical exponents for gelation in gellan gum aqueous solutions upon cooling. *European Polymer Journal* **44,** 4012–4019 (2008).

120. Liu S Li, H, Tang, B, Bi, S & Li, L. Scaling law and microstructure of alginate hydrogel. *Carbohydrate Polymers* **135,** 101–109 (2016).

121. Lu, L, Liu, X, Tong, Z & Gao, Q. Critical exponents and self-similarity for sol-gel transition in aqueous alginate systems induced by in situ release of calcium cations. *Journal of Physical Chemistry B* **110,** 25013–25020 (2006).

122. Hsu, S & Jamieson, A. M. Viscoelastic behaviour at the thermal sol-gel transition of gelatin. *Polymer* **34,** 2602–2608 (1993).

123. Winegard, T *et al.* Coiling and maturation of a high-performance fibre in hagfish slime gland thread cells. *Nature Communications* **5,** 3534 (2014).

124. Fudge, D & Schorno, S. The Hagfish Gland Thread Cell: A Fiber-Producing Cell Involved in Predator Defense. *Cells* **5,** 25 (2016).

125. Kabla, A & Mahadevan, L. Nonlinear mechanics of soft fibrous networks. *The Journal of the Royal Society Interface* **4,** 99–106 (2007).

126. Audoly, B & Pomeau, Y. *Elasticity and geometry: from hair curls to the non-linear response of shells* (Oxford University Press, 2010).

127. Broedersz, C. P. & Mackintosh, F. C. Modeling semiflexible polymer networks. *Reviews of Modern Physics* **86,** 995–1036 (2014).

128. Janmey, P. A., Euteneuer, U, Traub, P & Schliwa, M. Viscoelastic properties of vimentin compared with other filamentous biopolymer networks. *Journal of Cell Biology* **113,** 155–160 (1991).

129. Lin, Y *et al.* Origins of elasticity in intermediate filament networks. *Physical Review Letters* **104,** 058101 (2010).

130. Fu, J, Guerette, P. A. & Miserez, A. Self-assembly of recombinant hagfish thread keratins amenable to a strain-induced α-helix to β-sheet transition. *Biomacromolecules* **16,** 2327–2339 (2015).

131. Spitzer, R. H., Downing, S. W., Koch, E. A., Salo, W. L. & Saidel, L. J. Hagfish slime gland thread cells: II. Isolation and characterization of intermediate filament components associated with the thread. *Journal of Cell Biology* **98,** 670–677 (Feb. 1984).

132. Landini, G. Fractals in microscopy. *Journal of Microscopy* **241,** 1–8 (2011).

133. Weibel, E. R. Fractal geometry: a design principle for living organisms. *American Journal of Physiology-Lung Cellular and Molecular Physiology* **261,** L361–L369 (1991).

134. Nonnenmacher, T. F., Losa, G. A. & Weibel, E. R. *Fractals in Biology and Medicine* (Birkhäuser, 2013).

135. Zosel, A. The effect of bond formation on the tack of polymers. *Journal of Adhesion Science and Technology* **11,** 1447–1457 (1997).

136. Smith, A. M. The structure and function of adhesive gels from invertebrates. *Integrative and Comparative Biology* **42,** 1164–1171 (2002).

137. Pawlicki, J. M. *et al.* The effect of molluscan glue proteins on gel mechanics. *Journal of Experimental Biology* **207,** 1127–1135 (2004).

138. Smith, A. M. in *Biological Adhesive Systems: From Nature to Technical and Medical Application* (eds von Byern, J & Grunwald, I) 41–51 (Springer Vienna, Vienna, 2010). ISBN: 978-3-7091-0286-2.

139. Iwamoto, M, Ueyama, D & Kobayashi, R. The advantage of mucus for adhesive locomotion in gastropods. *Journal of Theoretical Biology* **353,** 133–141 (2014).

140. Li, J *et al.* Tough adhesives for diverse wet surfaces. *Science* **357,** 378–381 (2017).

141. Fuoss, R. M. Polyelectrolytes. *Discussions of the Faraday Society* **11,** 125–134 (1951).

142. Dobrynin, A. V., Colby, R. H. & Rubinstein, M. Scaling theory of polyelectrolyte solutions. *Macromolecules* **28,** 1859–1871 (1995).

143. Bray, D. J., Walsh, T. R., Noro, M. G. & Notman, R. Complete structure of an epithelial keratin dimer: implications for intermediate filament assembly. *PloS one* **10,** e0132706 (2015).

144. Feng, X. & Coulombe, P. A. A role for disulfide bonding in keratin intermediate filament organization and dynamics in skin keratinocytes. *J Cell Biol* **209,** 59–72 (2015).

145. Clague, D., Kandhai, B., Zhang, R & Sloot, P. M. Hydraulic permeability of (un) bounded fibrous media using the lattice Boltzmann method. *Physical Review E* **61,** 616 (2000).

146. White, J. A. & Deen, W. M. Agarose-dextran gels as synthetic analogs of glomerular basement membrane: water permeability. *Biophysical journal* **82,** 2081–2089 (2002).

147. Manley, S., Skotheim, J., Mahadevan, L & Weitz, D. A. Gravitational collapse of colloidal gels. *Physical review letters* **94,** 218302 (2005).

148. Shogren, R., Gerken, T. A. & Jentoft, N. Role of glycosylation on the conformation and chain dimensions of O-linked glycoproteins: light-scattering studies of ovine submaxillary mucin. *Biochemistry* **28,** 5525–5536 (1989).

149. Witten, J., Samad, T. & Ribbeck, K. Selective permeability of mucus barriers. *Current opinion in biotechnology* **52,** 124–133 (2018).

150. Pusey, P. N. & Megen, W. V. Phase behaviour of concentrated suspensions of nearly hard colloidal spheres. *Nature* **320,** 340–342 (1986).

151. Pusey, P. N. & van Megen, W. Observation of a glass transition in suspensions of spherical colloidal particles. *Phys. Rev. Lett.* **59,** 2083–2086 (18 1987).

152. Hunter, G. L. & Weeks, E. R. The physics of the colloidal glass transition. *Reports on Progress in Physics* **75,** 066501 (2012).

153. Vlassopoulos, D. & Cloitre, M. Tunable rheology of dense soft deformable colloids. *Current Opinion in Colloid Interface Science* **19,** 561–574 (2014).

154. Menut, P., Seiffert, S., Sprakel, J. & Weitz, D. A. Does size matter? Elasticity of compressed suspensions of colloidal- and granular-scale microgels. *Soft Matter* **8,** 156–164 (2012).

155. Paloli, D., Mohanty, P. S., Crassous, J. J., Zaccarelli, E. & Schurtenberger, P. FluidâĂŞsolid transitions in soft-repulsive colloids. *Soft Matter* **9,** 3000–3004 (11 2013).

156. Mohanty, P. S., Paloli, D., Crassous, J. J., Zaccarelli, E. & Schurtenberger, P. Effective interactions between soft-repulsive colloids: Experiments, theory, and simulations. *The Journal of chemical physics* **140,** 094901 (2014).

157. Seth, J. R., Mohan, L., Locatelli-Champagne, C., Cloitre, M. & Bonnecaze, R. T. A micromechanical model to predict the flow of soft particle glasses. *Nature materials* **10,** 838 (2011).

158. Romeo, G. & Ciamarra, M. P. Elasticity of compressed microgel suspensions. *Soft Matter* **9,** 5401–5406 (22 2013).

159. Basu, A. *et al.* Rheology of soft colloids across the onset of rigidity: scaling behavior, thermal, and non-thermal responses. *Soft matter* **10,** 3027–3035 (2014).

160. Pellet, C. & Cloitre, M. The glass and jamming transitions of soft polyelectrolyte microgel suspensions. *Soft Matter* **12,** 3710–3720 (2016).

161. Yang, J. & Schweizer, K. S. Glassy dynamics and mechanical response in dense fluids of soft repulsive spheres. I. Activated relaxation, kinetic vitrification, and fragility. *The Journal of chemical physics* **134,** 204908 (2011).

162. Yang, J. & Schweizer, K. S. Glassy dynamics and mechanical response in dense fluids of soft repulsive spheres. II. Shear modulus, relaxation-elasticity connections, and rheology. *The Journal of chemical physics* **134,** 204909 (2011).

163. Bonn, D., Denn, M. M., Berthier, L., Divoux, T. & Manneville, S. Yield stress materials in soft condensed matter. *Reviews of Modern Physics* **89,** 1–40 (2017).

164. Bachman, H. *et al.* Ultrasoft, highly deformable microgels. *Soft Matter* **11,** 2018–2028 (2015).

165. Gao, J. & Frisken, B. J. Cross-Linker-Free N -Isopropylacrylamide Gel Nanospheres. *Langmuir* **19,** 5212–5216 (2003).

166. Saunders, B. R. & Vincent, B. Microgel particles as model colloids: theory, properties and applications. *Advances in Colloid and Interface Science* **80,** 1–25 (1999).

167. Liu, A. J., Ramaswamy, S., Mason, T. G., Gang, H. & Weitz, D. A. Anomalous Viscous Loss in Emulsions. *Phys. Rev. Lett.* **76,** 3017–3020 (16 1996).

168. Christopoulou, C., Petekidis, G., Erwin, B., Cloitre, M. & Vlassopoulos, D. Ageing and yield behaviour in model soft colloidal glasses. *Philosophical Transactions of the Royal Society A: Mathematical, Physical and Engineering Sciences* **367,** 5051–5071 (2009).

169. Flory, P. J. *Principles of polymer chemistry* 1953rd ed. (Cornell University Press, 1953).

170. Rubinstein, M. & Colby, R. H. *Polymer physics* (Oxford University Press, 2003).

171. Nelson, A. Z. & Ewoldt, R. H. Design of yield-stress fluids: a rheology-to-structure inverse problem. *Soft Matter* **13,** 7578–7594 (41 2017).

172. Bonnecaze, R. T. & Cloitre, M. Micromechanics of Soft Particle Glasses. *High Solid Dispersions Advances in Polymer Science,* 117–161 (2010).

173. Scheffold, F, Cardinaux, F & Mason, T. G. Linear and nonlinear rheology of dense emulsions across the glass and the jamming regimes. *Journal of Physics: Condensed Matter* **25,** 502101 (2013).

174. Likos, C. N. Colloidal interactions: From effective potentials to structure. *Physics of Complex Colloids* **184,** 1 (2013).

175. Erwin, B. M., Cloitre, M., Gauthier, M. & Vlassopoulos, D. Dynamics and rheology of colloidal star polymers. *Soft Matter* **6,** 2825–2833 (12 2010).

176. Schweizer, K. S. Derivation of a microscopic theory of barriers and activated hopping transport in glassy liquids and suspensions. *The Journal of Chemical Physics* **123,** 244501 (2005).

177. Berndt, I. & Richtering, W. Doubly Temperature Sensitive CoreâĹŠShell Microgels. *Macromolecules* **36,** 8780–8785 (2003).

178. Conley, G. M., Aebischer, P., Nöjd, S., Schurtenberger, P. & Scheffold, F. Jamming and overpacking fuzzy microgels: Deformation, interpenetration, and compression. *Science Advances* **3,** 1–8 (2017).

179. Rovigatti, L., Gnan, N., Ninarello, A. & Zaccarelli, E. *On the validity of the Hertzian model: the case of soft colloids* 2018. eprint: `arXiv:1808.04769`.

180. Hansen, J.-P. & McDonald, I. R. *Theory of simple liquids* (Elsevier Science, 2014).

181. Zwanzig, R. *Nonequilibrium Statistical Mechanics* (Wiley-Blackwell, 2001).

182. Saltzman, E. J. & Schweizer, K. S. Transport coefficients in glassy colloidal fluids. *The Journal of Chemical Physics* **119,** 1197–1203 (2003).

183. Mirigian, S. & Schweizer, K. S. Dynamical Theory of Segmental Relaxation and Emergent Elasticity in Supercooled Polymer Melts. *Macromolecules* **48,** 1901–1913 (2015).

184. Mirigian, S. & Schweizer, K. S. Elastically cooperative activated barrier hopping theory of relaxation in viscous fluids.I.General formulation and application to hard sphere fluids. *The Journal of Chemical Physics* **140,** 194506 (2014).

185. Kobelev, V. & Schweizer, K. S. Strain softening, yielding, and shear thinning in glassy colloidal suspensions. *Phys. Rev. E* **71,** 021401 (2 2005).

186. Zhang, R. & Schweizer, K. S. Theory of nonlinear elasticity, stress-induced relaxation, and dynamic yielding in dense fluids of hard nonspherical colloids. *The Journal of Chemical Physics* **136,** 154902 (2012).

187. Chen, K., Saltzman, E. J. & Schweizer, K. S. Molecular Theories of Segmental Dynamics and Mechanical Response in Deeply Supercooled Polymer Melts and Glasses. *Annual Review of Condensed Matter Physics* **1,** 277–300 (2010).

188. Chen, Y.-L. & Schweizer, K. S. Microscopic theory of gelation and elasticity in polymerâĂŞparticle suspensions. *The Journal of Chemical Physics* **120,** 7212–7222 (2004).

189. Ramakrishnan, S., Chen, Y.-L., Schweizer, K. S. & Zukoski, C. F. Elasticity and clustering in concentrated depletion gels. *Phys. Rev. E* **70,** 040401 (4 2004).

190. Rao, R. B., Kobelev, V. L., Li, Q., Lewis, J. A. & Schweizer, K. S. Nonlinear Elasticity and Yielding of Nanoparticle Glasses. *Langmuir* **22.** PMID: 16519437, 2441–2443 (2006).

191. Kramb, R. C., Zhang, R., Schweizer, K. S. & Zukoski, C. F. Glass Formation and Shear Elasticity in Dense Suspensions of Repulsive Anisotropic Particles. *Phys. Rev. Lett.* **105,** 055702 (5 2010).

192. Yang, J. & Schweizer, K. S. Tunable dynamic fragility and elasticity in dense suspensions of many-arm-star polymer colloids. *EPL (Europhysics Letters)* **90,** 66001 (2010).

193. Zhang, Z. *et al.* Thermal vestige of the zero-temperature jamming transition. *Nature* **459,** 230–233 (2009).

194. Seth, J. R., Cloitre, M. & Bonnecaze, R. T. Elastic properties of soft particle pastes. *Journal of Rheology* **50,** 353–376 (2006).

195. Zwanzig, R. & Mountain, R. D. High-Frequency Elastic Moduli of Simple Fluids. *The Journal of Chemical Physics* **43,** 4464–4471 (1965).

196. Mohan, L. & Bonnecaze, R. T. Short-ranged pair distribution function for concentrated suspensions of soft particles. *Soft Matter* **8,** 4216–4222 (2012).

197. Chatterjee, A. P. & Schweizer, K. S. Liquid-State Theory of Semidilute and Concentrated Polymer Solutions. *Macromolecules* **31,** 2353–2367 (1998).

198. Yan, X., Wang, F., Zheng, B. & Huang, F. Stimuli-responsive supramolecular polymeric materials. *Chemical Society Reviews* **41,** 6042–6065 (2012).

199. Ghosh, A. *et al.* Linear and nonlinear rheology and structural relaxation in dense glassy and jammed soft repulsive pNIPAM microgel suspensions. *Soft Matter* **15,** 1038–1052 (5 2019).

200. Cai, S. & Suo, Z. Mechanics and chemical thermodynamics of phase transition in temperature-sensitive hydrogels. *Journal of the Mechanics and Physics of Solids* **59,** 2259–2278 (2011).

201. Chaudhary, G. *et al.* Thermoresponsive Stiffening with Microgel Particles in a Semiflexible Fibrin Network. *Macromolecules* **52,** 3029–3041 (2019).

202. Van der Linden, H., Olthuis, W. & Bergveld, P. An efficient method for the fabrication of temperature-sensitive hydrogel microactuators. *Lab on a Chip* **4,** 619–624 (2004).

203. Romeo, G., Fernandez-Nieves, A., Wyss, H. M., Aciernoand, D. & Weitz, D. A. Temperature-controlled transitions between glass. liquid, and gel states in dense p-NIPA suspensions. *Advanced Materials* **22,** 3441–3445 (2010).

204. Urich, M. & Denton, A. R. Swelling, structure, and phase stability of compressible microgels. *Soft Matter* **12,** 9086–9094 (44 2016).

205. Stuart, M. A. C. *et al.* Emerging applications of stimuli-responsive polymer materials. *Nature materials* **9,** 101 (2010).

206. Wei, M., Gao, Y., Li, X. & Serpe, M. J. Stimuli-responsive polymers and their applications. *Polym. Chem.* **8,** 127–143 (1 2017).

207. Zeng, H., Wasylczyk, P., Wiersma, D. S. & Priimagi, A. Light robots: bridging the gap between microrobotics and photomechanics in soft materials. *Advanced Materials* **30,** 1703554 (2018).

208. Strozyk, M. S., Jimenez de Aberasturi, D. & Liz-Marzán, L. M. Composite Polymer Colloids for SERS-Based Applications. *The Chemical Record* **18,** 807–818 (2018).

209. Bausch, A. & Kroy, K. A bottom-up approach to cell mechanics. *Nature physics* **2,** 231 (2006).

210. Fletcher, D. A. & Mullins, R. D. Cell mechanics and the cytoskeleton. *Nature* **463,** 485 (2010).

211. Wen, Q. & Janmey, P. A. Polymer physics of the cytoskeleton. *Current Opinion in Solid State and Materials Science* **15,** 177–182 (2011).

212. Pollard, T. D. & Borisy, G. G. Cellular motility driven by assembly and disassembly of actin filaments. *Cell* **112,** 453–465 (2003).

213. Janmey, P. A. & Weitz, D. A. Dealing with mechanics: mechanisms of force transduction in cells. *Trends in biochemical sciences* **29,** 364–370 (2004).

214. Ridley, A. J. *et al.* Cell migration: integrating signals from front to back. *Science* **302,** 1704–1709 (2003).

215. Pollard, T. D. & Cooper, J. A. Actin, a central player in cell shape and movement. *Science* **326,** 1208–1212 (2009).

216. Gardel, M. L. *et al.* Prestressed F-actin networks cross-linked by hinged filamins replicate mechanical properties of cells. *Proceedings of the National Academy of Sciences* **103,** 1762–1767 (2006).

217. Gardel, M. L. *et al.* Prestressed F-actin networks cross-linked by hinged filamins replicate mechanical properties of cells. *Proceedings of the National Academy of Sciences* **103,** 1762–1767 (2006).

218. Piechocka, I. K., Bacabac, R. G., Potters, M., Mackintosh, F. C. & Koenderink, G. H. Structural Hierarchy Governs Fibrin Gel Mechanics. *Biophysical Journal* **98,** 2281–2289 (2010).

219. Palmer, J. S. & Boyce, M. C. Constitutive modeling of the stress-strain behavior of F-actin filament networks. *Acta Biomaterialia* **4,** 597–612 (2008).

220. Blundell, J. R. & Terentjev, E. M. Stretching Semiflexible Filaments and Their Networks. *Macromolecules* **42,** 5388–5394 (2009).

221. Meng, F. & Terentjev, E. M. Nonlinear elasticity of semiflexible filament networks. *Soft Matter* **12,** 6749–6756 (2016).

222. Wilhelm, J. & Frey, E. Radial Distribution Function of Semiflexible Polymers. *Physical Review Letters* **77,** 2581–2584 (1996).

223. Jadrich, R. B. & Schweizer, K. S. Directing Colloidal Assembly and a Metal-Insulator Transition Using a Quench-Disordered Porous Rod Template. *Physical Review Letters* **113** (2014).

224. Bharadwaj, N. A. K. *et al.* Integration of colloids into a semi-flexible network of fibrin. *Soft Matter* **13,** 1430–1443 (2017).

225. Almeida, P. D. *et al.* Cytoskeletal stiffening in synthetic hydrogels. *Nature Communications* **10** (2019).

226. O'Brien, F. J. Biomaterials scaffolds for tissue engineering. *Materials Today* **14,** 88 –95 (2011).

227. Tozluoglu, M. *et al.* Matrix geometry determines optimal cancer cell migration strategy and modulates response to interventions. *Nature Cell Biology* **15,** 751–762 (2013).

228. Kratz, K., Hellweg, T. & Eimer, W. Structural changes in PNIPAM microgel particles as seen by SANS, DLS, and EM techniques. *Polymer* **42,** 6631–6639 (2001).

229. Douglas, A. M. *et al.* Dynamic assembly of ultrasoft colloidal networks enables cell invasion within restrictive fibrillar polymers. *Proceedings of the National Academy of Sciences* **114,** 885–890 (2017).

230. Jaspers, M. *et al.* Ultra-responsive soft matter from strain-stiffening hydrogels. *Nature Communications* **5,** 1–8 (2014).

231. Jaspers, M. *et al.* Bundle Formation in Biomimetic Hydrogels. *Biomacromolecules* **17,** 2642–2649 (2016).

232. Jaspers, M. *et al.* Nonlinear mechanics of hybrid polymer networks that mimic the complex mechanical environment of cells. *Nature Communications* **8,** 1–10 (2017).

233. Wen, Q., Basu, A., Winer, J. P., Yodh, A. & Janmey, P. A. Local and global deformations in a strain-stiffening fibrin gel. *New Journal of Physics* **9** (2007).

234. Hashmi, S. M. & Dufresne, E. R. Mechanical properties of individual microgel particles through the deswelling transition. *Soft Matter* **5,** 3682–3688 (2009).

235. Van Der Linden, H., Olthuis, W. & Bergveld, P. An efficient method for the fabrication of temperature-sensitive hydrogel microactuators. *Lab on a Chip* **4,** 619–624 (2004).

236. Ryan, E. A., Mockros, L. F., Weisel, J. W. & Lorand, L. Structural origins of fibrin clot rheology. *Biophysical Journal* **77,** 2813–2826 (1999).

237. Gardel, M. L. *et al.* Elastic behavior of cross-linked and bundled actin networks. *Science* **304,** 1301–1305 (2004).

238. Meng, F. & Terentjev, E. M. Theory of semiflexible filaments and networks. *Polymers* **9,** 1–28 (2017).

239. Onck, P. R., Koeman, T., Van Dillen, T. & Van Der Giessen, E. Alternative explanation of stiffening in cross-linked semiflexible networks. *Physical Review Letters* **95,** 19–22 (2005).

240. Fu, S. Y., Feng, X. Q., Lauke, B. & Mai, Y. W. Effects of particle size, particle/matrix interface adhesion and particle loading on mechanical properties of particulate-polymer composites. *Composites Part B: Engineering* **39,** 933–961 (2008).

241. Ewoldt, R. H. Defining nonlinear rheological material functions for oscillatory shear. *Journal of Rheology* **57,** 177–195 (2013).

242. Hu, J. *et al.* Microgel-reinforced hydrogel films with high mechanical strength and their visible mesoscale fracture structure. *Macromolecules* **44,** 7775–7781 (2011).

243. Meid, J., Friedrich, T., Tieke, B., Lindner, P. & Richtering, W. Composite hydrogels with temperature sensitive heterogeneities: Influence of gel matrix on the volume phase transition of embedded poly-(N- isopropylacrylamide) microgels. *Physical Chemistry Chemical Physics* **13,** 3039–3047 (2011).

244. Meid, J. *et al.* Mechanical properties of temperature sensitive microgel/polyacrylamide composite hydrogels - From soft to hard fillers. *Soft Matter* **8,** 4254–4263 (2012).

245. Retzinger, G. S., DeAnglis, A. P. & Patuto, S. J. Adsorption of fibrinogen to droplets of liquid hydrophobic phases: Functionality of the bound protein and biological implications. *Arteriosclerosis, Thrombosis, and Vascular Biology* **18,** 1948–1957 (1998).

246. Xu, L. C. & Siedlecki, C. A. Effects of surface wettability and contact time on protein adhesion to biomaterial surfaces. *Biomaterials* **28,** 3273–3283 (2007).

247. Van Oosten, A. S. *et al.* Uncoupling shear and uniaxial elastic moduli of semiflexible biopolymer networks: Compression-softening and stretch-stiffening. *Scientific Reports* **6,** 1–9 (2016).

248. Jawerth, L. M. *The Mechanics of Fibrin Networks and Their Alterations by Platelets* PhD thesis (Harvard University, 2013).

249. Bharadwaj, N. A. *Asymptotically nonliner oscillatory shear: theory, modeling, measurements and applications of nonlinear elasticity to stimuli-responsive composites* PhD thesis (University of Illinois at Urbana-Champaign, 2016).

250. Langer, B., Weisel, J., Dinauer, P. A., Nagaswami, C & Bell, W. R. Deglycosylation of fibrinogen accelerates polymerization and increases lateral aggregation of fibrin fibers. *Journal of Biological Chemistry* **263,** 15056–15063 (1988).

251. Ivaneyko, D., Toshchevikov, V. & Saphiannikova, M. Dynamic moduli of magnetosensitive elastomers: a coarse-grained network model. *Soft Matter* **11,** 7627–7638 (2015).

252. Gong, X., Chen, L & Li, J. Study of utilizable magnetorheological elastomers. *International Journal of Modern Physics B* **21,** 4875–4882 (2007).

253. Stepanov, G. *et al.* Effect of a homogeneous magnetic field on the viscoelastic behavior of magnetic elastomers. *Polymer* **48,** 488–495 (2007).

254. Yu, M., Ju, B., Fu, J., Liu, X. & Yang, Q. Influence of composition of carbonyl iron particles on dynamic mechanical properties of magnetorheological elastomers. *Journal of Magnetism and Magnetic Materials* **324,** 2147–2152 (2012).

255. Mitsumata, T., Ohori, S., Honda, A. & Kawai, M. Magnetism and viscoelasticity of magnetic elastomers with wide range modulation of dynamic modulus. *Soft Matter* **9,** 904–912 (2013).

256. Boczkowska, A. & Awietjan, S. F. Smart composites of urethane elastomers with carbonyl iron. *Journal of Materials Science* **44,** 4104–4111 (2009).

257. Deng, H. & Gong, X. Adaptive tuned vibration absorber based on magnetorheological elastomer. *Journal of intelligent material systems and structures* **18,** 1205–1210 (2007).

258. Abdeen, A. A., Lee, J., Bharadwaj, N. A., Ewoldt, R. H. & Kilian, K. A. Temporal Modulation of Stem Cell Activity Using Magnetoactive Hydrogels. *Advanced Healthcare Materials* **5,** 2536–2544 (2016).

259. Filipcsei, G., Csetneki, I., Szilágyi, A. & Zrínyi, M. in *Oligomers - Polymer Composites - Molecular Imprinting* 137–189 (Springer Berlin Heidelberg, Berlin, Heidelberg, 2007). ISBN: 978-3-540-46830-1.

260. Carlson, J. & Jolly, M. R. MR fluid, foam and elastomer devices. *Mechatronics* **10,** 555–569 (2000).

261. Rich, J. P., Lammerding, J., Mckinley, G. H. & Doyle, P. S. Nonlinear microrheology of an aging, yield stress fluid using magnetic tweezers. *Soft Matter* **7,** 9933 (2011).

262. Ivaneyko, Toshchevikov, Saphiannikova & Heinrich. Effects of particle distribution on mechanical properties of magneto-sensitive elastomers in a homogeneous magnetic field. *Condensed Matter Physics* **15,** 33601 (2012).

263. Ivaneyko, D., Toshchevikov, V., Saphiannikova, M. & Heinrich, G. Mechanical properties of magneto-sensitive elastomers: unification of the continuum-mechanics and microscopic theoretical approaches. *Soft Matter* **10,** 2213–2225 (2013).

264. Biller, A. M., Stolbov, O. V. & Raikher, Y. L. Modeling of particle interactions in magnetorheological elastomers. *Journal of Applied Physics* **116,** 114904 (2014).

265. Bozorth, R. M. *Ferromagnetism* (Institute of Electrical and Electronics Engineers, 1978).

266. Mengüç, Y *et al.* in *Robotics and Automation (ICRA), 2013 IEEE International Conference on* (2013), 5309–5316.

267. Rus, D. & Tolley, M. T. *Nature* **521,** 467 (2015).

268. Xiao, C., Jahanian, O., Schnorenberg, A., Slavens, B. & Hsiao-Wecksler, E. in *2017 DMD* (2017), V001T11A021–V001T11A021.

269. Awad, L. N. *et al. Sci. Transl. Med* **9,** eaai9084 (2017).

270. Hinton, T. J. *et al. Sci. Adv* **1,** e1500758 (2015).

271. Feinberg, A. W. *Annu. Rev. Biomed. Eng* **17,** 243–265 (2015).

272. Miao, S. *et al. Mater. Today* (2017).

273. Hu, W., Lum, G. Z., Mastrangeli, M. & Sitti, M. *Nature* (2018).

274. Nawroth, J. C. *et al. Nat. Biotechnol.* **30,** 792 (2012).

275. Park, S.-J. *et al. Science* **353,** 158–162 (2016).

276. Autumn, K. *et al.* Evidence for van der Waals adhesion in gecko setae. *Proceedings of the National Academy of Sciences* **99,** 12252–12256 (2002).

277. Kirmse, R. *et al.* Plasticity of intermediate filament subunits. *PloS one* **5,** e12115 (2010).

278. Higham, T. E., Day, S. W. & Wainwright, P. C. Multidimensional analysis of suction feeding performance in fishes: fluid speed, acceleration, strike accuracy and the ingested volume of water. *Journal of Experimental Biology* **209,** 2713–2725 (2006).

279. Day, S. W., Higham, T. E. & Wainwright, P. C. Time resolved measurements of the flow generated by suction feeding fish. *Experiments in Fluids* **43,** 713–724 (2007).

280. Van Wassenbergh, S. & Aerts, P. Aquatic suction feeding dynamics: insights from computational modelling. *Journal of The Royal Society Interface* **6,** 149–158 (2009).

281. Skorczewski, T., Cheer, A., Cheung, S. & Wainwright, P. C. Use of computational fluid dynamics to study forces exerted on prey by aquatic suction feeders. *Journal of the Royal Society Interface* **7,** 475–484 (2009).

282. Day, S. W., Higham, T. E., Holzman, R. & Van Wassenbergh, S. Morphology, kinematics, and dynamics: the mechanics of suction feeding in fishes. *Integrative and Comparative Biology* **55,** 21–35 (2015).

283. Hatami-Marbini, H & Picu, C. R. in *Advances in Soft Matter Mechanics* 119–145 (Springer, 2012).

284. Schindelin, J *et al.* Fiji: an open-source platform for biological-image analysis. *Nature Methods* **9,** 676–682 (2012).

285. Roy, A, Perfect, E, Dunne, W. M. & McKay, L. D. Fractal characterization of fracture networks: An improved box-counting technique. *Journal of Geophysical Research: Solid Earth* **112** (2007).

286. Harris, J. W. & Stöcker, H. *Handbook of mathematics and computational science* (Springer Science & Business Media, 1998).

287. López-León, T. & Fernández-Nieves, A. Macroscopically probing the entropic influence of ions: Deswelling neutral microgels with salt. *Phys. Rev. E* **75,** 011801 (1 2007).